

**METALORGANIC CHEMICAL VAPOR DEPOSITION OF  
GALLIUM NITRIDE ON SACRIFICIAL SUBSTRATES**

A Dissertation  
Presented to  
The Academic Faculty

By

William Edward Fenwick

In Partial Fulfillment  
Of the Requirements for the Degree  
Doctor of Philosophy in the  
School of Electrical and Computer Engineering

Georgia Institute of Technology

August, 2009

Copyright © William Edward Fenwick, 2009

# Metalorganic Chemical Vapor Deposition of Gallium Nitride on Sacrificial Substrates

Approved by:

**Ian T. Ferguson, Advisor**  
Electrical and Computer Engineering  
Materials Science and Engineering  
*Georgia Institute of Technology*

**Benjamin D.B. Klein**  
Electrical and Computer Engineering  
*Georgia Institute of Technology*

**Linda Milor**  
Electrical and Computer Engineering  
*Georgia Institute of Technology*

**Abdallah Ougazzaden, Co-advisor**  
Electrical and Computer Engineering  
*Georgia Institute of Technology*

**Joseph L.A. Hughes**  
Electrical and Computer Engineering  
*Georgia Institute of Technology*

**Nazanin Bassiri-Gharb**  
Mechanical Engineering  
Materials Science and Engineering  
*Georgia Institute of Technology*

Date Approved: June 8, 2009

*“If we knew what we were doing, it would not be called research, would it?”*

-Albert Einstein

*To my grandfather, Pop'...*

## ACKNOWLEDGEMENTS

I would like to thank my advisor, Prof. Ian Ferguson, for his support and encouragement, and my co-advisor, Prof. Abdallah Ougazzaden, for his guidance. I would also like to thank the members, past and present, of the Solid State Lighting/MOCVD group at Georgia Tech including, but not limited to, Dr. Vincent Woods, Dr. Martin Strassburg, Dr. Ming Pan, Dr. Adam Payne, Dr. Eun Hyun Park, Dr. Shen-Jie Wang, Dr. Hongbo Hu, Dr. David Nicol, Dr. Matthew Kane, Dr. Hun Kang, Dr. Shalini Gupta, Dr. Omkar Jani, Dr. Muhammad Jamil, Dr. Enno Malguth, Dr. Nola Li, Ali Asghar, Andrew Melton, Tahir Zaidi, Tianming Xu, Balakrishnam Jampana, Peter Speirs, Olivier Hamard, Petko Petkov, and Yong Huang for their support and team work. Angela Yvonne also deserves special acknowledgement for all of her time and administrative support.

I am grateful to Dr. Nikolaus Dietz at Georgia State University for his guidance, support, and technical input, and to Dr. Benjamin Klein for his support and technical guidance regarding device simulation. Thanks also to Rick Brown for the technical advice and the welcome distractions.

Those educators who were instrumental in my development as a student and as a person, in particular Ms. Sheila Smith and Mr. Scott Merrell, taught me to ask questions and to seek answers, and have had a lasting impact on my thought processes. Thanks to both of you. I am deeply grateful to my family – my parents and my sister, Kelly – for their love and support. Finally, I would like to thank my wife, Jaime, for her unwavering love and support in finishing this work.

# TABLE OF CONTENTS

<b>LIST OF TABLES .....</b>	<b>x</b>
<b>LIST OF FIGURES .....</b>	<b>xi</b>
<b>LIST OF SYMBOLS AND ABBREVIATIONS .....</b>	<b>xvi</b>
<b>SUMMARY .....</b>	<b>xviii</b>
<b>CHAPTER 1: INTRODUCTION.....</b>	<b>1</b>
1.1    STATE OF THE ART IN SOLID STATE LIGHTING .....	1
1.1.1    Semiconductor Materials for SSL.....	2
1.1.2    GaN Growth Technology.....	7
1.1.3    Design and Fabrication of GaN-based Emitters.....	8
1.1.4    Current Challenges facing SSL .....	10
1.1.4.1    Efficacy and Efficiency.....	10
1.1.4.2    Thermal Management.....	11
1.1.4.3    Color.....	12
1.1.4.4    Cost.....	13
1.2    ALTERNATIVE SUBSTRATES .....	15
1.3    RESEARCH OBJECTIVES.....	17
1.4    CONTRIBUTIONS.....	17
1.5    MATERIAL PROPERTIES.....	18
1.5    SUMMARY.....	18
<b>CHAPTER 2: BACKGROUND .....</b>	<b>21</b>
2.1    SI AS A SUBSTRATE FOR GAN EPITAXY.....	21
2.1.1    Advantages of Silicon as a Substrate.....	21
2.1.2    Challenges for GaN growth on Silicon.....	22
2.1.3    Literature Review.....	24
2.2    ZNO AS A SUBSTRATE FOR GAN EPITAXY.....	34
2.2.1    Advantages of ZnO as a Substrate.....	34
2.2.2    Challenges for GaN Growth on ZnO.....	36
2.2.3    Literature Review.....	36
2.3    SUMMARY.....	39
<b>CHAPTER 3: EXPERIMENTAL EQUIPMENT AND TECHNIQUES .....</b>	<b>40</b>
3.1    MODELING.....	40
3.2    GROWTH.....	40
3.2.1    MOCVD Growth.....	41
3.2.1.1    Thermodynamics.....	41
3.2.1.2    Kinetics .....	43
3.2.1.3    Fluid Dynamics and Mass Transport .....	46
3.2.1.4    MOCVD Growth of GaN.....	48
3.2.2    ALD Growth.....	54
3.3    CHARACTERIZATION .....	55
3.3.1    Structural Characterization.....	55
3.3.1.1    X-ray Diffraction (XRD).....	56
3.3.1.2    X-ray Reflectivity (XRR) .....	58

3.3.1.3	Raman Spectroscopy.....	59
3.3.2	Surface Characterization.....	61
3.3.2.1	Atomic Force Microscopy (AFM) .....	62
3.3.2.2	Scanning Electron Microscopy (SEM).....	63
3.3.2.3	Transmission Electron Microscopy (TEM).....	63
3.3.3	Optical Characterization.....	64
3.3.3.1	Photoluminescence Spectroscopy (PL).....	64
3.3.3.2	Optical Transmission.....	65
3.3.4	Electrical Characterization .....	66
3.3.4.1	Hall Effect Measurement .....	66
3.3.4.2	Secondary Ion Mass Spectrometry (SIMS).....	67
3.3.5	Device Characterization.....	69
3.3.5.1	Current-Voltage (I-V) Measurement .....	69
3.3.5.2	Electroluminescence (EL).....	70
3.3.5.3	Optical Power Measurements.....	71
3.4	DEVICE PROCESSING.....	71
3.4.1	Annealing.....	73
3.4.2	Photolithography .....	73
3.4.3	Etching.....	74
3.4.4	Metal Deposition .....	74
3.5	SUMMARY.....	75
<b>CHAPTER 4: MOCVD GROWTH OF GaN AND <math>\text{In}_x\text{Ga}_{1-x}\text{N}</math> ON ZnO .....</b>		<b>76</b>
4.1	INITIAL CHALLENGES.....	76
4.1.1	Reactivity of ZnO in $\text{H}_2$ .....	76
4.1.1.1	Carrier Gases.....	77
4.1.1.2	Nitrogen Precursors.....	79
4.1.2	Diffusion.....	81
4.1.2.1	Zinc and Oxygen Diffusion into GaN.....	81
4.2	$\text{In}_x\text{Ga}_{1-x}\text{N}$ GROWTH ON ZNO .....	87
4.2.1	Structural Properties.....	87
4.2.2	Optical Properties.....	93
4.2.3	Impurity Diffusion .....	93
4.3	GROWTH ON ZNO/SAPPHIRE TEMPLATES.....	96
4.4	SUMMARY.....	97
<b>CHAPTER 5: DIFFUSION BLOCKING.....</b>		<b>98</b>
5.1	FERMI LEVEL PINNING .....	98
5.1.1	Zinc Diffusion in AlAs – GaAs .....	98
5.1.2	Point Defect Formation in GaN.....	100
5.1.3	Impurity Diffusion in GaN.....	102
5.2	ALN BUFFER LAYERS .....	104
5.2.1	Structural Properties.....	104
5.2.2	Optical Properties.....	108
5.3	$\text{Al}_x\text{Ga}_{1-x}\text{N}/\text{GAN}$ SUPERLATTICES .....	111
5.3.1	Structural Properties.....	112
5.3.2	Optical Properties.....	116
5.3.3	Impurity Diffusion .....	116
5.4	$\text{In}_x\text{Ga}_{1-x}\text{N}/\text{GAN}$ MULTIPLE QUANTUM WELLS.....	119

5.4.1	Structural Properties.....	119
5.4.2	Optical Properties.....	122
5.5	ALD-GROWN $\text{Al}_2\text{O}_3$ INTERLAYERS.....	122
5.5.1	Growth Parameters.....	124
5.5.2	Impurity Diffusion.....	125
5.6	SUMMARY.....	128
<b>CHAPTER 6: ATOMIC LAYER DEPOSITION OF <math>\text{Al}_2\text{O}_3</math> ON Si.....</b>		<b>129</b>
6.1	AS-GROWN FILMS.....	129
6.2	ANNEALING STUDIES.....	131
6.2.1	Structural Properties.....	131
6.2.2	Surface Morphology.....	134
6.3	SUMMARY.....	141
<b>CHAPTER 7: MOCVD GROWTH OF GaN ON SILICON.....</b>		<b>142</b>
7.1	MOCVD GROWTH OF GaN ON SILICON.....	142
7.1.1	Buffer Layers.....	142
7.1.2	Si-doped GaN Layers.....	149
7.1.3	LT-AlN Interlayers.....	151
7.1.3.1	Structural Properties.....	151
7.1.3.2	Optical Properties.....	153
7.1.3.3	Surface Morphology.....	156
7.1.4	Progress and Remaining Issues.....	158
7.2	MOCVD GROWTH OF GaN ON ALD- $\text{Al}_2\text{O}_3$ /SILICON.....	160
7.2.1	Fundamental Growth Parameters.....	160
7.2.1.1	Carrier Gas.....	161
7.2.1.2	Temperature Ramp Time.....	161
7.2.1.3	Buffer Layer.....	161
7.2.2	$\text{Al}_x\text{Ga}_{1-x}\text{N}$ /GaN Superlattices on ALD- $\text{Al}_2\text{O}_3$ /Silicon.....	166
7.2.3	Effects of the ALD- $\text{Al}_2\text{O}_3$ layer on Silicon.....	168
7.2.3.1	Structural Properties.....	168
7.2.3.2	Optical Properties.....	177
7.2.3.3	Surface Morphology.....	179
7.3	SUMMARY.....	181
<b>CHAPTER 8: GaN-BASED DEVICES ON ZnO AND Si.....</b>		<b>184</b>
8.1	DEVICES ON ZnO.....	184
8.1.1	Structures.....	184
8.1.2	Luminescence.....	185
8.1.3	Electrical Properties.....	185
8.1.4	Processing.....	188
8.2	DEVICES ON SILICON.....	188
8.2.1	Structures.....	188
8.2.2	Electrical Properties.....	191
8.2.3	Optical Properties.....	195
8.2.4	Efficiency.....	197
8.4	SUMMARY.....	199
<b>CHAPTER 9: MODELING OF GaN-BASED DEVICES ON ZnO AND Si.....</b>		<b>201</b>
9.1	POLARIZATION IN NITRIDES.....	201

9.2	GAN-BASED DEVICES ON ZnO.....	206
9.2.1	Device Structure on ZnO.....	206
9.2.2	Modeled Device Performance.....	208
9.3	SUMMARY.....	211
<b>CHAPTER 10: CONCLUSIONS AND FUTURE WORK.....</b>		<b>213</b>
10.1	CONCLUSIONS.....	213
10.2	FUTURE WORK.....	215
10.2.1	GaN Growth on ZnO.....	216
10.2.1	GaN Growth on Silicon.....	216
10.3	SUMMARY.....	218
<b>BIBLIOGRAPHY.....</b>		<b>219</b>

## LIST OF TABLES

Table 1.1:	Properties of various materials used as substrates for GaN epitaxy.....	5
Table 1.2:	Cost of ownership model for GaN MOCVD production systems, showing substrate-related costs.....	16
Table 1.3:	Material properties used in this work.....	20
Table 5.1:	Bond strength for AlN, GaN, and InN.....	105
Table 6.1:	Summary of ex-situ annealing conditions for ALD-grown Al <sub>2</sub> O <sub>3</sub> layers on Si(111).....	132
Table 6.2:	EDS data showing composition of pits in Al <sub>2</sub> O <sub>3</sub> surface. ....	140
Table 7.1:	Material properties obtained on bare silicon by MOCVD. ....	159
Table 7.2:	Dependence of the GaN (002) FWHM on carrier gas ratio for GaN thin films on both silicon and ALD-Al <sub>2</sub> O <sub>3</sub> /Si(111) substrates.....	164
Table 7.3:	Material properties obtained using various approaches on silicon.....	183
Table 9.1:	Spontaneous polarization values, lattice parameters, elastic coefficients, dielectric coefficients, and piezoelectric coefficients used in this work.....	203
Table 9.2	Simulated performance characteristics of LEDs on GaN and ZnO substrates.....	212

## LIST OF FIGURES

Figure 1.1:	Bandgap v. lattice constant for significant semiconductor materials. (from [5]) .....	3
Figure 1.2:	External quantum efficiency (EQE) as a function of wavelength for nitride and phosphide materials. (from [16]) .....	5
Figure 1.3:	Substrates used in GaN-based LED production (from [15]) .....	6
Figure 1.4:	Typical surface-emitting LED structure used in this work, showing p-type and n-type contacts from the top. ....	9
Figure 1.5:	Schematic of a phosphor-coated white LED. (from [40]) .....	14
Figure 1.6:	Power spectrum of a phosphor-coated white LED showing the blue emission peak from the LED and the yellow phosphor peak. ....	14
Figure 2.1:	Thermal expansion coefficients for GaN and some common substrates for GaN epitaxy as a function of temperature. ....	23
Figure 2.2:	SEM images of GaN grown on nano-faceted silicon substrates showing preferential nucleation on the Si(111) surfaces. (from [59]) .....	25
Figure 2.3:	TEM image of a GaN layer on silicon using three LT-AlN interlayers. (from [69]) .....	29
Figure 2.4:	TEM image of a GaN layer on Si(111) using three $Al_xGa_{1-x}N$ layers on a $Si_xN_y$ interlayer. (from [73]) .....	31
Figure 2.5:	Schematic of a structure studied for monolithic integration of MBE-grown GaAs with silicon. (from [80]) .....	35
Figure 2.6:	(top) Band bending induced by polarization effects in bulk ZnO crystals. (from [83]) (bottom) Average band offset at the GaN/ZnO interface. (from [85]) .....	38
Figure 3.1:	Dependence of growth rate on growth temperature for GaN using different $NH_3$ precursors. Lines denote kinetically limited growth (lower temperatures) and mass transport-limited growth (higher temperatures). (from [92]) .....	44
Figure 3.2:	Temperature-dependent decomposition of TMGa under various atmospheres. (from [95]) .....	50
Figure 3.3:	In-site reflectivity measured during the growth of a standard $2\mu m$ -thick GaN template on sapphire. ....	51
Figure 3.4:	Modified EMCORE D-125 GaN MOCVD system used in this work. ....	53
Figure 3.5:	Diffraction of X-rays from a thin film surface showing the Bragg angle, $\theta$ .....	57
Figure 3.6:	Raman vibrational modes in a wurtzite crystal. The $B_1$ modes are 'silent' in Raman spectroscopy .....	60

Figure 3.7:	Typical LED structure used in this work. P-type contacts are the large circles, and n-type contacts are the smaller circles. Each device is 350 $\mu$ m on a side.....	72
Figure 4.1:	Etch rate of ZnO in a hydrogen atmosphere. A typical GaN growth temperature is marked for reference. ....	78
Figure 4.2:	XRD pattern of GaN grown on ZnO using DMHy as a nitrogen precursor. The shoulder on the high angle side is due to the GaN (002) reflection.....	80
Figure 4.3:	(a)XRD pattern of GaN grown on ZnO using NH <sub>3</sub> as a nitrogen precursor. (b) Unpolarized Raman spectrum of the same sample.....	83
Figure 4.4:	RT-PL spectrum of a GaN layer grown on ZnO using a LT-GaN nucleation layer.....	84
Figure 4.5:	SIMS depth profile of a GaN layer on ZnO showing zinc, oxygen, and carbon impurity concentrations.....	86
Figure 4.6:	XRD 2 $\theta$ - $\omega$ scans of InGaN epilayers grown with and without a LT-GaN nucleation layer.....	88
Figure 4.7:	XRD 2 $\theta$ - $\omega$ scan of a single-phase InGaN thin film grown on ZnO(0002). ....	90
Figure 4.8:	Raman scattering spectra of GaN and InGaN layers grown on ZnO substrates.....	92
Figure 4.9:	Polarized Raman spectra from a thick In <sub>x</sub> Ga <sub>1-x</sub> N layer on ZnO. Polarization dependence follows that of the GaN A <sub>1</sub> (LO). ....	92
Figure 4.10:	RT-PL spectra of GaN thin films grown on ZnO substrates both with and without LT-GaN nucleation layers.....	94
Figure 4.11:	SIMS depth profile of a thin InGaN layer on ZnO.....	95
Figure 5.1:	Calculated formation energies for various intrinsic defects in GaN. (from [118]).....	101
Figure 5.2:	2DEG density as a function of AlGaIn thickness at an AlGaIn/GaN interface. (from [120]).....	103
Figure 5.3:	(a) XRD 2 $\theta$ - $\omega$ scan showing a shoulder on the high angle side of the ZnO (002), which is related to the GaN (002) reflection.....	105
Figure 5.4:	Raman spectra of GaN thin films on ZnO grown using different V/III ratios.....	106
Figure 5.5:	RT-PL spectrum of a GaN thin film on ZnO using an AlN buffer layer.....	109
Figure 5.6:	ZnO-AlN-GaN (top) and ZnO-GaN (bottom) band offsets calculated from PL data. ....	110
Figure 5.7:	(a) XRD rocking curve scan and simulated curve of AlGaIn/GaN superlattice on GaN/sapphire. (b) Rocking curve scans of AlGaIn/GaN superlattices grown under different conditions on sapphire.....	113

Figure 5.8:	XRD rocking curve scans of AlGa <sub>x</sub> N/GaN superlattices grown on ZnO substrates at different temperatures. Samples ZA, ZB, and ZC were grown at 550, 770, and 820 °C, respectively. ....	115
Figure 5.9:	RT-PL of AlGa <sub>x</sub> N/GaN samples grown on ZnO (0001) substrates. Samples ZA, ZB, and ZC were grown at 550, 770, and 820 °C, respectively. ....	117
Figure 5.10:	SIMS depth profile of an AlGa <sub>x</sub> N/GaN superlattice grown on ZnO at 770 °C. ....	118
Figure 5.11:	XRD of five multiple quantum wells on GaN/sapphire template. ....	120
Figure 5.12:	Basic structure used to investigate In <sub>x</sub> Ga <sub>1-x</sub> N/GaN MQWs on ZnO. ....	121
Figure 5.13:	XRD of multiple quantum well structure on ZnO. ....	121
Figure 5.14:	RT-PL of an InGa <sub>x</sub> N/GaN MQW structure on ZnO. ....	123
Figure 5.15:	(a) Low-temperature GaN layer grown on AlGa <sub>x</sub> N/GaN superlattice on Al <sub>2</sub> O <sub>3</sub> /ZnO. (b) High-temperature GaN layer grown on AlGa <sub>x</sub> N/GaN superlattice on Al <sub>2</sub> O <sub>3</sub> /ZnO. ....	126
Figure 5.16:	SIMS depth profile of a 1 um-thick GaN layer on [AlGa <sub>x</sub> N/GaN]/Al <sub>2</sub> O <sub>3</sub> /ZnO. ....	127
Figure 6.1:	SEM image of the surface of an ALD-grown Al <sub>2</sub> O <sub>3</sub> layer on Si(111). ....	130
Figure 6.2:	XRD 2θ-ω scans of annealed ALD-grown Al <sub>2</sub> O <sub>3</sub> layers on Si(111). ....	132
Figure 6.3:	Dependence of the XRD FWHM of the Al <sub>2</sub> O <sub>3</sub> (104) peak on layer thickness and annealing temperature in air (a), and nitrogen (b). Dependence of XRD FWHM of the Al <sub>2</sub> O <sub>3</sub> (110) peak on layer thickness and annealing temperature in air (c), and nitrogen (d). Note the sharp decrease in linewidth for thicker layers annealed at high temperatures in air. ....	133
Figure 6.4:	SEM images of the surface of a 10nm ALD-grown Al <sub>2</sub> O <sub>3</sub> layer on Si(111). ....	135
Figure 6.5:	SEM images of the surface of a 50nm ALD-grown Al <sub>2</sub> O <sub>3</sub> layer on Si(111). ....	136
Figure 6.6:	SEM images of the surface of a 100nm ALD-grown Al <sub>2</sub> O <sub>3</sub> layer on Si(111). ....	138
Figure 6.7:	Arrhenius plot of pit density v. reciprocal temperature. The behavior suggests a thermally activated process. ....	140
Figure 7.1:	AlN (002) FWHM as a function of V/III ratio. ....	144
Figure 7.2:	SEM images of GaN layers on Si using AlN buffer layers at various stages of growth. ....	145
Figure 7.3:	(a) GaN (002) rocking curve scan on HT-AlN/Si. (b) GaN (102) rocking curve scan on HT-AlN/Si. ....	147

Figure 7.4:	(a) RT-PL spectrum of a GaN layer on silicon with simple HT-AlN buffer layer. (b) AFM image of the a GaN layer on silicon with simple HT-AlN buffer layer. ....	148
Figure 7.5:	(a) 20x optical microscope image of an undoped GaN layer on bare Si. (b) 20x optical microscope image of a Si-doped GaN layer on bare silicon. ....	150
Figure 7.6:	XRD scans of the (002) (a) and (102) (b) reflections of a GaN thin film grown on silicon using LT-AlN interlayers.....	152
Figure 7.7:	Raman spectrum of a GaN thin film grown on silicon using LT-AlN interlayers to relieve strain and increase crystal quality.....	154
Figure 7.8:	(a) RT-PL spectra of GaN layers on silicon using a simple HT-AlN buffer layer, and LT-AlN interlayers. (b) Normalized spectra showing the redshift from the unstrained bandedge position.....	155
Figure 7.9:	AFM images of a GaN template on sapphire (a), a GaN thin film on silicon with a simple HT-AlN buffer layer (b), and a GaN thin film on silicon using LT-AlN interlayers (c). ....	157
Figure 7.10:	Dependence of the GaN (002) FWHM on carrier gas ratio for GaN thin films on both silicon and ALD-Al <sub>2</sub> O <sub>3</sub> /Si(111) substrates.....	162
Figure 7.11:	(a) SEM image of a HT-AlN buffer surface on Si(111). (b) SEM image of a LT-GaN buffer layer on Si(111).....	164
Figure 7.12:	Dependence of the GaN (002) linewidth on AlN thickness.....	165
Figure 7.13:	(a) XRD 2θ-ω scan of GaN on bare silicon using two AlGaN layers. (b) Same structure as (a), on ALD-Al <sub>2</sub> O <sub>3</sub> /Si. (c) XRD 2θ-ω scan of GaN on bare silicon using three AlGaN layers. (d) Same structure as (c), on ALD-Al <sub>2</sub> O <sub>3</sub> /Si.....	167
Figure 7.14:	Dependence of the GaN (002) linewidth on ALD-Al <sub>2</sub> O <sub>3</sub> thickness.....	169
Figure 7.15:	Williamson-Hall plot of the (002), (004), and (006) reflections of GaN thin films on bare silicon and ALD-Al <sub>2</sub> O <sub>3</sub> /Si.....	171
Figure 7.16:	Lateral coherence length and tilt angle for GaN thin films as a function of Al <sub>2</sub> O <sub>3</sub> thickness.....	171
Figure 7.17:	Calculated screw dislocation density as a function of ALD-Al <sub>2</sub> O <sub>3</sub> thickness.....	173
Figure 7.18:	Unpolarized Raman spectra of GaN thin films grown on silicon using various buffer layers and interlayers.....	174
Figure 7.19:	Shift of the GaN E <sub>2</sub> (high) mode with varying ALD-Al <sub>2</sub> O <sub>3</sub> thickness.....	176
Figure 7.20:	Intensity of unidentified peaks as a function of ALD-Al <sub>2</sub> O <sub>3</sub> thickness.....	176
Figure 7.21:	Bandedge position as a function of ALD-Al <sub>2</sub> O <sub>3</sub> thickness.....	178
Figure 7.22:	(a) AFM image of a GaN thin film on HT-AlN/Si. (b) AFM image of a GaN thin film on 5nm ALD-Al <sub>2</sub> O <sub>3</sub> /Si. (c) AFM image of a GaN thin film on 20nm ALD-Al <sub>2</sub> O <sub>3</sub> /Si. ....	180
Figure 7.23:	Total consumption of precursors using the three approaches compared in this chapter.....	183

Figure 8.1:	LED structure investigated on ZnO.....	186
Figure 8.2:	(a) PL of $\text{In}_{0.18}\text{Ga}_{0.82}\text{N}$ -based LED on GaN/sapphire. (b) PL of $\text{In}_{0.18}\text{Ga}_{0.82}\text{N}$ -based LED on ZnO.....	186
Figure 8.3:	I-V curve of $\text{In}_{0.18}\text{Ga}_{0.82}\text{N}$ LED on a GaN/sapphire template.....	187
Figure 8.4:	(a) In-situ reflectivity showing the growth of a green GaN LED on silicon. (b) In-situ reflectivity curve showing the growth of a blue GaN LED on silicon. ....	189
Figure 8.5:	(a) XRD $2\theta$ - $\omega$ scan of a green GaN LED on silicon. (b) XRD $2\theta$ - $\omega$ scan of a blue GaN LED on silicon. ....	190
Figure 8.6:	RT-PL of green (a) and blue (b) GaN-based LEDs on ALD- $\text{Al}_2\text{O}_3/\text{Si}$ .....	192
Figure 8.7:	Photos of GaN-based LEDs on GaN/ $\text{Al}_2\text{O}_3/\text{Si}$ (top) and GaN/Sapphire (bottom).....	193
Figure 8.8:	I-V curves for GaN LEDs on GaN/ $\text{Al}_2\text{O}_3/\text{Si}(111)$ and GaN/sapphire. ....	194
Figure 8.9:	EL spectra for GaN LEDs on GaN/Sapphire (a) and GaN/ $\text{Al}_2\text{O}_3/\text{Si}(111)$ (b). ....	196
Figure 8.10:	L-I curves for GaN LEDs showing a higher efficiency at high drive currents for the device on GaN/ $\text{Al}_2\text{O}_3/\text{Si}(111)$ compared to that on GaN/Sapphire. ....	198
Figure 8.11:	IQE as a function of temperature GaN LEDs on GaN/ $\text{Al}_2\text{O}_3/\text{Si}(111)$ and on GaN/Sapphire. Inset shows IQE as a function of wavelength for GaN LEDs on ALD- $\text{Al}_2\text{O}_3/\text{Si}$ . ....	198
Figure 8.12:	EQE of GaN-based LEDs on GaN/ $\text{Al}_2\text{O}_3/\text{Si}(111)$ and GaN/Sapphire.....	200
Figure 9.1:	$\text{In}_{0.18}\text{Ga}_{0.82}\text{N}$ LED simulated on both ZnO and GaN substrates.....	207
Figure 9.2:	Electric field distribution in $\text{In}_{0.18}\text{Ga}_{0.82}\text{N}$ -based LEDs on both ZnO (top) and GaN (bottom).....	207
Figure 9.3:	I-V curves of $\text{In}_{0.18}\text{Ga}_{0.82}\text{N}$ -based LEDs simulated on both ZnO (solid line) and GaN (dashed line).....	209
Figure 9.4:	Electroluminescence intensity of $\text{In}_{0.18}\text{Ga}_{0.82}\text{N}$ -based LEDs on ZnO (red) and GaN (black). ....	209
Figure 9.5:	Internal quantum efficiency of $\text{In}_{0.18}\text{Ga}_{0.82}\text{N}$ -based LEDs on ZnO (red) and GaN (black). Note the higher efficiency on ZnO.....	210

## LIST OF SYMBOLS AND ABBREVIATIONS

$\alpha$	thermal expansion coefficient
$\delta_0$	boundary layer thickness
$\epsilon$	dielectric constant
$X$	light extraction efficiency
$\eta_{\text{ext}}$ , EQE	external quantum efficiency
$\eta_{\text{int}}$ , IQE	internal quantum efficiency
$\chi$	light extraction efficiency
$\mu_i$	chemical potential
$\lambda$	wavelength
$\theta$	diffraction angle
$\Theta_i$	fraction of occupied sites for component $i$
$\rho_i$	mass density
$\omega$	rotation speed
$a$	a-axis lattice parameter
$a_i$	activity coefficient
ALD	atomic layer deposition
$\text{Al}_x\text{Ga}_{1-x}\text{N}$	aluminum gallium nitride with aluminum composition ‘x’
$c$	c-axis [0001] lattice parameter
$c_{13}$	piezoelectric coefficient
$c_{33}$	piezoelectric coefficient
$d$	spacing between atoms
$e_{31}$	elastic coefficient
$e_{33}$	elastic coefficient
$E_a$	activation energy
$E_{b,w}$	Electric field in well (w) and barrier (b)
$E_c$	conduction band minimum
$E_g$	bandgap energy
$E_v$	valence band maximum
$G$	Gibbs free energy
$h k l$	Miller indices
$H$	enthalpy
$\text{In}_x\text{Ga}_{1-x}\text{N}$	indium gallium nitride with indium composition ‘x’
$k$	rate constant
$k$	Boltzmann’s constant
$L$	layer thickness
LED	light emitting diode
MOCVD	metalorganic chemical vapor deposition
$n$	index of refraction
$n_i$	molar concentration of component $i$
$P_{\text{tot}}$	Total polarization
$P_{\text{sp}}$	Spontaneous polarization
$P_{\text{pz}}$	Piezoelectric polarization
$q$	conductive heat flux
$q$	electronic charge

$R$	gas constant
RGB	red – green – blue
$S$	entropy
$\text{Si}_x\text{N}_y$	silicon nitride
SSL	solid state lighting
$T$	temperature
$v$	average velocity
$V$	voltage
$V_0$	junction potential

## SUMMARY

GaN-based light emitting diodes (LEDs) face several challenges if the technology is to continue to make a significant impact in general illumination, and on technology that has become known as solid state lighting (SSL). Two of the most pressing challenges for the continued penetration of SSL into traditional lighting applications are efficacy and total lumens from the device, and their related cost. The development of alternative substrate technologies is a promising avenue toward addressing both of these challenges, as both GaN-based device technology and the associated metalorganic chemical vapor deposition (MOCVD) technology are already relatively mature technologies with a well-understood cost base. Zinc oxide (ZnO) and silicon (Si) are among the most promising alternative substrates for GaN epitaxy. These substrates offer the ability to access both higher efficacy and lumen devices (ZnO) at a much reduced cost. This work focuses on the development of MOCVD growth processes to yield high quality GaN-based materials and devices on both ZnO and Si.

ZnO is a promising substrate for growth of low defect-density GaN because of its similar lattice constant and thermal expansion coefficient. The major hurdles for GaN growth on ZnO are the instability of the substrate in a hydrogen atmosphere, which is typical of nitride growth conditions, and the inter-diffusion of zinc and oxygen from the substrate into the GaN-based epitaxial layer. A process was developed for the MOCVD growth of GaN and  $\text{In}_x\text{Ga}_{1-x}\text{N}$  on ZnO that attempted to address these issues. The structural and optical properties of these films were studied using various techniques. X-ray diffraction (XRD) showed the growth of wurtzite GaN on ZnO, and room-temperature photoluminescence (RT-PL) showed near bandedge luminescence from the GaN and  $\text{In}_x\text{Ga}_{1-x}\text{N}$  layers. However, high zinc and oxygen concentrations due to interdiffusion near the ZnO substrate remained an issue; therefore, the diffusion of zinc and oxygen into the

subsequent GaN layer was studied in more detail. Several approaches were investigated – for example, transition layers such as  $\text{Al}_2\text{O}_3$  and  $\text{Al}_x\text{Ga}_{1-x}\text{N}/\text{GaN}$  – to minimize diffusion of these impurities into the GaN layer.

Silicon, due to its prevalence, is the most promising material for the development of an inexpensive, large-area substrate technology. The challenge in MOCVD growth of GaN on Si is the tensile strain induced by the lattice and thermal mismatch between GaN and Si and the formation of anti-phase boundaries. Typical approaches to solve these problems involve complicated and multiple buffer layer structures, which lead to relatively slow growth rates. In this work, a thin atomic layer deposition (ALD)-grown  $\text{Al}_2\text{O}_3$  interlayer was employed to relieve strain and increase material quality while also simplifying the growth process. While some residual strain was still observed in the GaN material by XRD and PL, the use of this oxide interlayer leads to an improvement in thin film quality as seen by a reduction in both crack density ( $<1 \text{ mm}^{-2}$ ) on ALD- $\text{Al}_2\text{O}_3/\text{Si}$ ) and screw dislocation density (from  $3 \times 10^9 \text{ cm}^{-2}$  on bare Si to  $2 \times 10^8 \text{ cm}^{-2}$  on ALD- $\text{Al}_2\text{O}_3/\text{Si}$ ) in the GaN films.

A side-by-side comparison of GaN-based multiple quantum well LEDs grown on sapphire and on  $\text{Al}_2\text{O}_3/\text{Si}$  shows similar performance characteristic for both device structures. A redshift in peak emission wavelength was also observed on silicon compared to sapphire, and this is attributed to higher indium content due to the slight tensile strain in the layers on silicon. IQE of the devices on silicon is  $\sim 32\%$  as measured by LT-PL, compared to  $\sim 37\%$  on sapphire, but this difference can be assigned to the difference in indium compositions. These results show a great promise toward an inexpensive, large-area, silicon-based substrate technology for MOCVD growth of the next generation of GaN-based optoelectronic devices for SSL and other applications.

## CHAPTER 1: INTRODUCTION

The development of blue and, in particular, white light emitting diodes (LEDs) in the past decade has given rise to solid state light (SSL) sources designed for general illumination. These sources promise significant savings in energy and cost while maintaining performance comparable to incandescent sources and more recently fluorescents (both tube and contact). Several technical issues remain, however, if solid state sources are to make a significant penetration into the general lighting market, and the most pressing of these are efficacy, thermal management, and color temperature. These issues must be addressed on multiple fronts in order to develop sustainable solid state light sources that are competitive in the general lighting market. Solid state lighting provides one possible route for sustainable 'green' sources that do not suffer the low efficacy of incandescent bulbs (10-15 lm/W) or the residual toxicity of mercury in compact fluorescents.

### 1.1 State of the Art in Solid State Lighting

The last decade has seen the development of high-brightness LEDs, both RGB and white, and their use in lighting applications ranging from signaling and automotive lighting to, more recently, illumination in residential and commercial buildings. [1] The two core areas of development in this technology have been materials and device growth, and device design and fabrication, and these will be discussed in this chapter. The current challenges before the scientific and engineering communities will be laid out here, with the aim of determining how to address these issues and push this technology toward a larger share of the general illumination market.

### 1.1.1 Semiconductor Materials for SSL

One of the most fundamental properties of a semiconductor material is its bandgap. The value of the energy gap determines the color of light emitted from the semiconductor and, thus, its usefulness in optoelectronic applications. A wide range of semiconductor material systems has been investigated over the past century for use in microelectronic and optoelectronic applications, Figure 1.1. The classic semiconductor material that has enabled the microelectronic revolution and had driven Moore's Law is silicon. However, silicon has an indirect bandgap, which means it neither absorbs nor emits light strongly, limiting its usefulness in optoelectronic applications. In addition, semiconductor materials such as silicon and germanium have narrow bandgaps that are outside the visible region. The need for semiconductor materials that strongly emit light and operate in the visible region has required the development of III-V compound semiconductor materials, Figure 1.1. Some of these materials and related devices, such as GaInAs/InP have become the backbone of the optical fiber network, while others such as the AlGaAs/GaAs and AlGaInP material systems have enabled red and other colored emitters such as LEDs and LASERs. Ultraviolet (UV), blue, and green LEDs are based on the III-V semiconductor GaN and its alloys with indium ( $\text{In}_x\text{Ga}_{1-x}\text{N}$ ) and aluminum ( $\text{Al}_x\text{Ga}_{1-x}\text{N}$ ). As shown in Figure 1.1, the bandgaps of the ternary alloys making up the nitride system span the spectrum from infrared (IR) to UV. This wide range of emission wavelengths is a major reason for the use of nitride semiconductors in optoelectronic applications, particularly in the blue and UV regions, as well as in white LEDs.

Nitride semiconductors, however, face several key challenges that have limited their performance to date. Polarization effects play a role in reducing device efficiency, as nitrides are polar materials along the (002) direction.[2-4] Polarization-induced electric fields in

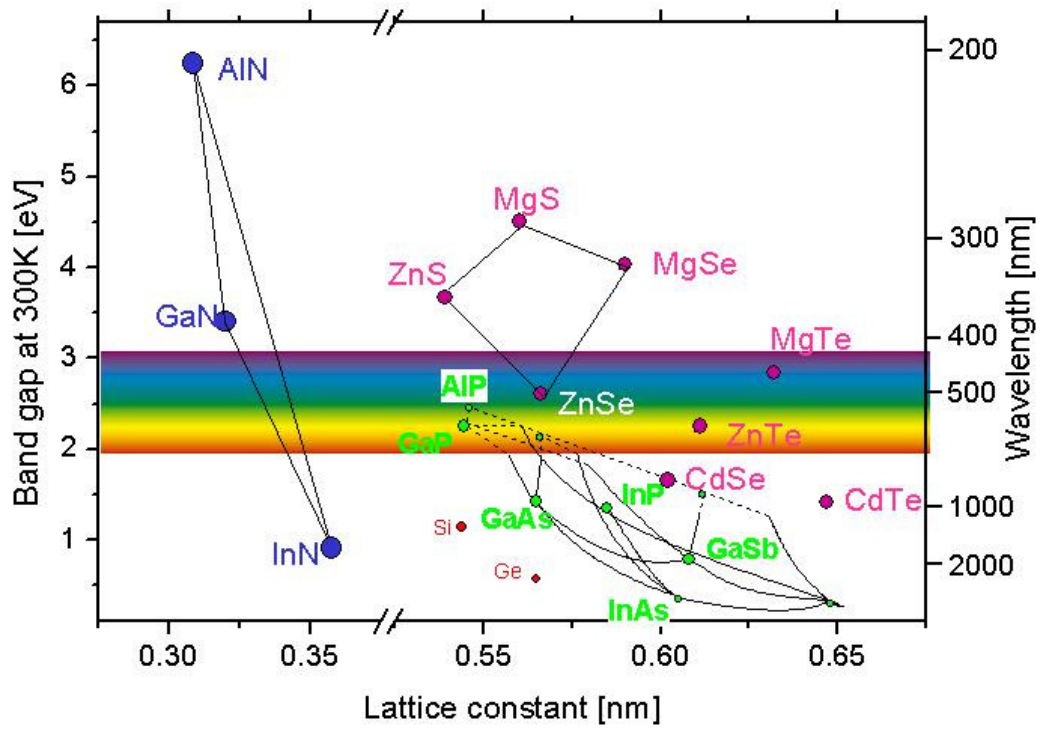


**Figure 1.1:** Bandgap v. lattice constant for significant semiconductor materials. (from [5])

GaN-based devices often lead to spatial separation of electrons and holes in the active region of LEDs, decreasing radiative recombination rates and, thus, efficiency.[6,7]

Another issue is the decrease in efficiency with higher indium content, Figure 1.2. As shown in Figure 1.1, indium is often incorporated into GaN to form an  $\text{In}_x\text{Ga}_{1-x}\text{N}$  alloy with a lower bandgap, allowing for blue and green emitters. Indium incorporation, however, often leads to a significant drop in LED efficiency toward the green region. This region is often called the “Green Gap” because most other III-V optoelectronic materials also lose efficiency in this region, but for different reasons. Though the physical mechanism for this drop in efficiency is not completely understood at this time and is still an issue of discussion within the community, it has been attributed to, for example, carrier delocalization in indium-rich regions [8,9] and carrier leakage at high current density[10]. Defect densities are also much higher, on average, in nitride thin films ( $10^8 - 10^{10} \text{ cm}^{-2}$ ) than in other semiconductor materials such as silicon (Si;  $\sim 0 \text{ cm}^{-2}$ ) or gallium arsenide (GaAs;  $10^2 - 10^4 \text{ cm}^{-2}$ ). [11-14]

The significantly higher defect densities in nitrides stem from the lattice mismatch between GaN thin films and the common substrates used for GaN epitaxy: c-plane sapphire and silicon carbide (SiC). Table 1.1 shows a summary of the pertinent physical properties and cost per unit area of various substrates used in GaN growth, both commercially and in research. Sapphire is by far the most common commercially used substrate for GaN-based LED growth, with SiC taking up the rest of the market, Figure 1.3.[15] The high defect densities induced by the large lattice and thermal mismatches on these substrates leave room for significant improvement in GaN-based devices. ZnO, in particular, is promising because of its lattice and thermal properties, which are similar to those of GaN.

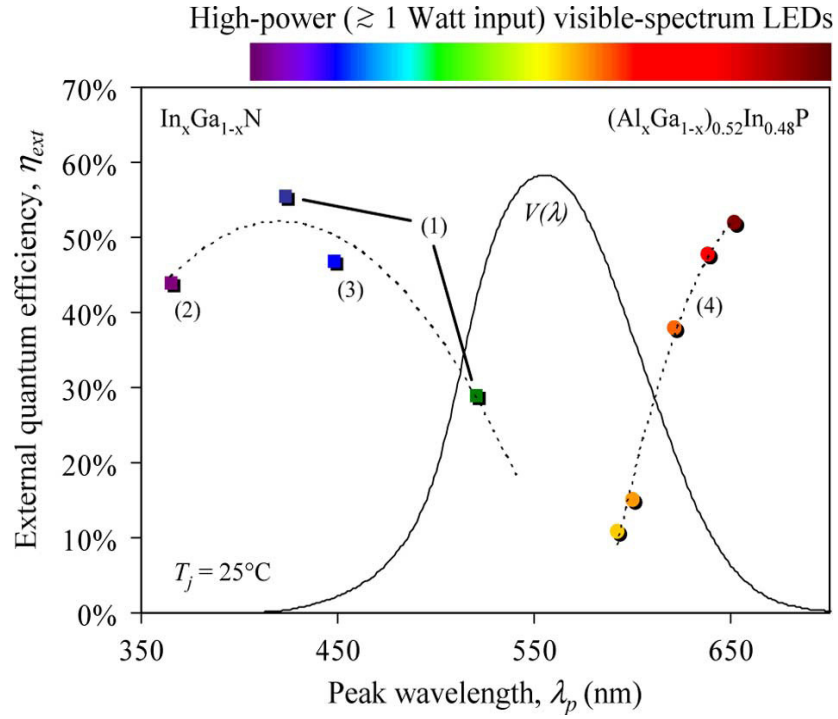


**Figure 1.2:** External quantum efficiency (EQE) as a function of wavelength for nitride and phosphide materials. (from [16])

Table 1.1: Properties of various materials used as substrates for GaN epitaxy.

<b>Material Parameters</b>			
	$a$ (Å)	$\alpha$ ( $\times 10^{-6} \text{ K}^{-1}$ )	Cost (\$/in <sup>2</sup> )
<i>GaN</i>	3.189	5.59	--
<i>Sapphire</i>	2.777*	8.4	12.73
<i>SiC</i>	3.0817	2.892	2,064.51
<i>Si(111)</i>	3.84*	2.6	3.42
<i>ZnO</i>	3.249	6.51	2,304.19

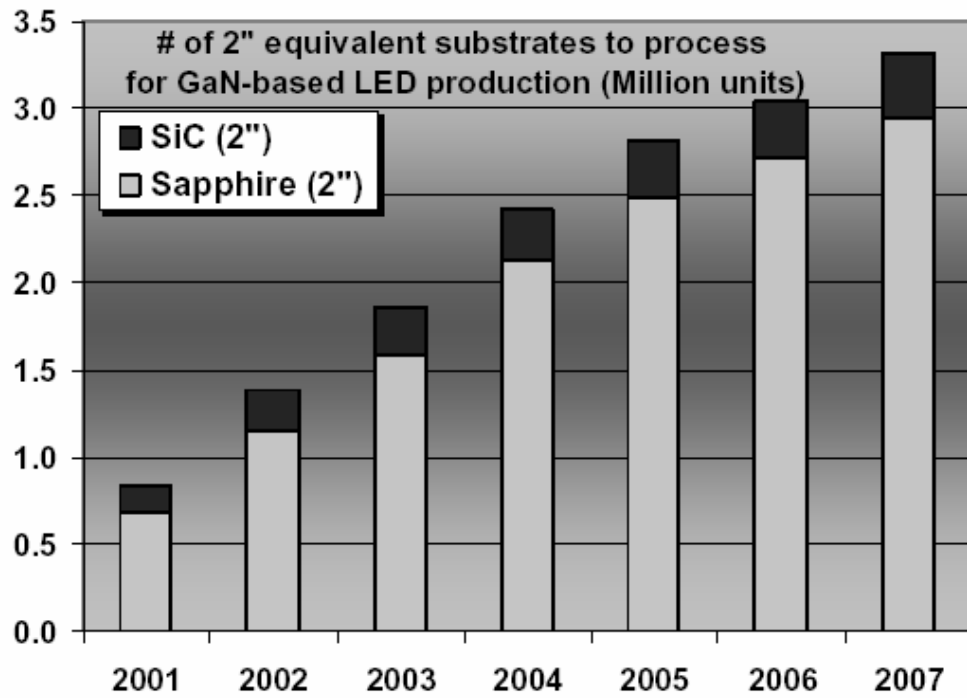


**Figure 1.3:**Substrates used in GaN-based LED production (from [15])

### 1.1.2 GaN Growth Technology

GaN-based devices have been grown by several techniques including molecular beam epitaxy (MBE), pulsed laser deposition (PLD), and hydride vapor phase epitaxy (HVPE). [17-21] The most common technique for the growth of GaN-based LEDs is metalorganic chemical vapor deposition (MOCVD).[22,23] MOCVD provides for sufficient control of the growth process and also allows for process scaling to levels required for large-scale production. MOCVD technology has matured alongside LED technology over the past decade due to its prevalence in the LED manufacturing industry. Details of MOCVD growth will be discussed elsewhere (Section 2.2.1), but a general overview of the technology as it relates to solid state lighting is given here.

MOCVD was first applied to the growth of GaAs-based devices, as it allows for sufficient control of growth surfaces and interfaces to grow high quality material suitable for optoelectronic devices while also offering reasonable growth rates.[24,25] Significant advances were also made in MOCVD technology with the research and development of nitride-based materials and devices in the 1980s and 1990s.[26,27] The use of nitrides in white LEDs today and the subsequent use of these white LEDs in solid state lighting applications has brought MOCVD technology to a state of relative maturity because of the increased demand for GaN-based materials and devices.

The development of MOCVD technology over the past few decades has proven the suitability of the technique for LED growth and enabled the rapid growth of the LED manufacturing industry.[28] However, a new set of challenges have emerged that must be met in order to push LEDs into the general lighting market. The major challenges facing MOCVD growth today are mainly cost-related – throughput, yield, and precursor efficiency – as LED manufacturers require high-volume production capabilities at low cost. [28]

Today's MOCVD systems are designed for this high-volume production, with multi-wafer capabilities (up to 49 x 2" wafers) and high temperature loading and unloading to minimize downtime.[28,29] These systems are also designed to make maximum use of precursors in order to reduce wastage. Cost-related issues will be discussed in more detail later (Section 1.1.4.4).

### 1.1.3 Design and Fabrication of GaN-based Emitters

Processing of an LED structure is determined largely by the desired device functionality. A typical surface-emitting LED structure used in this work is shown in Figure 1.4. Device design takes into account several factors including light extraction, thermal management, and current spreading. Surface roughening is often employed to increase light extraction efficiency, as the roughened surface helps to decrease internal reflection, thus increasing extraction efficiency. Random roughening of the LED surface has been shown to increase light extraction efficiency over non-roughened LEDs. [30] Periodic photonic crystal structures have also been used to increase light extraction efficiency.[31]

One technique that is often employed in LED processing is laser lift-off.[30] This allows the removal of the substrate, leaving only the free-standing GaN LED. Removal of the substrate leads to better current spreading and heat dissipation in the LED, and such a free-standing device allows for new approaches to light extraction and thermal management that are not possible when the device is attached to a substrate.[32,33]

Laser lift-off techniques also suffer from low yield, as it is a time-consuming technique. In addition, the very high temperatures induced by laser lift-off can lead to degradation of the emitter surface at the interface. Novel substrate technologies and simpler approaches

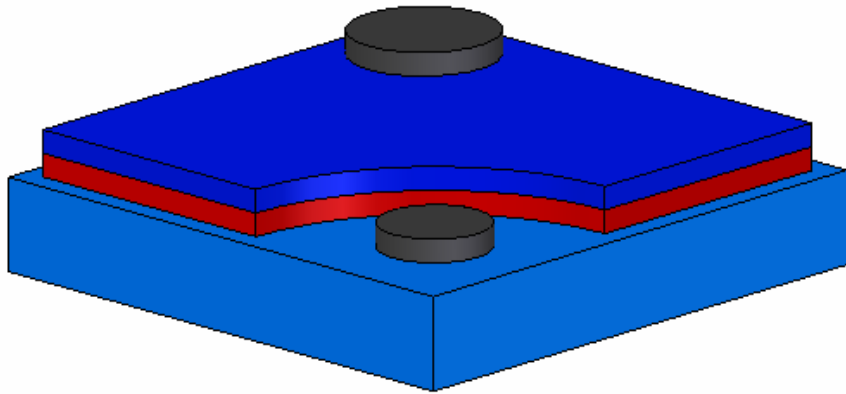


**Figure 1.4:** Typical surface-emitting LED structure used in this work, showing p-type and n-type contacts from the top.

for substrate removal would allow for a much higher yield without degradation of the emitter surface at the substrate interface.

#### 1.1.4 Current Challenges facing SSL

Recent developments in LED materials, growth, and processing have resulted in SSL luminaires with performance nearing that of incandescent and fluorescent sources. There remain, however, several obstacles to be overcome if this technology is to take hold and become a viable option for general illumination applications. The major issues facing white LEDs today are efficacy and efficiency, thermal management, color, and cost.

##### *1.1.4.1 Efficacy and Efficiency*

Efficacy describes the amount of light emitted from a source per unit of electrical power into the device, and is most often given in lumens per Watt. Efficacy is one of the key metrics used to describe the light output of a source, and the highest efficacies reported for cool white LEDs today are near 150 lm/W. [[1]] The practical maximum efficacy for cool white LEDs is near 228 lm/W, leaving ample room for improvement in current device technology. Losses in other parts of the luminaire also decrease overall efficacy, so improvements in device efficacy are very important to improvements in overall luminaire performance.

Efficiency also remains one of the major challenges for solid state lighting technology. Three different quantities are used to describe the efficiency of LEDs: external quantum efficiency (EQE), internal quantum efficiency (IQE), and light extraction efficiency. The relationship between these quantities is shown in Equation (0.1)

$$\eta_{ext} = \chi \cdot \eta_{int} \quad (0.1)$$

where  $\eta_{ext}$  is external quantum efficiency (EQE),  $\chi$  is light extraction efficiency, and  $\eta_{int}$  is internal quantum efficiency (IQE). It is clear that EQE is dependent on the two more fundamental quantities, IQE and light extraction efficiency, and an improvement in EQE can only result from an improvement in one of these two quantities. An improvement in IQE can be brought about by an improvement in material quality or by design of the active region to allow more overlap between electron and hole wave functions. Improvements in light extraction efficiency are most often brought about by improvements in processing techniques, as previously discussed.

#### *1.1.4.2 Thermal Management*

Thermal management of LEDs and LED clusters is also a major concern, as high-brightness GaN-based LEDs tend to get quite hot during operation. The major quantity of interest in thermal management is the junction temperature. A high junction temperature reduces the efficiency of the device, and an unstable junction temperature causes fluctuations in peak wavelength, making it difficult to control color temperature. Junction temperature can be calculated from the slope of the electroluminescence (EL) spectrum on the short wavelength side of the EL maximum of the LED.[34] Junction temperature can also be calculated from the shift of the  $E_2(\text{high})$  mode in the Raman spectrum of the LED. [35] Typical thermal resistance values for GaN LED packages today are in the range of 5 – 10 °C/W, and typical junction temperatures are in the range of ~125 °C.[36,37]

Several different schemes exist to remove heat from the LED. Active cooling schemes, i.e. those using a fan or some other device to cool the LED, are undesirable because of the extra power consumption and additional failure points introduced into the system. High-brightness LED fixtures most often make use of an external heat sink to maintain junction temperature in the device. The two most common approaches are the use of an aluminum

heat sink with fins and the use of a copper slug. [38] Heat pipes, a thermal solution that is more common in cooling high-power CPUs, are also a relatively new method for thermal management in LEDs. [39] They are most often used in conjunction with aluminum heat sinks.

Substrate materials with more favorable thermal properties – and substrates that can be removed – would help to develop new thermal management schemes for LEDs. Specifically, materials with a low thermal expansion coefficient and high thermal conductivity are desirable. By these criteria, silicon is a much more desirable substrate for thermal management of GaN-based devices than sapphire. [36] Thus, the use of silicon as a substrate for GaN-based LEDs would allow for more efficient thermal management, making LEDs more practical for general lighting applications. Moreover, both ZnO and silicon substrates would be relatively simple to remove, and substrate removal would allow for free-standing GaN-based emitters with novel thermal management schemes.

#### *1.1.4.3 Color*

The power spectrum of the source is a major factor in lighting technologies, and solid state lighting is no different. The correlated color temperature (CCT) and color rendering index (CRI) of SSL sources must be similar to those of incandescent and CFL sources in order for SSL sources to compete in the general lighting market.

White LEDs are typically made from a GaN-based blue LED coated with a yellow phosphor, Figure 1.5. The concept is similar to a fluorescent source, in which excited mercury vapor produces short wavelength UV light to excite a phosphor that is coated on the inner surface of the tube. The blue emission from the LED, coupled with the broader yellow emission from the phosphor, produces a white light with a relatively broad spectrum, Figure 1.6. As the CCT of a typical white LED is often high relative to incandescent sources, GaN-based LEDs that emit a warmer white light (lower CCT) must be developed. The

color of the phosphor is crucial in determining the CCT of the white LED since the emission wavelength of the GaN-based LED is fixed. The development of cheaper and more efficient GaN-based LEDs will allow for cheaper and higher efficiency warm white emitters for use in general illumination applications.

#### *1.1.4.4 Cost*

The average price of an SSL luminaire (~\$100) is much higher than either an incandescent (\$1 - \$2) or compact fluorescent (\$5 - 10) source, and the largest part of this cost is the LED itself. The increased price relative to other types of sources stems in part from the high cost of LED growth and processing equipment. Precursors and substrates constitute another large expense in the production of LEDs. Therefore, more efficient use of these materials – or the development of new, less expensive materials with the same capabilities – will significantly reduce overall expenses. Specifically, the development of inexpensive, large-area substrates for GaN epitaxy will ultimately reduce the cost of SSL luminaires, leading to a more significant market penetration by SSL technology.

A cost-of-ownership (CoO) model has been developed for commercial MOCVD growth systems to quantify both substrate-related expenses in LED production and the reduction in these expenses with the introduction of novel substrate technologies. The model has been developed for current EMCORE E300 technology and the new Applied Materials (AM) MOCVD system that is currently operational at Taiwan Semiconductor Manufacturing Company (Epistar). The Epistar/AM tool can grow on 52 wafers per growth run, resulting in ~3,150 wafers per week with an estimated cost of ~\$28/wafer including the substrate. The cost per wafer for the E300 tool of \$43.66 reduces to a cost per wafer of \$28.26 for the AM tool using similar variables. The estimated cost of the epitaxial material is now close to the industry metric of about 1.5x the wafer cost. Thus, additional cost savings can now only

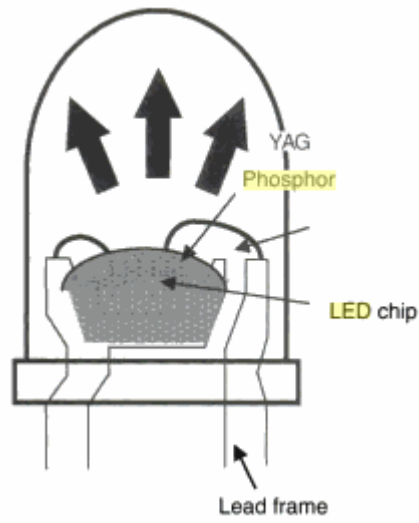


Figure 1.5: Schematic of a phosphor-coated white LED. (from [40])

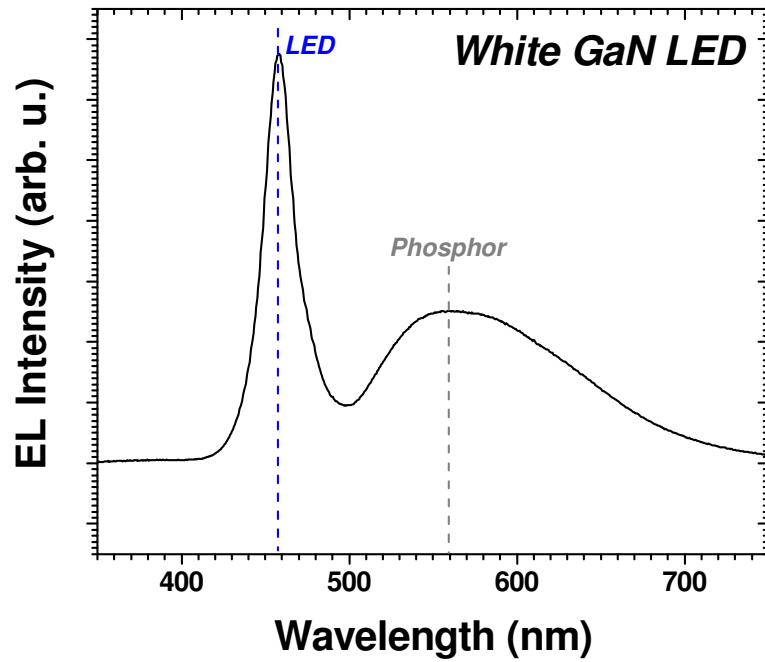


Figure 1.6: Power spectrum of a phosphor-coated white LED showing the blue emission peak from the LED and the yellow phosphor peak.

be made with a reduction in the cost of the substrate material. Using an equivalent cost per square inch for silicon results in a factor of four (4) reduction in the substrate cost compared to sapphire. Table 1.2 summarizes costs associated with ownership and operation of an MOCVD production system. This full CoO model shows that using a silicon substrate results in a reduction of ~33% in yielded cost of LED wafers (\$28.26 to \$18.84).

## 1.2 ALTERNATIVE SUBSTRATES

The physical properties of ZnO are very similar to the properties of GaN, making the integration of these two materials promising for new device technologies.[41-44] The near lattice match of GaN and ZnO should allow for the growth of low defect density GaN, in turn leading to more efficient GaN-based devices. The lattice match of ZnO with  $\text{In}_{0.18}\text{Ga}_{0.82}\text{N}$  may also lead to a reduction in strain in  $\text{In}_x\text{Ga}_{1-x}\text{N}$  quantum wells, thereby increasing efficiency. The use of ZnO as a substrate will also allow for the removal of the substrate by wet etching, allowing for new approaches to both light extraction and thermal management in LEDs.

Si, while presenting serious challenges in terms of physical properties, is the most inexpensive substrate material. It is also particularly interesting as a substrate because of the dominance of silicon in the microelectronics industry and the possibility of integrating additional functionality into the SSL source using the silicon substrate. The development of silicon as a large-area substrate for MOCVD growth of GaN would lead to a 33% cost reduction in production of GaN-based LEDs, provided that quality similar to that of GaN on sapphire can be obtained.

Table 1.2: Cost of ownership model for GaN MOCVD production systems, showing substrate-related costs.

System Process Wafer Size	<b>E300 LED (Sapphire) 2"</b>	<b>AM (52 wafers) LED (Sapphire) 2"</b>	<b>AM (52 wafers) LED (Silicon) 2"</b>
Capital for basic system(s) (\$)	\$1,600,000.00	\$3,000,000.00	\$3,000,000.00
<b>Facilitation costs (\$)</b>	<b>\$160,000.00</b>	<b>\$300,000.00</b>	<b>\$300,000.00</b>
<b>Total capital required (\$)</b>	<b>\$1,760,000.00</b>	<b>\$3,300,000.00</b>	<b>\$3,300,000.00</b>
Time to depreciate (years)	7	7	7
<b>Annual depreciation (\$/year)</b>	<b>\$251,428.57</b>	<b>\$471,428.57</b>	<b>\$471,428.57</b>
Required floor space (sq. meter)	26.00	26.00	26.00
Cost per square meter (\$/sq.m/month)	\$30.00	\$30.00	\$30.00
Average Power required (kw.hr)	30.00	30.00	30.00
Cost per kilowatt hour (\$/kw.hr)	\$0.10	\$0.10	\$0.10
Number of operators required/system	0.50	0.50	0.50
Operator's Salary + Overhead (\$/hr)	\$15.00	\$15.00	\$15.00
Cost of epi materials (\$/run)	\$400.00	\$600.00	\$600.00
<b>Operating Cost @ full utilization (\$)</b>	<b>\$1,378,991.56</b>	<b>\$2,032,966.58</b>	<b>\$2,032,966.58</b>
<b>Total Annual Operating Cost (\$)</b>	<b>\$1,630,420.13</b>	<b>\$2,504,395.15</b>	<b>\$2,504,395.15</b>
<b>For required number of systems</b>			
<b>CPWP @ full utilization</b>	<b>\$27.89</b>	<b>\$15.65</b>	<b>\$15.65</b>
<b>CPWP @ user rate</b>	<b>\$27.97</b>	<b>\$15.70</b>	<b>\$15.70</b>
Cost of substrate wafer (\$)	\$15.00	\$12.00	\$3.00
<b>Yielded cost of wafer (\$)</b>	<b>\$15.70</b>	<b>\$12.56</b>	<b>\$3.14</b>
<b>CPWP + Substrate @ full utilization</b>	<b>\$43.59</b>	<b>\$28.21</b>	<b>\$18.79</b>
<b>CPWP + Substrate @ user rate</b>	<b>\$43.66</b>	<b>\$28.26</b>	<b>\$18.84</b>

A summary of the issues associated with GaN growth on both ZnO and silicon substrates is given in Chapter 2 along with a review of the current status of this work in the literature.

### **1.3 RESEARCH OBJECTIVES**

The objective of this research is the development of an MOCVD growth process for GaN on alternative substrates, specifically ZnO and Si. This objective consists of five subtasks related to various aspects of the work:

- 1) Modeling of GaN-based devices on ZnO and Si substrates
- 2) MOCVD growth of GaN-based materials on ZnO substrates
- 3) ALD growth of Al<sub>2</sub>O<sub>3</sub> layers on Si substrates
- 4) MOCVD growth of GaN-based materials on Al<sub>2</sub>O<sub>3</sub>/Si substrates
- 5) MOCVD growth of GaN-based LEDs on sacrificial substrates.

GaN-based LEDs will be modeled on both ZnO and Si substrates in order to gain a clearer understanding of the benefits of growth on these two substrates. An MOCVD process will also be developed for growth of high quality GaN thin films on these sacrificial substrates. Finally, GaN-based device structures will be grown on both ZnO and Si and tested for their optical and electrical properties. This research will contribute to the development of novel substrates technologies for GaN-based LEDs, enabling the production of higher efficiency and lower cost LEDs.

### **1.4 CONTRIBUTIONS**

This work makes several contributions to the state of the art in GaN growth on alternative substrates. MOCVD growth processes for GaN growth on both ZnO and silicon substrates were developed. Diffusion of zinc and oxygen into the GaN epilayer was studied

in detail, and GaN-based device structures emitting in the green region were grown on ZnO substrates. The major contributions to GaN growth on silicon are a reduction in crack density with the use of an Al<sub>2</sub>O<sub>3</sub> interlayer to <1 mm<sup>-2</sup>, and a reduction in screw dislocation density from 3x10<sup>9</sup>cm<sup>-2</sup> on bare silicon to 2x10<sup>8</sup>cm<sup>-2</sup> on Al<sub>2</sub>O<sub>3</sub>/Si. GaN-based emitters on silicon showed a redshift in peak wavelength compared to similar structures on GaN/sapphire templates. This redshift is attributed to increased indium incorporation in the films on silicon due to tensile strain. Emitters on Al<sub>2</sub>O<sub>3</sub>/Si also showed an IQE of 32%, compared to 37% on GaN/sapphire, and the difference is assigned to the difference in indium content. These results show a great promise toward an inexpensive, large-area, silicon-based substrate technology for MOCVD growth of the next generation of GaN-based optoelectronic devices for SSL and other applications.

## **1.5 MATERIAL PROPERTIES**

Material properties used throughout this work are based on commonly reported literature values. Where discrepancies exist, the most commonly reported experimental values were used. In cases where little or no experimental reports exist, for example in the case of InN piezoelectric constants, the best theoretical estimates were used. Table 1.3 summarizes the values used in this work for various important material properties.

## **1.6 SUMMARY**

The major issues facing GaN-based LEDs today are efficacy and efficiency, thermal management, color, and cost. These issues must be addressed if LEDs are to take a significant share of the general illumination market. One approach to address these issues is the development of alternative substrate technologies for GaN growth. The use of lattice-matched substrates (e.g., ZnO) could lead to much lower defect densities, increasing

efficiency significantly over current technology. The use of inexpensive, large-area substrates (i.e., silicon) would also reduce the cost of production of LEDs. The ability to easily remove both substrates also promises novel approaches to thermal management and light extraction. For these reasons, this work focuses on the development of ZnO and silicon substrate technologies for MOCVD growth of GaN.

Table 1.3: Material properties used in this work.

	$E_g$	$e31$	$e33$	$c13$	$c33$	$a$ (Å)	$P_{sp,z}$	$\epsilon$
<i>AlN</i>	6.11	-0.59	1.41	115	390	3.112	-0.081	9.0
<i>InN</i>	0.69	-0.22	0.43	95	200	3.548	-0.032	15.3
<i>GaN</i>	3.42	-0.33	0.65	105	395	3.189	-0.029	8.9
<i>ZnO</i>	3.37	-0.62	0.96	106	210	3.250	-0.050	8.75

## CHAPTER 2: BACKGROUND

Work toward MOCVD growth of GaN on alternative substrates focuses on many different issues, but the ultimate goal is the development of a process that can consistently yield high quality materials and devices that can compete with GaN devices on both sapphire and SiC in terms of cost and/or performance. This chapter summarizes the state of the art in GaN growth on alternative substrates.

### 2.1 SI AS A SUBSTRATE FOR GAN EPITAXY

A significant amount of work has been done toward MOCVD growth of GaN on Si in the last decade. This work has focused on the development of techniques to relieve strain in GaN layers on silicon and match the quality of GaN layers grown on sapphire and SiC. If successful, this work will have two major benefits.

#### 2.1.1 Advantages of Silicon as a Substrate

First, Si substrates are cheaper than other commercially used substrates, such as sapphire and SiC. This reduction in substrate cost will lead to a reduction in overall cost of production of GaN-based LEDs. Second, MOCVD growth of high quality GaN on Si will allow for monolithic integration of GaN-based optoelectronics with Si-based microelectronics, opening the door for a wide range of novel applications in communications, computation, and related areas.[45,46] The dissimilarity of the two materials, however, presents major technical challenges that must be overcome if the integration of these technologies is to have an impact on the microelectronics and optoelectronics industries in the future.

## 2.1.2 Challenges for GaN growth on Silicon

The physical properties of Si are dissimilar to those of GaN in several ways that make the integration of these two materials problematic. The first major issue that must be overcome is the possibility of a Ga-Si eutectic reaction at the GaN/Si interface during growth. The Ga-Si system is simple eutectic, with the eutectic point being 30°C. The formation of a eutectic reaction at such a low temperature relative to growth temperatures leads to Ga meltback etching of the Si substrate, which presents a problem for nucleation of GaN on Si.[47] This problem necessitates the use of a material other than GaN as a buffer layer, and AlN is most often the material of choice because of its compatibility with GaN. The absence of a eutectic reaction allows for better control over the interface and for fewer dislocations at the interface, leading to higher quality material in subsequent layers.

The crystal structures of GaN and Si also present challenges to their integration. GaN is a hexagonal wurtzite crystal with lattice parameters  $c = 5.185 \text{ \AA}$ , and  $a = 3.189 \text{ \AA}$ , while Si is a face-centered cubic crystal with lattice parameter  $a = 5.431 \text{ \AA}$ . The most common Si orientation for MOCVD growth of GaN is the (111) plane because of the smaller lattice mismatch it provides.[48,49] There is also a large mismatch between thermal expansion coefficients ( $\alpha_{\text{GaN}} = 5.59 \times 10^{-6} \text{ K}^{-1}$ ;  $\alpha_{\text{Si}} = 2.6 \times 10^{-6} \text{ K}^{-1}$ ). Figure 2.1 shows the thermal expansion coefficients for GaN, AlN,  $\text{Al}_2\text{O}_3$ , and Si as a function of temperature. Coupled together, the large mismatches between lattice parameters and thermal expansion coefficients often induce significant tensile strain in the GaN epilayers, leading to higher defect densities and cracking in the thin films, despite the use of AlN as a buffer layer.[48,50] These problems have led to the investigation of several different approaches to relieve strain, reduce defect densities, and prevent cracking in GaN thin films on Si so that device quality material can be obtained.

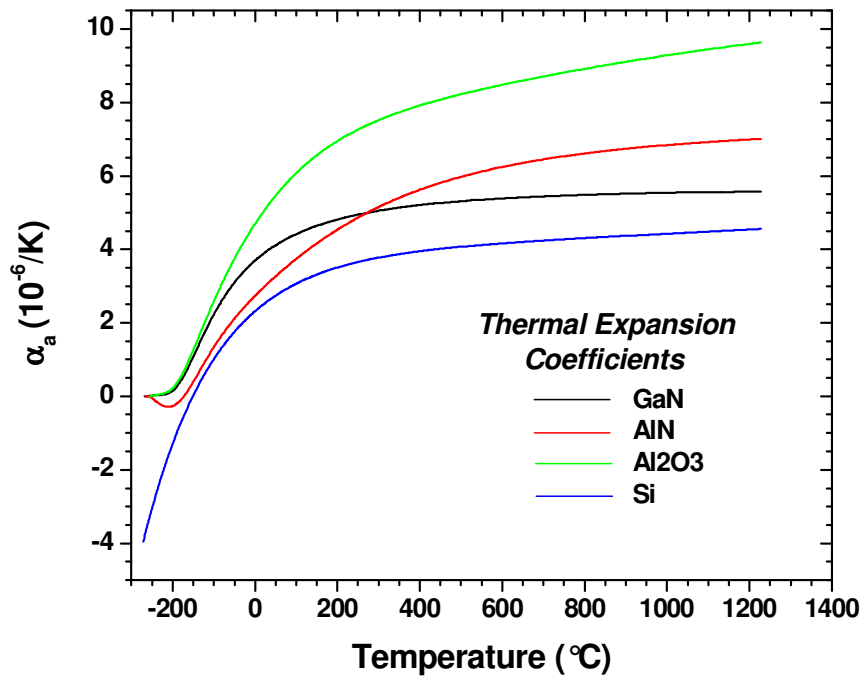


**Figure 2.1:** Thermal expansion coefficients for GaN and some common substrates for GaN epitaxy as a function of temperature.

### 2.1.3 Literature Review

A large body of work exists in MOCVD growth of GaN on Si. Approaches for GaN growth on Si vary in complexity from simple AlN buffer layers [51,52] to more complex  $\text{Al}_x\text{Ga}_{1-x}\text{N}/\text{GaN}$  superlattice structures and graded  $\text{Al}_x\text{Ga}_{1-x}\text{N}$  layers [53]. The use of  $\text{Si}_x\text{N}_y$  interlayers and various oxide interlayers have also been studied [54-57]. The goal of each approach is the development of a process that will consistently yield device quality GaN thin films on Si substrates, but the growth of crack-free GaN on Si has proven quite difficult because of the aforementioned challenges.

Of course substrate orientation is of great importance in determining the amount of strain induced in the epilayer and, subsequently, the material quality. Most work to date has been done on Si(111) substrates, as the (111) face of Si provides hexagonal symmetry and a smaller lattice mismatch than the (001) face. The effective lattice constant for GaN on Si(111) is 3.84 Å due to this hexagonal symmetry. Though the (111) plane is the most common orientation for GaN growth on Si, the effects of substrate orientation on film nucleation and growth have been investigated. Nanoscale-faceted Si substrates exposing both the (001) and (111) faces have been used for MOCVD growth of GaN.[58] Under normal GaN nucleation conditions, it was found that GaN nucleation occurred much more readily on the (111) face of Si than on the (001) face. Figure 2.2 shows SEM images of the nanoscale faceted Si, with the (001) face exposed at the bottom and top of the troughs and the (111) face exposed on the sidewalls. Figure 2.2(a) shows a top view SEM image of the GaN layer grown on faceted Si in which the facets of the substrate remain visible in the thin (~75nm) GaN epilayer. Figure 2.2(b) shows a side view, and Figure 2.2(c) shows a close-up side view in which the boundary between substrate and epilayer is marked with a dashed line. This clearly shows preferential GaN nucleation and growth on the Si(111) faces, with the

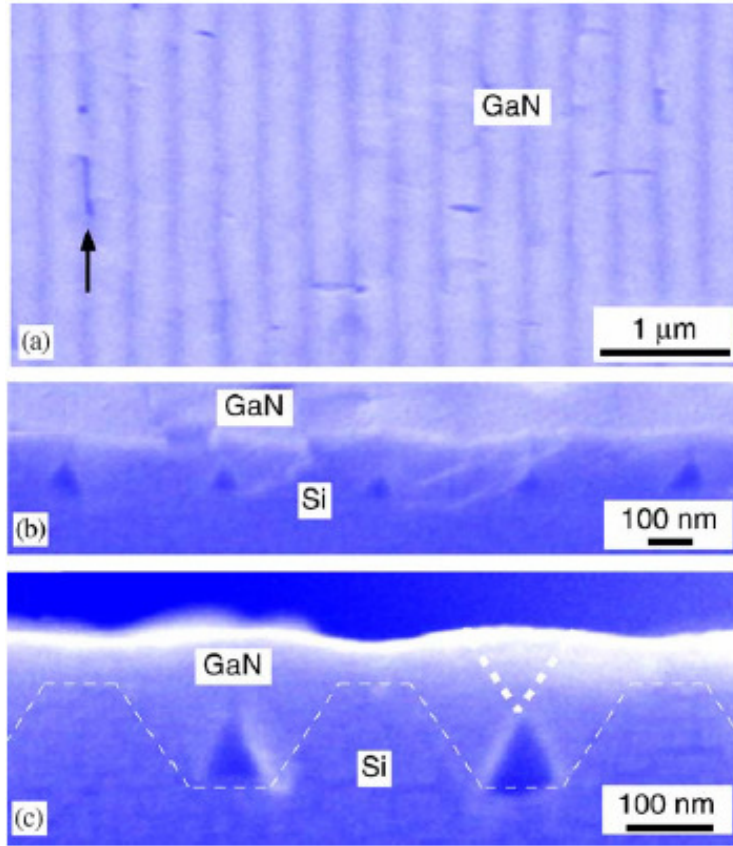


**Figure 2.2:** SEM images of GaN grown on nano-faceted silicon substrates showing preferential nucleation on the Si(111) surfaces. (from [59])

voids that are visible in both Figures 2.2(b) and 2.2(c) due to the complete lack of nucleation and growth on the Si(001) face.

Many aluminum-containing compounds have been studied as buffer layer materials for GaN growth on Si as well. Among these are AlN, AlAs, and Al<sub>2</sub>O<sub>3</sub>. Hageman et al. report the optimization of AlN buffer layers for GaN growth on Si(111) substrates.[51] However, the 3 $\mu$ m GaN layers in this study were still cracked, even under optimized growth conditions. Lu et al. also showed optimization of AlN buffer layers on Si(111) substrates for GaN epitaxy.[60] This work suggests that at low nucleation temperatures, the AlN is polycrystalline and does not allow for sufficient coalescence of the subsequent GaN layer. Also, at higher temperatures, Si diffused from the substrate begins to affect GaN nucleation so that the GaN islands do not completely coalesce, leading to degradation in the structural quality of the GaN layer. Typical XRD spectra show linewidths of the GaN (002) reflection between 500 arcsec and 800 arcsec, though thickness of these layers varies.[61-64] This shows that the material lacks the structural quality of typical GaN layers on sapphire, and that there is room for improvement in this technology.

The major issue with the use of a simple AlN buffer layer remains that the GaN layers are often cracked due to tensile stress induced by the large lattice and thermal mismatch between GaN and Si. Stress-thickness measurements of GaN layers on Si using a high temperature (1100 °C) AlN buffer layer have shown that, from a stress point of view, growth proceeds in two stages. The first stage is a compressive state due to the lattice mismatch between GaN and the underlying AlN buffer layer, while the second stage is a tensile state that occurs after coalescence. The two main features observed by AFM with the transition to a tensile state are coalescence of the GaN films and an increase in lateral grain size, which leads to a reduction in dislocation density. [52,53] However, the evolution of this tensile

stress during growth remains unclear, with some reports showing an increase in tensile stress up to a critical thickness of a few hundred nm and a decrease in stress after this critical thickness [60], and some reports showing a constant tensile stress with increasing film thickness up to  $\sim 1\mu\text{m}$  [52,53]. What remains clear, though, is that the issue of GaN cracking on Si is yet to be solved with a simple AlN buffer layer.

The difficulty in relieving strain and preventing cracking in the GaN epilayer has led to the investigation of several other approaches to grow crack-free GaN on Si. One common approach is the use of low temperature AlN (LT-AlN) interlayers to relieve strain. This approach is based on previous work on growth of thick  $\text{Al}_x\text{Ga}_{1-x}\text{N}$  layers on GaN using LT-AlN interlayers.[65,66] Approaches using relatively thin AlN interlayers have been shown to produce crack-free GaN layers on Si. It is thought that the AlN interlayers can prevent dislocations from propagating further and that they can relieve strain in subsequent GaN layers.

Dadgar et al. were the first to demonstrate thick, crack-free GaN layers on Si(111) grown by MOCVD.[67] They used 15-nm-thick LT-AlN:Si interlayers grown at  $\sim 550^\circ\text{C}$  to obtain crack-free GaN on Si. This work was continued by Bläsing et al., who studied the mechanism by which AlN interlayers relieve strain in GaN layers on Si. Their work suggests that the growth temperature of the AlN interlayer affects the degree of relaxation in the GaN layer, with lower growth temperatures leading to unstrained material. These LT-AlN layers also induce slightly compressive strain in the subsequent GaN layer during growth, helping to prevent cracking while cooling down.[68] Cong et al. have also studied the use of LT-AlN interlayers, showing that the structural quality of the GaN layer depends significantly on the thickness and number of AlN interlayers.[69] This work has shown that an increase in the number of AlN interlayers (from 1 to 3) can decrease strain in the GaN

layer, thereby reducing dislocation density and increasing crystal quality. Cong et al. also observed an increase in the GaN thickness required for coalescence with increasing AlN interlayer thickness. Thus, thick AlN interlayers also slow the coalescence of the GaN layer, thereby reducing crystal quality.[69] Figure 2.3 shows TEM images of a GaN layer on Si(111) using three LT-AlN interlayers. Note the formation and annihilation of dislocations at the GaN/AlN interfaces. The use of multiple LT-AlN interlayers makes the blocking of dislocations more likely than the formation of new ones, thus reducing the overall dislocation density in the topmost GaN layer, though it remains under tensile stress.

Another approach that has been studied to decrease stress in the GaN layer and increase structural quality is the use of a graded  $\text{Al}_x\text{Ga}_{1-x}\text{N}$  layer. The use of step-graded  $\text{Al}_x\text{Ga}_{1-x}\text{N}$  layers produces films under biaxial tensile stress with reduced crack densities [70], while the use of thick (1-2  $\mu\text{m}$ ) buffer layers graded from AlN to GaN has been shown to induce a compressive stress in the subsequent GaN layer and to prevent cracking [52,53,71]. The thickness of the graded layer is an important parameter, with thicker graded layers increasing the thickness at which the subsequent GaN layer undergoes the transition from compressive stress to tensile stress.[53] The layer grown on a 100nm AlN buffer in this work transitions from compressive to tensile stress near 200nm, and the stress remains constant through the rest of the film. However, the layers grown on thick graded buffer layers do not undergo a transition from compressive to tensile stress, instead maintaining a constant compressive stress at thicknesses up to 1 $\mu\text{m}$ . The suggested explanation for this behavior is that the thick graded layer allows the increase in lateral grain size (which is named as a source of tensile stress in the GaN films) to cease, thus decreasing the source of tensile stress in the subsequent GaN films and allowing for the growth of thicker layers that are under compressive stress.[53] However, this complicates the growth process significantly, adding to

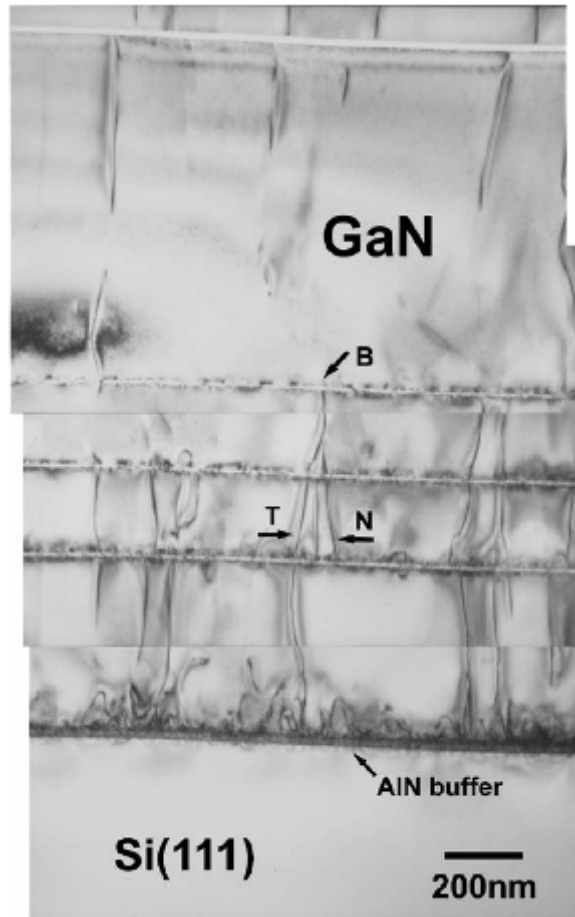


**Figure 2.3:** TEM image of a GaN layer on silicon using three LT-AlN interlayers. (from [69])

the overall growth time and increasing the amount of precursors consumed during a single growth run, thus nullifying the cost advantages of Si as a substrate.

One approach that has been taken to improve crystal quality of GaN layers grown using LT-AlN interlayers and graded  $\text{Al}_x\text{Ga}_{1-x}\text{N}$  layers on Si is the use of a  $\text{Si}_x\text{N}_y$  mask layer to promote lateral GaN growth. The  $\text{Si}_x\text{N}_y$  mask can be deposited directly on the substrate (in the case of sapphire)[54,57,72] or it can be deposited as an interlayer in the GaN epilayer, which is the most common approach taken on a Si substrate.[55,56] The  $\text{Si}_x\text{N}_y$  mask inhibits GaN growth since Si is an antisurfactant, thus reducing the number of available GaN nucleation sites in either case. This decreases island density and leads to a change in growth mode from 2D to 3D. The GaN islands will coalesce again after a certain thickness, and the growth mode will return from 3D back to 2D, leading to a smooth surface with device-quality material properties. [73] This approach was first shown to reduce defect densities in GaN grown on sapphire. [54-56] The reasonable success of  $\text{Si}_x\text{N}_y$  masking for GaN growth on sapphire led to its transfer to Si substrates for GaN growth. [51,67,74]

$\text{Si}_x\text{N}_y$  mask layers for GaN grown on Si, however, are often used to increase crystal quality in conjunction with AlN interlayers or  $\text{Al}_x\text{Ga}_{1-x}\text{N}$  layers, which are used to reduce tensile strain. For example, Cheng et al. have reported the use of a  $\text{Si}_x\text{N}_y$  interlayer in conjunction with step-graded  $\text{Al}_x\text{Ga}_{1-x}\text{N}$  layers on a Si(111) substrate to grow crack-free GaN with dislocation densities as low as  $3.0 \times 10^8 \text{ cm}^{-2}$ . [73] Figure 2.4 shows a cross-sectional TEM image with layers in the following order on a Si(111) substrate: AlN buffer layer, step-graded  $\text{Al}_x\text{Ga}_{1-x}\text{N}$  layers, 400-500nm of GaN,  $\text{Si}_x\text{N}_y$  interlayer, and topmost GaN layer. This structure is typical of work done using  $\text{Si}_x\text{N}_y$  masks on Si substrates. Hageman et al. also show a significant improvement in both structural and optical quality of  $3 \mu\text{m}$  GaN layers grown on Si(111) with the use of a  $\text{Si}_x\text{N}_y$  mask layer. [51] The insertion of a  $\text{Si}_x\text{N}_y$  mask layer

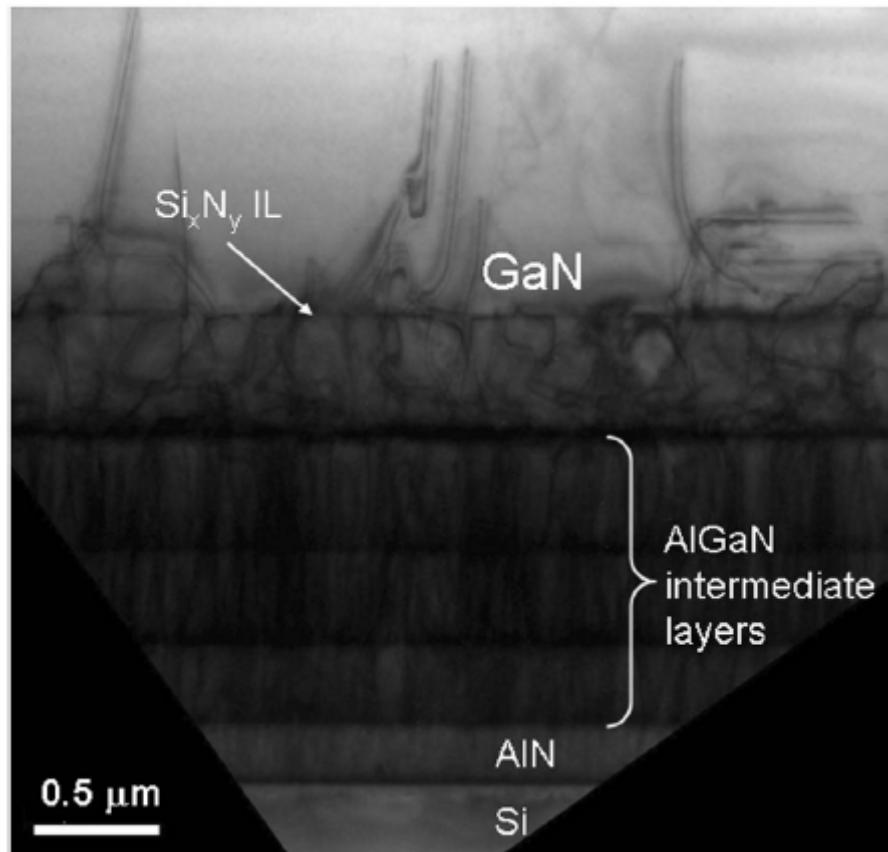


**Figure 2.4:** TEM image of a GaN layer on Si(111) using three Al<sub>x</sub>Ga<sub>1-x</sub>N layers on a Si<sub>x</sub>N<sub>y</sub> interlayer. (from [73])

after  $1\mu\text{m}$  of GaN showed a decrease in PL linewidth from  $17.6\text{meV}$  to  $10\text{meV}$  at  $4\text{K}$ , indicating improved optical quality and fewer electronic defects in the GaN layer grown with the  $\text{Si}_x\text{N}_y$  mask.

Dadgar et al. have extended this approach to the growth of crack-free GaN LEDs on Si. [67] They grew  $\sim 2.8\mu\text{m}$ -thick LED structures on Si(111) using a LT-AlN buffer layer and two LT-AlN interlayers.  $200\text{nm}$  of GaN were deposited after the second LT-AlN interlayer, and then a  $\text{Si}_x\text{N}_y$  mask layer was inserted before the growth of the LED structure. Electroluminescence measurements showed an output power of  $152\mu\text{W}$  at  $20\text{mA}$  and  $455\text{nm}$ , which is a five-fold increase in intensity in the sample with the *in situ*  $\text{Si}_x\text{N}_y$  mask compared to the sample without the mask.

Most work using a  $\text{Si}_x\text{N}_y$  mask layer has involved micron-sized pores in the  $\text{Si}_x\text{N}_y$ . However, the size and distribution of pores in the mask layer have an effect on the coalescence thickness and, thus, material quality. Smaller pores are thought to lead to quicker coalescence and fewer dislocations in a smaller thickness of material. Nanopatterned  $\text{SiO}_2$  has also been used to investigate this phenomenon. [75] Like the  $\text{Si}_x\text{N}_y$  masks reported previously, the  $\text{SiO}_2$  was deposited on a GaN epilayer that was grown on a  $100\text{nm}$  AlN buffer layer on Si(111). The 3D growth mode continues until the islands coalesce and the layer returns to a 2D growth mode with a smooth surface. The advantage of the nanopatterned mask is that the islands coalesce much more quickly (within  $\sim 50\text{nm}$  of the  $\text{SiO}_2$  mask), thus reducing the dislocation density more quickly than if the GaN islands were much larger and spaced further apart.

Nanoheteroepitaxy of GaN on Si has also been studied without the use of AlN buffer layers or LT-AlN interlayers. Hersee et al. report the use of a  $\text{SiO}_2$  mask to promote GaN island growth, and the spacing of these islands to allow for coalescence in small areas over

the substrate. [59] They observed a significant reduction in threading dislocation density compared with GaN grown on large-area Si. The most prevalent type of defects, in fact, were stacking faults, which were confined to an area near the GaN/Si interface and do not propagate through the entire layer, as threading-type dislocations often do. These layers showed some cracking, however, due to the large thermal mismatch between the two materials, though they showed significantly lower defect densities in the upper GaN layer ( $3 \times 10^9 \text{ cm}^{-2}$ ) compared to GaN layers grown on large area, unpatterned substrates.[59,76]

While the use of a  $\text{Si}_x\text{N}_y$  mask layer improves the structural quality of GaN thin films grown on Si, it does not negate the need for LT-AlN interlayers or  $\text{Al}_x\text{Ga}_{1-x}\text{N}$  layers to relieve tensile stress in the GaN layer. Thus, it further complicates the growth process for GaN on Si and negates the advantages of Si as a substrate for MOCVD growth of GaN. This makes clear the need to investigate other methods for growing high quality GaN on Si and, in particular, the need to simplify the growth process for GaN on Si if it is to become a viable commercial technology. To this end, other approaches have been studied to simplify the growth of GaN on Si while maintaining device quality material.

Strittmatter et al. took a slightly different approach to the use of buffer layers, nucleating with AlAs at 450 °C and then growing a thin layer of AlAs at 720 °C.[77,78] The total thickness of the AlAs buffer layer was ~40 nm. A thin AlN layer was then deposited on this AlAs buffer layer, and finally a 1  $\mu\text{m}$ -thick high temperature GaN layer was grown. They also studied the formation of a single AlN buffer layer by nitridation of the AlAs layer at 950 °C and obtained similar results.[77] Structural and optical quality of these layers was on par with other reports of MOCVD-grown GaN on Si(111) with a simple AlN buffer, but the layers remained cracked.

Attempts to simplify the growth process for GaN on Si using materials other than III-nitrides as buffer layers have also led to the investigation of various oxides as transition layers. BaTiO<sub>3</sub> (BTO) and SrTiO<sub>3</sub> (STO) have been investigated as transition layers for growth of GaAs on Si. Yu et al. reported the MBE growth of single crystal BTO and STO on Si (001) substrates.[79] BTO and STO were chosen because of their near lattice match with Si when rotated 45° on the [001] axis. These layers were then used for the growth of high quality GaAs, from which metal epitaxial semiconductor field effect transistors (MESFETs) were fabricated. Figure 2.5 shows a schematic of the structures investigated in this work. [80]

AlO<sub>x</sub> has also been investigated as an oxide transition layer on Si.[81] Al strips were oxidized by Napierala et al. and used as nucleation sites to promote lateral overgrowth of GaN. This work led to high quality GaN layers on Si, and it shows the promise of Al<sub>2</sub>O<sub>3</sub> as an oxide transition layer to simplify MOCVD growth of GaN on Si.

## **2.2 ZNO AS A SUBSTRATE FOR GAN EPITAXY**

ZnO has been the focus of intense research recently because of its physical properties such as bandgap ( $E_g = 3.37$  eV) and exciton binding energy (~60 meV), which offer promise for more efficient emitters at room temperature. The similarity of ZnO and GaN has also led to investigations into the integration of these two materials.[41-44]

### 2.2.1 Advantages of ZnO as a Substrate

The near lattice match of GaN and ZnO should allow for the growth of low defect density GaN, in turn leading to more efficient GaN-based devices. The use of ZnO as a substrate will also allow the removal of the substrate by wet etching, allowing for new approaches to both light extraction and thermal management in LEDs. The fundamental

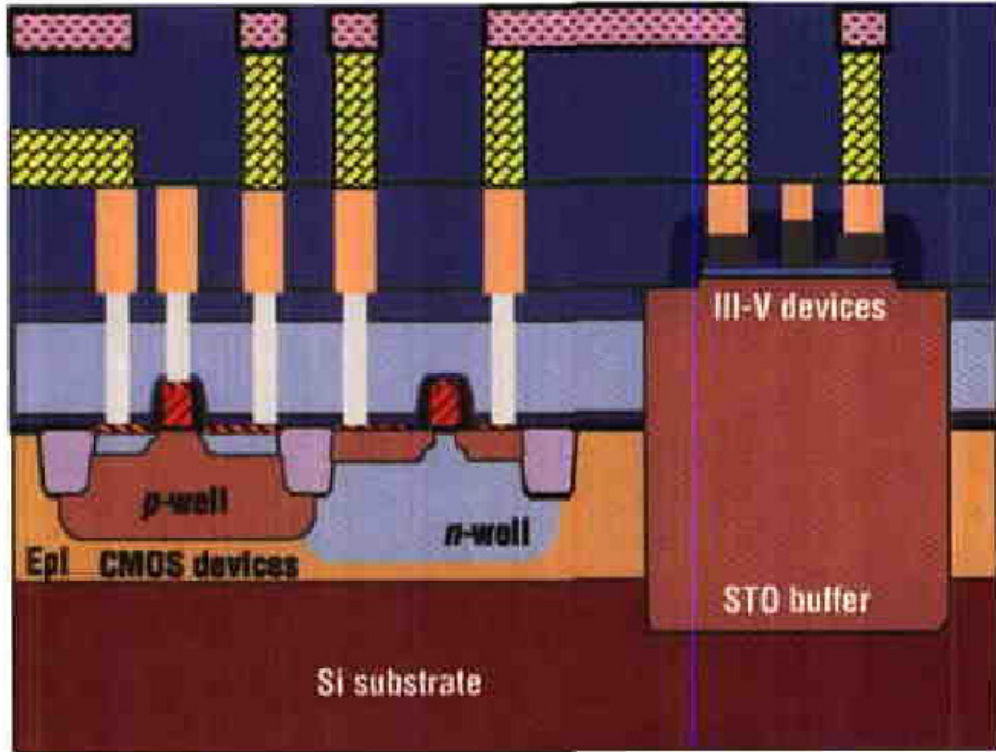


**Figure 2.5:** Schematic of a structure studied for monolithic integration of MBE-grown GaAs with silicon. (from [80])

problems of interdiffusion at the interface and ZnO instability in H<sub>2</sub> remain to be solved, however, if ZnO is to become a significant substrate material in the GaN-based LED market.

### 2.2.2 Challenges for GaN Growth on ZnO

Both GaN and ZnO are hexagonal wurtzite crystals, with a lattice mismatch in the *a*-direction of 1.8%. These similarities make ZnO a very promising substrate for GaN growth. However, there are two major challenges to be overcome in GaN growth on ZnO. The first is the instability of ZnO at high temperatures in H<sub>2</sub>. H<sub>2</sub> is commonly used as a carrier gas in MOCVD growth of GaN, and NH<sub>3</sub> is the most common nitrogen precursor. This hydrogen, however, etches the ZnO substrate, roughening the surface and inhibiting growth of high quality GaN.[82] The second challenge is the diffusion of Zn and O from the substrate into the GaN layer. Zn, in particular, diffuses quickly and degrades overall material quality as well as interface quality of subsequent multiple quantum wells (MQWs) or superlattices (SLs).

### 2.2.3 Literature Review

The physical properties of ZnO, including its wide bandgap ( $E_g = 3.37$  eV), near lattice match with GaN (1.8%), and similar thermal expansion coefficients make it a promising material for use as a substrate for GaN epitaxy. ZnO (0001) substrates are commonly used for investigations into GaN epitaxy because of the near lattice match. However, this presents the problem of growing a polar thin film (c-plane GaN) on a polar substrate (c-plane ZnO). The strong polarization fields in these materials necessitate a clear understanding of the GaN/ZnO interface in order to develop an MOCVD process for high quality GaN on ZnO. Allen et al. studied the electrical properties and polarization effects in bulk ZnO substrates.[83]

They found that free carriers in the bulk ZnO move toward the surface to compensate for the bound spontaneous polarization charge at the surface. Significant band bending was observed, however, in samples with low free carrier concentrations. This band bending leads to the formation of an inversion layer near the ZnO surface, compensating the bound spontaneous polarization charge at the surface, Figure 2.6(a). Differences in surface morphology have also been observed between Zn-polar and O-polar material, with Zn-polar surfaces often showing triangular steps or pits. It is thought that these triangular pits result in a net electric field that compensates for the electrostatic instability at the Zn-polar surface.[84]

Nakayama et al. investigated the GaN/ZnO band alignment, which is a Type II band offset, with both the bottom of the ZnO conduction band and the top of the ZnO valence band being below those of GaN, Figure 2.6(b). Calculations were made using a local density approximation, and the average valence band offset was calculated to be 1.6 eV. Actual values ranged from 1.0 eV to 2.2 eV, however, depending on ZnO surface conditions and treatment.[85] This work also suggested a slight band bending in the GaN thin film ( $\sim 100$  meV/Å) induced by charge transfer from the interface to the GaN layer. The GaN/ZnO interface was modeled in more detail by von Pezold et al.[86], who suggest that cation compensation is more likely at the interface (relative to anion compensation) from a formation energy perspective.

MBE growth of GaN on O-face substrates using a LT-GaN buffer layer resulted in a GaN surface with RMS roughness = 11nm. The GaN layers in this work were deposited on both O-face and Zn-face substrates, and with both LT-GaN and LT-AlN buffer layers. The LT-GaN buffer layer on O-face ZnO showed the smoothest surface and highest quality as observed by XRD.[87] Only a few reports of MOCVD growth of GaN on ZnO have been

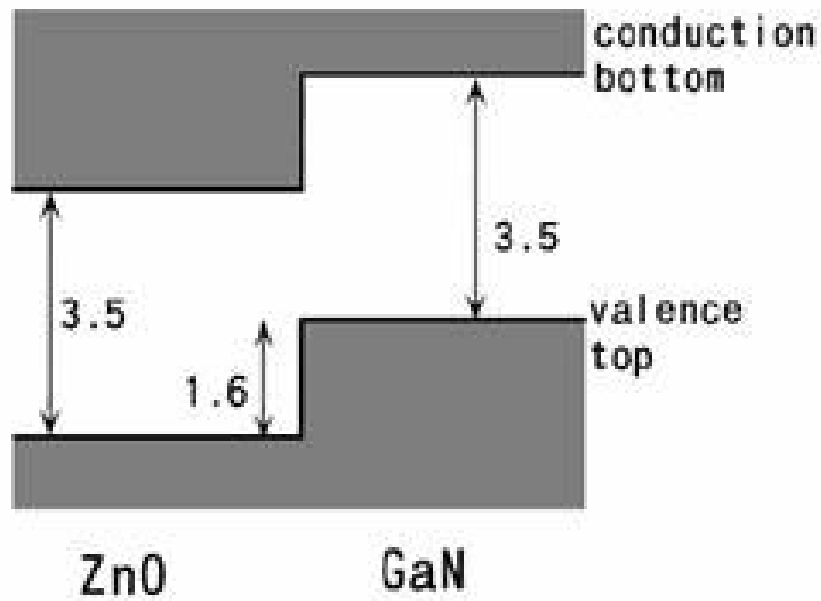
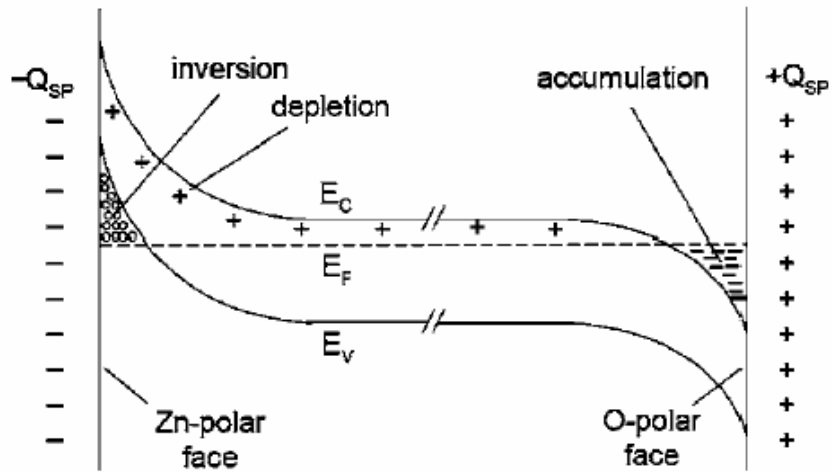


**Figure 2.6:** (top) Band bending induced by polarization effects in bulk ZnO crystals. (from [83]) (bottom) Average band offset at the GaN/ZnO interface. (from [85])

published, though, due to the problems of interdiffusion and ZnO instability in H<sub>2</sub>. Kobayashi et al. report the MOCVD growth of GaN on Zn-face ZnO substrates at 700 °C. Significant interdiffusion was observed at the interface, even at these relatively low growth temperatures.[88] Kawai et al. also report the MOCVD growth of In<sub>x</sub>Ga<sub>1-x</sub>N films on c-plane (0001), a-plane (11-20), and m-plane (1-100) ZnO substrates in the temperature range 550 °C to 680 °C.[89] This work showed decreased crystal quality as observed by XRD for the films grown on c-plane ZnO compared to those on both a-plane and m-plane ZnO. These initial reports suggest that ZnO is a promising substrate for GaN growth, though much work remains to be done in order to develop an MOCVD growth process that can yield device quality GaN on ZnO.

### **2.3 SUMMARY**

While a significant amount of work has been done toward MOCVD growth of GaN-based materials and devices on silicon, the solutions that have been shown to work remain somewhat complicated and costly, as they require thick Al<sub>x</sub>Ga<sub>1-x</sub>N layers or Al<sub>x</sub>Ga<sub>1-x</sub>N/GaN superlattices. Oxide layers have been used to integrate other III-V materials with silicon, and this work will investigate the use of oxide layers to integrate GaN and silicon.

GaN growth on ZnO substrates is less understood than GaN growth on silicon, and diffusion and substrate stability remain the major issues to be solved. This work will investigate GaN growth on ZnO by MOCVD, with an eye toward suppressing zinc and oxygen diffusion and growing high-quality GaN thin films on ZnO.

## **CHAPTER 3: EXPERIMENTAL EQUIPMENT AND TECHNIQUES**

There are several different aspects of this work, including modeling, materials growth, characterization, and processing. This chapter describes the techniques used and the specific equipment employed in each aspect of this research.

### **3.1 MODELING**

Simulations of GaN-based emitters on various substrates were performed in this work using the nitride simulation package SiLENSe. One-dimensional simulations of various emitter structures were performed in order to determine the effects of substrate-induced strain on the optical and electrical properties of GaN-based emitters. Efficiency was also calculated from these simulations.

### **3.2 GROWTH**

Epitaxial growth techniques lie at the heart of both LED production and semiconductor thin film research. Several different growth techniques have been used to deposit wide bandgap materials, including pulsed laser deposition (PLD), molecular beam epitaxy (MBE), and hydride vapor phase epitaxy (HVPE). MOCVD technology provides the control, flexibility, and scalability necessary for high-volume production of high-quality optoelectronic devices, and it has matured over the past decade into the major technique used in production of LEDs today. MOCVD is used in this for this reason.

### 3.2.1 MOCVD Growth

MOCVD growth involves the use of metalorganic precursors (e.g., trimethylgallium) to provide a sufficient vapor pressure to allow for transport of the constituent elements (gallium, indium, and aluminum, in the case of nitride materials) in vapor phase. It is a complex process involving many chemical and physical processes, and these processes and their effects on one another are not all clearly understood. In general, the growth process can be described in terms of thermodynamics and kinetics, with thermodynamics describing the driving forces behind growth and kinetics describing the rate at which these reactions occur.

#### *3.2.1.1 Thermodynamics*

Thermodynamics describes the driving forces behind the overall growth process. It is useful in determining the solid composition of a multi-component system as well as in determining the composition of a solid with varying temperature and pressure. Thermodynamic calculations are done for a system in equilibrium, which is defined as the state in which the Gibbs free energy is a minimum. Gibbs free energy is given in Equation (3.1)

$$G = H - TS \quad (3.1)$$

where  $H$  and  $S$  are enthalpy and entropy, respectively. While MOCVD is a non-equilibrium technique, thermodynamics is very useful in describing the driving forces behind epitaxial growth and in determining the solid composition and maximum growth rate of the film.

For a simple two-phase system with phases  $\alpha$  and  $\beta$ , moving a small amount of component  $i$  between phases causes no change in  $G$ . This is described in Equation (3.2):

$$\left(\frac{\partial G}{\partial n_i}\right)_{T,P,n_j}^{\alpha} - \left(\frac{\partial G}{\partial n_j}\right)_{T,P,n_i}^{\beta} = 0 \quad (3.2)$$

Here,  $n_i$  is the molar concentration of component  $i$ , and P and T are pressure and temperature, respectively. The partial derivative of G with respect to  $n_i$  is known as the chemical potential, and for non-ideal cases, it is expressed as

$$\mu_i = \mu_i^0 + RT \ln(a_i) \quad (3.3)$$

where  $\mu_i$  is the chemical potential,  $\mu_i^0$  is the chemical potential at some arbitrary standard state, R is the gas constant, and  $a_i$  is known as the activity coefficient.

When the system is in a non-equilibrium state, the difference in chemical potential is non-zero. This has been called the “driving force” for epitaxy[90,91], and is described mathematically by Equation (3.4):

$$\Delta\mu = \mu_A - \mu_B \quad (3.4)$$

From a thermodynamic perspective, a non-equilibrium gas phase is intentionally created in the MOCVD reactor to drive the reaction at the surface and, therefore, growth. The formation of the solid phase decreases the difference in chemical potential, pushing the system back toward equilibrium. The maximum growth rate achievable is simply the amount of material that would return the system to complete equilibrium.[91] Of course, the maximum growth rate is also dependent on reactor geometry and total flow rates.

The observed growth rate is often much lower than that calculated from thermodynamics, however. Mass transport and surface reaction rates also have an effect on the growth rate, which is determined by the flux of atoms reaching the film surface from the gas phase. The percentage of atoms injected in the gas phase that actually reach the film surface is quite small. Thus, it is possible for near-equilibrium conditions to exist near the

film surface even when a large difference in chemical potential exists in the gas phase. Such a situation occurs when the surface reactions proceed more rapidly than the mass transport, and is referred to as mass transport-limited growth. In MOCVD growth of III-V materials, an effort is usually made to stay within this growth regime.

In typical III-V growth conditions, the V/III ratio is much greater than 1. This overpressure of the Group V element – nitrogen in the case of GaN growth – means that much less gallium is available to diffuse to the growth surface compared to nitrogen. Thus, the growth rate in mass-transport limited growth is directly proportional to the gallium flow rate. Figure 3.1 shows the dependence of growth rate on growth temperature, with mass-transport limited growth and kinetically limited growth labeled. A plot of  $\log(\text{growth rate})$  versus  $1000/T$  is often used for this purpose. These growth regimes will be discussed in greater detail in the following sections.

Thermodynamics is able to explain the overall driving force in MOCVD growth, but it is unable to describe the rates at which these processes occur or the steps involved in the process. A closer examination of kinetics and mass transport is necessary to develop a more complete understanding of the growth process and the steps involved.

#### *3.2.1.2 Kinetics*

Kinetics describes the steps involved in the MOCVD growth process as well as the rates at which those steps proceed. A major part of kinetics in MOCVD growth is describing the chemical reactions that occur both in the gas phase and at the solid surface. The equilibrium system considered by thermodynamics assumes a completely reversible reaction, with the forward and reverse reactions proceeding at the same rate. As MOCVD is a non-equilibrium process, this assumption is not entirely true; however, the difference in reaction

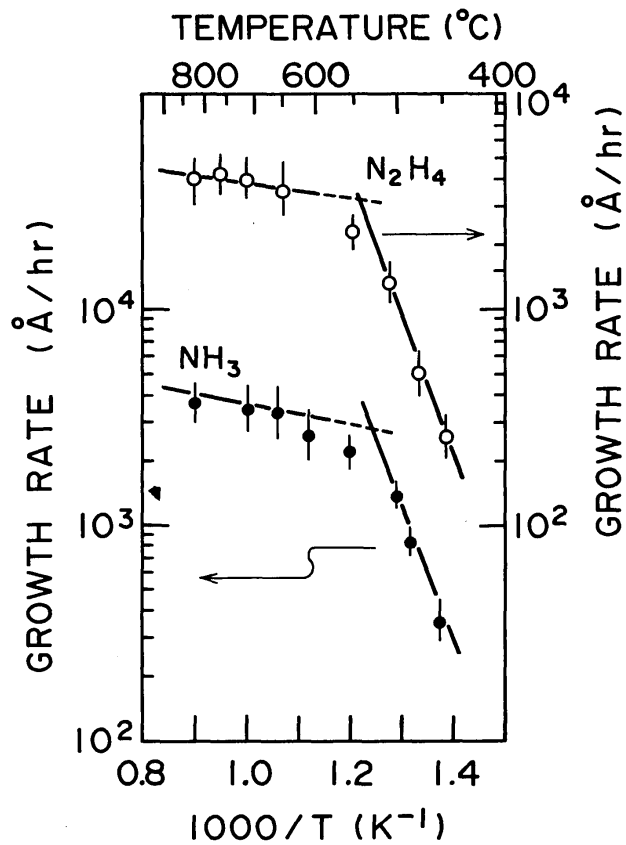


**Figure 3.1:** Dependence of growth rate on growth temperature for GaN using different NH<sub>3</sub> precursors. Lines denote kinetically limited growth (lower temperatures) and mass transport-limited growth (higher temperatures). (from [92])

rates near the solid surface is very small compared to the reaction rates themselves, leading to very small growth rates and near-equilibrium conditions at the solid surface.[91]

For a given chemical reaction, the rate of the forward and reverse reactions is given by the product of the concentration and the rate constant,  $k$ , which is often expressed using the Arrhenius equation:

$$k = Ae^{-E_a/RT} \quad (3.5)$$

where  $E_a$  is the activation energy and A is a pre-exponential factor. Chemical reactions occurring purely in the gas phase are called homogeneous reactions, while those occurring at the solid interface are called heterogeneous reactions.

There are two basic types of homogeneous reactions: unimolecular and bimolecular reactions. In a unimolecular reaction, a single parent molecule breaks apart into two separate molecules. The reaction rate is proportional to the concentration of the species. In a bimolecular reaction, two parent molecules react to form a complex, which may also undergo a unimolecular reaction. [91] For a bimolecular reaction between two species A and B, the reaction rate is proportional to the rate of collisions between A and B.

Heterogeneous reactions are of great significance in MOCVD, as thin film growth is the ultimate goal, and this involves reactions at the solid-vapor interface. Heterogeneous reactions in MOCVD are most often described using the Langmuir adsorption model, which assumes that there are a fixed number of sites on the surface onto which an atom can adsorb, and that a certain percentage of these sites is occupied.[93] The Langmuir adsorption equation – also known as the Langmuir isotherm – is given in Equation (3.6):

$$\Theta_i = \frac{k_a P_i}{k_d + k_a P_i} \quad (3.6)$$

Typical growth of high-quality thin films proceeds with adsorption, diffusion of reactants across the surface, attachment to a surface site, and desorption of products. This process often proceeds by the formation of steps on the surface, with the diffusion of adsorbed atoms across the surface and attachment to a step. [91] A sufficient number of empty sites must be available in order to allow for diffusion across the surface, so the fraction of occupied sites  $\theta$  for each component must be much less than one. This makes the growth rate proportional to the partial pressures of the components in vapor phase at the solid-vapor interface.

MOCVD growth often consists of a complex series of these reactions – both homogeneous and heterogeneous, proceeding in forward and reverse – and not all of them are clearly understood. Early investigations of the pyrolysis of metalorganic precursors involved the study of a single reaction or a single chain of reactions. [91] This, however, is of limited use in describing the MOCVD process as a whole, in which both cation and anion precursors are pyrolyzed and react with the surface simultaneously. Also, the presence of  $H_2$ , which is often used in both III-V and II-VI MOCVD, affects the rate at which these reactions occur as well as the order and likelihood of the reactions. [94] Kinetics is useful in explaining the MOCVD growth process and the chemical reactions involved despite these limitations. However, MOCVD is a complex process with many factors involved, and a clear understanding can only be reached by considering the aspects of fluid dynamics and mass transport in addition to both thermodynamics and kinetics.

### *3.2.1.3 Fluid Dynamics and Mass Transport*

A third important aspect of MOCVD growth is that of gas flow inside the reactor, also known as fluid dynamics, or hydrodynamics. Fluid dynamics depends on the reactor geometry and experimental equipment more than any other aspect of MOCVD growth. Gas

flow through an MOCVD reactor is by forced convection, meaning that gas flows because of the intentional pressure gradient across the reactor. The velocity vectors are parallel to each other and parallel to the walls of the reactor, which is known as laminar flow. In the laminar flow regime, both convection effects created by rapid heating of injected gases and mass diffusion of precursors to the substrate caused by a gradient in chemical potential play a significant role in determining the growth rate. Because temperature plays a role in both of these processes, there exists in standard MOCVD processes a growth regime in which the growth rate is limited by fluid dynamics and mass transport effects. [90,91]

A mathematical description of gas flow in an MOCVD reactor involves the solution of three partial differential equations. The first equation describes conservation of mass:

$$\frac{\partial}{\partial t} \rho_i = -\nabla \cdot [\rho_i \mathbf{v} + \mathbf{j}_i] = -\nabla \cdot \mathbf{n}_i \quad (3.7)$$

where  $\rho$  is mass density,  $\mathbf{v}$  is average velocity,  $\mathbf{n}_i$  is the total mass flux of component  $i$ , and  $\mathbf{j}_i$  is the diffusive flux with respect to  $\mathbf{v}$ . The second equation is known as the Navier-Stokes equation, and it describes conservation of momentum:

$$\frac{\partial}{\partial t} \rho \mathbf{v} = -[\nabla \cdot \{\rho \mathbf{v} \mathbf{v} + \Pi\}] + \sum_i \rho_i \mathbf{g}_i \quad (3.8)$$

where  $\rho$  is total mass density,  $\mathbf{v} \mathbf{v}$  is a second-order tensor,  $\Pi$  is the pressure tensor, and  $\mathbf{g}_i$  is the sum of the external forces per unit mass on component  $i$ . The third equation describes conservation of energy:

$$\frac{\partial}{\partial t} \rho \left( E + \frac{1}{2} v^2 \right) = -\nabla \cdot \left\{ \rho \left( E + \frac{1}{2} v^2 \right) \mathbf{v} + \mathbf{q} + [\Pi \cdot \mathbf{v}] \right\} + \sum_i \rho_i \mathbf{g}_i \quad (3.9)$$

where  $E$  is the internal energy per unit mass, and  $\mathbf{q}$  is the conductive heat flux. [90,91] Equations (3.7) through (3.9) must be solved by imposing certain boundary conditions, and computer modeling software is often used. For example, the boundary condition at any

surface is that velocity perpendicular to the surface is zero. Also, velocity parallel to the surface decreases as the surface is approached, leading to the formation of a boundary layer across which precursor atoms diffuse to adsorb onto the surface of the growing film. In vertical injection, rotating disk reactors, the boundary layer thickness can be given by the expression

$$\delta_0 \cong 4 \left( \frac{\nu}{\omega} \right)^{\frac{1}{2}} \quad (3.10)$$

Where  $\nu$  is the kinematic viscosity and  $\omega$  is the rotation speed of the disk. Thus, the boundary layer thickness decreases with an increase in rotation speed. This model cannot account for effects such as growth rate non-uniformity and convection in real MOVCD reactors, however, as no such stagnant boundary layer actually exists. [90,91]

The complex processes involved in MOCVD growth make it difficult to paint a clear picture of the entire process. However, a clear understanding of gas flow inside the reactor and the issues pertaining to fluid dynamics in MOCVD provides much deeper insight into the mechanisms at work in the growth process. Fluid dynamics, along with thermodynamics and kinetics, can be used to paint a reasonably clear picture of the MOCVD process. These major areas will be used in the next section to discuss issues that are unique to MOCVD growth of GaN.

#### *3.2.1.4 MOCVD Growth of GaN*

Nitride growth by MOCVD is relatively new compared to other III-V materials, such as GaAs. However, a significant amount of work that has gone into understanding MOCVD growth of GaAs applies directly to GaN growth as well. This is particularly true when dealing with pyrolysis of gallium precursors. Trimethylgallium (TMGa) is the most common gallium precursor in MOCVD growth of GaN. Larsen et al. showed that TMGa is

completely pyrolyzed at 550 °C, regardless of carrier gas, Figure 3.2. [91,95] Other results have shown the major products of TMGa pyrolysis in both H<sub>2</sub> and N<sub>2</sub> ambient to be CH<sub>4</sub>. [95]

Triethylgallium (TEGa) is often used when growing In<sub>x</sub>Ga<sub>1-x</sub>N/GaN quantum wells. TEGa pyrolyzes at much lower temperatures than TMGa, being completely pyrolyzed at 400 °C. [91] This is similar to the decomposition temperature of trimethylindium (TMIn), which makes it useful in growing In<sub>x</sub>Ga<sub>1-x</sub>N/GaN quantum well structures. Studies in H<sub>2</sub>, N<sub>2</sub>, and He show the main decomposition mechanism to be a β-hydride elimination mechanism, by which the TEGa molecule loses a C<sub>2</sub>H<sub>4</sub> molecule. [96]

Ammonia (NH<sub>3</sub>) is the most common nitrogen precursor used in GaN growth. NH<sub>3</sub> decomposes at much higher temperatures than the metalorganic precursors used in GaN growth. Dietz et al. showed the decomposition of NH<sub>3</sub> at atmospheric pressure to take place above 600 °C, with complete decomposition at 800 °C. [97] This is one reason that typical GaN growth temperatures are much higher than typical GaAs growth temperatures.

Another issue with MOCVD growth of GaN is the lack of a lattice-matched substrate, necessitating growth on substrates such as sapphire and SiC, which have a large thermal and lattice mismatch with GaN. Growth processes on these substrates must address the lattice and thermal mismatch as well as material quality, leading to more complex nucleation processes and buffer layers.

An in-situ reflectivity curve showing a typical GaN growth process on sapphire is shown in Figure 3.3. The substrate is first annealed under H<sub>2</sub> ambient at high temperature. Typical GaN growth on sapphire involves growth of a thin (20-30 nm) low-temperature (~520 °C) GaN layer and annealing of that layer to recrystallize it. The reflectivity curve drops significantly upon annealing of the LT-GaN nucleation layer due to surface roughening. A

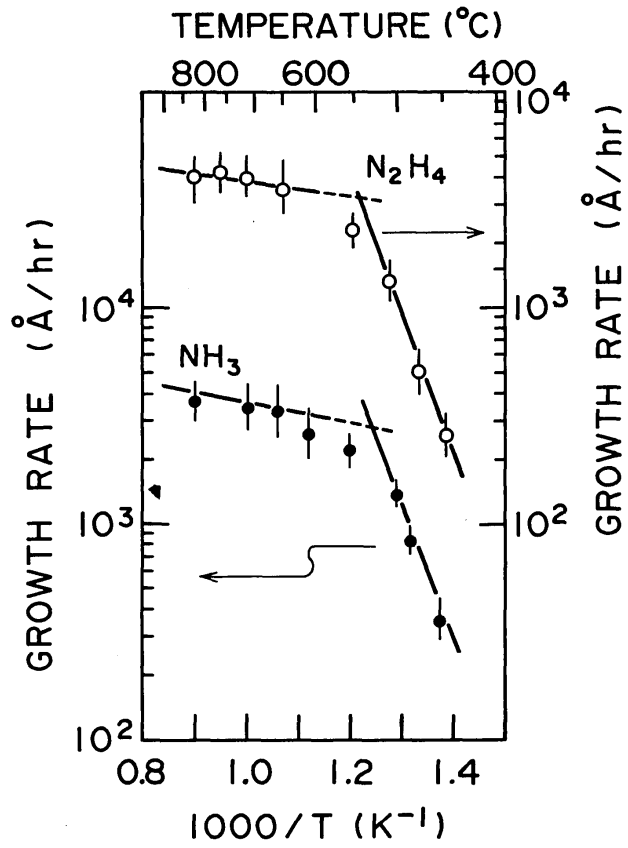


**Figure 3.2:** Temperature-dependent decomposition of TMGa under various atmospheres. (from [95])

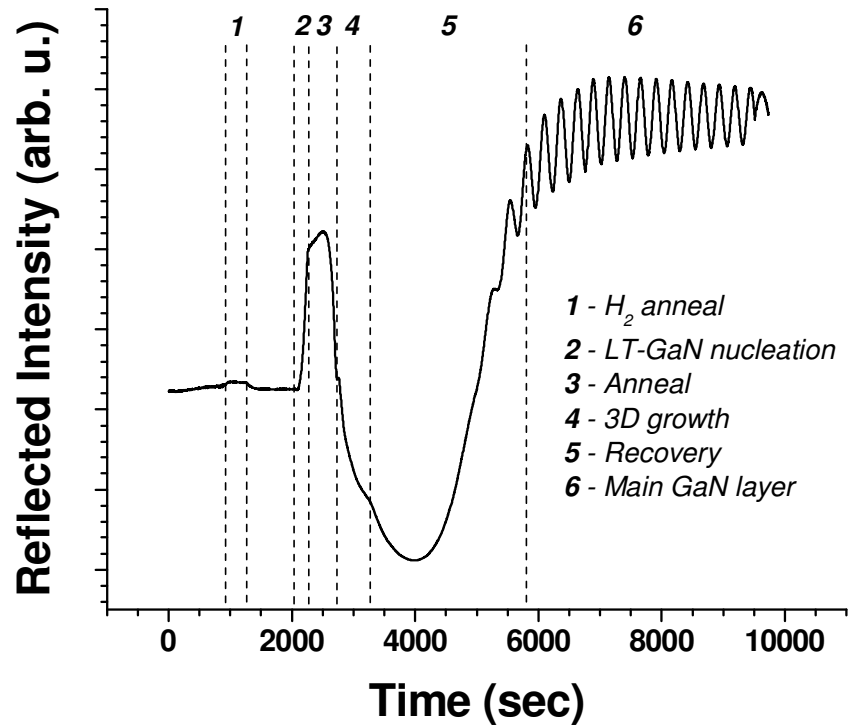


**Figure 3.3:** In-site reflectivity measured during the growth of a standard 2  $\mu$ m-thick GaN template on sapphire.

three-dimensional growth mode ensues, often with a much higher V/III ratio than the final GaN layer to promote lateral growth. The islands formed during nucleation begin to coalesce during this three-dimensional growth, leading to recovery of the surface and return to a two-dimensional, step-flow growth for the final GaN layer. The final GaN layer is grown at a substrate temperature of  $\sim 1020$  °C with a growth rate of  $\sim 2$   $\mu\text{m/hr}$ .

Doping is another issue that must be addressed in MOCVD growth, and p-type doping is particularly difficult in GaN. Intrinsic defects in GaN are donor-like defects ( $V_N$  and  $Ga_i$ ), leading to intrinsically n-type material when undoped. Undoped GaN typically has an n-type free carrier concentration on the order of  $10^{16}$   $\text{cm}^{-3}$ . This intrinsic concentration must be overcome in order to p-dope the material. Another issue with p-type doping is that Mg – the common p-type dopant in GaN – often incorporates during growth as a Mg-H complex, which is also a donor-type defect. A subsequent annealing step in a hydrogen-free environment is needed to remove the hydrogen and activate the Mg as an acceptor.

MOCVD growth of  $\text{In}_x\text{Ga}_{1-x}\text{N}$  requires a much higher V/III ratio and much lower substrate temperatures. The higher V/III ratio is necessary because of the much higher equilibrium vapor pressure of nitrogen over InN. Indium incorporation into these films is controlled by the substrate temperature, with lower substrate temperatures leading to more indium content. Above a substrate temperature of  $\sim 800$  °C, almost no indium is incorporated into the film.

The MOCVD growth system used in this work is an EMCORE D-125 GaN growth system, Figure 3.4. It is a vertical injection, rotating disk reactor with a short jar configuration. Dual injector blocks allow for separation of incompatible precursors before injection.  $\text{H}_2$  is typically used as the carrier gas, but the system also has the capability to flow  $\text{N}_2$  as a carrier gas. A load lock system allows for control of the reactor environment to

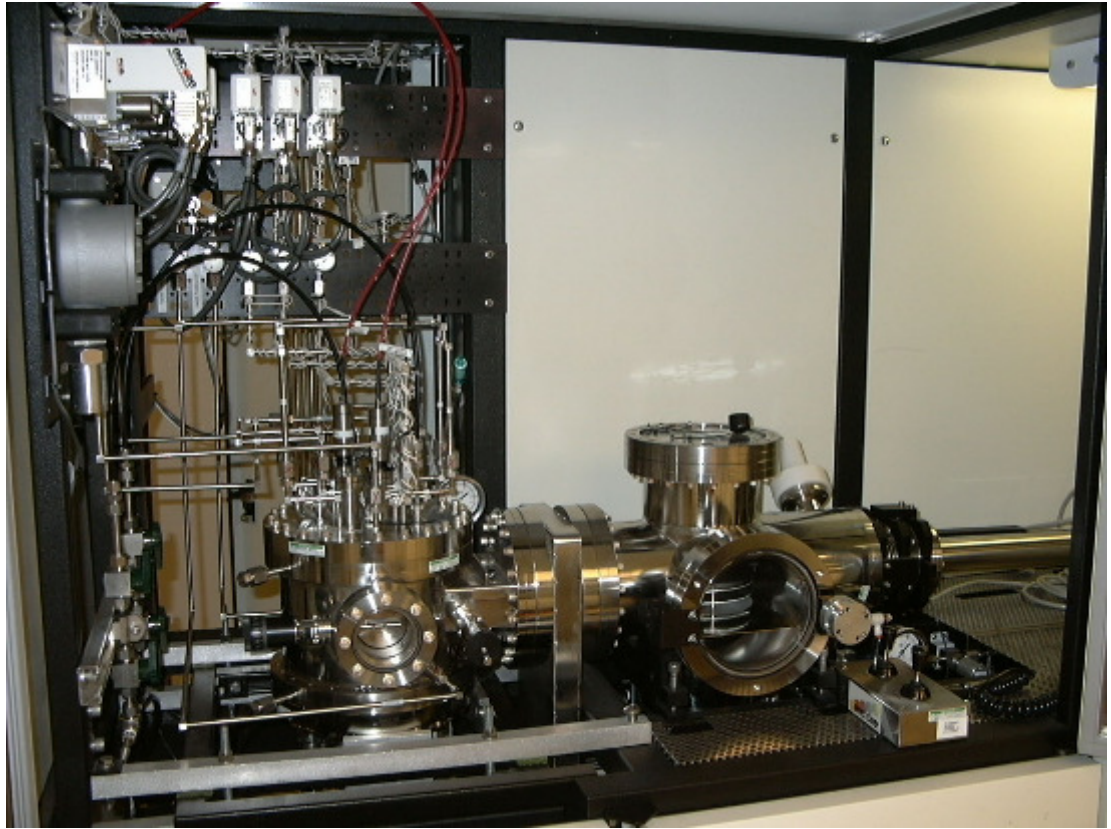


**Figure 3.4:** Modified EMCORE D-125 GaN MOCVD system used in this work.

ensure that no impurities enter the reactor from the atmosphere. TMGa and NH<sub>3</sub> were used as the gallium and nitrogen precursors, respectively, with TMIIn and TMAI as the precursors for indium and aluminum, respectively. Silicon was used as the n-type dopant, with SiH<sub>4</sub> as the precursor, and bis-cyclopentadienyl magnesium (Cp<sub>2</sub>Mg) was used as the Mg precursor for p-type doping. Mg activation was done in a rapid thermal annealer (RTA) in N<sub>2</sub> at 800 °C for 4 minutes.

### 3.2.2 ALD Growth

Atomic layer deposition (ALD) allows for finer control over the growth surface and growth rate. ALD-grown thin films are deposited one atomic layer at a time by pulsing the precursors through the reactor. This pulsing scheme allows for much finer control over layer thickness and uniformity, making the growth of very thin layers much more controllable than in MOCVD growth. However, it introduces a slightly different perspective on pyrolysis and adsorption of precursors.

In order to ensure proper deposition of each atomic layer, the precursor atoms must adsorb onto the surface until  $\Theta = 1$ . Also, the precursors must not be completely pyrolyzed, or a metallic layer will result due to the extremely low vapor pressure of metal elements such as gallium and aluminum. Partially pyrolyzed precursors allow for the transport of the group III atom in the gas phase and subsequent desorption of products after the group III atom adsorbs onto the surface. The most common method to ensure incomplete decomposition is the use of low temperatures and low pressures. At sufficiently low temperatures, most metalorganic molecules are only partially decomposed, and low growth pressures reduce the possibility of homogeneous reactions in the gas phase, ensuring that the reaction takes place

mostly on the growth surface. At higher temperatures, however, the desorption rate can become high enough that it prevents the deposition of a complete atomic layer. [91]

The films in this work were deposited in a temperature range of 100 °C to 250 °C using TMAI and water vapor as the aluminum and oxygen precursors, respectively. Two custom-built ALD systems were used to deposit Al<sub>2</sub>O<sub>3</sub> thin films on both ZnO and silicon substrates. The reactor itself is a horizontal quartz tube reactor that is heated by a tube furnace. Nitrogen was used as the carrier gas. The second system that was used in this work is a vertical injection system using the same precursors. Film quality was found to be similar for the two systems.

### **3.3 CHARACTERIZATION**

Semiconductor thin films and substrates exhibit several types of properties that must be studied to gain a clear picture of material quality and functionality in optoelectronic devices. The major properties pertaining to this work are structural, surface, optical, and electrical properties. This section describes in detail the equipment and techniques used to study these properties.

#### **3.3.1 Structural Characterization**

The crystal lattice – a periodic arrangement of atoms with a regular spacing – is the structural basis of all semiconductor materials. The lattice is described by the crystal structure (hexagonal, zinc-blende, etc.) and the lattice constant, which is the spacing between atoms. The regular ordering of atoms in semiconductor materials allows for their structural properties to be investigated using various types of radiation incident on the surface. The major techniques employed in this work have been X-ray diffraction (XRD) (and X-ray reflectivity (XRR), which is closely related), and Raman spectroscopy.

### 3.3.1.1 X-ray Diffraction (XRD)

XRD is the use of short-wavelength radiation (X-rays) to probe the structural properties of a material. The diffraction of X-rays from a crystal can be described by Bragg's law:

$$n\lambda = 2d \cdot \sin \theta \quad (3.11)$$

where  $n$  is an integer,  $\lambda$  is the X-ray wavelength, and  $d$  is the spacing between atoms. This relationship states that, for a given X-ray wavelength, the angle at which X-rays are diffracted is determined by the atomic spacing  $d$ , as illustrated in Figure 3.5. Because the exact atomic spacing is unique to a material, XRD can be used to identify unknown materials by comparing the spectrum of the unknown sample to that of a known standard. XRD can also be used to extract such information as strain, grain size, and defect density.

The periodicity of a crystal provides multiple reflection planes for XRD, and the Bragg angle of each of these reflections is determined by the atomic spacing of the atoms and the orientation of the reflection plane. The relationship of the Bragg angle to the reflection plane and atomic spacing in hexagonal crystals is given in Equation (3.12):

$$\theta_{\text{hexagonal}} = \sin^{-1} \left( \frac{\lambda}{2} \sqrt{\frac{4}{3} \left( \frac{h^2 + hk + k^2}{a^2} \right) + \frac{l^2}{c^2}} \right) \quad (3.12)$$

$\lambda$  is the X-ray wavelength;  $h$ ,  $k$ , and  $l$  are the Miller indices describing the reflection plane and  $a$  and  $c$  are the lattice constants. The (002) reflection is commonly taken as a measure of crystal quality in c-plane GaN, as the (002) reflection plane is perpendicular to the growth axis, allowing probing of the  $c$  lattice constant and providing a good gauge of crystal orientation and quality. Determination of the  $a$  lattice constant in hexagonal materials must be done using an off-axis reflection such as the (102) reflection.

The linewidth of the diffraction peak can also be taken as a measure of overall crystal quality, and a significant amount of work has been done toward determining and separating

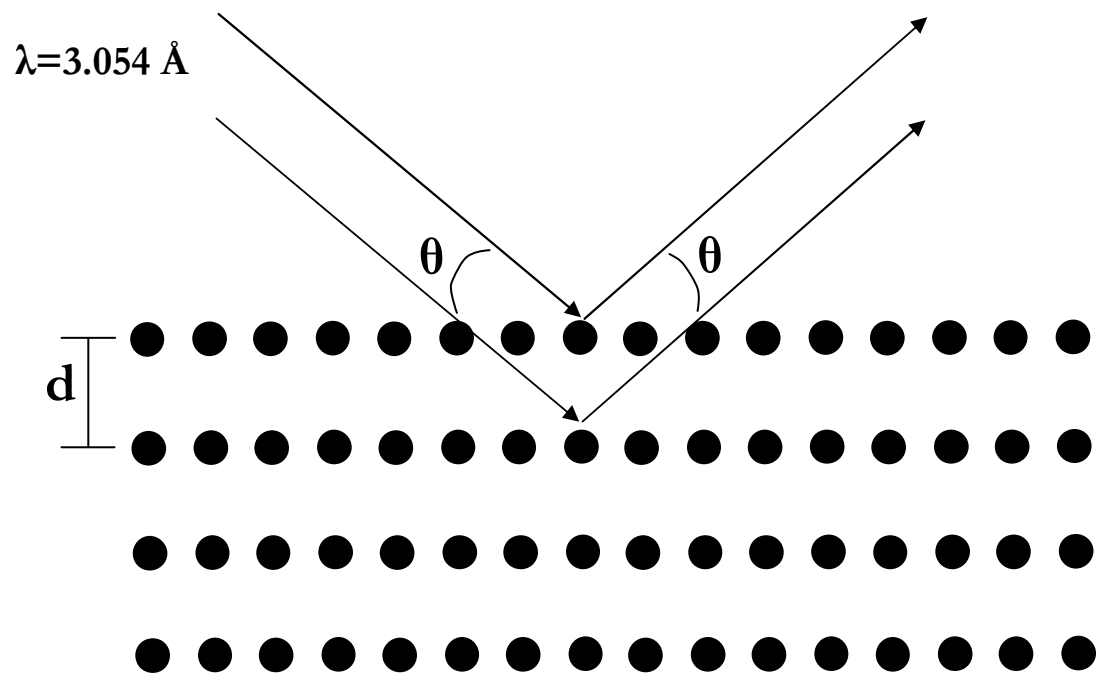


**Figure 3.5:** Diffraction of X-rays from a thin film surface showing the Bragg angle,  $\theta$ .

the various contributions to line broadening in XRD. The method developed by Williamson and Hall in 1953 [98] can be used to calculate dislocation density from the Bragg angle and linewidth of the diffraction peak. The Williamson-Hall plot is made by plotting the product of the linewidth and  $\sin(\theta)/\lambda$  versus  $\sin(\theta)/\lambda$  (where  $\theta$  is the Bragg angle and  $\lambda$  is the X-ray wavelength) for sequential reflections in a material, such as the (002), (004), and (006). The coherence length, tilt and twist angles, and dislocation density can be calculated from this plot, providing valuable structural information about the materials being investigated. [99]

In this work, XRD was performed with a Philips X'Pert Pro MRD diffractometer using a  $1/4^\circ$  slit on both the incident and diffracted beam optics, unless otherwise indicated. The same system was used for XRR measurements, as the necessary equipment is very similar.

### 3.3.1.2 X-ray Reflectivity (XRR)

The refractive index of a material at X-ray wavelengths is often less than unity, and can be expressed as

$$n = 1 - \delta - i\beta \quad (3.13)$$

where  $\delta$  and  $\beta$  are material-specific dispersion and absorption coefficients, respectively. This implies total external reflection for low angles less than a certain critical angle. For thin films and multilayered structures, reflections from the multiple interfaces lead to interference fringes that are observable beyond the critical angle. The frequency and intensity of these oscillations can provide information about the interfacial roughness and density of the film. XRR is the observation of these phenomena to provide a clearer picture of the properties of very thin films. The technique is useful in determining thickness, roughness, mass density, and electron density profile of very thin (<100 nm) films.

The XRR pattern of multilayered thin film structures can also be modeled using a method developed by Parratt in 1954 [100]. The Nevot-Croce approximation also allows for

the incorporation of interfacial roughness into this model.[101]. In this work, XRR was used to determine the thickness of thin films deposited on both ZnO and silicon substrates.

### 3.3.1.3 Raman Spectroscopy

The elastic scattering of light by matter is known as Rayleigh scattering, while inelastic scattering of light by matter is known as Raman scattering. In Raman scattering, the energy of the scattered light either increases (anti-Stokes scattering) or decreases (Stokes scattering) relative to the incident laser radiation so that the energy shift of the scattered light can be measured.[102] The Stokes and anti-Stokes shifts are symmetric about the Rayleigh band, and only certain values of the shift are allowed for a specific crystal. These values correspond to rotational and vibrational modes of molecules in the material, and are referred to as phonon modes. Raman spectroscopy is a non-destructive technique that allows for the investigation of such phonon modes and their relation to crystal structure and point defects by measuring the Stokes (or anti-Stokes) shift in a certain material.

Six optical phonon modes are expected in hexagonal wurtzite crystals, Figure 3.6. Of these, four are Raman-active, with the  $B_1(\text{low})$  and  $B_1(\text{high})$  being ‘silent’. Which mode or combination of modes is visible in the Raman spectrum, however, also depends on the geometry of the measurement, described using Porto notation. An example of Porto notation is  $\tilde{\nu}(x,y)-\tilde{\nu}$ . In this example,  $\tilde{\nu}$  refers to the direction of the incident light, and  $-\tilde{\nu}$  refers to the direction of the scattered light. Polarization of the incident and scattered light is described in parentheses, with  $x$  referring to the polarization of incident light and  $y$  referring to the polarization of the collected (scattered) light. In this work, the z-axis is taken as parallel to the c-axis of the materials being investigated.

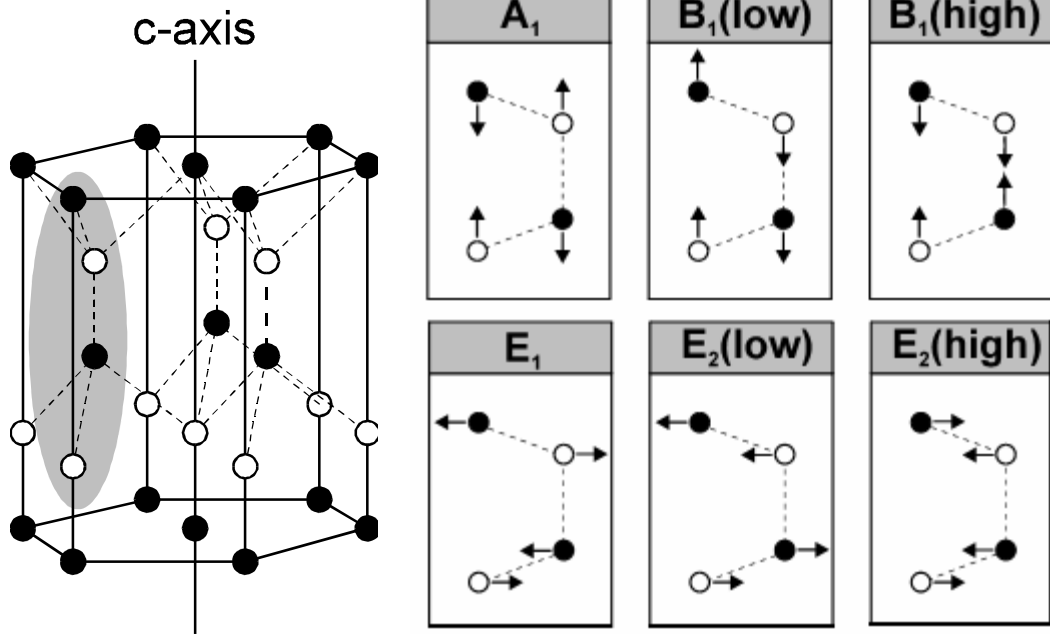


**Figure 3.6:** Raman vibrational modes in a wurtzite crystal. The B<sub>1</sub> modes are 'silent' in Raman spectroscopy.

The most common features in the unpolarized Raman spectrum of hexagonal GaN are the  $E_2$  and  $A_1$  modes. The  $E_2(\text{high})$  mode is commonly used to investigate strain, as it shifts with compressive or tensile strain in the material to higher or lower wavenumbers, respectively. The  $A_1(\text{LO})$  mode can be used as a gauge of free carrier concentration, as coupling of free carriers to this mode causes broadening with increasing carrier concentration. The  $A_1(\text{LO})$  mode is also sensitive to angular dispersion, and can be useful in determining the orientation of the crystal relative to the optical axis.[103] Local vibrational modes due to impurities and point defects can also be observed via Raman spectroscopy, providing insight into the ways in which impurities incorporate into the material and the effects of these impurities on crystal quality. [102,104]

A Renishaw micro-Raman system with a 488 nm Ar-ion laser has been used in this work. All measurements were taken in the backscattering configuration at room temperature, unless otherwise indicated.

### 3.3.2 Surface Characterization

Surface characterization is also very important for thin film growth. The surface morphology of a semiconductor thin film is indicative of the mechanisms involved in growth. Surface morphology can also be very instructive in determining the abruptness of interfaces in superlattice and multiple quantum well structures. Many different microscopy techniques are available to characterize semiconductor surfaces. The three used in this work are atomic force microscopy (AFM), scanning electron microscopy (SEM), and transmission electron microscopy (TEM).

### 3.3.2.1 Atomic Force Microscopy (AFM)

An AFM consists of a very small cantilever with a probe on the end. A laser is often used to measure the deflection of the probe. This is done by shining a laser on the probe tip and measuring the deflection using a photodiode array. As the probe is scanned over the sample surface, surface features cause it to deflect the laser light. The amount of deflection observed by the photodiode array gives an indication of the deflection of the probe tip, and, therefore, the surface morphology. An image of the surface can be obtained by scanning the probe tip in both the  $x$  and  $y$  axes and using the resulting data points to create a map of the surface. Piezoelectric crystals are often used to scan the tip in the  $x$ ,  $y$ , and  $z$  directions.

Many different types of forces can be at work between the probe tip and the sample surface, however. Two scanning modes exist to deal with different types of samples and different types of surface forces: contact mode and non-contact mode. Contact mode is, of course, used when the sample is in contact with the surface. In contact mode, the tip deflection is measured and directly related to the surface morphology. Probe tips for contact mode AFM scans are often more flexible than their non-contact counterparts. This is because of noise introduced by the measurement of the static tip deflection.

Non-contact mode can be used for imaging surfaces that are slightly rougher and may risk damaging the cantilever in contact mode. In non-contact mode, the probe tip is held a few nanometers above the surface and oscillated at a frequency slightly higher than the resonant frequency. Van der Waals forces extending up to 10 nm above the surface cause a shift in the resonant frequency, which causes a decrease in the amplitude of the tip oscillations. At each data point, the probe tip is adjusted in the  $z$ -direction to maintain a specific frequency. The shift in the  $z$ -direction is directly related to the surface morphology,

so this shift can be used to create a map of the sample surface. PSIA XE-100 atomic force microscope was used in this work.

### *3.3.2.2 Scanning Electron Microscopy (SEM)*

A sample, such as a thin film, can be imaged using a beam of high energy electrons incident on the sample. Such a beam produces several different types of interactions between the sample and the electrons, including transmitted electrons, secondary electrons, and backscattered electrons. A scanning electron microscope scans this high-energy beam of electrons across a sample surface in a raster fashion, detecting electrons of various types, depending on the image desired. SEM images produce a good depth of field, and are quite useful in studying the microstructure of a thin film surface. Incident electrons can also produce X-rays with a wavelength that is characteristic of the sample composition. Measuring the relative intensities of these X-rays to determine composition of a sample surface is known as energy-dispersive X-ray spectroscopy (EDS).

### *3.3.2.3 Transmission Electron Microscopy (TEM)*

Transmission electron microscopy (TEM) involves the transmission of a beam of electrons through a very thin sample. The interaction of the electrons with the sample produces a pattern that allow for imaging of thin samples at very high magnifications. Electrons can be transmitted directly through the sample, absorbed, or diffracted. The pattern of diffracted electrons can be useful in determining crystal structure and quality, and the absorption of electrons can help to create contrast in both bright-field and dark-field TEM images. TEM is a very powerful technique for studying the crystal quality of thin layers and interfaces because of the high resolution it offers.

### 3.3.3 Optical Characterization

Careful examination of the optical properties of semiconductors can yield a wealth of information about overall material quality, strain, impurities, and native defects. The temperature dependence of these properties can also yield information about the energy level of impurities. One of the most common methods of investigating optical properties in semiconductors is photoluminescence (PL) spectroscopy. PL was employed in this work, along with optical transmission, to study the optical properties of the GaN layers on both ZnO and silicon.

#### *3.3.3.1 Photoluminescence Spectroscopy (PL)*

Photoluminescence is the process by which a material absorbs photons of one wavelength and emits photons of another wavelength. Absorption of energy from the photoexcitation source excites electrons to higher energy states. These electrons then return to their ground state via a radiative recombination mechanism, emitting a photon in the process. Photoluminescence is distinguished from other types of luminescence by photoexcitation. Photoluminescence spectroscopy is the study of these radiative recombination mechanisms in materials. In semiconductor materials, PL spectroscopy is used to study many properties including the bandgap energy, electronic defects, strain, and general optical quality of the material.

The near-bandgap emission is often the most prominent feature in the PL spectrum of a semiconductor material taken with above bandgap excitation. However, PL also shows radiative transitions involving impurities and electronic defects in the material. Typical radiative transitions observable in the PL spectra of wide bandgap semiconductors include near-bandedge transitions, transitions to(from) defect levels from(to) the bandedge, and

donor-acceptor pair transitions. The energy of such transitions is useful in determining defect levels in semiconductors.

Features in a PL spectrum can be studied more closely by varying both the temperature and excitation power. The dependence of the bandgap on temperature is often given by the Varshni relation in Equation (3.14) [105]:

$$E_g(T) = E_g(0) - \frac{\alpha T^2}{T - \beta} \quad (3.14)$$

where  $\alpha$  and  $\beta$  are material-specific constants. The intensity of the near bandedge luminescence also decreases significantly with increasing temperature, while the linewidth increases. The increased linewidth is due to thermal broadening of the near bandedge emission.

The dependence of PL features on excitation power can also provide insight into the origin of the peaks. A change in intensity with excitation power can be indicative of recombination lifetime, and some defect-related peaks with long lifetimes tend to saturate in intensity at very low excitation power. A shift of peak position with excitation power has been observed in some defect-related peaks as well, though the mechanisms vary.[106]

PL spectra were taken with two different experimental setups in this work. A 325 nm Melles-Griot He-Cd laser with an Acton Spectra Pro 2300i monochromator and PIXIS 100 CCD camera was used for temperature-dependent measurements. A 238 nm pulsed Ne-Cu laser with a CVI monochromator and a Hamamatsu photomultiplier tube (PMT) was used for room temperature measurements.

### 3.3.3.2 *Optical Transmission*

Another useful technique to examine the optical properties of a material is optical transmission. Both GaN and ZnO are transparent throughout the visible spectrum, allowing light of a lower energy than the bandgap to pass through the material. Examining the

percent transmission as a function of wavelength can give information about the bandedge as well as electronic defects that are not visible in PL spectra.

Defects are often visible in a transmission spectrum as an absorption band that causes a drop in the transmission signal below the bandgap energy. Optical transmission also provides information about intra-atomic transitions, such as d-d transitions in transition metals, and d-f transitions in rare earth elements. [107] These measurements require a smooth surface on both top and bottom of the film, however, as a rough surface will scatter the transmitted light and decrease signal intensity significantly.

Optical transmission measurements were done using a broadband source and a spectrometer to measure the intensity of transmitted light at each wavelength.

### 3.3.4 Electrical Characterization

Electrical characterization techniques yield information about the free carrier concentration as well as conductivity and resistivity of the material. This information is useful in determining impurity levels and overall material quality, as some key impurities in GaN, such as oxygen (a shallow donor), contribute to conduction. Thus, in addition to providing crucial electrical information, electrical characterization techniques, when properly interpreted, also provide information regarding impurity levels and overall material quality.

#### *3.3.4.1 Hall Effect Measurement*

The Hall effect is observable when a magnetic field is applied perpendicular to the flow of current in a semiconductor bar, deflecting the path of the carriers. In a right-handed coordinate system, if the magnetic field is applied in the  $z$  direction, and current flows in the  $x$  direction, then the force experienced by the carriers is given as

$$F_y = q(\mathcal{E}_y - v_x \mathcal{B}_z) \quad (3.15)$$

where  $\mathcal{E}_y$  is the electric field in the  $y$  direction,  $v_x$  is carrier velocity in the  $x$  direction, and  $\mathcal{B}_z$  is the magnetic field applied in the  $z$  direction. The result of Equation (3.15) is that carriers will experience a net force in the  $-y$  direction unless an electric field equal in magnitude to  $v_x \mathcal{B}_z$  is created to compensate. The shift of the carriers along the  $y$ -axis, however, creates this compensating electric field and allows the carriers to maintain the  $x$ -axis as their overall direction.[108]

The compensating electric field that is generated by the Hall effect is proportional to the product of magnetic flux density and current density. The proportionality constant is known as the Hall coefficient:

$$R_H = \frac{1}{qp_0} \quad (3.16)$$

where  $p_0$  is the carrier density. Thus, for a known current and magnetic field, the free carrier concentration can be calculated by measuring the induced voltage across the sample. Other information, including the resistivity, conductivity, and carrier mobility, can be determined using the Hall effect as well.

The Hall effect was measured in this work using a Lakeshore HMS3000 Hall effect measurement system with a 0.51 T applied field. Samples were cut to 1 cm x 1 cm for the measurements.

#### 3.3.4.2 Secondary Ion Mass Spectrometry (SIMS)

While SIMS is not specifically an electrical characterization technique, it provides information on the types and concentrations of impurities in samples. A primary ion beam is used to sputter away material from the sample surface, producing secondary ions. These secondary ions are then separated by a mass spectrometer to determine the elemental composition of the sample. SIMS can provide information on the molecular and elemental

composition of a sample as well as the specific isotopes present for a given element. The absolute concentration of impurities can only be determined if the results are compared to those of a known standard, however. Ion-implanted samples for which the concentration profile is well-known are typically used as standards.

Typical ions used for SIMS include  $\text{Ar}^+$ ,  $\text{O}^-$ , and  $\text{Cs}^+$ . The type of ion used determines the elements to which SIMS is sensitive. In this work,  $\text{O}^-$  and  $\text{Cs}^+$  beams were used to detect positive and negative ions, respectively.  $\text{O}^-$  ions typically enhance the concentration of positive ions, while  $\text{Cs}^+$  ions typically enhance the concentration of negative ions. As the ion beam sputters material away from the surface, the surface being analyzed moves deeper into the material. Thus, SIMS can provide a depth profile for concentrations of elements in semiconductors.

The sensitivity of SIMS is different for each element, however, and it depends on several factors. The first is the ionization efficiency, or the efficiency with which the primary ion beam ionizes atoms of a given element. Different elements have different ionization efficiencies. Sensitivity also depends on the background impurities present in the vacuum system, and on their concentrations. For example, the sensitivity for such elements as nitrogen and oxygen is limited by the background concentration of these elements in the system, as these elements are typically present in trace amounts in vacuum systems.

SIMS was used in this work to determine the concentration of typical impurities in GaN, including oxygen and carbon. The diffusion profile of zinc and oxygen into the GaN layer was also studied in order to gain a better understanding of interdiffusion at the GaN/ZnO interface.

### 3.3.5 Device Characterization

There are two main aspects to the characterization of LEDs. The first aspect is the electrical properties of the device. This includes measurement of I-V curves and series resistance. The second aspect is the measurement of optical properties, i.e. spectrum and total output power. Device efficiency can be determined by correlating electrical and optical properties of LEDs. This section describes the details of these measurements as well as the information that can be obtained from them.

#### 3.3.5.1 *Current-Voltage (I-V) Measurement*

The most fundamental property of a diode is its I-V characteristics. The I-V curve is what identifies the device as a diode. A semiconductor diode consists of a p-n junction, and current flow through the device is controlled by the voltage across the junction.

There are two types of current in a p-n junction: drift and diffusion. Electrons and holes diffuse across the junction due to the steep concentration gradients at the junction. This diffusion of carriers, however, leads to the formation of a space-charge region consisting of uncompensated donors and acceptors. The uncompensated charge near the interface leads to an electric field pointing from the n-region toward the p-region. This electric field induces a drift current that, at equilibrium, exactly cancels the diffusion current.

Applying a voltage so that the p-region is at a positive potential with respect to the n-region reduces the electric field across the junction. This reduction in electric field makes the diffusion of carriers across the junction more likely by an exponential factor that is dependent on the forward voltage. Thus, the total current through the junction with forward bias applied is the total diffusion current minus the total drift current. This relationship can be expressed as

$$I = I_0 \left( e^{qV/kT} - 1 \right) \quad (3.17)$$

where  $I_0$  is the absolute value of the drift current,  $q$  is electronic charge,  $V$  is the voltage across the junction, and  $k$  is Boltzmann's constant.[109] The series resistance – a measure of the on resistance of the device – can also be calculated from the I-V curve.

The current-voltage characteristics of a device are key to understanding the mechanisms at work in the device as well as determining its usefulness in a given application. A Keithley 2420 sourcemeter was used in this work to evaluate the I-V characteristics of the devices.

### 3.3.5.2 Electroluminescence (EL)

Light is generated in an LED by regeneration of carriers in the active region of the device. The color of light is determined by the bandgap energy,  $E_g$ , of the semiconductor material. More precisely, when an electron is excited into the conduction band and then recombines with a hole in the valence, it loses the energy difference,  $E_g$ , in the form of a photon.

Electrons in the conduction band follow a Boltzmann distribution with an average kinetic energy of  $kT$ . Near the conduction band edge, the density of electrons per unit energy is also limited by the electron density of states. This energy distribution also holds true for holes in the valence band. Recombination of these electrons and holes leads to an emission spectrum that follows the relationship

$$I(E) = \sqrt{E - E_g} e^{-E/kT} \quad (3.18)$$

where  $I(E)$  is the emission intensity as a function of energy.[109] A homojunction LED in which the emitted light is equal to or slightly above the bandgap of the material, however, suffers from reabsorption in the bulk, degrading efficiency. One solution to this problem is the use of quantum wells in the active region, as in  $\text{In}_x\text{Ga}_{1-x}\text{N}/\text{GaN}$  multiple quantum well

LEDs. Quantum well structures in the active region of LEDs typically emit light at an energy lower than the bandgap of the surrounding material, suppressing reabsorption in the surrounding layers and increasing the amount of light extracted from the device.

$\text{In}_x\text{Ga}_{1-x}\text{N}/\text{GaN}$  multiple quantum well LEDs were grown in this work. The EL properties were measured using a Keithley 2420 sourcemeter, OL-770 spectrometer, and IS-670 integrating sphere from Optronic Laboratories.

### *3.3.5.3 Optical Power Measurements*

Total light output from an LED is of great importance in solid state lighting applications. The ratio of optical power emitted from an LED to electrical power consumed by the LED is known as the external quantum efficiency (EQE). EQE is the product of the light extraction efficiency and internal quantum efficiency (IQE), which is the ratio of photons generated in the active region of the LED to electrons injected into the active region. These quantities – optical power, EQE, and IQE – are used to describe the efficiency of an LED. The measurements in this work were taken using the Keithley sourcemeter and Optronic Laboratories equipment described above.

## **3.4 DEVICE PROCESSING**

A standard process for fabrication of GaN-based LEDs was used in this work. The end result of the process is a wafer with vertically-emitting devices that are  $350\mu\text{m}$  on each side, Figure 3.7. The exact steps of the process are as follows:

- 1) Annealing for p-GaN activation
- 2) Metal deposition for current spreading layer
- 3) Annealing current spreading layer
- 4) Photolithography for mesa pattern

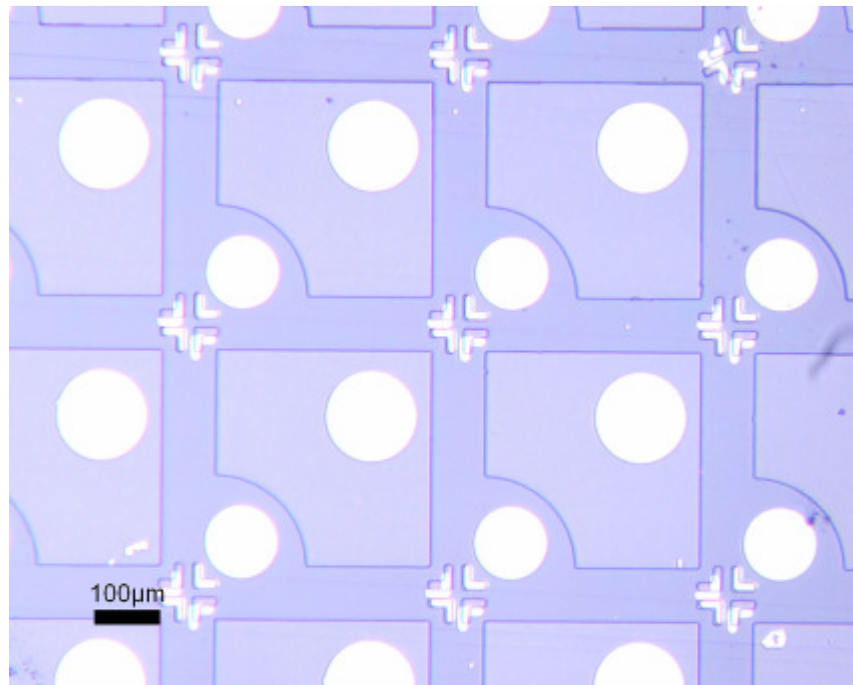


**Figure 3.7:** Typical LED structure used in this work. P-type contacts are the large circles, and n-type contacts are the smaller circles. Each device is  $350\mu\text{m}$  on a side.

- 5) Etch – removal of current spreading layer
- 6) Hard bake to cure photoresist
- 7) Dry etch to define mesa
- 8) Removal of baked photoresist
- 9) Transfer of p-type contact pattern
- 10) Deposition of p-type contact metal
- 11) Lift-off of p-type contact metal
- 12) Transfer of n-type contact pattern
- 13) Deposition of n-type contact metal
- 14) Lift-off of n-type contact metal

The major steps involved in this process are annealing, photolithography, etching, and metal deposition. Each of these steps will be discussed in more detail in the following sections.

#### 3.4.1 Annealing

Activation of the Mg acceptors in GaN is required for reliable p-type material. This is due to the formation of Mg-H donor complexes during growth. Annealing in a nitrogen atmosphere drives out the hydrogen and activates the Mg as an acceptor in GaN. In this work, p-GaN activation was done in an RTA system at 800 °C for 4 minutes under N<sub>2</sub> ambient. The current spreading layer was also annealed at 500 °C for 2 minutes in an RTA under atmospheric ambient. The presence of oxygen allows for oxidation of the Ni-Au layer, forming NiO, which provides a better ohmic contact to p-type GaN.

#### 3.4.2 Photolithography

Patterns are transferred to the wafer using photolithography. A thin layer of photoresist is applied to the wafer by spinning at 2500 rpm for 30 seconds. Two layers of photoresist

are typically used in this process. The photoresist is then cured by baking it at 100 °C for one and a half minutes. Next, a mask is used to expose the photoresist with the desired pattern, and another bake is performed. Finally, the photoresist is developed in AZ-400K developer, leaving the desired pattern on the wafer.

### 3.4.3 Etching

Two types of etching are involved in the LED fabrication process: wet etching and dry etching. Wet etching is used to remove the Ni-Au layer deposited for the current spreading layer. Potassium iodide is used as the etchant in this process.

Dry etching is also performed to create the mesa pattern. Dry etching of GaN is done using chlorine gas in a reactive ion etching (RIE) system. The chlorine ions incident on the surface etch both the GaN and the photoresist. However, as the photoresist is thicker than the desired etch depth, the areas covered with photoresist are protected from etching. The percentage of chlorine ions incident on the sidewalls is also very low, leading to a high degree of anisotropy.

### 3.4.4 Metal Deposition

Metal contacts are deposited using electron beam evaporation. A focused electron beam is used to heat the metal charge until it evaporates at a controlled rate. The evaporated metal is then deposited on the patterned wafer. The metal source is placed inside a crucible in a vacuum chamber. The patterned wafer is then placed in the chamber with the patterned side facing the metal charge. This method allows for deposition of metals such as aluminum, titanium, nickel, and gold, all of which are common contact metals for GaN-based LEDs.

### **3.5 SUMMARY**

This chapter summarizes the growth, characterization, and processing techniques used in this work as well as the equipment for each of the techniques. MOCVD growth was used in this work because of its flexibility and its applicability to commercial processes. The structural, optical, surface, and electrical properties of the thin films were investigated. GaN-based materials were grown and characterized, and GaN-based LEDs were fabricated and studied, using the methods described herein.

## CHAPTER 4: MOCVD GROWTH OF GaN AND $\text{In}_x\text{Ga}_{1-x}\text{N}$ ON ZnO

An MOCVD growth process was developed for GaN growth on ZnO. Initial investigations identified the key issues, and further refinement of the process yielded GaN thin films on ZnO. This chapter discusses results of the initial investigations into MOCVD growth of GaN on ZnO, and the properties of initial GaN and  $\text{In}_x\text{Ga}_{1-x}\text{N}$  layers grown on ZnO.

### 4.1 INITIAL CHALLENGES

An initial study was done to identify the key materials- and growth-related issues facing MOCVD growth of GaN on ZnO. The major issues identified in these early investigations were the instability of the ZnO substrate in a hydrogen atmosphere, and the diffusivity of Zn and O into the GaN layer, degrading both interface and thin film quality. A process was developed to address both of these issues and yield high quality GaN on ZnO.

The ZnO substrates used in this study were grown using a modified bulk crystal melt growth. The boule creates its own crucible, therefore allowing for contamination-free growth. Two inch wafers are available with this growth method, and samples show an etch pit density of  $10^4/\text{cm}^2$ . The aim is to replicate the low etch pit density in the ZnO substrate into the GaN film.

#### 4.1.1 Reactivity of ZnO in $\text{H}_2$

The first step in the development process was to investigate the stability of the ZnO substrate in a hydrogen atmosphere. Taken together, the hydrogen carrier gas and the overpressure of the Group V precursor ( $\text{NH}_3$ ) required for high quality GaN by MOCVD

provide a significant amount of hydrogen to the growth surface, and a substrate that is unstable in a hydrogen atmosphere will prove problematic for MOCVD growth of GaN.

#### 4.1.1.1 Carrier Gases

Hydrogen is typically used in GaN growth because it leads to higher material quality, though the exact reasons for this are still under investigation. It has been found that H<sub>2</sub> carrier gas is beneficial to the surface morphology, structural quality, and electrical properties of GaN thin films relative to those grown with N<sub>2</sub>. [94,110] It has been proposed that H<sub>2</sub> back-etching of the LT-GaN nucleation layer results in larger islands and a longer coalescence time compared to N<sub>2</sub>. The longer coalescence time and larger islands lead to smaller edge dislocation densities in the GaN layer. [110]

Wang et al. also observe a change in surface morphology with changing  $\frac{N_2}{N_2 + H_2}$  ratio. Increasing the ratio led to a rough surface and a decrease in structural quality of the material, while using pure H<sub>2</sub> led to a mirror-like surface morphology. They attribute this change in surface morphology to a decrease in diffusion length of the reactants on the growth surface caused by the increased gas density near the interface with increasing nitrogen. [94]

As an initial study of the stability of ZnO in H<sub>2</sub>, ZnO substrates were exposed to H<sub>2</sub> at typical GaN growth temperatures, and the etch rate was measured. Figure 4.1 shows the temperature dependence of the ZnO etch rate in H<sub>2</sub>. The dependence of the etch rate in H<sub>2</sub> on reciprocal temperature shows an Arrhenius dependence with a calculated activation energy of 63 meV. An extrapolation to lower growth temperatures (~600 °C) suggests that the ZnO substrate is still unstable at relatively low growth temperatures, necessitating the development of a near H<sub>2</sub>-free approach to GaN growth on ZnO. Such an approach can be problematic for GaN growth, however, as discussed previously. Nitrogen was used as the

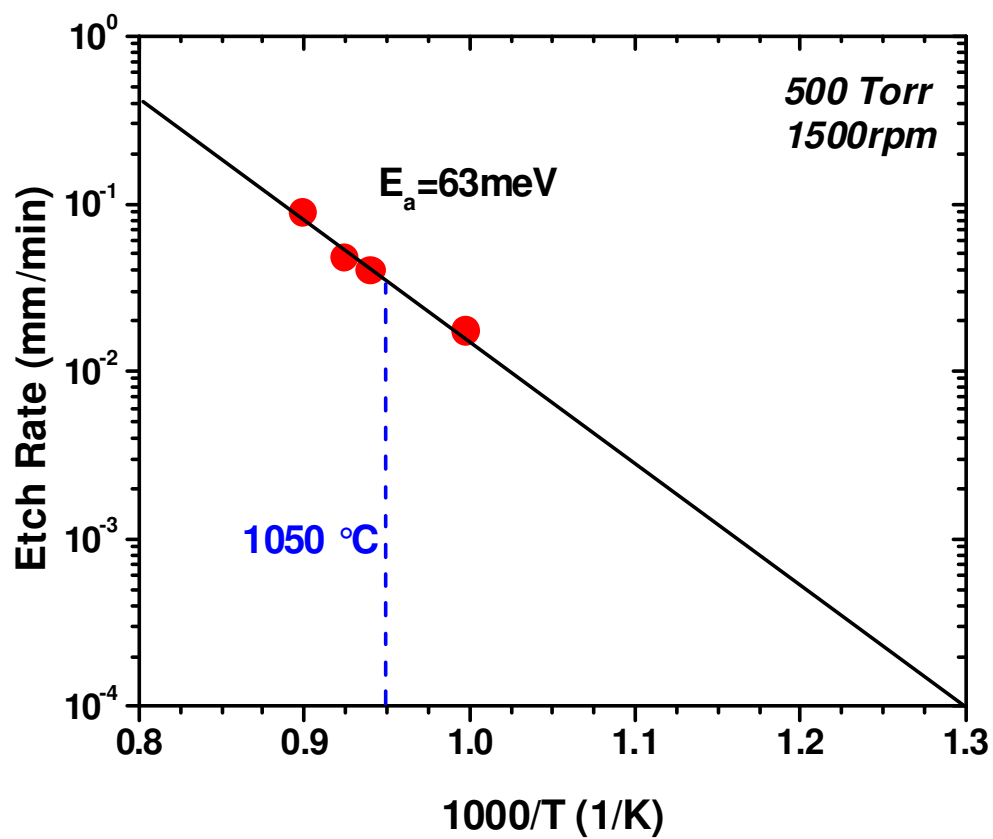


**Figure 4.1:** Etch rate of ZnO in a hydrogen atmosphere. A typical GaN growth temperature is marked for reference.

carrier gas in this work because of the reactivity of ZnO with hydrogen at elevated temperatures.

#### 4.1.1.2 Nitrogen Precursors

Ammonia ( $\text{NH}_3$ ) is the most common nitrogen precursor used in MOCVD growth of GaN. The large amount of hydrogen that is delivered to the growth surface upon breakdown of  $\text{NH}_3$ , however, may lead to degradation of the ZnO substrate. Specifically, ZnO substrates etch very quickly under typical GaN growth conditions, which involve high  $\text{NH}_3$  flow rates ( $\sim 6\text{-}8$  slm) and high growth temperatures ( $\sim 1020$  °C).

Dimethylhydrazine (DMHy) was investigated as a nitrogen source for this reason, since it decomposes around 500 °C.[43] The low decomposition temperature should allow for GaN growth at much lower temperatures compared to GaN growth using  $\text{NH}_3$ , which decomposes at much higher temperatures compared to DMHy. In fact, DMHy has been used in low-temperature GaN growth with good results. [43] In this work, DMHy was used as a nitrogen precursor with growth temperatures varying from 550 °C to 950 °C. Figure 4.2 shows an XRD 2 $\theta$ -w scan of the (0002) reflection a GaN layer grown on ZnO using DMHy as the nitrogen precursor. The GaN (0002) reflection is visible on the high angle side of the ZnO peak, though it is relatively weak. There are several reasons for the low crystal quality in the films grown using DMHy. The first is that the low growth temperature may not allow for sufficient diffusion of adatoms on the growth surface. The second reason is the high carbon content in the films compared to GaN layers using  $\text{NH}_3$  as a precursor.

At typical V/III ratios ( $\gg 1$ ), carbon incorporation was a significant problem. A drop in V/III ratio reduced carbon incorporation significantly, though carbon content was still high relative to typical GaN films grown with  $\text{NH}_3$ . The high carbon content also had a

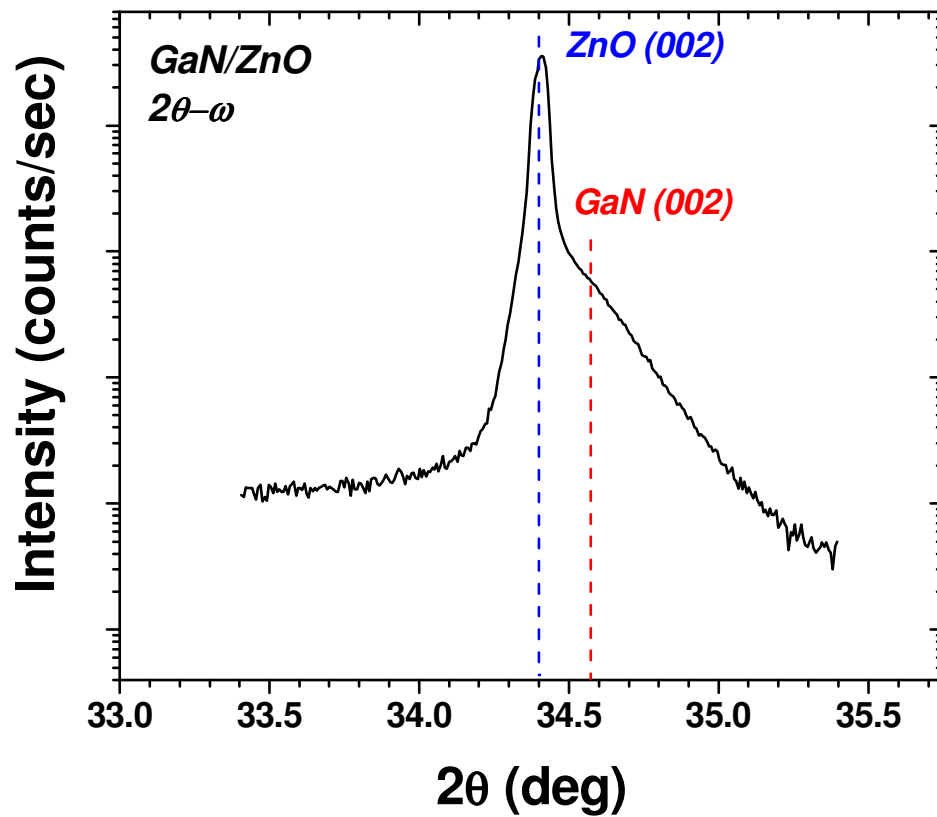


**Figure 4.2:** XRD pattern of GaN grown on ZnO using DMHy as a nitrogen precursor. The shoulder on the high angle side is due to the GaN (002) reflection.

detrimental effect on optical quality of the material, as no bandedge emission was observable in layers grown using DMHy.

Tertiary butylhydrazine (TBHy) was also investigated as a nitrogen precursor with similar results. The carbon content in films grown using metalorganic nitrogen precursors was too high to make the films useful for devices applications. Clearly, reaction kinetics change when changing precursors, and the optimum reactor geometry for growth with  $\text{NH}_3$  may be dissimilar to that for growth with DMHy or TBHy. While other researchers have reported growth of GaN on ZnO using DMHy [43], the most promising nitrogen precursor for GaN growth on ZnO in this system is  $\text{NH}_3$ , and  $\text{NH}_3$  was used for the rest of the work on ZnO.

#### 4.1.2 Diffusion

Zinc diffusion has been a problem in other semiconductor systems, including the AlAs/GaAs system, and MOCVD growth of GaN on ZnO is no different, owing to the high growth temperatures. [111] An initial study of Zn diffusion was done in order to determine its effects on the optical and structural properties of the GaN epilayers.

##### 4.1.2.1 *Zinc and Oxygen Diffusion into GaN*

A baseline sample was grown with a low temperature GaN layer of  $\sim 20$  nm, and then increased in temperature up to  $\sim 750$  °C for the main GaN layer. This low growth temperature was used for the main GaN layer because of the instability of ZnO in a hydrogen atmosphere at typical GaN growth temperatures, as mentioned previously. The low growth temperature decreases  $\text{NH}_3$  cracking efficiency, thus decreasing the amount of hydrogen delivered to the growth surface, allowing the nucleation and growth of a GaN thin film on ZnO without degrading the substrate surface prior to growth. It can also provide a

clear picture of the effects of zinc and oxygen diffusion into GaN, even at relatively low growth temperatures.

Figure 4.3(a) shows XRD data from a  $2\Theta-\omega$  scan of the (002) reflection of a GaN layer on ZnO, where the linewidth of the GaN peak is 211.8 arcsec. Omega scans of the (002) reflections were very broad, however, indicating poor crystal quality and a high defect density. Raman spectroscopy was used to gain deeper insight into the crystal structure of these films, Figure 4.3(b). The absence of a clear  $E_2(\text{high})$  mode suggests poor crystal quality in the GaN layer. The only GaN mode that is visible is the mode near  $732\text{ cm}^{-1}$ . This is considered to be the  $A_1(\text{LO})$  mode, and it is shifted from its unstrained position to lower wavenumbers. Though the reason for this shift is unclear, it may be an indication of tilt or twist in the GaN layer, as the  $A_1(\text{LO})$  mode is sensitive to angular dispersion as well as to biaxial strain. [103]

RT-PL measurements show a strong ZnO bandedge, as expected, and a relatively weak GaN bandedge, Figure 4.4. The GaN bandedge luminescence is reduced most likely due to diffusion of Zn and O impurities into the GaN layer. Reabsorption by the ZnO substrate may also contribute to the low luminescence signal observed from the GaN layer.

The origin of the defect peak near 700 nm also remains unclear, though there are several possibilities. First, it may be due to the formation of a second phase at the GaN/ZnO interface.  $\text{Zn}_3\text{N}_2$  has a much lower bandgap than GaN, and the incorporation of high zinc levels into GaN may result in the formation of a  $\text{Zn}_x\text{N}_y$  phase near the interface that emits at a much lower energy than the GaN layer. However, no macroscopic second phase was observable via XRD, which showed only hexagonal GaN. It would be expected that the formation of a  $\text{Zn}_x\text{N}_y$  second phase near the interface might lead to cubic GaN, or at least to

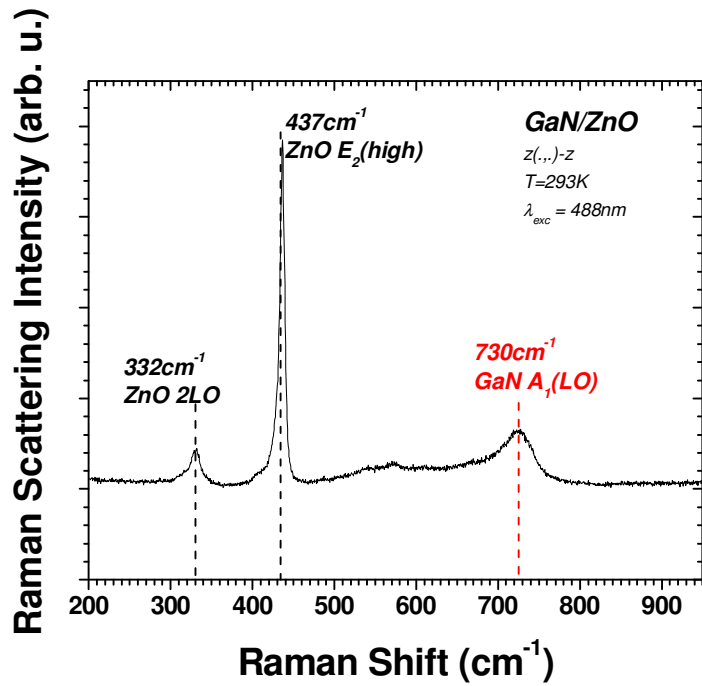
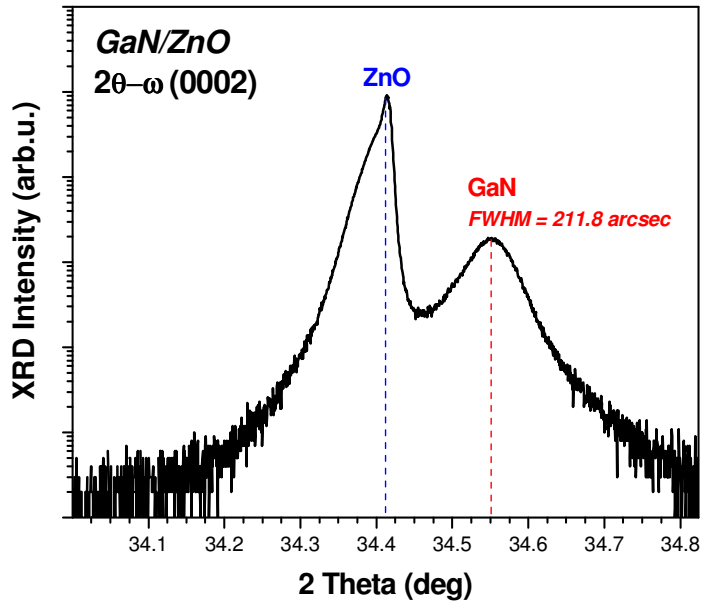


**Figure 4.3:** (a) XRD pattern of GaN grown on ZnO using  $NH_3$  as a nitrogen precursor. (b) Unpolarized Raman spectrum of the same sample.

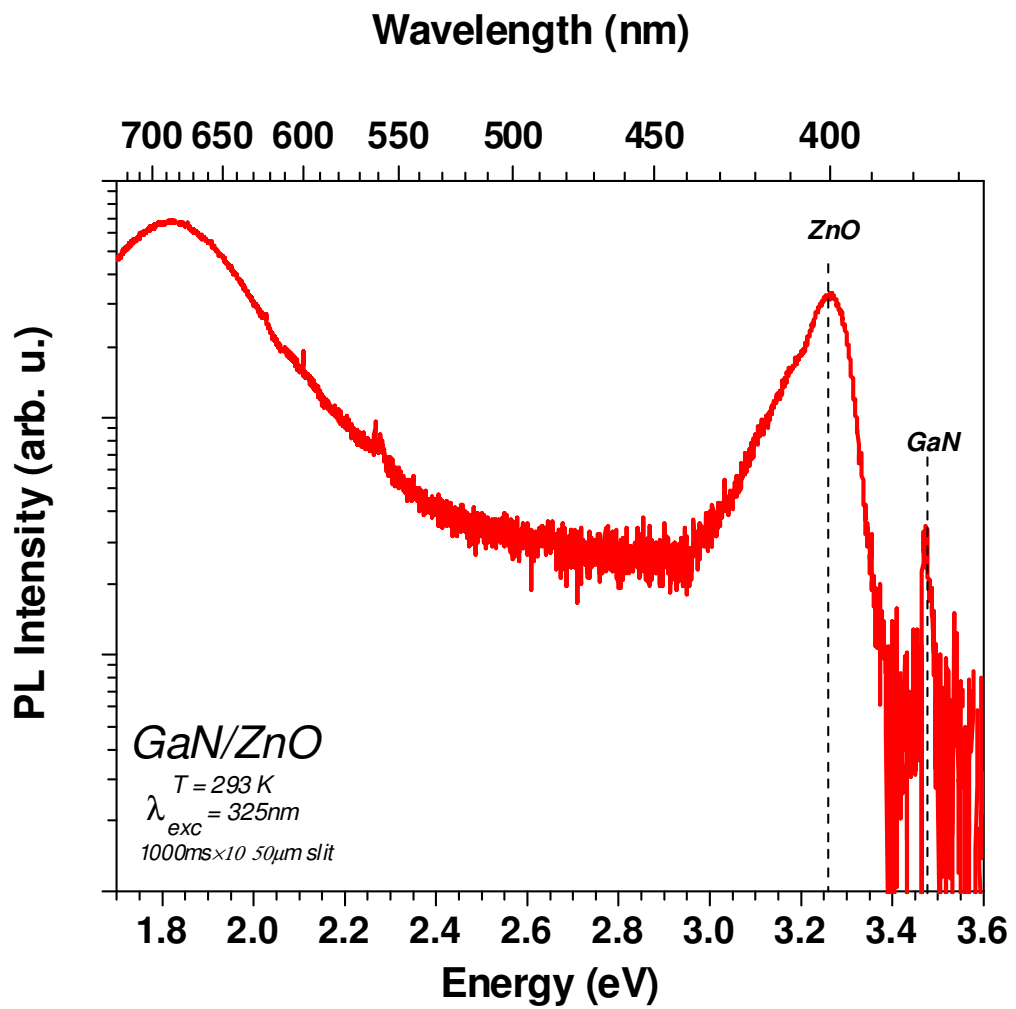


**Figure 4.4:** RT-PL spectrum of a GaN layer grown on ZnO using a LT-GaN nucleation layer.

mixed-phase GaN, as  $Zn_3N_2$  is a cubic material. However, the hexagonal GaN layer suggests that no cubic phase forms at the GaN/ZnO interface.

Second, the feature near 700 nm may be related to the band offset between GaN and ZnO. It has been shown that the average band offset at the GaN/ZnO interface is  $\sim 2$  eV, depending on polarity and surface treatment.[85,86] A transition from the ZnO conduction band minimum to the GaN valence band maximum near the interface would lead to emission in this region. The Type II band offset, with both the conduction and valence bands of GaN being higher than those of ZnO, may also cause electrons that are excited in the GaN layer to move toward the ZnO substrate. This would lead to a high concentration of electrons at the ZnO conduction band minimum and a high concentration of holes near the GaN valence band maximum, making this transition likely. This is not the case, however, as removal of the ZnO substrate results only in an increase in intensity of this peak. Clear observation of this peak after the substrate is removed suggests that the feature near 700 nm is due to the GaN layer itself.

The third – and most likely – origin of this feature is the presence of high levels of zinc in the GaN layer. Several different peaks have been observed in GaN doped with high levels of zinc, with the highest zinc doping levels leading to defect-related peaks near 1.9 eV and 2.3 eV. The different peak positions have been attributed to different charge states of zinc. [106] Thus, the observation of this peak is taken as evidence of zinc diffusion into the GaN layer.

SIMS was performed in order to study impurity concentrations in LT-GaN on ZnO and to investigate the diffusion of both zinc and oxygen into GaN, Figure 4.5. The GaN/ZnO interface is marked in the figure, and these results clearly show diffusion of both zinc and oxygen into the GaN layer as well as gallium and nitrogen diffusion into the ZnO substrate.

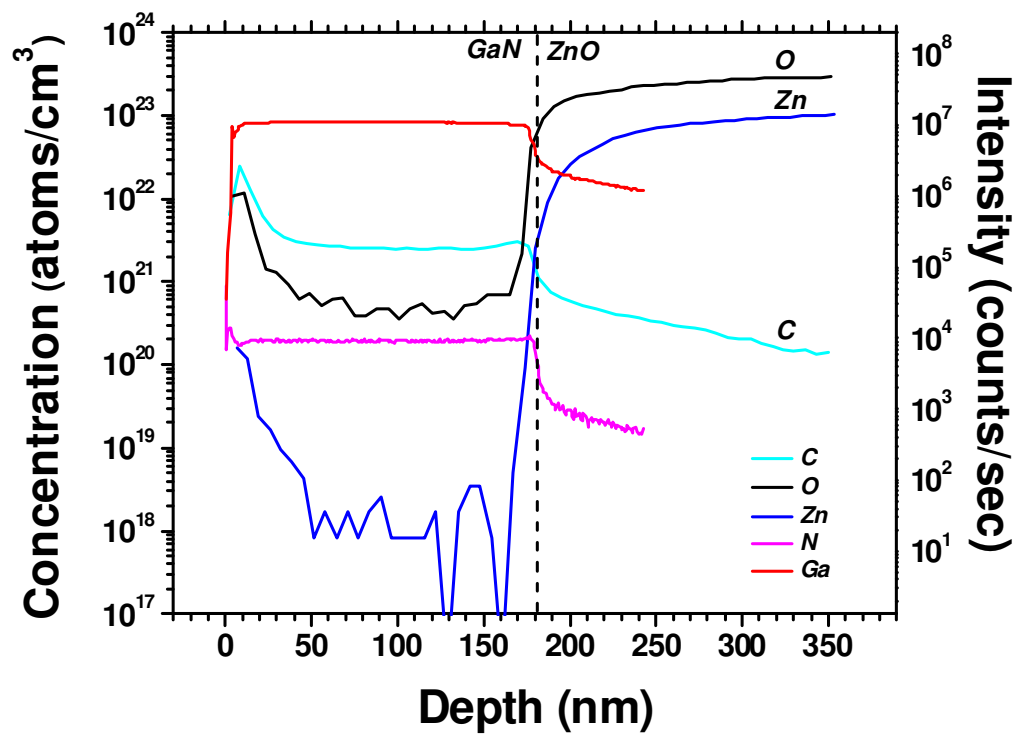


**Figure 4.5:** SIMS depth profile of a GaN layer on ZnO showing zinc, oxygen, and carbon impurity concentrations.

High impurity levels are observed for both zinc ( $\sim 5 \times 10^{19} \text{ cm}^{-3}$ ) and oxygen ( $\sim 5 \times 10^{21} \text{ cm}^{-3}$ ) in the GaN layer. These high impurity levels are a clear indication that the major challenge with GaN growth on ZnO is suppression of diffusion from the substrate. Alternative techniques must be developed in order to suppress out-diffusion from the substrate and grow high quality GaN on ZnO.

## 4.2 $\text{In}_x\text{Ga}_{1-x}\text{N}$ GROWTH ON ZNO

$\text{In}_x\text{Ga}_{1-x}\text{N}$  growth was investigated on ZnO because of both the lattice match with ZnO and the lower growth temperatures relative to typical GaN growth. Structural and optical properties were investigated as well as impurity concentrations in the epilayers.

### 4.2.1 Structural Properties

The first  $\text{In}_x\text{Ga}_{1-x}\text{N}$  thin films were grown on ZnO by developing a process on sapphire for  $\text{In}_{.18}\text{Ga}_{.82}\text{N}$  and transferring that to ZnO. No nucleation layer or buffer layer was used in order to take full advantage of the lattice matched substrate.  $\text{NH}_3$  flow was lowered relative to the growth process on sapphire because of the reactivity of ZnO in hydrogen, as discussed previously. It was found that  $\text{NH}_3$  flows typical of  $\text{In}_x\text{Ga}_{1-x}\text{N}$  on sapphire ( $\sim 12.5$  slm in this growth system) etched the surface of the ZnO so that little or no growth took place. Under these conditions, phase separation was observed on ZnO. Two separate InN phases – the (002) and (102) reflections – were observed via XRD, Figure 4.6. Surface roughness was also an issue when growing lattice-matched  $\text{In}_{.18}\text{Ga}_{.82}\text{N}$  directly on sapphire, as the surface began to deteriorate beyond a thickness of about 100 nm.

A LT-GaN layer was introduced as the first step in the growth process, similar to GaN growth on sapphire, to improve roughness of the growth surface. Normal-incidence reflectivity curves showed that the LT-GaN layer helped improve surface quality during

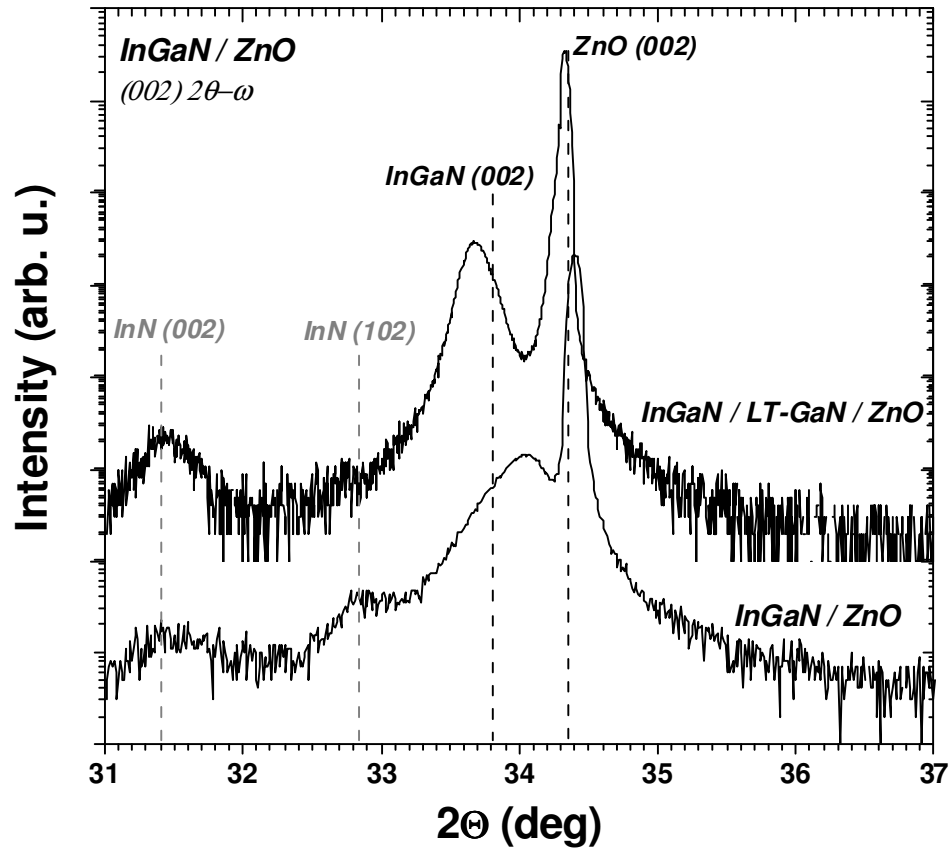


**Figure 4.6:** XRD  $2\theta$ - $\omega$  scans of InGaN epilayers grown with and without a LT-GaN nucleation layer.

growth, as less deterioration in the intensity of reflected light was observed during the course of growth. XRD, however, showed the formation of a second phase – InN (002) – despite the use of the LT-GaN nucleation layer. However, the formation of the InN (102) phase was suppressed, Figure 4.6. The indium content in the layer using LT-GaN was also increased over the layer that was grown directly on ZnO, as evidenced by the shift of the  $\text{In}_x\text{Ga}_{1-x}\text{N}$  (002) peak to lower angles. The reason for this shift is not clear, however.

The formation of InN-related second phases during growth on ZnO may be related to the decrease in  $\text{NH}_3$  flow, which leads to a lower V/III ratio. Typical V/III ratios for  $\text{In}_x\text{Ga}_{1-x}\text{N}$  growth are much higher than those for GaN, owing to the large difference in equilibrium vapor pressure between indium and nitrogen. [91]

Because of the detrimental effects of a lower V/III ratio on  $\text{In}_x\text{Ga}_{1-x}\text{N}$  quality on ZnO, the  $\text{NH}_3$  flow was increased to conditions typical of GaN growth on sapphire. An interlayer with a low V/III ratio was inserted above the LT-GaN nucleation layer in order to ensure proper substrate coverage. This approach led to a single-phase  $\text{In}_x\text{Ga}_{1-x}\text{N}$  layer, as observed via XRD, Figure 4.7.

A comparison of the growth conditions that led to the growth of single-phase  $\text{In}_x\text{Ga}_{1-x}\text{N}$  on both sapphire and ZnO helps to determine some of the differences introduced by the ZnO substrate. The  $\text{NH}_3$  flow was the same for both substrates, being held constant at 12.5 slm. While the total Group III flow rate was similar for both conditions – between 15 and 16  $\mu\text{mol}/\text{min}$  – the  $\frac{\text{In}}{\text{In} + \text{Ga}}$  ratio changed significantly. The ratio on sapphire was 0.5076, with TMIIn flow rate of 8.319  $\mu\text{mol}/\text{min}$  and a TEGa flow rate of 8.07  $\mu\text{mol}/\text{min}$ . However, the ratio on ZnO was 0.3958, with a TMIIn flow rate of 6.024  $\mu\text{mol}/\text{min}$  and a TMGa flow rate of 9.196  $\mu\text{mol}/\text{min}$ . The decrease in indium flow and corresponding increase in gallium

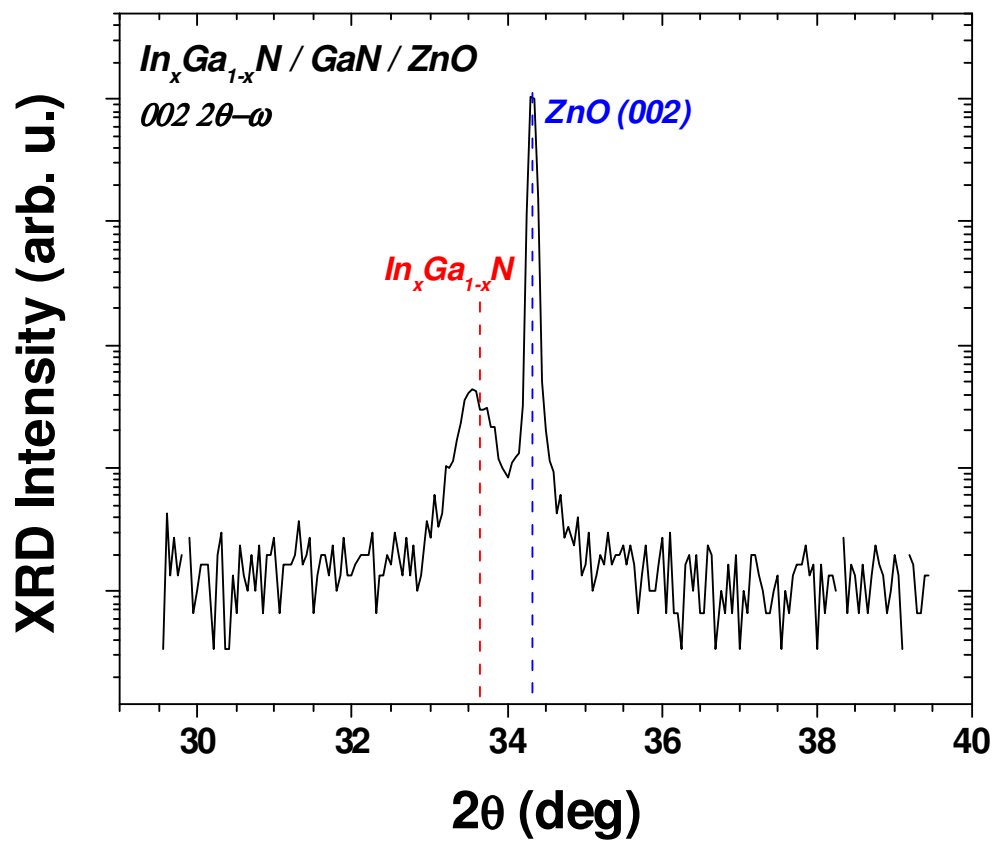


**Figure 4.7:** XRD  $2\theta-\omega$  scan of a single-phase InGaN thin film grown on ZnO(0002).

flow to obtain single-phase  $\text{In}_x\text{Ga}_{1-x}\text{N}$  on ZnO substrates suggests that indium incorporates more easily when growing on ZnO. This conclusion is also supported by the observation that typical GaN growth conditions on sapphire lead to phase-separated material on ZnO. The reason for this increased incorporation is unclear, though, and may be related to the difference in strain state of the epilayer, which has been shown to affect indium incorporation.[112]

Structural properties of both the GaN and  $\text{In}_x\text{Ga}_{1-x}\text{N}$  epilayers on ZnO were investigated more closely using Raman spectroscopy. Raman scattering spectra from wurtzite crystals typically show two prominent modes: the  $E_2$  and the  $A_1(\text{LO})$ . These modes appear in GaN near  $567\text{ cm}^{-1}$  ( $E_2(\text{high})$ ) and near  $735\text{ cm}^{-1}$  ( $A_1(\text{LO})$ ). Raman spectra taken from both GaN and  $\text{In}_x\text{Ga}_{1-x}\text{N}$  layers on ZnO are shown in Figure 4.8. The features near  $332\text{ cm}^{-1}$  and  $437\text{ cm}^{-1}$  are related to a second-order phonon in ZnO and the ZnO  $E_2(\text{high})$  mode, respectively. Noticeably absent from the spectrum of the GaN epilayer is the  $E_2(\text{high})$ , with only a slight shoulder appearing between  $565\text{ cm}^{-1}$  and  $570\text{ cm}^{-1}$ .

The most prominent GaN-related feature in the Raman spectra is the peak near  $705\text{ cm}^{-1}$  in the  $\text{In}_x\text{Ga}_{1-x}\text{N}$  layer and near  $730\text{ cm}^{-1}$  in the GaN layer, which is attributed to the GaN  $A_1(\text{LO})$  mode. The absence of the  $E_2(\text{high})$ , coupled with the slight shift from the literature value of  $735\text{ cm}^{-1}$ , however, suggests that further investigation is necessary to ensure this assignment.

Polarized Raman spectra were taken in the backscattering configuration in order to further investigate the modes observed in the unpolarized spectra. The polarized Raman spectra for the  $\text{In}_x\text{Ga}_{1-x}\text{N}$  layer on ZnO, taken under crossed polarization and parallel polarization configurations, are shown in Figure 4.9. The intensity of the mode decreases significantly under crossed polarization relative to parallel polarization. This behavior is

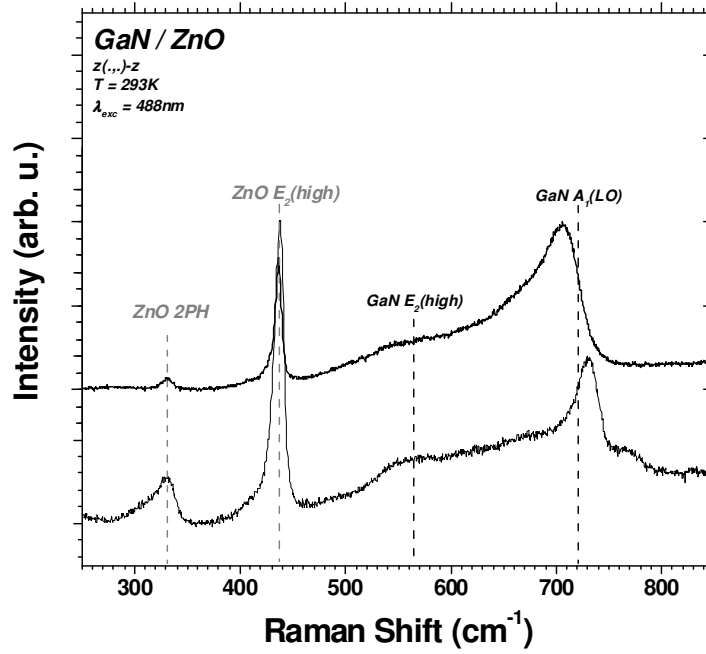


**Figure 4.8:** Raman scattering spectra of GaN and InGaN layers grown on ZnO substrates.

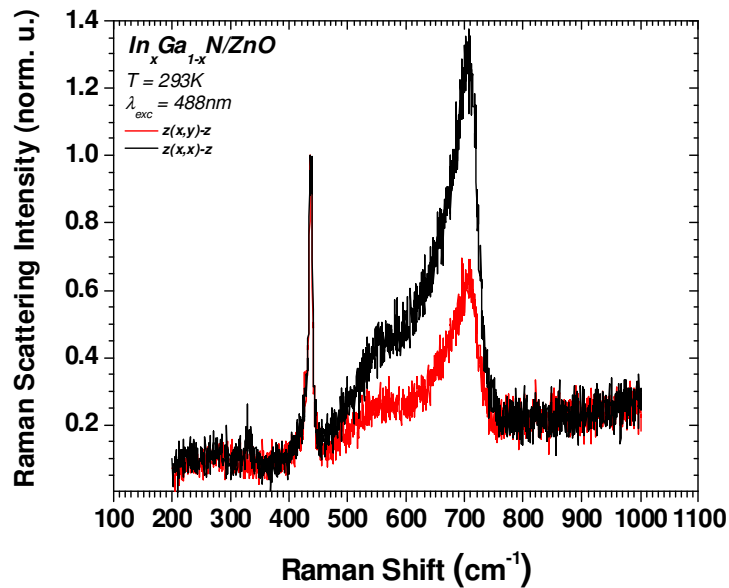


**Figure 4.9:** Polarized Raman spectra from a thick  $\text{In}_x\text{Ga}_{1-x}\text{N}$  layer on ZnO. Polarization dependence follows that of the GaN  $A_1(\text{LO})$ .

expected of the GaN  $A_1(\text{LO})$  mode, and confirms the assignment made previously. [103] The fact that the  $A_1(\text{LO})$  mode is still visible under the crossed polarization configuration suggests a relaxation of the Raman selection rules, most likely due to poor crystal quality in the material.

The  $A_1(\text{LO})$  mode is also observed to shift from its theoretical position of  $735 \text{ cm}^{-1}$  to lower wavenumbers for the GaN layer on ZnO. Two phenomena can cause a shift in the position of the  $A_1(\text{LO})$  mode: strain and angular dispersion. As a shift of  $\sim 6 \text{ cm}^{-1}$  is relatively large to attribute to tensile strain in the material, the most likely cause for this shift is angular dispersion, which is also suggestive of a lack of crystal quality in these initial GaN and  $\text{In}_x\text{Ga}_{1-x}\text{N}$  thin films grown on ZnO.

#### 4.2.2 Optical Properties

Optical properties of the  $\text{In}_x\text{Ga}_{1-x}\text{N}$  layers on ZnO were studied using RT-PL spectroscopy. RT-PL spectra taken from  $\text{In}_x\text{Ga}_{1-x}\text{N}$  layers on ZnO both with and without a LT-GaN nucleation layer are shown in Figure 4.10. The difference in bandedge emission suggests a higher indium content in the layer grown using a LT-GaN nucleation layer. The reason for this higher content remains unclear; however, it may be related to a difference in strain state of the two layers. As the GaN lattice constant is slightly smaller than that of ZnO, GaN will be under tensile strain when grown on ZnO. This tensile strain may lead to an incorporation of more indium in the layer. A similar effect was observed for GaN thin films on silicon in this work, and will be discussed in Chapter 8.

#### 4.2.3 Impurity Diffusion

Impurity diffusion into MOCVD-grown  $\text{In}_x\text{Ga}_{1-x}\text{N}$  epilayers on ZnO was studied using SIMS. Zinc and oxygen concentrations as a function of depth are shown in Figure 4.11.

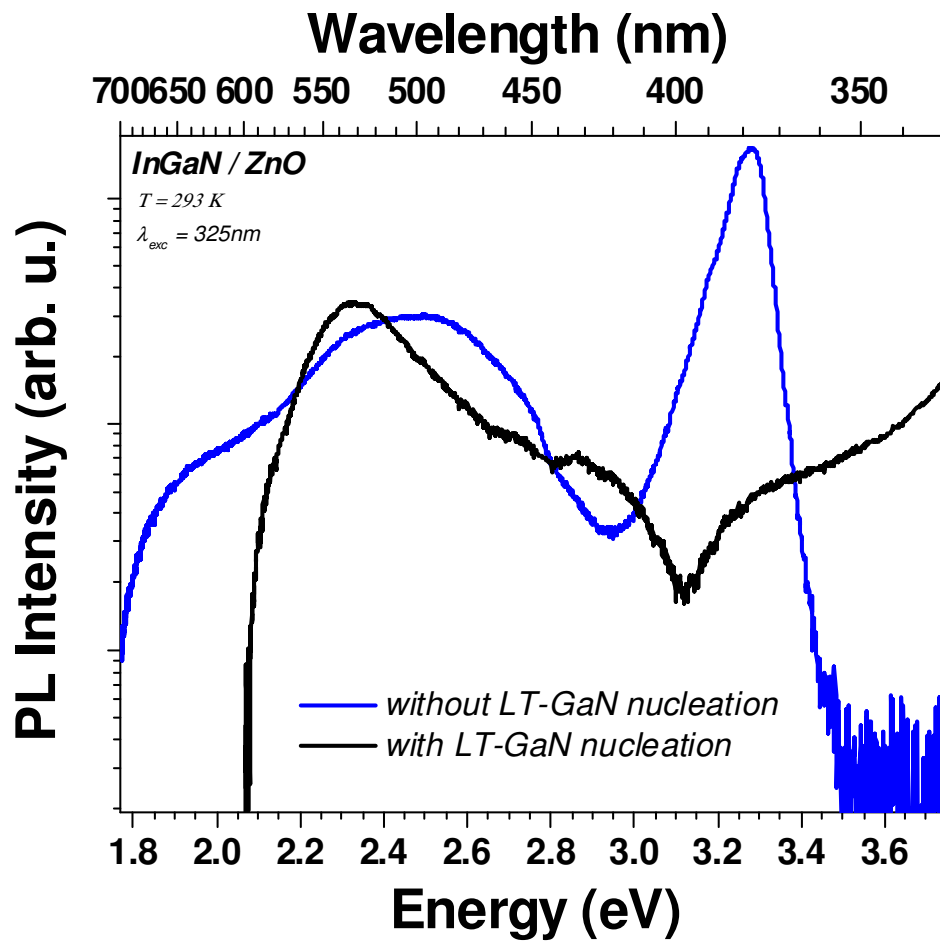


**Figure 4.10:** RT-PL spectra of GaN thin films grown on ZnO substrates both with and without LT-GaN nucleation layers.

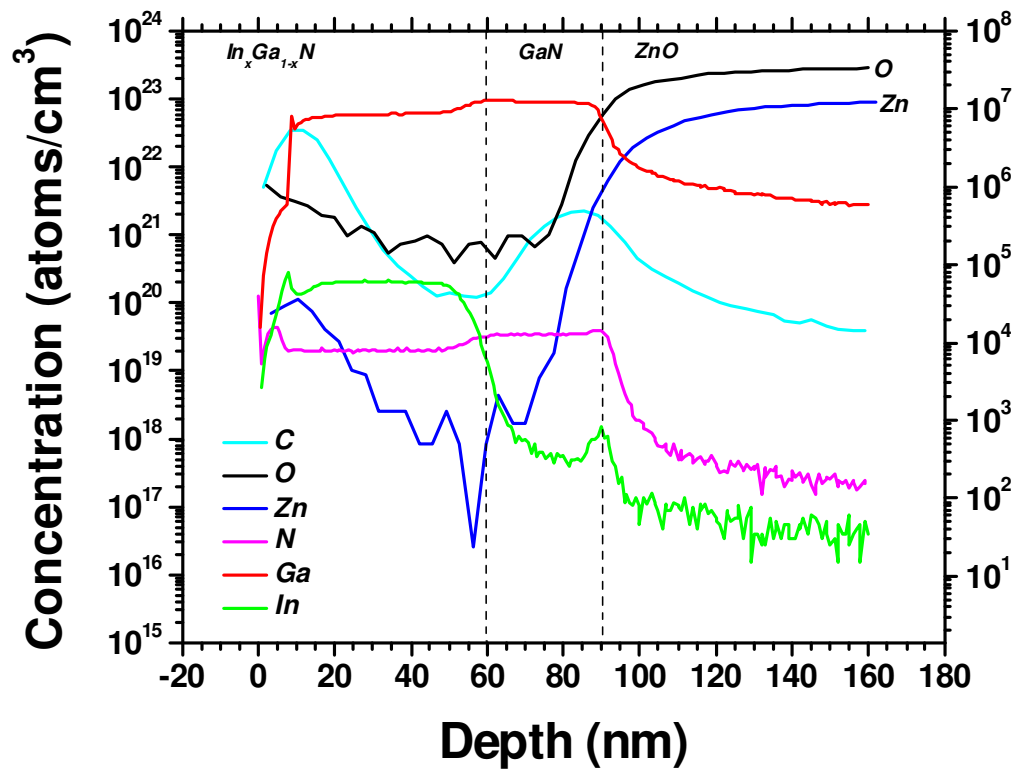


Figure 4.11: SIMS depth profile of a thin InGaN layer on ZnO.

The figure also shows carbon concentration, which increases significantly in the LT-GaN nucleation layer. The ZnO substrates were cleaned in acetone for three minutes and then in methanol for three minutes, and then rinsed with de-ionized water. The cleaning in methanol is intended to remove any carbon residue from the acetone.

The reason for the significant increase in impurity concentration near the surface is unclear; however, the concentration is taken from a depth of ~40 nm in this work. The possibility of an increase in concentration near the surface will be investigated further in Chapter 6. While the zinc and oxygen concentrations are similar for the GaN and  $\text{In}_x\text{Ga}_{1-x}\text{N}$  epilayers, the concentrations are slightly higher in the  $\text{In}_x\text{Ga}_{1-x}\text{N}$  layer compared to the GaN layer. A comparison of the In-N and Ga-N bond strengths shows that the In-N bond is weaker, perhaps allowing diffusion to proceed more rapidly than in pure GaN.

#### **4.3 GROWTH ON ZNO/SAPPHIRE TEMPLATES**

ZnO thin films on sapphire were investigated as an alternative to bulk, single crystal ZnO substrates. An MOCVD process for the growth of ZnO thin films on sapphire was developed to yield ZnO thin films that are both consistent and uniform. [82] One  $\mu\text{m}$ -thick ZnO thin films were deposited on sapphire as substrates for subsequent nitride MOCVD growth.  $\text{In}_x\text{Ga}_{1-x}\text{N}$  thin films were grown on these ZnO/sapphire substrates alongside bulk ZnO. However, surface roughness was much higher (>20 nm) on the ZnO/sapphire templates, and this is most likely due to the fact that the roughness of the ZnO thin film itself (~10 nm) was much higher than that of the single crystal substrates. No GaN (0002) peak was observable via XRD on the ZnO/sapphire templates, though a blueshift was observed in the RT-PL spectra relative to the same layers grown on bulk ZnO. The reason

for this blueshift remains unclear, however, and the poor structural quality of the layers on ZnO/sapphire templates prevented the further development of this process.

#### 4.4 SUMMARY

GaN and  $\text{In}_x\text{Ga}_{1-x}\text{N}$  epilayers have been grown by MOCVD on ZnO (0001) substrates, and the major issues with GaN growth on ZnO have been identified. The first major issue is the reactivity of the substrate with hydrogen, and the second is diffusion of zinc and oxygen from the substrate into the GaN layer. Alternative nitrogen precursors were investigated in this work, including DMHy; however, carbon incorporation from these precursors was much too high for the material to prove useful in devices. Therefore,  $\text{NH}_3$  was identified as the most favorable nitrogen precursor, and methods were developed to prevent hydrogen etching of the substrate due to decomposition of  $\text{NH}_3$ .

SIMS was also used to investigate both zinc and oxygen concentrations in GaN and  $\text{In}_x\text{Ga}_{1-x}\text{N}$  layers on ZnO. Regardless of the mechanisms of diffusion, it is clear that the impurity concentrations in these materials are too high to be useful in device applications, and methods must be investigated to suppress this diffusion. In order to suppress the diffusion, an understanding of the mechanisms involved is also necessary. These mechanisms, and methods to suppress them, will be investigated in the next chapter.

## CHAPTER 5: DIFFUSION BLOCKING

Diffusion of zinc and oxygen into the GaN layer is the major issue with GaN growth on ZnO. This chapter outlines general principles of diffusion in semiconductors and discusses results of different approaches that were investigated to suppress diffusion from the ZnO substrate into the GaN layer.

### 5.1 FERMIL LEVEL PINNING

Diffusion of impurities in semiconductors is mediated by point defects, and a clear understanding of point defect formation in nitrides is necessary to understand diffusion mechanisms in these materials. Zinc diffusion, in particular, has been investigated in other III-V systems, such as the AlAs – GaAs system, with an eye toward suppressing unwanted diffusion. Fermi level pinning turns out to play an important role in zinc diffusion in GaAs, and this section discusses that role as well as the role that Fermi level pinning plays in GaN-based materials and devices.

#### 5.1.1 Zinc Diffusion in AlAs – GaAs

While nitrides are different from arsenides in many fundamental respects, previous work done on zinc diffusion in GaAs provides some insight into the mechanisms at work in III-V semiconductors. Zinc is a shallow acceptor in GaAs and thus an important dopant atom, and this importance fueled the investigation into zinc diffusion in GaAs over a decade ago. GaAs homoepitaxy is the most common, with high quality GaAs substrates readily available. Zinc doping in MOCVD-grown GaAs leads to zinc diffusion into the substrate. N-type GaAs substrates have also been used for epitaxial growth of p-type ZnSe, which also leads to zinc diffusion into the GaAs substrate.

It is generally accepted that zinc diffuses in GaAs by a kick-out mechanism in which zinc diffuses as an interstitial atom and then replaces a gallium atom.[111,113] This leads to the conclusion that zinc diffusion in GaAs is mediated by Ga. [114-116] Zinc diffusion profiles in GaAs show a typical kink-and-tail profile that clearly shows two different regions.[113,117] Tan suggests that the region from the kink to the diffusion front has in fact reached the solid solubility limit of gallium, with gallium precipitates forming because of the kick-out mechanism by which zinc diffuses. The region near the surface consists mainly of  $Zn_s$ , with the replaced gallium atoms having diffused to the surface of the crystal.[114] Thus, regardless of ambient atmosphere, zinc diffusion into GaAs must first produce gallium-rich material. In arsenic-rich ambient, the near-surface region can become arsenic-rich, but the region near the diffusion front will remain gallium-rich because of the kick-out diffusion mechanism.

Zinc has also been shown to cause – and even enhance – disordering in AlAs – GaAs superlattices (SLs).[111] Disordering of the SL takes place mainly in the zinc diffusion front region, where interstitial cations replaced by zinc atoms diffuse toward the surface, resulting in a disordered  $Al_xGa_{1-x}As$  crystal. This phenomenon is explained by the same mechanism just discussed for zinc diffusion in GaAs. In both cases, an understanding of point defect formation and diffusion are crucial to understanding the mechanisms at work in zinc diffusion, and the same is the case for GaN-based materials.

Reichert et al. observed that the concentration of zinc in typical MOCVD-grown GaAs:Zn is supersaturated relative to the vapor, leading to point defect concentrations that are above the equilibrium values. They explain the supersaturation of zinc in the solid relative to the vapor by suggesting that the Fermi level is pinned at the surface during growth,

and that as growth proceeds, the surface concentration, which is supersaturated, becomes the bulk concentration.

### 5.1.2 Point Defect Formation in GaN

Native defects in MOCVD-grown GaN are typically donor-type defects, specifically nitrogen vacancies ( $V_N$ ) and gallium interstitials ( $Ga_i$ ). The most likely type of defect to form in GaN is the nitrogen vacancy, by energy formation considerations, Figure 5.1. [118] Figure 5.1 shows calculated formation energies as a function of Fermi level for the six main intrinsic defects in GaN: vacancies, interstitials, and antisites for both cations and anions. It can be seen from the figure that  $V_N$  is the most likely type of defect to form under normal (undoped) growth conditions. However, the  $V_{Ga}$  formation energy drops with increasing  $E_F$ , corresponding to heavily n-type material.

Calculations of the migration barrier for each type of defect show that diffusion on the cation sublattice is most likely to be mediated by  $Ga_i$  in p-type GaN and by  $V_{Ga}$  in n-type GaN. Diffusion on the nitrogen sublattice is most likely to be mediated by nitrogen vacancies. Also, no anisotropy is to be expected for diffusion of native defects in GaN, as the lowest energy migration path moves both parallel and perpendicular to the c-axis in wurtzite GaN. [118]

Fermi level pinning has been observed in GaN films at different energy levels. Deep defect levels pinning the Fermi level at  $E_c - 0.6$  eV are a common observation, though the origin of these defects is not clear at this time.[118,119] Limpijumnong and Van de Walle attribute these defects to dangling bonds from gallium adatoms on the GaN surface. [118] They also calculate surface states at  $E_v + 1.7$  eV that may pin the Fermi energy below its intrinsic level. This pinning of the Fermi energy is significant, as it affects both the

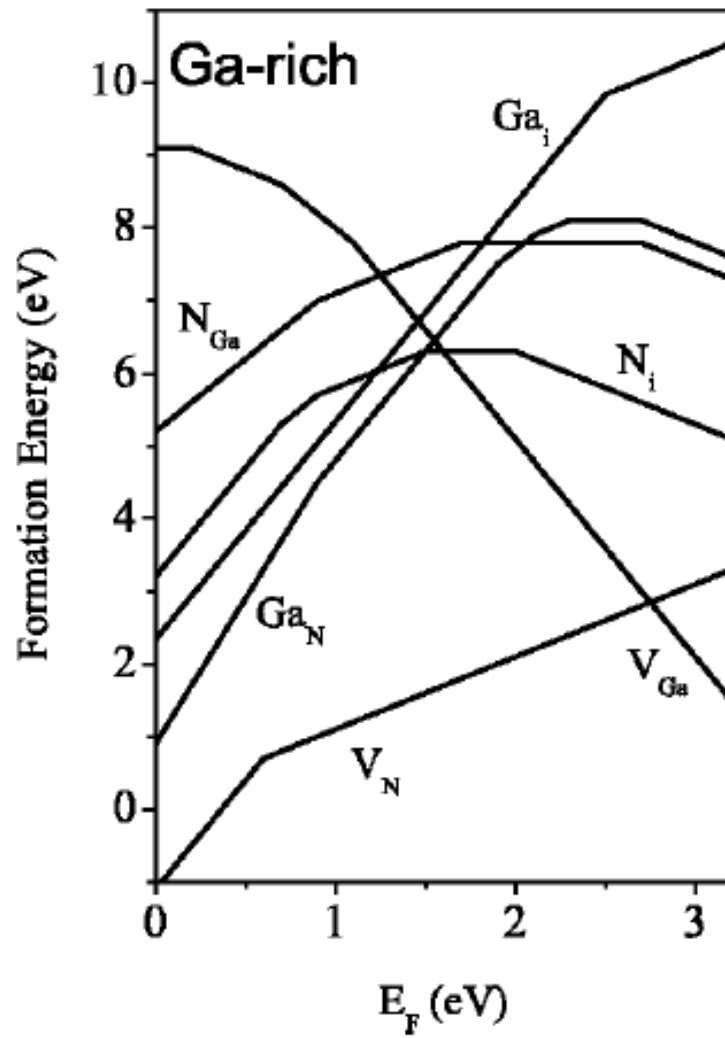


**Figure 5.1:** Calculated formation energies for various intrinsic defects in GaN. (from [118])

formation of point defects in the material and the diffusion of impurities. Band bending has also been observed near the GaN surface due to this Fermi level pinning.

Pinning of the Fermi level at the  $\text{Al}_x\text{Ga}_{1-x}\text{N}/\text{GaN}$  interface is also a well-known phenomenon, and is used to create a two-dimensional electron gas (2DEG) at the interface in high electron mobility transistors (HEMTs). Heikman et al. report the pinning of the Fermi level at 1.7 eV below the conduction band for an  $\text{Al}_{0.32}\text{Ga}_{0.68}\text{N}$  surface and at 0.9 – 1.0 eV below the conduction band for a GaN surface. This Fermi level pinning combines with band bending at the  $\text{Al}_x\text{Ga}_{1-x}\text{N}/\text{GaN}$  interface to form the 2DEG that is an integral part of GaN-based HEMT devices.[120] At a single  $\text{Al}_x\text{Ga}_{1-x}\text{N}/\text{GaN}$  heterointerface, the density of the 2DEG is dependent on the  $\text{Al}_x\text{Ga}_{1-x}\text{N}$  thickness, Figure 5.2. Pinning of the Fermi level by surface and/or interface states in GaN is a common observation, and this work attempts to use this phenomenon to help suppress diffusion of zinc and oxygen from ZnO substrates into GaN thin films.

### 5.1.3 Impurity Diffusion in GaN

Impurity diffusion in GaN is most often mediated by point defects. The specific type of point defect that mediates diffusion of a given impurity is usually determined by the way in which that impurity incorporates into the lattice. Magnesium, for example, incorporates on the gallium lattice site, so gallium-related point defects – either vacancies or interstitials – govern magnesium diffusion.

Polyakov et al. showed that hydrogen diffusion in GaN is dependent on the Fermi level. Heavily p-doped material showed significantly more hydrogen diffusion in GaN compared to weakly p-type material or n-type material, in which little hydrogen diffusion was

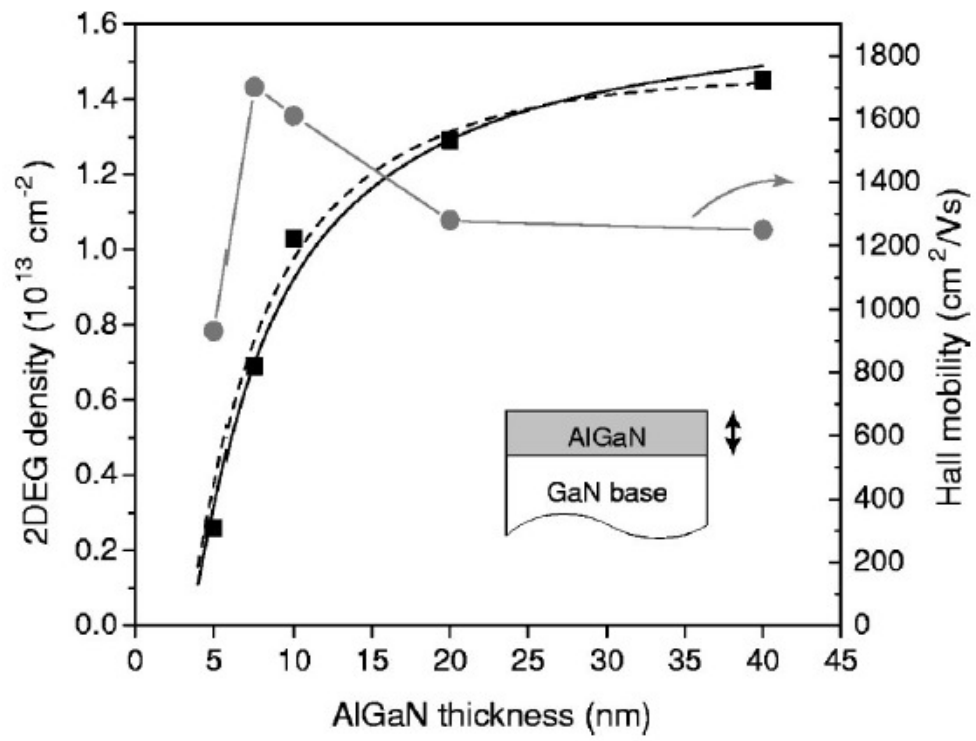


**Figure 5.2:** 2DEG density as a function of AlGaN thickness at an AlGaN/GaN interface. (from [120])

detected.[121] Oxygen diffusivity in p-type GaN layers has also been studied, and it has been found that oxygen diffusion depth is strongly dependent on dislocation density as well.[122]

Formation of intrinsic defects in GaN is also doping-dependent, as nitrogen vacancies often form to self-compensate the crystal when doping with deep-level acceptors, such as Mn. [104] Formation of nitrogen vacancies has been shown to depend on doping, and can be suppressed by doping with silicon, which is a shallow donor in GaN, and the most common n-type dopant. The factors involved in formation of native defects and the mediation of impurity diffusion by these defects must be taken into account when studying diffusion of impurities such as zinc and oxygen in GaN. The next section describes investigations into suppression of both zinc and oxygen, taking into account the formation of native defects and the effects that these defects (and doping) have on Fermi level.

## **5.2 ALN BUFFER LAYERS**

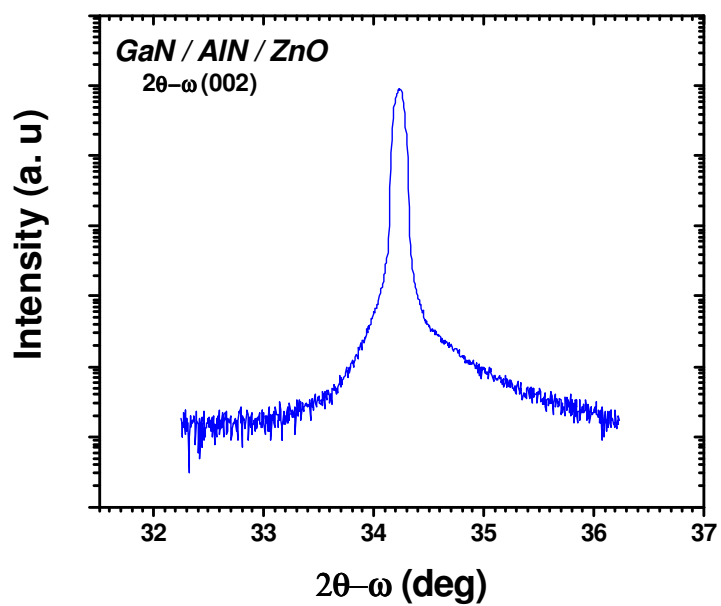
LT-GaN buffer layers were used in the initial work to improve both GaN and  $\text{In}_x\text{Ga}_{1-x}\text{N}$  crystal quality, though out-diffusion from the substrate remained a problem. The bond strength for aluminum, gallium, and indium with nitrogen are shown in Table 5.1. The increased Al-N bond strength relative to other Group III elements may help to prevent diffusion. For this reason, a first attempt to block zinc and oxygen diffusion was made using AlN buffer layers. General growth parameters were investigated, and the effect of these parameters on subsequent material quality was also studied.

### 5.2.1 Structural Properties

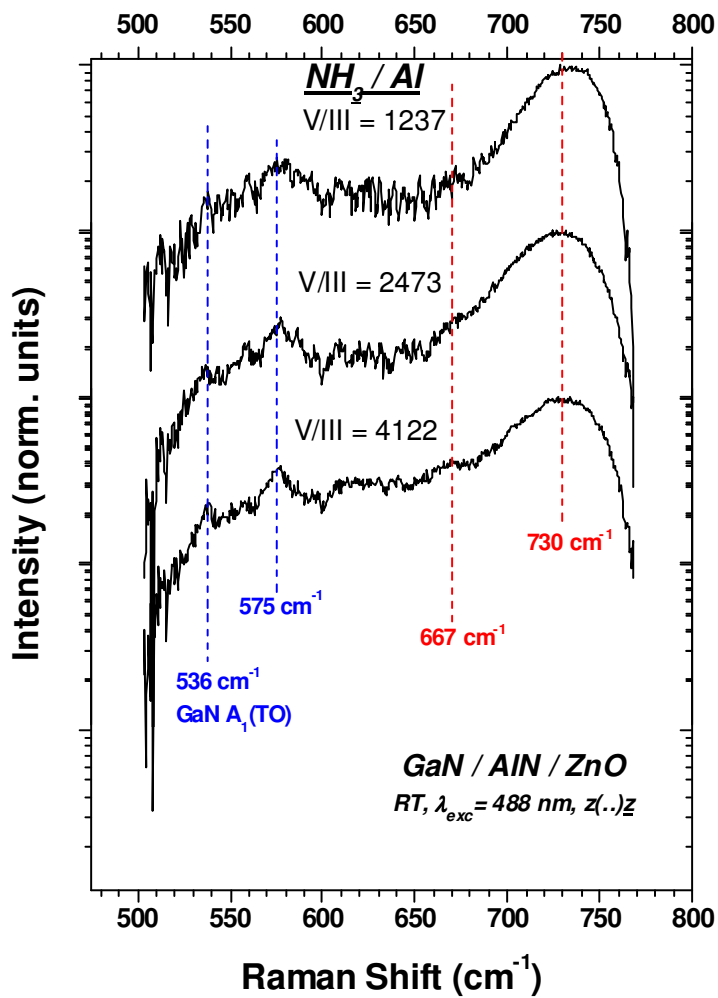
Typical AlN growth temperatures are relatively high (between 1050 °C and 1150 °C). However, the reactivity of the ZnO substrate with hydrogen hampers growth at these high temperatures, even with relatively low  $\text{NH}_3$  flow rates. For this reason, LT-AlN nucleation

Table 5.1: Bond strength for AlN, GaN, and InN

<i>Cation</i>	<i>Bond Strength</i>
Aluminum	11.52 eV/atom
Gallium	8.92 eV/atom
Indium	7.72 eV/atom



**Figure 5.3:** (a) XRD  $2\theta$ - $\omega$  scan showing a shoulder on the high angle side of the ZnO (002), which is related to the GaN (002) reflection.



**Figure 5.4:** Raman spectra of GaN thin films on ZnO grown using different V/III ratios.

layers were grown at temperatures ranging from 700 °C to 800 °C. In this work, AlN buffer layers were grown under different conditions in order to study the effects of the buffer layer on strain and crystal quality in the subsequent GaN epilayer. The V/III ratio was investigated first in order to determine optimal conditions for nucleation of AlN on ZnO. The V/III ratio was varied from 1200 to 4200. XRD data shows a shoulder on the high angle side of the ZnO peak, which is attributed to the GaN (0002) reflection, Figure 5.3.

Raman spectroscopy was used to study the structural properties of the GaN films grown using AlN buffer layers on ZnO. Figure 5.4 shows Raman spectra of GaN films grown under identical conditions on AlN buffer layers. The AlN buffer layers were grown with different V/III ratios. The V/III ratio was varied by holding the NH<sub>3</sub> flow constant at 1 SLM and varying the trimethyl aluminum (TMAI) flow. Note that the GaN A<sub>1</sub>(LO) mode near 730cm<sup>-1</sup> shifts to higher energies (toward the unstrained position at 735 cm<sup>-1</sup>) with increasing TMAI flow, suggesting less strain in the GaN layer with higher V/III ratio in the buffer layer. A second mode near 667cm<sup>-1</sup> also becomes more visible with increasing V/III ratio. The origin of this mode is unclear, as it may be related to point defects in the GaN layer or to the crystallinity of the AlN buffer layer. The E<sub>1</sub>(TO) mode of AlN is located at 669cm<sup>-1</sup>, though it is disallowed in the backscattering geometry. The presence of this mode in the Raman spectra would indicate a relaxation of the selection rules and decreased crystal quality, as would be expected in a low-temperature buffer layer. One noticeable feature in the Raman spectra of these samples is the absence of the GaN E<sub>2</sub>(high), located near 567cm<sup>-1</sup>. One possible explanation for this is that the GaN layers are relatively thin compared to the excitation wavelength used in the Raman study (488 nm). This may suppress absorption in the GaN layer and thus suppress the response of the GaN E<sub>2</sub>(high) mode in these samples.

The absence of GaN (0002) peaks in XRD  $2\theta$ - $\omega$  and  $\omega$ -scans suggests low long-range crystal quality, however.

### 5.2.2 Optical Properties

Optical properties were studied in order to determine the optical quality of the GaN thin films and to study electronic defects in the material. The RT-PL spectrum of a GaN thin film grown on ZnO using an AlN buffer layer is shown in Figure 5.5. Three distinct features are clearly visible in the RT-PL spectrum of the layer on an AlN buffer layer. The peak near 3.42 eV is attributed to the near-bandedge emission of wurtzite GaN. The peak near 3.27 eV is attributed to the near-bandedge emission of the ZnO substrate. The third, and most interesting, feature is at 3.08 eV. While it is possible that this peak is due to zinc or oxygen in the GaN layer, no defect-related peaks have been reported for wurtzite GaN at this position.[106] The same is true of ZnO, as no defect-related peaks have been reported near 3.08 eV. A comparison of this spectrum to that of Figure 5.4, grown using a LT-GaN buffer layer, shows that the bandedge luminescence is significantly enhanced using the AlN buffer layer compared to the LT-GaN buffer layer. The peak near 1.9 eV, which is very strong in the layer grown using a LT-GaN buffer layer, also vanishes when using AlN as a buffer layer.

These observations lead to the conclusion that the peaks near 3.08 eV in Figure 5.5 and near 1.9 eV in Figure 5.4 are related to the ZnO-AlN and ZnO-GaN band offsets, respectively. The transition near 3.08 eV is attributed to a radiative transition from the ZnO conduction band to the AlN valence band, and the transition near 1.9 eV is attributed to a radiative transition from the ZnO conduction band to the GaN valence band, Figures 6.6(a) and 6.6(b), respectively. In the sample grown using a LT-GaN buffer layer, the Type II band offset makes it likely that electrons generated in the thin GaN layer may move



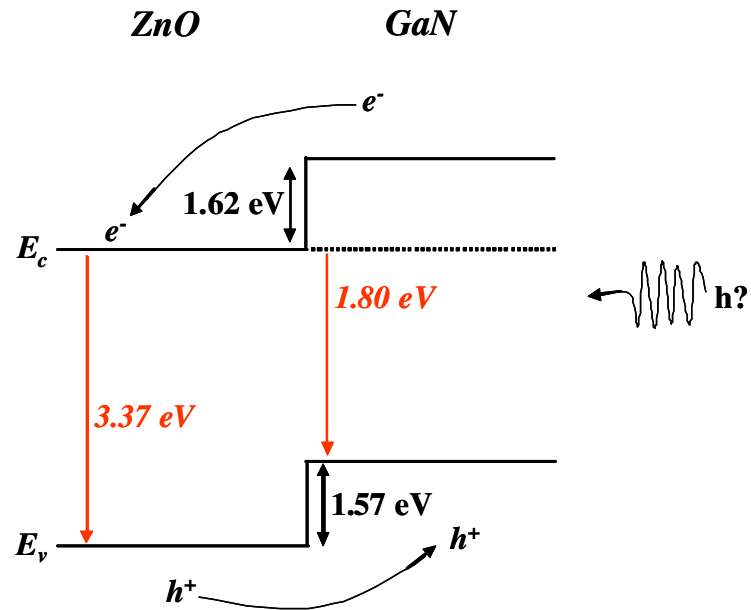
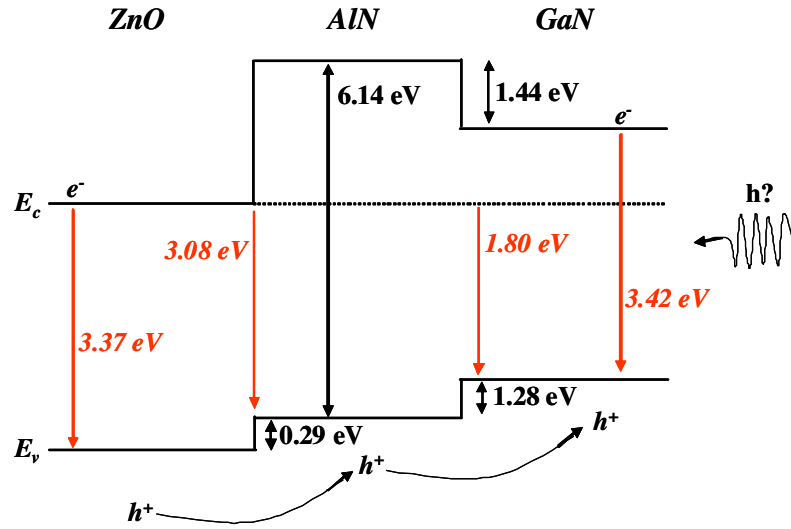


Figure 5.6: ZnO-AlN-GaN (top) and ZnO-GaN (bottom) band offsets calculated from PL data.

across the interface to the ZnO conduction band, which is at a lower energy than the GaN conduction band. This also explains the relatively weak GaN bandedge luminescence observed in this sample. The addition of the AlN buffer layer makes the movement of electrons across the interface less likely, thus maintaining a higher concentration of excited electrons in the GaN layer and significantly increasing the intensity of the GaN near-bandedge luminescence. This explanation fits with other calculations and experimental verification of the ZnO-GaN band offset [85,123]. The ZnO-AlN band offset is also within error of the value calculated by Veal et al. using XPS measurements [123]. While the AlN-GaN conduction band offset necessitated by these measurements is slightly lower than what is reported, it is possible that zinc and oxygen diffusion lead to non-abrupt interfaces, causing slight difference between actual band offset and what is measured via these radiative transitions.

While a comparison of the optical properties of GaN thin films on ZnO using both LT-GaN and AlN buffer layers is useful in studying band offsets and defect formation in these materials, structural properties were not sufficient to warrant further investigation. The lack of an improvement in structural quality with AlN buffer layers over LT-GaN buffer layers led to the investigation of other techniques to suppress diffusion and increase GaN material quality on ZnO.

### **5.3 $\text{Al}_x\text{Ga}_{1-x}\text{N}/\text{GaN}$ SUPERLATTICES**

$\text{Al}_x\text{Ga}_{1-x}\text{N}/\text{GaN}$  superlattices were also studied as a method to suppress zinc and oxygen diffusion into GaN and to increase crystal quality. Similar structures have been used successfully in GaN growth on silicon to reduce strain and increase material quality. The

possibility of controlling zinc and oxygen diffusion by pinning the Fermi level at the  $\text{Al}_x\text{Ga}_{1-x}\text{N}/\text{GaN}$  interface was also investigated in this work.

### 5.3.1 Structural Properties

The first set of  $\text{Al}_x\text{Ga}_{1-x}\text{N}/\text{GaN}$  samples were grown on sapphire in order to optimize growth conditions and provide a control against which to compare the GaN thin films on ZnO. In this set of growths, three samples were grown on 2  $\mu\text{m}$  GaN templates on sapphire substrates. The first sample was grown using  $\text{H}_2$ -rich mixed carrier gas ( $\text{H}_2:\text{N}_2 = 5:1$ ), while the second was grown using only  $\text{N}_2$  as carrier gas to match the requirement of growth on ZnO. The growth conditions of the third sample were identical to those of the second except that TMIIn (5.7  $\mu\text{mol}/\text{min}$ ) was introduced in the reactor during  $\text{Al}_x\text{Ga}_{1-x}\text{N}$  growth. Other growth conditions for the three samples were constant. Although the samples were grown at relatively low temperature (790  $^\circ\text{C}$ ), a high crystalline structure of the superlattice was achieved after optimization of the growth conditions, as demonstrated by XRD. The  $2\theta$ - $\omega$  XRD pattern of the sample grown in  $\text{H}_2$  and its simulated curve are shown in Figure 5.7(a). As shown in this figure, the main diffraction peak is from the GaN template, and high orders (higher than 7) of superlattice-related satellite peaks are clearly observed from the XRD scan, attesting to the good periodicity and smoothness of the interfaces. The thicknesses of GaN and  $\text{Al}_x\text{Ga}_{1-x}\text{N}$  in the superlattice are fitted to be 11.8nm and 12.0nm, respectively, with an Al fraction of  $x=0.24$  in  $\text{Al}_x\text{Ga}_{1-x}\text{N}$  layers. However, when the carrier gas was switched to  $\text{N}_2$ , the interfacial quality of the superlattice deteriorated remarkably, as shown in Figure 5.7(b). The order of the satellite peaks is lower and intensities of the satellite peaks are much weaker compared to the sample grown using  $\text{H}_2$ -rich carrier gas. This is because the carrier gas affects the diffusion length of the reactants. With increasing  $\text{N}_2$  ratio

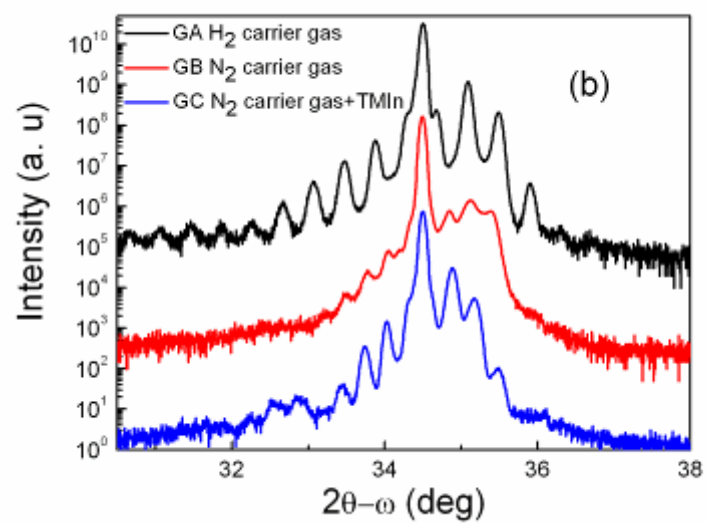
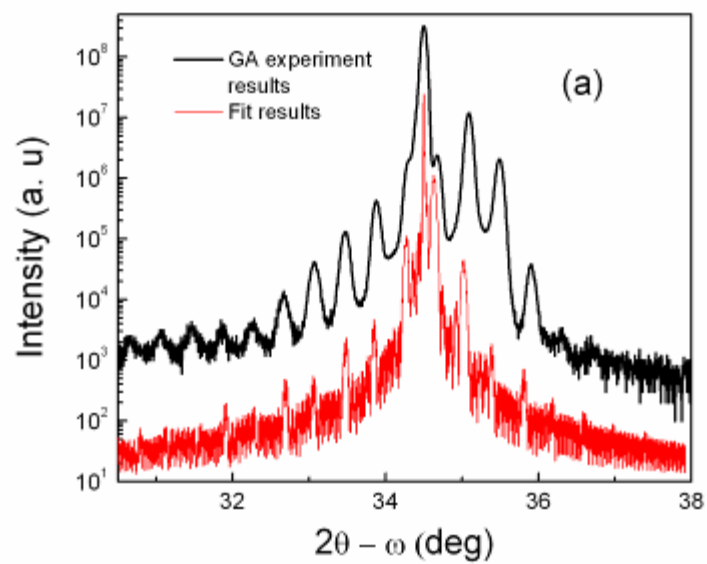


**Figure 5.7:** (a) XRD rocking curve scan and simulated curve of AlGaN/GaN superlattice on GaN/sapphire. (b) Rocking curve scans of AlGaN/GaN superlattices grown under different conditions on sapphire.

in the carrier gas, the density of gas molecules near the reaction interface increases, thereby decreasing the length of the mean free path of the reactant molecules. This leads to a rough GaN surface [124]. TMIIn has been reported to enhance the lateral growth of GaN and improve the interfacial quality of AlN/GaN as a surfactant [94,125]. As shown in Figure 5.7(b), clearer and stronger superlattice-related peaks are observed from the sample with additional TMIIn flow compared to the sample without TMIIn flow. To evaluate the In content in the AlGa(In)N epilayer, a 0.5 $\mu$ m-thick Al<sub>x</sub>Ga<sub>1-x</sub>N layer was grown on undoped GaN using the same growth conditions as the Al<sub>x</sub>Ga<sub>1-x</sub>N layer in the superlattice with TMIIn flow. Energy Dispersive X-ray analysis (EDX) experimental results show that the indium content in the alloy is 0.8%. Thus, high quality Al<sub>x</sub>Ga<sub>1-x</sub>N/GaN superlattices can be achieved using N<sub>2</sub> carrier gas at relatively low growth temperatures, which are suitable for MOCVD growth of GaN on ZnO.

The growth process was subsequently transferred to ZnO (0001) substrates. Three samples were grown. For all cases, the growths were initiated with a 10 nm-thick GaN cover layer, which was deposited at 550, 770 and 820 °C for the three samples. The superlattice growth temperatures of the first two samples was 790°C, while it was increased to 840°C for the third sample.

XRD  $2\theta$ - $\omega$  scans of the three samples grown on ZnO are shown in Figure 5.8. The main XRD diffraction peaks are from the ZnO substrate. The first sample with a 550 °C cover layer does not display clear superlattice-related peaks, while superlattice-related satellite peaks are observed in the second sample, with a higher temperature (770 °C) cover layer. When the growth temperatures of both GaN cover layer and superlattice are further increased (+50°C), higher order satellite peaks are observed, indicating improved interfacial quality. A relatively

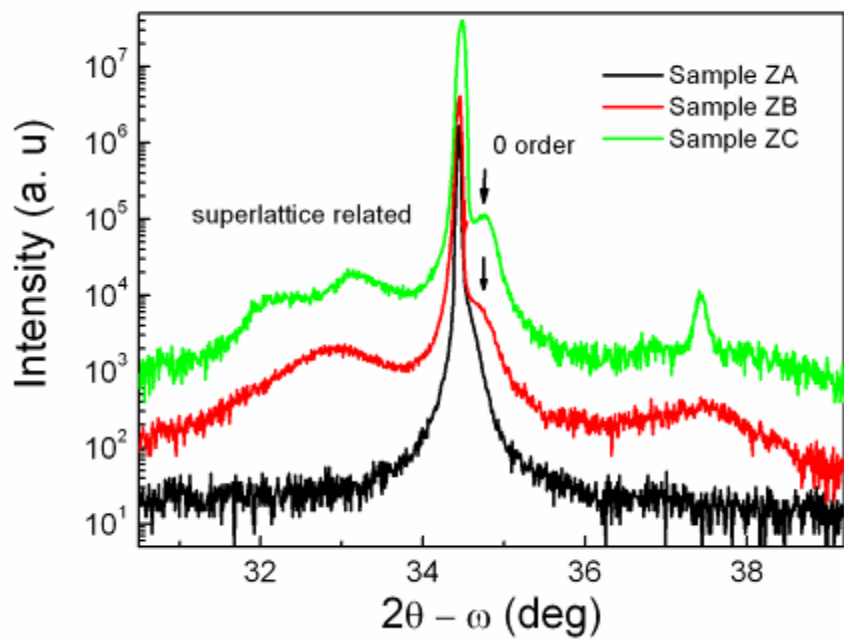


**Figure 5.8:** XRD rocking curve scans of AlGaIn/GaN superlattices grown on ZnO substrates at different temperatures. Samples ZA, ZB, and ZC were grown at 550, 770, and 820 °C, respectively.

high growth temperature can help to enhance the reactant mobility on the epilayer surface during growth, which can improve the crystalline quality and interfacial smoothness of the superlattice. However, it is also found that a high growth temperature will cause surface reactions. A diffraction peak at  $37.4^\circ$  was observed from the high-temperature sample, and can be identified as  $\text{Ga}_2\text{ZnO}_4$ , forming by the reaction between Ga and ZnO substrate at high growth temperature [126]. The growth temperature must be chosen with these two factors in mind, with too low a growth temperature leading to poor quality material and too high a temperature causing reactions at the GaN/ZnO interface and formation of the spinel  $\text{Ga}_2\text{ZnO}_4$ .

### 5.3.2 Optical Properties

The optical properties of these layers were studied in detail in order to better the electronic defects in the layers. Figure 5.9 shows the RT-PL spectrum of a GaN epilayer grown on ZnO with an  $\text{Al}_x\text{Ga}_{1-x}\text{N}/\text{GaN}$  superlattice buffer structure. The figure shows Gaussian fits to both the ZnO and GaN bandedges. Bandedge luminescence from the GaN layer is clearly observed at 3.41 eV, though it is not as strong as the ZnO bandedge. This may be due to reabsorption of some of the emitted light in the ZnO substrate, as the GaN bandedge emission is at a higher energy than that of ZnO. However, no significant shift is observed in the GaN bandedge, suggesting that there is little strain in the layer.

### 5.3.3 Impurity Diffusion

Impurity concentrations (zinc, oxygen, and carbon) for the GaN thin films grown using  $\text{Al}_x\text{Ga}_{1-x}\text{N}/\text{GaN}$  superlattices were measured via SIMS, Figure 5.10. SIMS results still show relatively high zinc and oxygen concentrations for these films, despite the addition of the superlattice structure to suppress diffusion. Co-doping of the  $\text{Al}_x\text{Ga}_{1-x}\text{N}/\text{GaN}$  superlattice

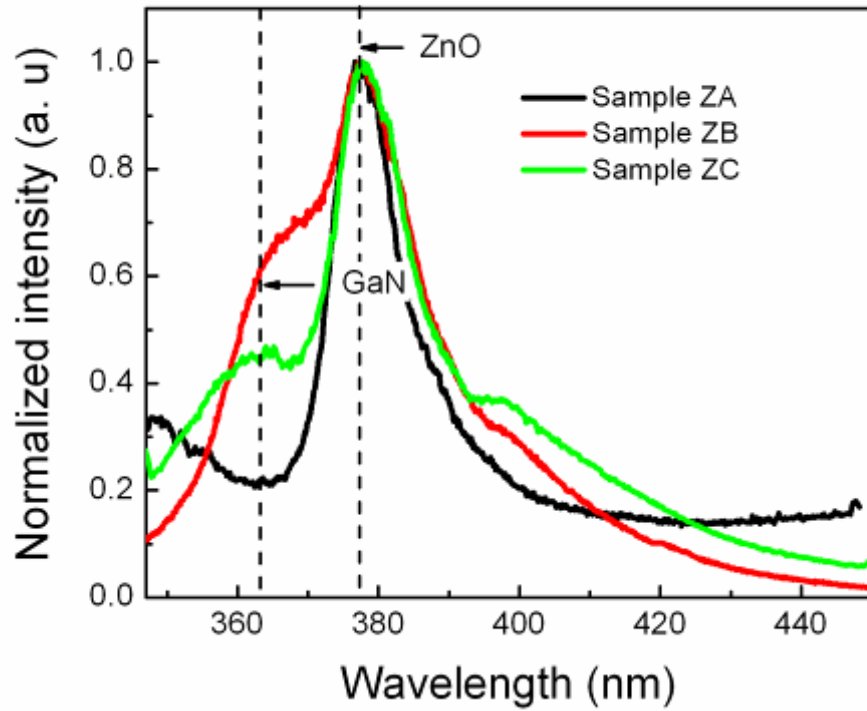


**Figure 5.9:** RT-PL of AlGaIn/GaN samples grown on ZnO (0001) substrates. Samples ZA, ZB, and ZC were grown at 550, 770, and 820 °C, respectively.

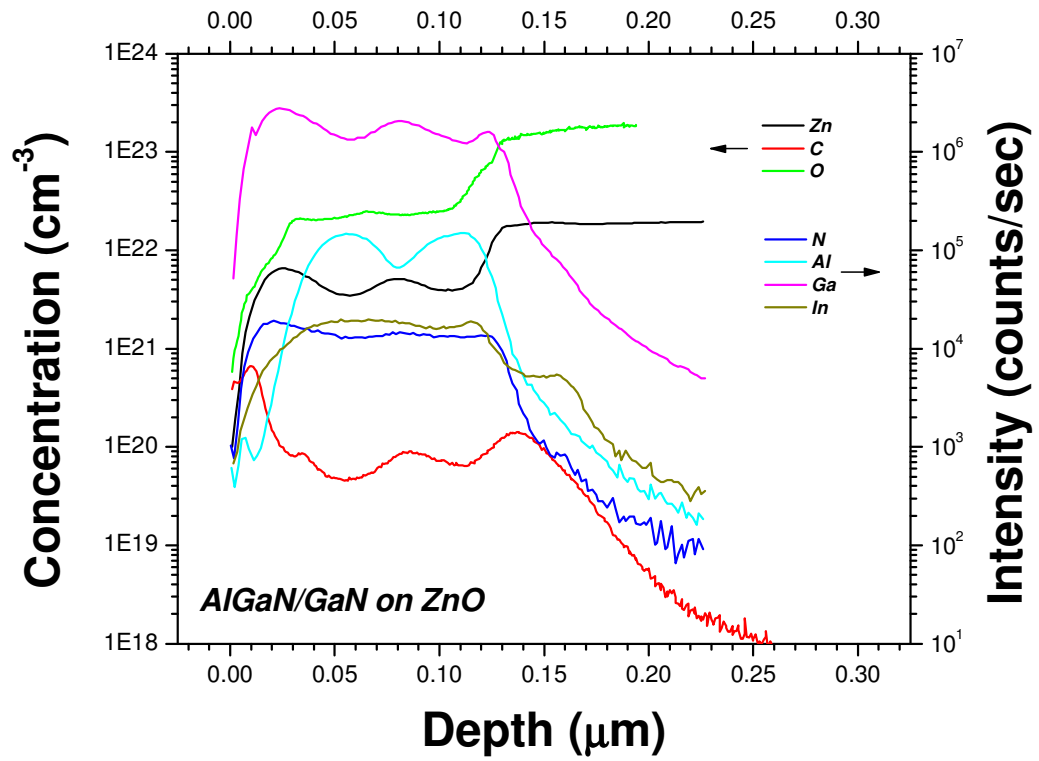


**Figure 5.10:** SIMS depth profile of an AlGaIn/GaN superlattice grown on ZnO at 770 °C.

to aid in pinning the Fermi level was also attempted in order to reduce out-diffusion from the substrate, with similar results.

## 5.4 $\text{In}_x\text{Ga}_{1-x}\text{N}/\text{GAN}$ MULTIPLE QUANTUM WELLS

$\text{In}_x\text{Ga}_{1-x}\text{N}/\text{GaN}$  multiple quantum well structures were investigated in order to suppress both zinc and oxygen diffusion by pinning the Fermi level at the interface and preventing diffusion of one or the other species. Different quantum well thicknesses and growth treatments were studied, and their ultimate effect on structural and optical properties of subsequent GaN and  $\text{In}_x\text{Ga}_{1-x}\text{N}$  thin films was investigated.

### 5.4.1 Structural Properties

A basic structure was developed in order to study the effects of  $\text{In}_x\text{Ga}_{1-x}\text{N}/\text{GaN}$  multiple quantum wells on zinc and oxygen diffusion. The baseline structure of five  $\text{In}_x\text{Ga}_{1-x}\text{N}/\text{GaN}$  multiple quantum wells was grown on a 2  $\mu\text{m}$ -thick GaN/sapphire template as a control before transferring the process to ZnO substrates. XRD for the structure on a GaN/sapphire template grown at 740°C shows clear satellite peaks, Figure 5.11. Target thicknesses for the wells and barriers were 3 nm and 12 nm, respectively. The process was then transferred to ZnO substrates to suppress outdiffusion from the substrate. The structure used a thin LT-GaN nucleation layer (~30 nm grown at 530 °C) and a subsequent thin (~5 nm)  $\text{In}_x\text{Ga}_{1-x}\text{N}$  (or GaN) buffer layer, Figure 5.12. The number of quantum wells was also increased from five to ten. Barriers were also doped with silicon, as this produces more abrupt interfaces and prevents intermixing of the well and barrier. A 50 nm GaN cap layer was grown on top of the multiple quantum well structure as well.

Structural properties of this basic structure were investigated using XRD. XRD results show the zero order for the MQWs and an InGaN well of 8% indium composition, Figure

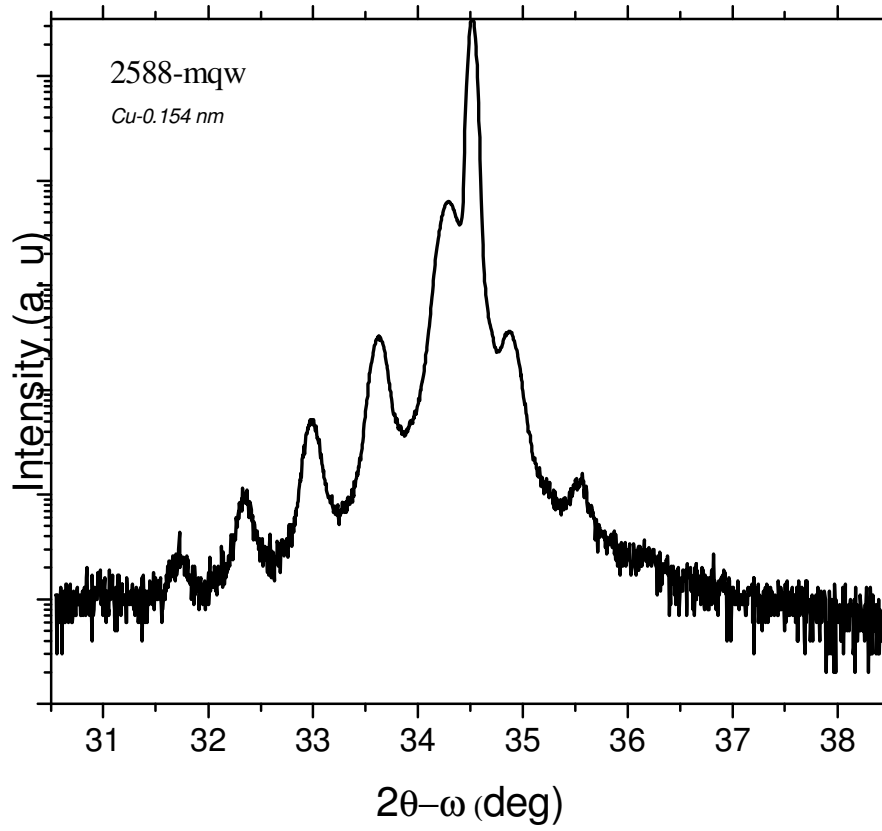


**Figure 5.11:** XRD of five multiple quantum wells on GaN/sapphire template.

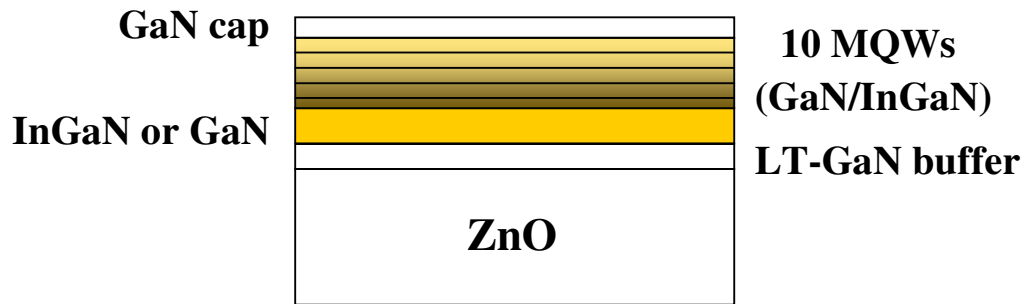


**Figure 5.12:** Basic structure used to investigate  $\text{In}_x\text{Ga}_{1-x}\text{N}/\text{GaN}$  MQWs on ZnO.

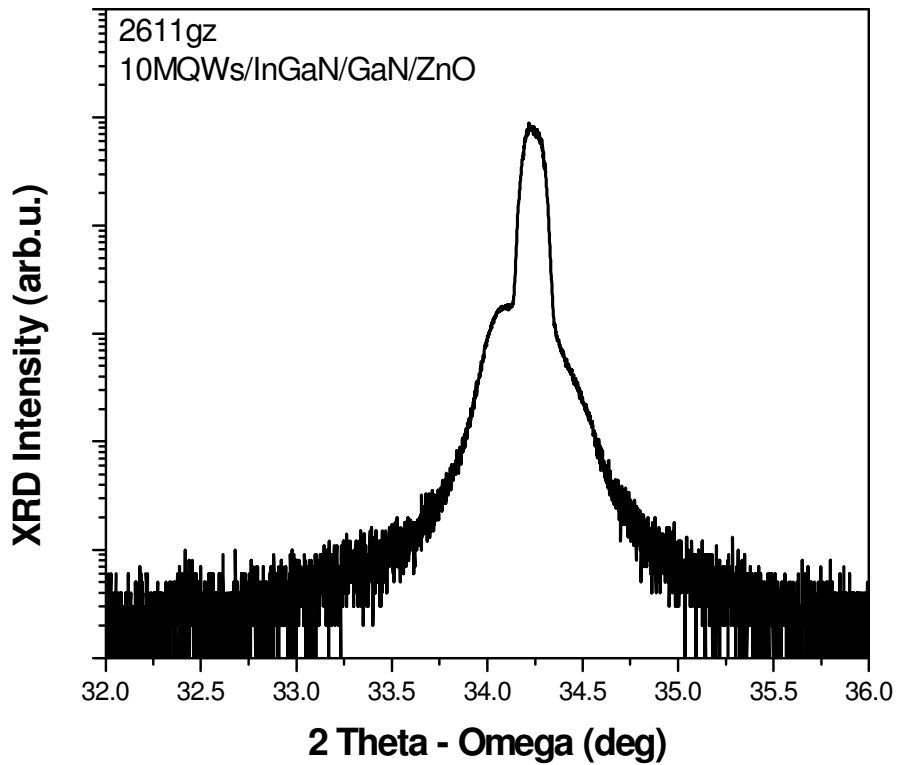


**Figure 5.13:** XRD of multiple quantum well structure on ZnO.

6.13. XRD also shows a shoulder on the right hand side of the ZnO peak from the GaN barriers. However, no significant satellite peaks are observed, suggesting poor interfacial quality in the quantum wells. The interface roughness and intermixing between barriers and wells may cause degradation of the MQWs. It is also possible that the underlying LT-GaN and  $\text{In}_x\text{Ga}_{1-x}\text{N}$  layers are too rough to provide a good surface for growth of the subsequent multiple quantum well structure, degrading both interfacial and optical quality.

#### 5.4.2 Optical Properties

RT-PL was used to study the optical properties of the multiple quantum well structures, and to study electronic defects in the material. The RT-PL spectrum of a 100 nm  $\text{In}_x\text{Ga}_{1-x}\text{N}$  layer grown on top of the basic structure is shown in Figure 5.14. The GaN and ZnO bandedges are relatively weak, as would be expected. However, two clear  $\text{In}_x\text{Ga}_{1-x}\text{N}$ -related peaks are observable at longer wavelengths. The peaks near 415 nm and 440 nm are attributed to the  $\text{In}_x\text{Ga}_{1-x}\text{N}/\text{GaN}$  multiple quantum well structure. The shorter wavelength emission is due to the multiple quantum wells, while the longer wavelength emission is due to the the bulk  $\text{In}_x\text{Ga}_{1-x}\text{N}$  layer on top of the basic structure. The relative intensity of the  $\text{In}_x\text{Ga}_{1-x}\text{N}$ -related emission peak suggests that the optical quality of the layer is improved over that of  $\text{In}_x\text{Ga}_{1-x}\text{N}$  layers on ZnO with a simple LT-AlN or LT-GaN buffer layer. However, the lack of interface-related peaks in the XRD data still suggest degraded interfacial quality due to diffusion of zinc and oxygen into the multiple quantum well structure.

### **5.5 ALD-GROWN $\text{Al}_2\text{O}_3$ INTERLAYERS**

The final approach that was investigated to suppress diffusion of zinc and oxygen into the GaN layer was the use of an ALD-grown  $\text{Al}_2\text{O}_3$  interlayer on the ZnO substrate. These

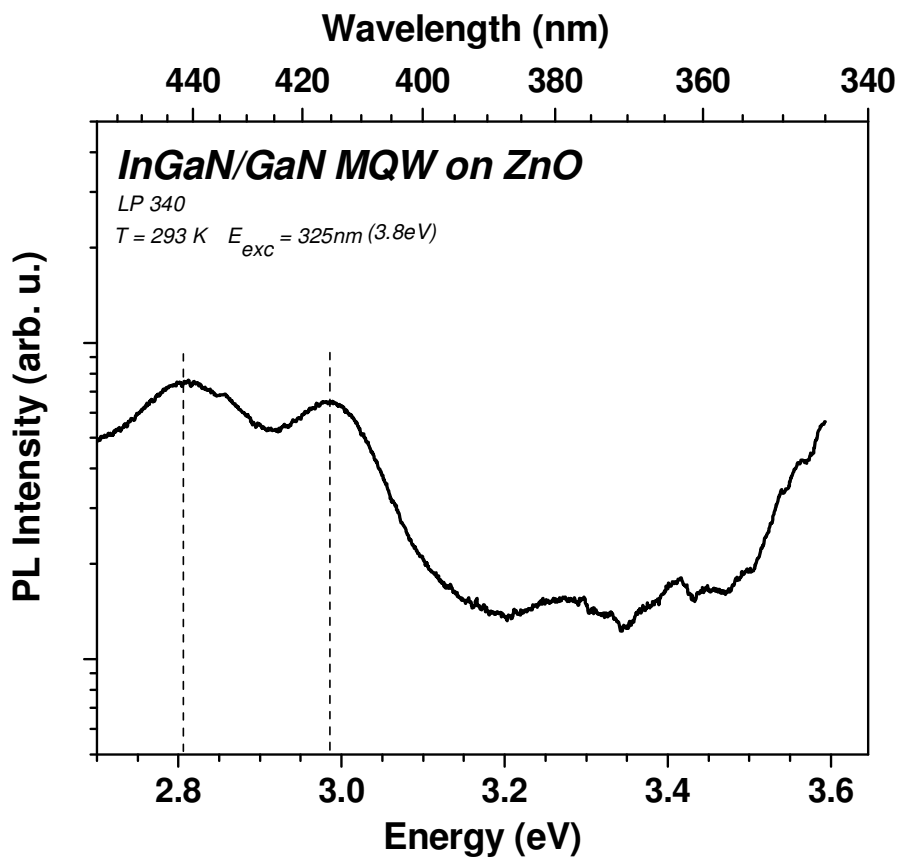


Figure 5.14: RT-PL of an InGaN/GaN MQW structure on ZnO.

layers were grown using the custom-built ALD system described earlier and range in thickness from 2 nm to 100 nm. This section describes results obtained from the study of these ALD- $\text{Al}_2\text{O}_3$  layers as interlayers for GaN growth on ZnO.

### 5.5.1 Growth Parameters

The effect of various growth parameters on GaN thin films grown using ALD- $\text{Al}_2\text{O}_3$  interlayers were studied first. As mentioned previously, the  $\text{NH}_3$  flow for a typical GaN process on ZnO is slightly lower than the same process on sapphire because of the reactivity of the substrate with hydrogen. This is especially true of  $\text{In}_x\text{Ga}_{1-x}\text{N}$  growth, in which the lower vapor pressure of indium necessitates the use of the very high V/III ratios and, thus, very high  $\text{NH}_3$  flow rates. The typical  $\text{In}_x\text{Ga}_{1-x}\text{N}$  process on sapphire used in this work uses an  $\text{NH}_3$  flow of 12.5 slm, compared to  $\sim 7$  slm on bare ZnO substrates. An increase beyond  $\sim 7$  slm on ZnO causes surface roughening and etching of the substrate when growing on bare ZnO. However, the addition of the ALD- $\text{Al}_2\text{O}_3$  layer sufficiently protects the substrate so that typical  $\text{In}_x\text{Ga}_{1-x}\text{N}$  growth conditions on sapphire can be transferred to ZnO. Specifically, the ALD- $\text{Al}_2\text{O}_3$  interlayer allows for the use of typical  $\text{NH}_3$  flows (12.5 slm) in  $\text{In}_x\text{Ga}_{1-x}\text{N}$  growth on ZnO. However, no improvement in crystal quality of the  $\text{In}_x\text{Ga}_{1-x}\text{N}$  layers was observed via XRD with the addition of the ALD- $\text{Al}_2\text{O}_3$  interlayer.

The previously studied  $\text{Al}_x\text{Ga}_{1-x}\text{N}/\text{GaN}$  superlattices showed promise toward increasing both optical and structural quality of the GaN layers. Thus, this structure was added to the ALD- $\text{Al}_2\text{O}_3$  layer in order to allow for growth under conditions that more closely match typical GaN growth conditions on sapphire. The structure of the first sample is shown in Figure 5.15(a). It consists of a thin (20 nm) ALD-grown  $\text{Al}_2\text{O}_3$  interlayer, two thin GaN buffer layers, a 4-period  $\text{Al}_x\text{Ga}_{1-x}\text{N}/\text{GaN}$  superlattice, and a 1  $\mu\text{m}$ -thick GaN layer grown

under typical GaN growth conditions on sapphire. The  $\text{Al}_x\text{Ga}_{1-x}\text{N}$  barriers were doped with silicon, and the GaN wells were doped with Mg in order to help pin the Fermi level at the  $\text{Al}_x\text{Ga}_{1-x}\text{N}/\text{GaN}$  interface and suppress diffusion. This sample was grown at a temperature of 750 °C and an  $\text{NH}_3$  flow of 8 slm. A second sample, the structure of which is shown in Figure 5.15(b), was grown under identical conditions, but with a higher GaN growth temperature (970 °C). In-situ reflectivity curves (not shown here) show that the surface roughness of the GaN layer, however, degrades as the growth proceeds. This observation is also born out by AFM images, which show an RMS surface roughness of  $\sim 30$  nm for the layer grown at 750 °C and  $\sim 25$  nm for the layer grown at 970 °C.

### 5.5.2 Impurity Diffusion

SIMS measurements were performed in order to investigate the zinc and oxygen concentrations in GaN thin films on ALD- $\text{Al}_2\text{O}_3/\text{ZnO}$  substrates. A relatively high concentration of both zinc and oxygen was observed in the GaN layers on ALD- $\text{Al}_2\text{O}_3$  using an  $\text{Al}_x\text{Ga}_{1-x}\text{N}/\text{GaN}$  superlattice, Figure 5.16. A concentration of  $10^{21} \text{ cm}^{-3}$  zinc and  $10^{21} \text{ cm}^{-3}$  oxygen was observed through the entire thickness of this sample. The relatively constant impurity concentrations throughout the sample suggest that diffusion may not occur simply from the substrate through the layer, but that the substrate may also break down to some degree, leading to the presence of zinc and oxygen in the ambient. This presence of both zinc and oxygen in the ambient near the growth surface may contribute to the high impurity concentrations observed via SIMS and negate any attempt to block diffusion from the substrate.

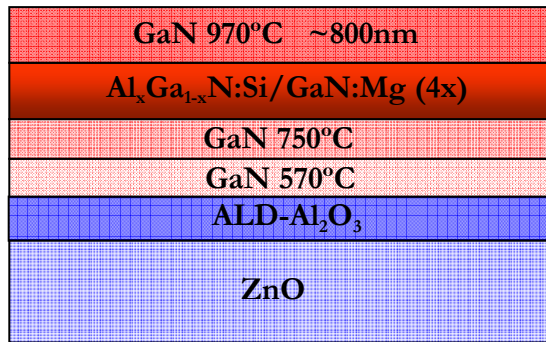
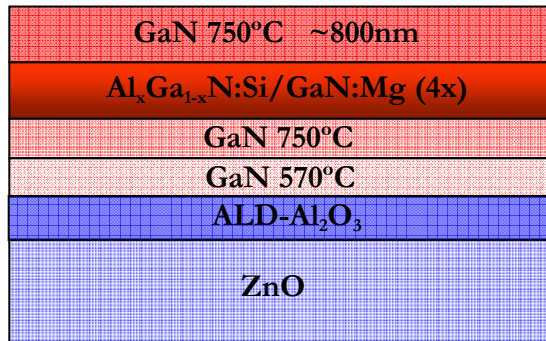


**Figure 5.15:** (a) Low-temperature GaN layer grown on AlGaInN/GaN superlattice on  $\text{Al}_2\text{O}_3/\text{ZnO}$ . (b) High-temperature GaN layer grown on AlGaInN/GaN superlattice on  $\text{Al}_2\text{O}_3/\text{ZnO}$ .

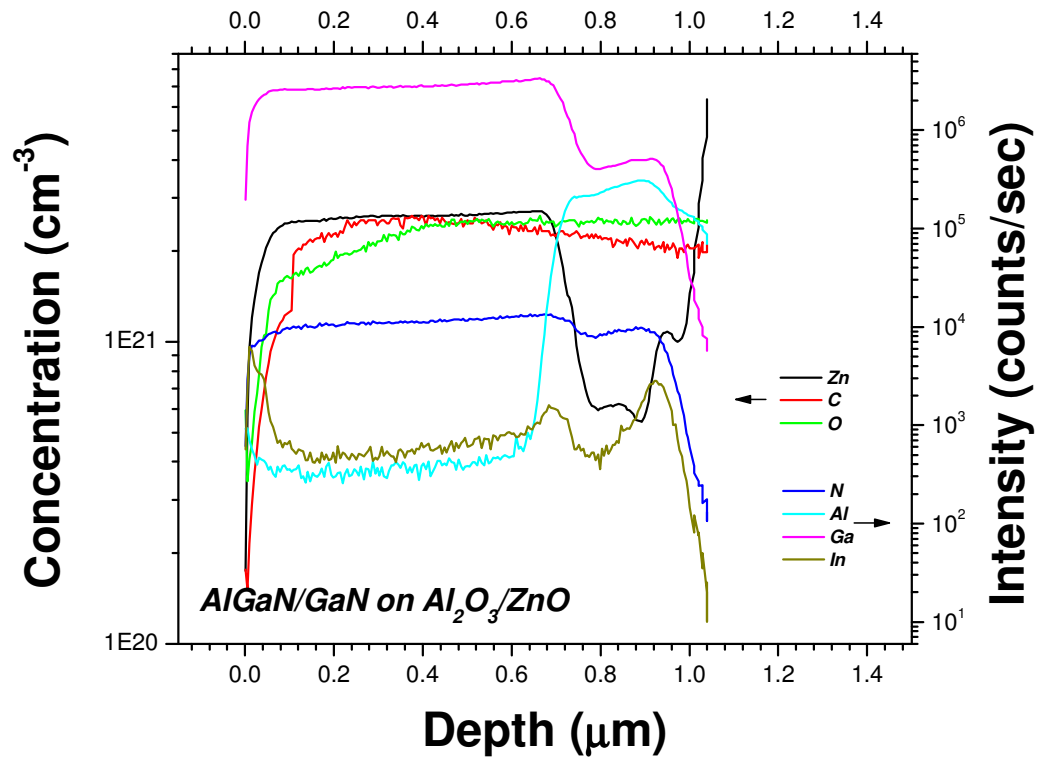


**Figure 5.16:** SIMS depth profile of a 1 μm-thick GaN layer on [AlGaN/GaN]/Al<sub>2</sub>O<sub>3</sub>/ZnO.

## 5.6 SUMMARY

Several different approaches were attempted to suppress outdiffusion of both zinc and oxygen into the GaN epilayers. GaN thin films on AlN buffer layers showed stronger bandedge emission, but structural quality was still poor. The most promising approaches for suppression of diffusion into the GaN thin film was the use of  $\text{Al}_x\text{Ga}_{1-x}\text{N}/\text{GaN}$  or  $\text{In}_x\text{Ga}_{1-x}\text{N}/\text{GaN}$  superlattice structures. The  $\text{Al}_x\text{Ga}_{1-x}\text{N}/\text{GaN}$  structures showed promise toward higher quality GaN on silicon because of the observation of the GaN near bandedge emission and the GaN (0002) reflection in the XRD patterns. However, SIMS results show that zinc and oxygen concentrations remained high, despite attempts to dope the  $\text{Al}_x\text{Ga}_{1-x}\text{N}$  and GaN layers and pin the Fermi level at the interface, suppressing diffusion.

## CHAPTER 6: ATOMIC LAYER DEPOSITION OF $\text{Al}_2\text{O}_3$ ON Si

Thin ALD-grown  $\text{Al}_2\text{O}_3$  layers were used as an interlayer to grow GaN-based materials on Si. The important properties – surface morphology and structural quality – of these layers were investigated to determine their suitability for MOCVD growth of subsequent GaN layers. Annealing studies were also done to study crystallization of the layers.

### 6.1 AS-GROWN FILMS

Details of the ALD growth process used in this work are given in Chapter 3. The surface morphology of these layers was investigated first, using both AFM and SEM. Plan-view SEM images show a smooth, mirror-like surface, Figure 6.1. No pits or pinholes are observable in the  $\text{Al}_2\text{O}_3$  surface in the SEM images. AFM images also reveal a relatively smooth surface.

Structural properties of the ALD-grown  $\text{Al}_2\text{O}_3$  layers on Si(111) were studied using XRD. Samples ranging in thickness from 2 nm to 200 nm were investigated, and XRD scans of the as-deposited samples showed no peaks that could be attributed to the  $\text{Al}_2\text{O}_3$  layer, indicating amorphous material. The only clear diffraction peaks are those that are from the Si(111) and (222) reflections. The absence of any diffraction peaks except the substrate suggests that the layer is amorphous. Raman spectroscopy of thick  $\text{Al}_2\text{O}_3$  layers on Si(111) showed no  $\text{Al}_2\text{O}_3$ -related Raman modes, suggesting little or no short-range ordering and poor overall crystalline quality.

Crystal structure of the layers is quite important for subsequent growth of nitride thin films, and amorphous material is not desirable for nucleation and growth of GaN.

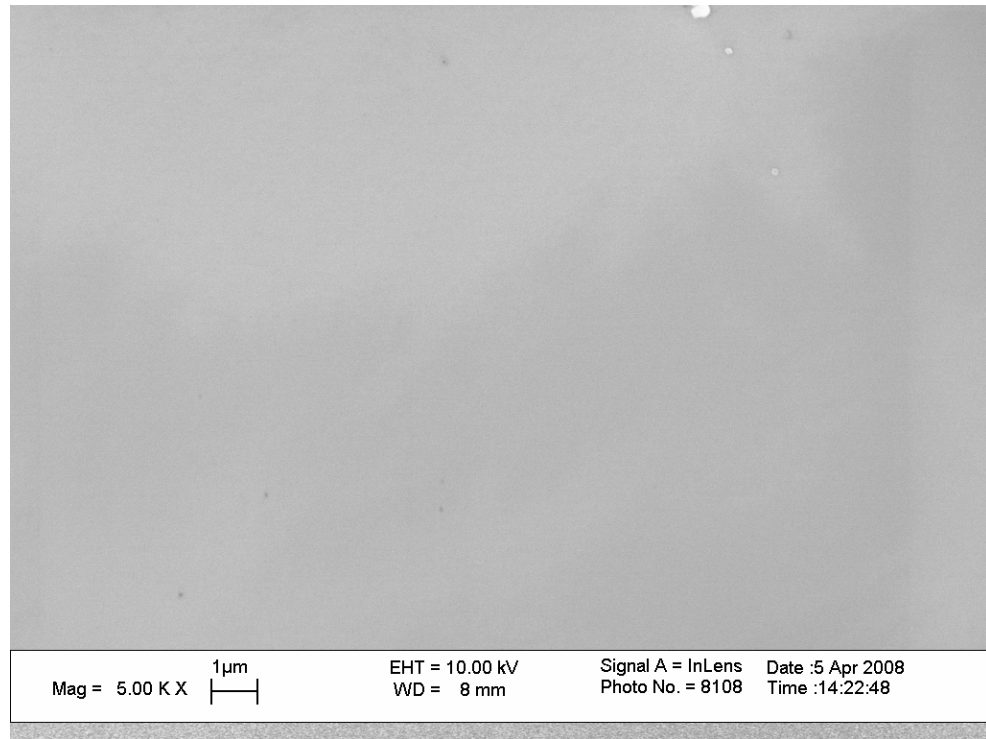


**Figure 6.1:**SEM image of the surface of an ALD-grown  $\text{Al}_2\text{O}_3$  layer on Si(111).

Annealing studies were performed to study the crystallization of the  $\text{Al}_2\text{O}_3$  layers and possibly to develop a process for crystallization before MOCVD growth.

## 6.2 ANNEALING STUDIES

Ex-situ annealing studies were done using an MHI high temperature tube furnace under either  $\text{N}_2$  or air ambient. Table 6.1 provides a summary of the ex-situ annealing conditions that were investigated.  $\text{Al}_2\text{O}_3$  thickness, annealing time, temperature, and atmosphere were varied in this study.

### 6.2.1 Structural Properties

Multiple crystalline phases were observed via XRD upon annealing, though the overall crystallinity of the  $\text{Al}_2\text{O}_3$  layers remains low. Five different peaks that are attributable to the  $\text{Al}_2\text{O}_3$  layer were observed in the XRD spectra, and the presence and behavior of each one depends on the layer thickness and annealing conditions. Figure 6.2 shows XRD spectra from two  $\text{Al}_2\text{O}_3$  layers (10 nm and 100 nm) that were annealed at 1300 °C for 90sec. Peaks near  $2\theta = 22^\circ$ ,  $2\theta = 34^\circ$ , and  $2\theta = 38^\circ$  appear in both samples, and an additional two peaks near  $2\theta = 44^\circ$  and  $2\theta = 82^\circ$  appear in the 100 nm sample. These last two peaks only appear in the XRD patterns of the thicker ( $>20$  nm) samples, suggesting either increased crystal quality in these samples or formation of multiple phases. The two most significant peaks are the peak near  $2\theta = 34^\circ$ , which is attributed to the  $\text{Al}_2\text{O}_3$  (104) reflection, and the peak near  $2\theta = 38^\circ$ , which is attributed to the  $\text{Al}_2\text{O}_3$  (110) reflection. The dependence of the FWHM of these peaks on both thickness and annealing temperature was plotted, and a 3D surface was fit to the data points. Figure 6.3(a) shows the dependence of the  $\text{Al}_2\text{O}_3$  (104) peak on thickness and annealing temperature in air, and Figure 6.3(b) shows the same dependence, annealed in nitrogen. Figure 6.3(c) and (d) represent the FWHM dependence of the  $\text{Al}_2\text{O}_3$

Table 6.1: Summary of ex-situ annealing conditions for ALD-grown  $\text{Al}_2\text{O}_3$  layers on Si(111).

Thickness (nm)	Temperature ( $^{\circ}\text{C}$ )	Time (sec)		Atmosphere
10	1300	90		Air
10	1100	30		$\text{N}_2$
10	1200	30		$\text{N}_2$
10	1200	90		Air
10	1200	180		Air
20	1100	30		$\text{N}_2$
20	1000	120		$\text{N}_2$
20	1100	120		$\text{N}_2$
20	1200	120		$\text{N}_2$
30	1100	30		$\text{N}_2$
30	1200	30		$\text{N}_2$
50	1200	90		Air
50	1200	180		Air
100	1300	90		Air
100	1200	90		Air
100	1200	180		Air
100	1100	90		Air
100	1100	180		Air
100	1200	90		Air

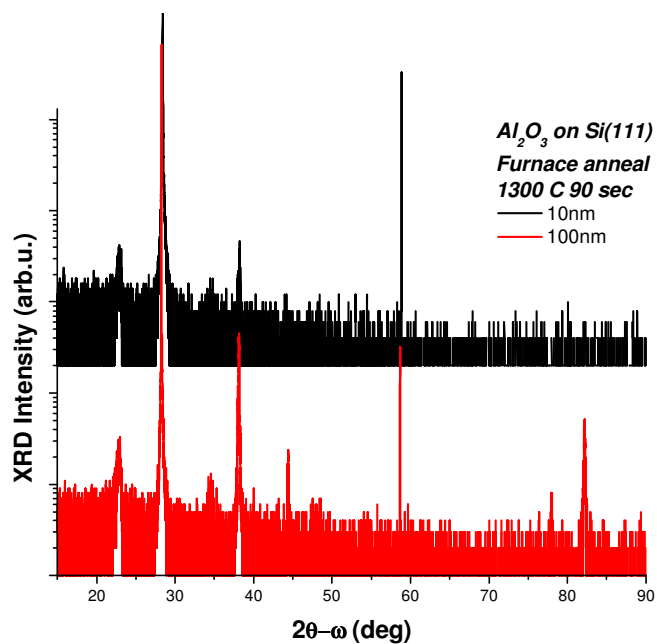
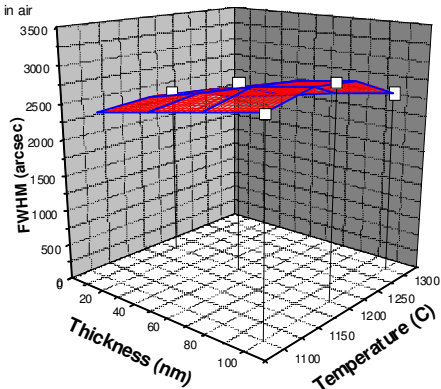
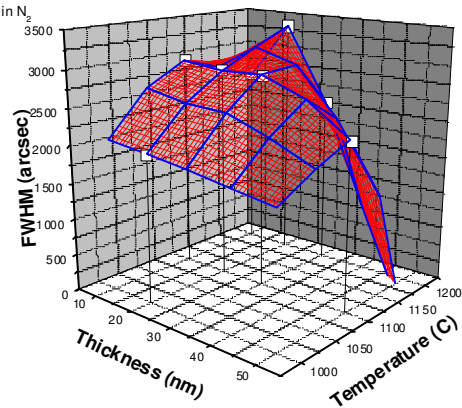


Figure 6.2: XRD  $2\theta$ - $\omega$  scans of annealed ALD-grown  $\text{Al}_2\text{O}_3$  layers on Si(111).

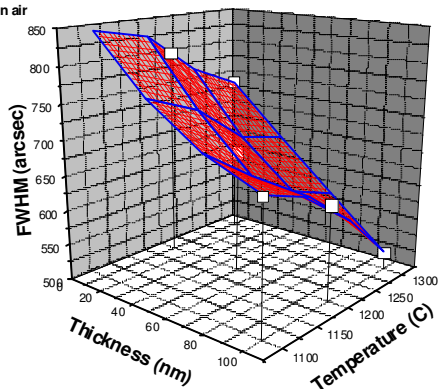
**$Al_2O_3$  (104) peak**  
Annealed in air



**$Al_2O_3$  (104) peak**  
Annealed in  $N_2$



**$Al_2O_3$  (110) peak**  
Annealed in air



**$Al_2O_3$  (110) peak**  
Annealed in  $N_2$

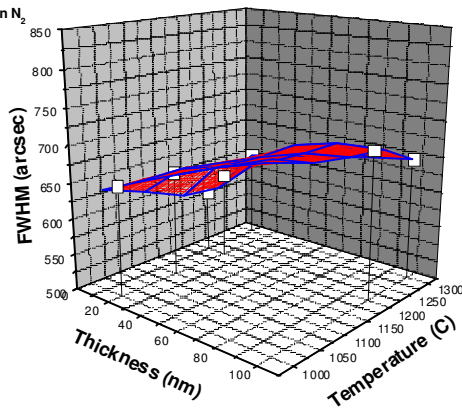


**Figure 6.3:** Dependence of the XRD FWHM of the  $Al_2O_3$  (104) peak on layer thickness and annealing temperature in air (a), and nitrogen (b). Dependence of XRD FWHM of the  $Al_2O_3$  (110) peak on layer thickness and annealing temperature in air (c), and nitrogen (d). Note the sharp decrease in linewidth for thicker layers annealed at high temperatures in air.

(110) peak annealed in air and nitrogen, respectively. The most interesting dependence is the  $\text{Al}_2\text{O}_3$  (110) peak annealed in air, suggesting that thicker samples annealed at higher temperatures show a higher degree of crystallinity in the (110) reflection. The difference between samples annealed in air and those annealed in nitrogen is most likely to be due to the presence of oxygen at the surface when annealing in air. This additional oxygen may allow for the formation of fewer point defects during annealing, leading to higher crystal quality compared to the samples annealed in  $\text{N}_2$ . Temperature-dependent Raman spectroscopy was used to study the short-range ordering of the  $\text{Al}_2\text{O}_3$  layers during annealing. No  $\text{Al}_2\text{O}_3$ -related modes were observable at temperatures up to  $1000^\circ\text{C}$ , indicating little or no short range ordering and low crystal quality upon annealing up to  $1000^\circ\text{C}$ .

However, surface morphology of these samples also changed significantly compared to both the as-grown layers and the thinner layers annealed at lower temperatures.

### 6.2.2 Surface Morphology

SEM images reveal more about the effects of heat treatment on the  $\text{Al}_2\text{O}_3$  layers. All as-grown layers were quite smooth, with a mirror-like surface, and the thin layers ( $\leq 20$  nm) showed relatively little change in surface morphology with annealing up to  $1300^\circ\text{C}$ , Figure 6.4. Figure 6.4 shows SEM images of an as-grown 10 nm  $\text{Al}_2\text{O}_3$  layer (Fig. 6.4(a)), and 10 nm  $\text{Al}_2\text{O}_3$  layers annealed for 30 seconds at  $1100^\circ\text{C}$  (Fig. 6.4(b)) and  $1200^\circ\text{C}$  (Fig. 6.4(c)). Figures 6.4(d)-(f) show the same  $\text{Al}_2\text{O}_3$  films at higher magnification. Relatively little change in surface morphology is observed with annealing.

Significant changes were observed, however, for thicker samples, Figure 6.5. Figures 7.5(a)-(c) show 50 nm  $\text{Al}_2\text{O}_3$  layers annealed for 90 seconds at  $1000^\circ\text{C}$ ,  $1100^\circ\text{C}$ , and  $1200^\circ\text{C}$ , respectively. A clear change in surface morphology compared to the as-grown layers is

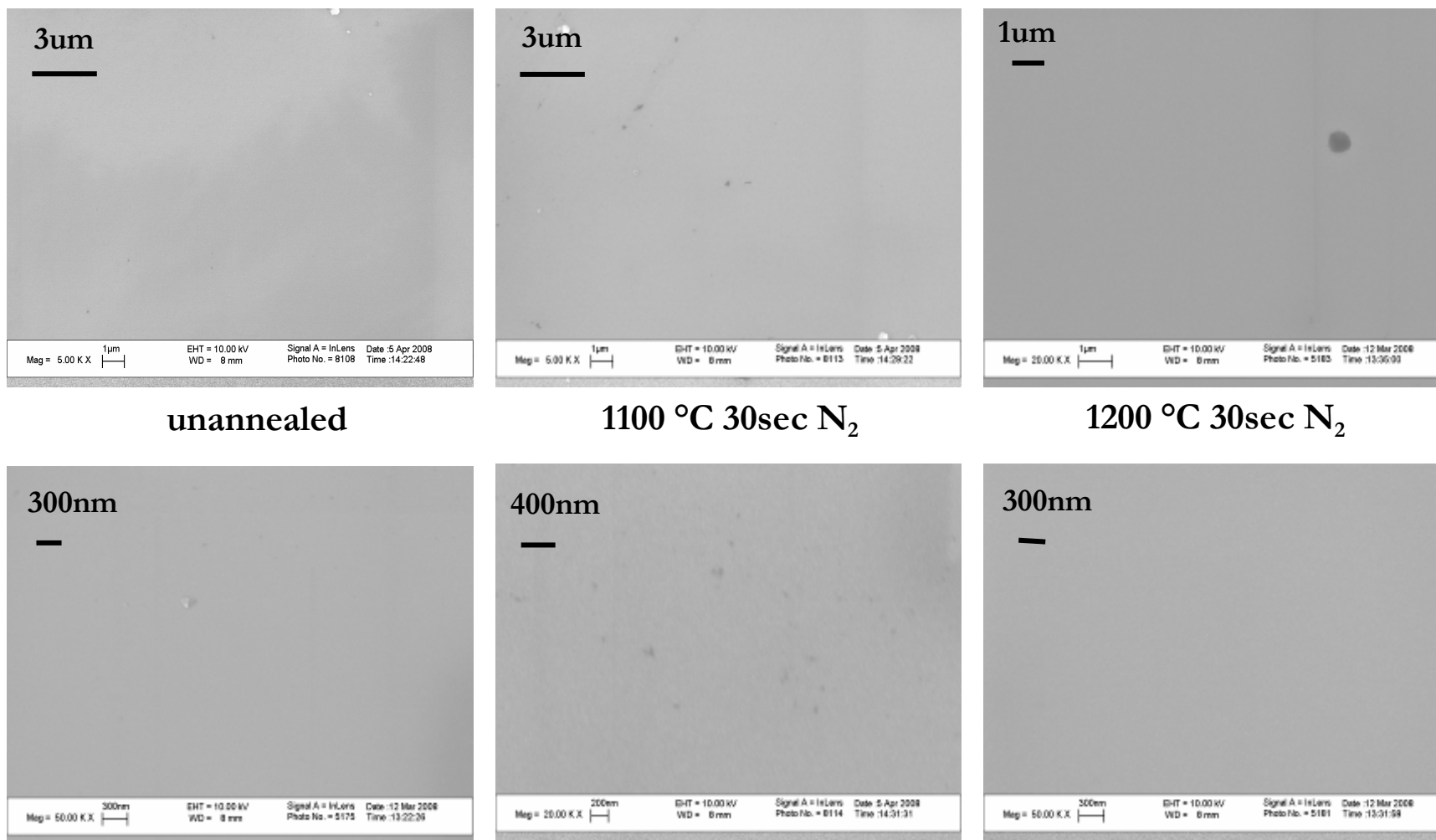


**Figure 6.4:** SEM images of the surface of a 10nm ALD-grown  $\text{Al}_2\text{O}_3$  layer on Si(111).

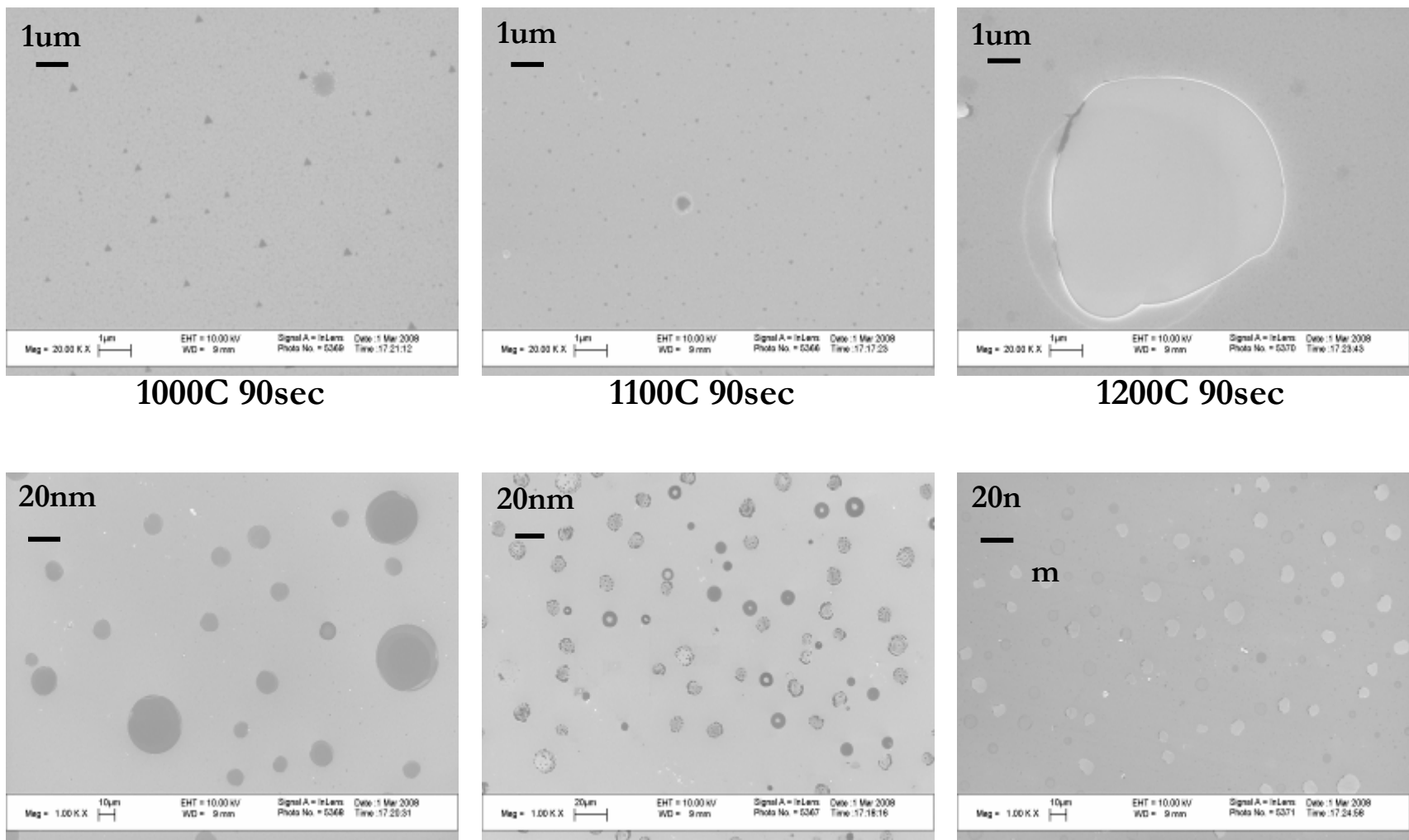


**Figure 6.5:** SEM images of the surface of a 50nm ALD-grown  $\text{Al}_2\text{O}_3$  layer on Si(111).

observable. Figures 6.5(d)-(f) show the same samples at a higher magnification. The major change in surface morphology is the formation of pits in the Al<sub>2</sub>O<sub>3</sub> surface. Pit formation is observable at 1000 °C. The pit size appears to have a bi-modal behavior, with the small pits ranging in diameter from ~8-12 μm and having a density of 3.56x10<sup>4</sup> cm<sup>-2</sup>. The large pits have a diameter of ~30 μm and a density of 6.7x10<sup>3</sup> cm<sup>-2</sup>. The dependence of pit density on annealing time and temperature will be discussed later in this section.

Surface morphology changes again with an increase in annealing temperature. The sample annealed at 1100 °C shows a higher pit density, at 1.25x10<sup>5</sup> cm<sup>-2</sup>, as well as a change in morphology of the pits, Figures 6.5(e) and (f). Small bubbles form around the edges of the pits with higher annealing temperature, though the origin of these bubbles remains unclear at this time. Also, the large pits with a ~30 μm diameter do not appear in the sample annealed at 1100 °C. The layer annealed at 1200 °C shows a surface morphology similar to that of the layer annealed at 1100 °C. The pit density is also slightly higher, 1.70x10<sup>5</sup> cm<sup>-2</sup>. Both the increase in pit density and the change in surface morphology with increasing annealing temperature suggest a degradation in the quality of the thicker Al<sub>2</sub>O<sub>3</sub> layer.

Pit formation was also observed in the 100 nm Al<sub>2</sub>O<sub>3</sub> layers, though the pit density decreased compared to the 50 nm layers annealed under similar conditions, Figure 6.6. Figures 6.6(a)-(c) show 100 nm Al<sub>2</sub>O<sub>3</sub> layers annealed under different conditions, while Figures 6.6(d)-(e) show the same samples at higher magnification. Figures 6.6(c) and (f) show that annealing at a temperature of 1300 °C changes the surface morphology again. The pits formed at 1300 °C are much darker in color than those formed at lower temperatures, and may be a result of the bubble formation that is observed at lower temperatures.

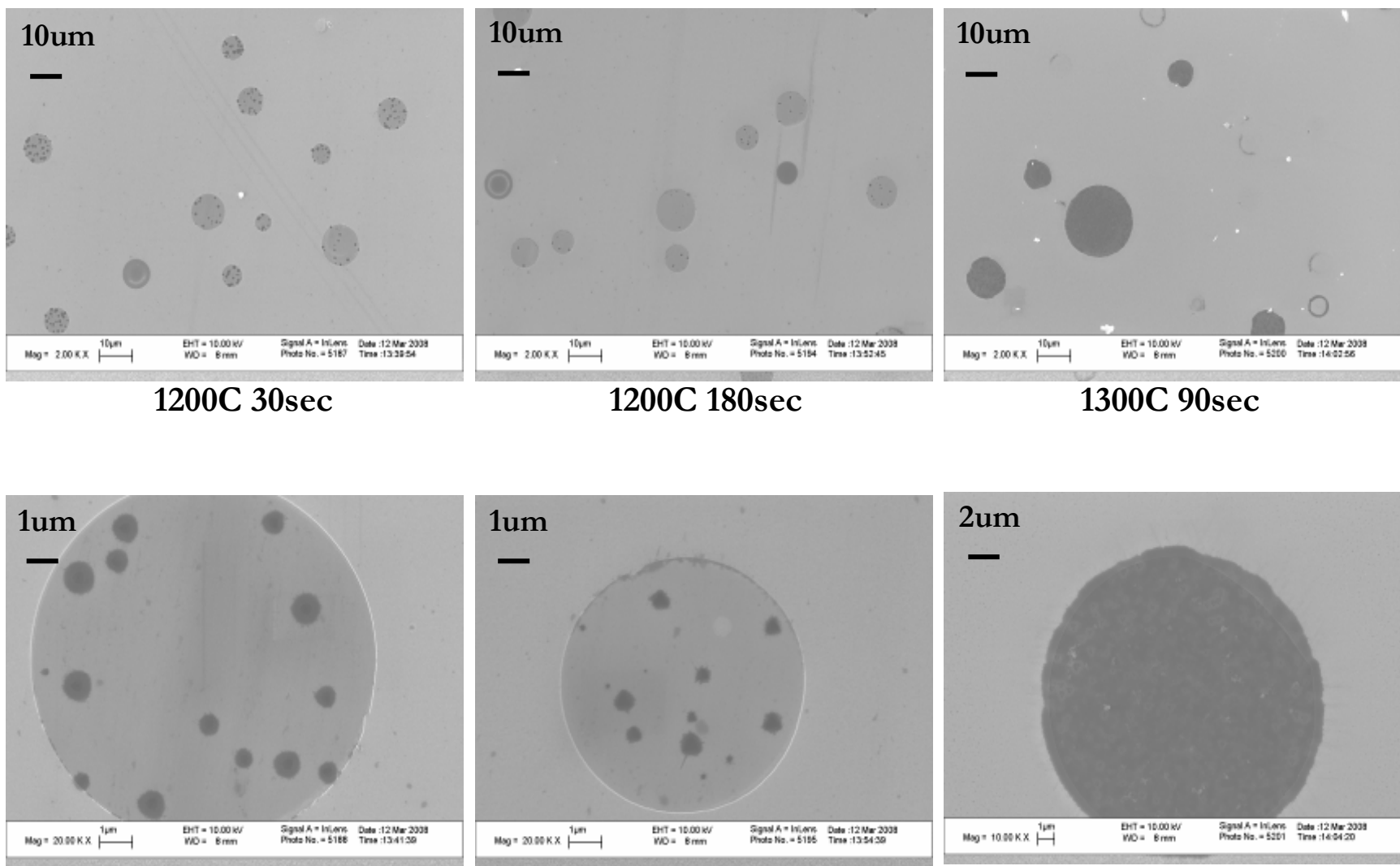


**Figure 6.6:** SEM images of the surface of a 100nm ALD-grown  $\text{Al}_2\text{O}_3$  layer on Si(111).

The surface composition was studied using EDS, Table 7.2. The smooth area around the pit is the  $\text{Al}_2\text{O}_3$  film, confirmed by the presence of both aluminum and oxygen on the surface, with a ratio of 59 at.% oxygen to 38 at.% aluminum. The composition changes significantly inside the pit, however. The bulk of the composition inside the pit is silicon, combined with a small amount of oxygen and virtually no aluminum. The smooth surface is  $\text{Al}_2\text{O}_3$ , while the circular pits are holes in the  $\text{Al}_2\text{O}_3$  layer that extend all the way to the Si substrate. Though the exact origin of these pits remains unclear, they are clearly more prevalent in the thicker  $\text{Al}_2\text{O}_3$  layers and most likely have a significant effect on growth.

The dependence of pit density on annealing temperature is plotted in Figure 6.7. Two regions are visible in the plot. The first region, at relatively low temperatures, shows an increase in pit density with increasing temperature, indicating a thermally activated process. Pit density is relatively independent of annealing temperature in the second region, at relatively high temperatures. The observation of pit formation in the  $\text{Al}_2\text{O}_3$  surface as opposed to cracking suggests that the change in surface morphology is not due to tensile strain induced by the large lattice and thermal mismatch between silicon and  $\text{Al}_2\text{O}_3$ , as is the case with GaN growth on silicon.

A comparison of the 10 nm, 50 nm, and 100 nm layers annealed under similar conditions shows a significant change in surface morphology with increasing thickness and annealing temperature. XRD results reveal an increase in crystallinity with these same annealing conditions, indicating that the change in surface morphology may be due to the change in structural properties of the films from amorphous to polycrystalline. The difference in thermal expansion coefficients between  $\text{Al}_2\text{O}_3$  and silicon may lead to tensile strain in the  $\text{Al}_2\text{O}_3$  layer, causing pit formation. It is possible that the crystallization process causes pit

Table 6.2: EDS data showing composition of pits in Al<sub>2</sub>O<sub>3</sub> surface.

Al <sub>2</sub> O <sub>3</sub> film	Element	Wt. %	At. %
Smooth surface	O	47.82	58.85
	Al	49.13	38.29
	Si	3.05	2.86
Hollow structure	O	4.98	8.66
	Al	0.18	0.25
	Si	94.84	91.09

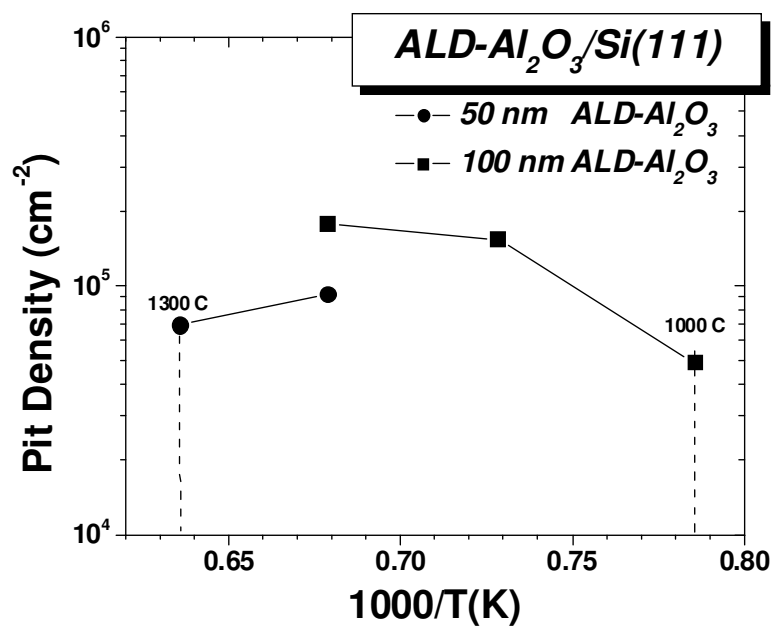


**Figure 6.7:** Arrhenius plot of pit density v. reciprocal temperature. The behavior suggests a thermally activated process.

formation by inducing strain in the  $\text{Al}_2\text{O}_3$  layer, which has a significant lattice and thermal mismatch with the underlying silicon substrate.

The degradation in surface morphology with annealing, however, can also be advantageous for GaN growth on silicon. Both porous and patterned  $\text{SiO}_2$  and  $\text{Si}_3\text{N}_4$  have been used as mask layers to promote nucleation and lateral growth of GaN islands on silicon substrates.[45,59,81] These approaches provide for areas of defect-free GaN, and reduce the overall dislocation density in subsequent GaN layers.

### 6.3 SUMMARY

$\text{Al}_2\text{O}_3$  thin films were grown by ALD to act as interlayers for GaN growth on Si. As-grown layers were amorphous, so annealing studies were done to investigate the crystallization of the  $\text{Al}_2\text{O}_3$  layers at high temperatures. XRD showed two main crystal orientations with annealing: the (110) reflection and the (104) reflection. The thicker layers ( $\geq 50$  nm) also showed a significant change in surface morphology with annealing, with pits forming in these layers. The pit density increases linearly at relatively low annealing temperatures, and then appears to become nearly independent of annealing temperature at high temperatures. Pits were not observed in the thin ( $\leq 20$  nm)  $\text{Al}_2\text{O}_3$ , however. For this reason, thin ALD- $\text{Al}_2\text{O}_3$  films were used in the work moving forward. AFM images show a relatively smooth surface, and little change in surface morphology with increasing ALD- $\text{Al}_2\text{O}_3$  thickness from 5 nm to 20 nm.

## CHAPTER 7: MOCVD GROWTH OF GaN ON SILICON

An MOCVD growth process was developed on bare silicon and then transferred to the ALD- $\text{Al}_2\text{O}_3/\text{Si}$  substrates investigated in the previous chapter. The oxide interlayer helps to reduce strain in the GaN layer and increase crystal quality, as evidenced by a reduction in both crack density (to  $< 1\text{mm}^{-2}$ ) and screw dislocation density (from  $3 \times 10^9\text{cm}^{-2}$  on bare silicon to  $2 \times 10^8\text{cm}^{-2}$  on ALD- $\text{Al}_2\text{O}_3/\text{Si}$ ). The effects of oxide layer thickness on subsequent GaN properties were also studied to determine favorable ALD- $\text{Al}_2\text{O}_3$  properties for GaN growth. The development of the MOCVD growth process on both bare silicon and ALD- $\text{Al}_2\text{O}_3/\text{Si}(111)$  is presented in this chapter.

### 7.1 MOCVD GROWTH OF GaN ON SILICON

The major challenge for GaN growth on silicon is the tensile strain induced by the lattice and thermal mismatch between GaN and silicon, which often leads to cracking in the GaN epilayers. Several approaches have been investigated to relieve this strain and prevent cracking. [22,48,127] This section discusses the development of an MOCVD growth process for GaN on bare silicon substrates using both a simple HT-AlN buffer layer and LT-AlN interlayers. This process will be used as a baseline for comparison of the samples grown on ALD- $\text{Al}_2\text{O}_3/\text{Si}$  substrates.

#### 7.1.1 Buffer Layers

MOCVD-grown GaN layers were first deposited on bare Si(111) substrates using a high-temperature AlN (HT-AlN) buffer layer to provide a baseline from which to work when growing on the  $\text{Al}_2\text{O}_3/\text{Si}$  substrates. The importance of AlN in GaN growth on Si has already been discussed, and the first step toward MOCVD growth in this work was to study

the AlN buffer layer quality and to determine favorable growth conditions for this layer. The growth temperature was fixed at  $\sim 1060$  °C, as temperature effects on AlN growth are well-studied. The V/III ratio, however, has a significant effect on AlN quality and is typically much lower than V/III ratios for GaN growth. The growth pressure was held at 50 torr, compared to the typical 200 torr for GaN growth. The decreased growth pressure is needed when growing AlN because of the increased probability of homogeneous reactions in the gas phase. The V/III ratio in this work was varied from 400 to 1200 to determine favorable conditions for high quality AlN growth. Figure 7.1 shows the dependence of the AlN (0002) rocking curve FWHM on V/III ratio for 100nm AlN layers on Si(111). Insufficient nitrogen is available at the growth surface at low V/III ratios, resulting in low-quality material. The material quality also degrades at higher V/III ratios. Based on XRD rocking curve scans of the AlN (0002) reflection, a V/III ratio of 824 was chosen for the work moving forward. Figure 7.2 shows SEM images of the structure at various times during growth and under various conditions. Figure 7.2(a) shows an SEM image of the 100 nm HT-AlN layer grown on Si(111) with a V/III ratio of 824. A smooth surface – suitable for GaN growth – is observed at a relatively high magnification of 20Kx.

GaN layers were first grown using the simple AlN buffer layer grown at  $\sim 1060$  °C as described above. A 40 nm-thick low-temperature GaN (LT-GaN) interlayer was inserted on the AlN layer in order to relieve strain and increase crystal quality in the GaN layer, similar to GaN growth on sapphire. However, the use of the LT-GaN interlayer led to poor crystal quality as observed by XRD, with a (0002) rocking curve linewidth of about 1200 arcsec. The linewidth of the near bandedge emission, however, was 37 meV, which is near the typical linewidth of  $\sim 30$  meV for GaN on sapphire. Figure 7.2(b) shows a plan-view image showing pits in the GaN surface. Figure 7.2(c) shows a cross-sectional SEM image in which

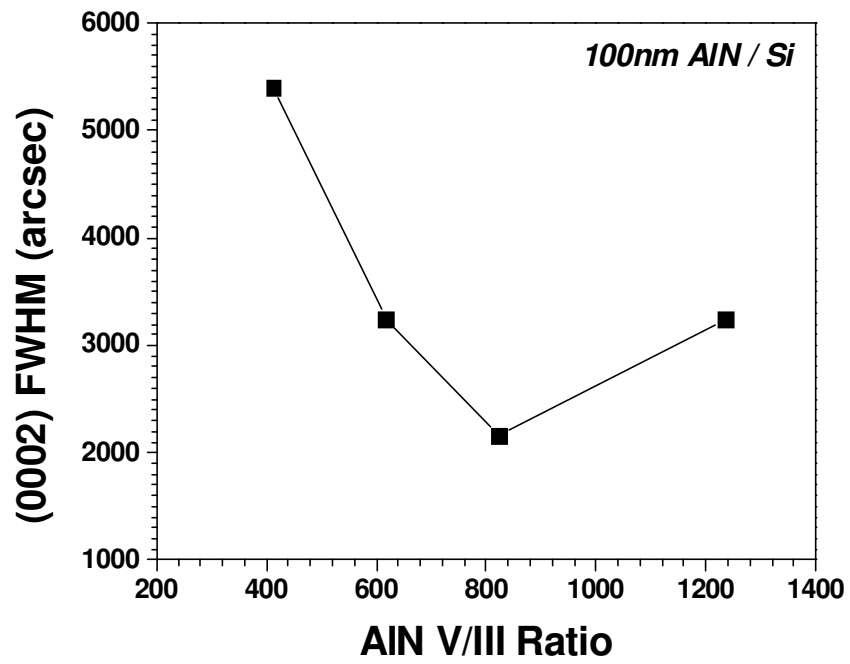
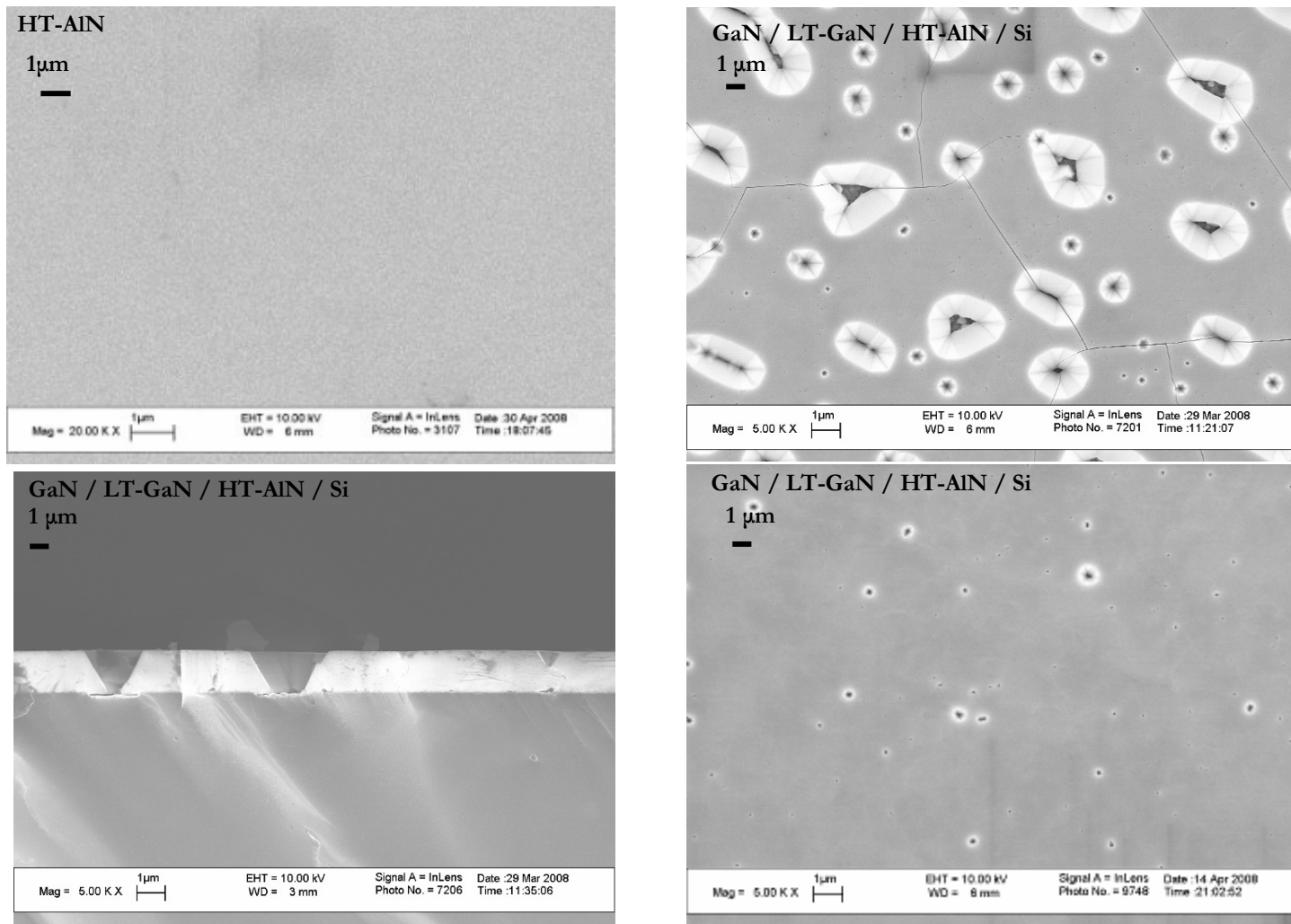


Figure 7.1: AIN (002) FWHM as a function of V/III ratio.



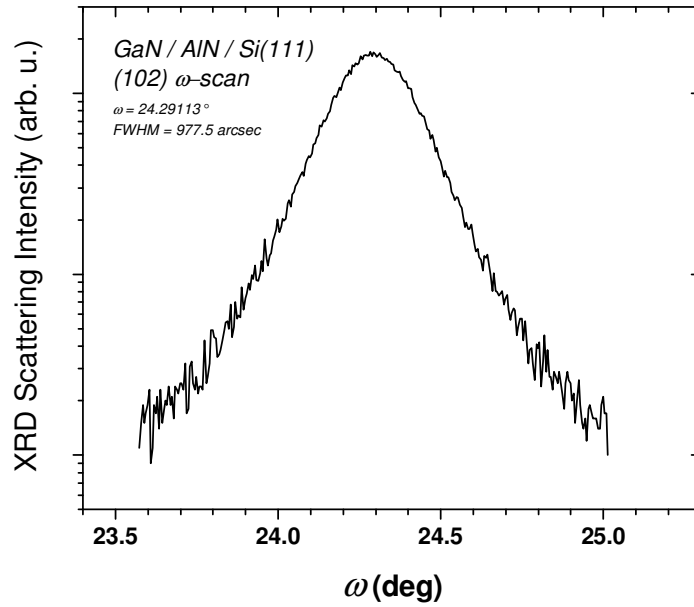
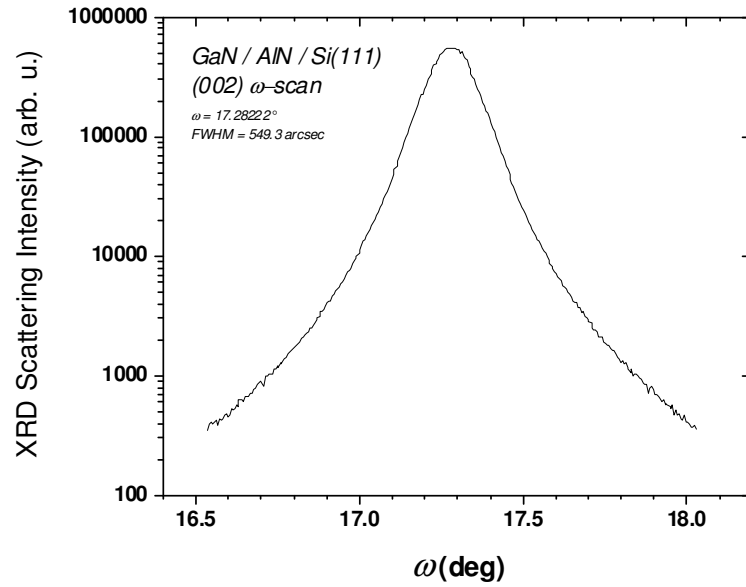
**Figure 7.2:** SEM images of GaN layers on Si using AlN buffer layers at various stages of growth.

these pits extend through the entire thickness of the GaN epilayer. The GaN surface is clearly unable to recover after 1 $\mu$ m of growth, and this may be due to the rough surface of the LT-GaN layer.

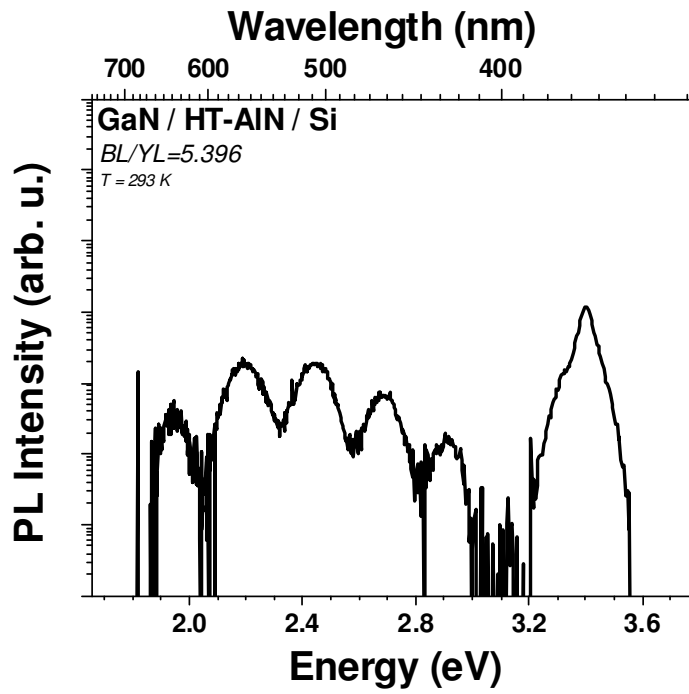
A second sample was grown using a thinner (25nm) LT-GaN layer on the AlN buffer layer, and Figure 7.2(d) shows an SEM image of the surface. It is clear that both the pit density and pit size are significantly reduced, though a few pits remain in the GaN surface. RT-PL also showed an improvement, with a decrease in linewidth to 30 meV, though XRD showed no improvement in structural quality compared to the sample with a 40nm LT-GaN layer. Also, both samples using LT-GaN interlayers exhibited cracking, suggesting that the use of the LT-GaN interlayer does not sufficiently alleviate tensile strain in the epilayer.

The next step was to remove the LT-GaN interlayer completely and grow a high temperature GaN layer directly on the HT-AlN buffer layer. Removal of the LT-GaN layer resulted in a marked increase in crystal quality. An XRD  $\omega$ -scan of the (002) reflection is shown in Figure 7.3(a) for a 1.5  $\mu$ m-thick GaN layer grown at high temperature directly on a HT-AlN buffer layer. Figure 7.3(b) shows a rocking curve scan of the GaN (102) reflection with a linewidth of 977.5 arcsec, suggesting that crystalline quality in the GaN layers on HT-AlN is significantly improved over the GaN layers using a LT-GaN nucleation layer.

RT-PL spectra of the GaN layers grown with a simple AlN buffer layer show a redshift in the bandedge luminescence, which is most likely due to tensile strain in the layers. Figure 7.4(a) shows a typical RT-PL spectrum taken from a GaN epilayer on Si. The linewidth of the bandedge emission is 54.8meV. The ratio of bandedge luminescence to yellow luminescence is also relatively low (BL/YL = 5.396) compared to GaN on sapphire, which may be an indication of a higher defect density in the layers on Si.



**Figure 7.3:** (a) GaN (002) rocking curve scan on HT-AlN/Si. (b) GaN (102) rocking curve scan on HT-AlN/Si.



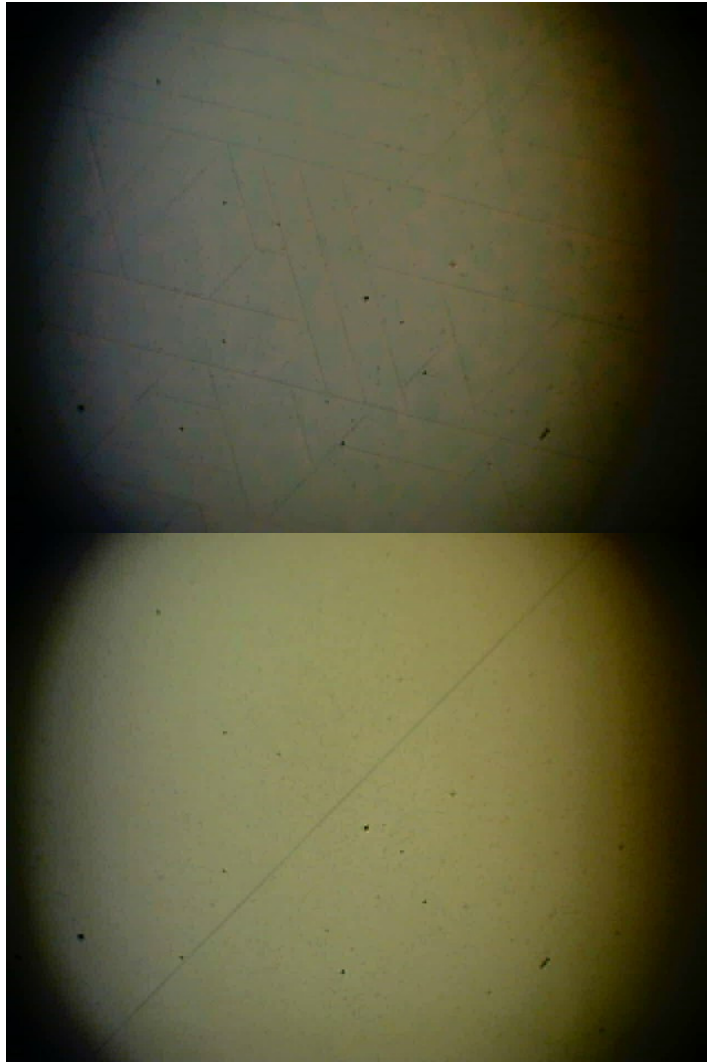
**Figure 7.4:** (a) RT-PL spectrum of a GaN layer on silicon with simple HT-AlN buffer layer. (b) AFM image of the a GaN layer on silicon with simple HT-AlN buffer layer.

Figure 7.4(b) shows an AFM image of the same layer with root mean square (RMS) surface roughness of 5.67 Å. While the RMS roughness of these layers is relatively smooth, the sponge-like surface morphology is an indication that the growth does not proceed in a step-flow-like manner. This morphology may also be due to polarity of the films. An Al seeding layer is used in the growth on Si before the AlN buffer layer, which may in turn lead to N-polar GaN. N-polar material is often reported to show a different (and rougher) surface morphology due to the higher density of dislocations terminating at the surface of the film.[128] Despite the good structural and optical quality of these layers, they remained cracked as a result of tensile strain.

### 7.1.2 Si-doped GaN Layers

All undoped GaN layers on bare Si exhibit cracks due to tensile strain induced by the thermal mismatch between GaN and silicon. Si, however, is an antisurfactant in GaN growth, and has been shown to relieve strain in GaN on sapphire.[129] For this reason, Si doping was also studied to determine its effect on strain and relaxation in GaN layers on Si substrates. Figure 7.5(a) shows a 20x optical microscope image of an undoped GaN layer on Si, while Figure 7.5(b) shows a 20x optical microscope image of a Si-doped GaN layer on Si. Si doping leads to a significant decrease in crack density of the GaN layers, as seen in the figure. This is due to the fact that Si acts as an antisurfactant, increasing surface tension and contributing to strain relaxation in the GaN layer.

RT-PL spectra, not shown here, showed a redshift in the near bandedge emission due to tensile strain in the layers. The silicon doping was unable to relieve the strain, and overall material quality as observed via XRD was poor, with very broad rocking curve linewidths for



**Figure 7.5:** (a) 20x optical microscope image of an undoped GaN layer on bare Si. (b) 20x optical microscope image of a Si-doped GaN layer on bare silicon.

the GaN (002) reflection. For this reason, silicon doping to relieve strain was not further investigated.

### 7.1.3 LT-AlN Interlayers

GaN layers were also grown on Si using LT-AlN interlayers, as has been reported elsewhere. [23,67] A relatively thin LT-AlN layer inserted into the GaN layer helps to relieve strain and increase crystal quality. GaN crystal quality should also increase with an increasing number of LT-AlN interlayers. In this work, three LT-AlN interlayers were used with a thickness of about 20 nm, essentially creating a GaN/AlN superlattice with GaN layers of about 100 nm. The LT-AlN interlayers increased crystal quality compared to the GaN layers grown using a simple AlN buffer layer.

#### *7.1.3.1 Structural Properties*

XRD scans of the (002) and (102) reflections of a GaN thin film grown on Si(111) using three HT-AlN interlayers are shown in Figures 7.6(a) and (b), respectively. The linewidth of the (002) reflection is 436.8 arcsec, which is a significant improvement over the GaN layers grown on bare silicon with a simple HT-AlN buffer layer. The linewidth of the (002) peak is related to the threading dislocation density in the film, and the decreased linewidth in the sample grown using multiple LT-AlN interlayers is an indication of a decrease in threading dislocation density [130]. The linewidth of the (102) reflection is related to edge dislocation density, and a reduction in edge dislocation density with the addition of LT-AlN interlayers (relative to the layers with a simple HT-AlN buffer layer) can be inferred from the decrease in the linewidth of the GaN (102) reflection as observed by XRD [99].

Raman spectroscopy was used to study the structural properties of the GaN layers more closely. The Raman spectrum of the sample grown using three LT-AlN interlayers is shown

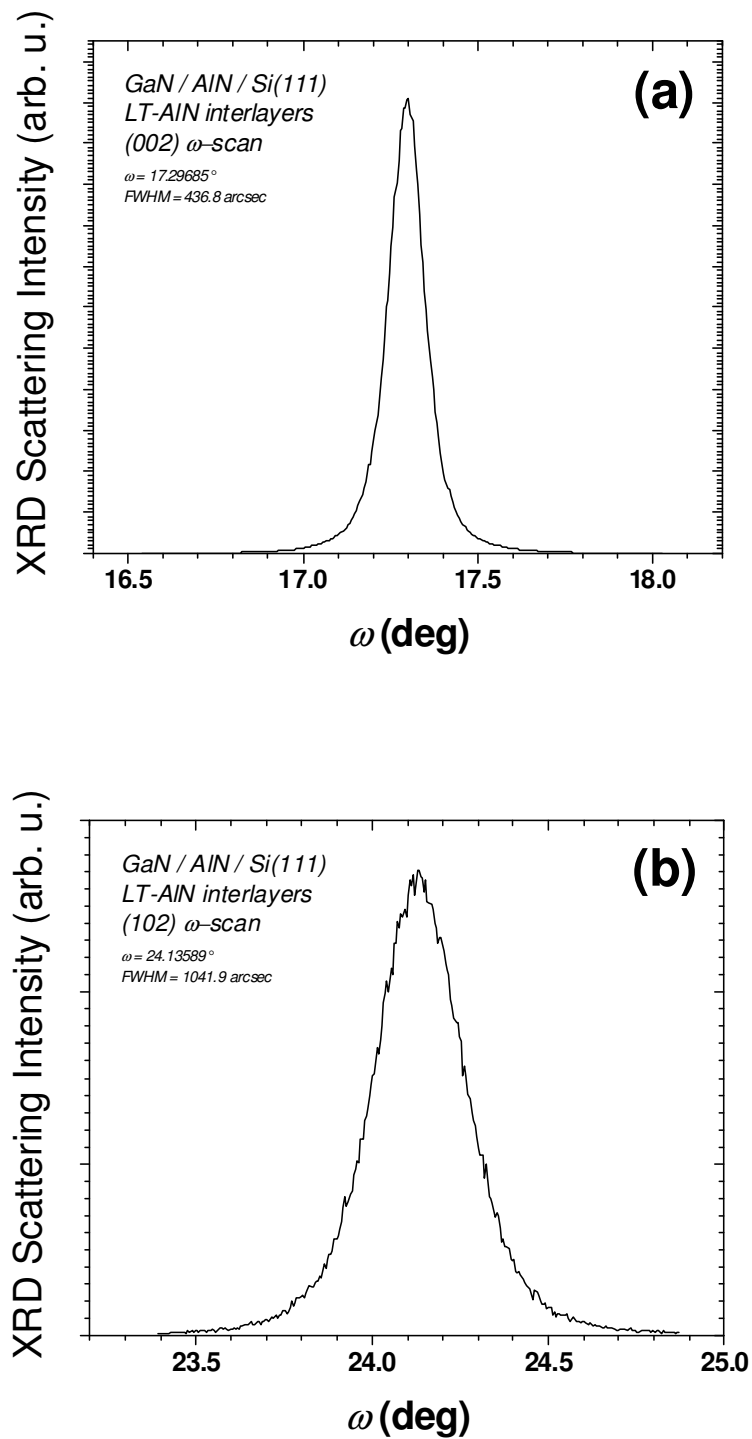


**Figure 7.6:** XRD scans of the (002) (a) and (102) (b) reflections of a GaN thin film grown on silicon using LT-AlN interlayers.

in Figure 7.7. The mode at  $520\text{ cm}^{-1}$  is related to the silicon substrate. The best indication of overall crystal quality is the GaN  $E_2(\text{high})$ , which is near  $566\text{ cm}^{-1}$  for this sample, compared to the unstrained position of  $567\text{ cm}^{-1}$ . The slight shift to lower wavenumbers is an indication of tensile strain in the layers, though this strain is slightly less than that in the GaN layers with a simple HT-AlN buffer layer. The linewidth of the  $E_2(\text{high})$  in this sample is  $5.5\text{ cm}^{-1}$ , which is also suggestive of good crystalline quality in the GaN layers using LT-AlN interlayers. The  $A_1(\text{LO})$  mode is near  $733\text{ cm}^{-1}$  and has a linewidth of  $8.0\text{ cm}^{-1}$ . The strong  $A_1(\text{LO})$  mode is an indication of a low free carrier concentration in the material, as free carriers coupling with this mode tend to decrease its intensity with increasing carrier concentration. [103]

The results from both XRD and Raman spectroscopy studies of samples on LT-AlN interlayers show an improvement in structural quality of the material over GaN films grown on silicon using a simple HT-AlN buffer layer, as expected. Further investigation was done to study both the optical properties and surface morphology of these samples in order to better understand the effects of the LT-AlN interlayers on the quality of the subsequent GaN layer.

### 7.1.3.2 Optical Properties

RT-PL measurements were performed to gain a better understanding of strain and electronic defects in the GaN layers. RT-PL spectra show a strong GaN bandedge with a linewidth of  $60.6\text{ meV}$ , though it is redshifted from the unstrained position of  $3.42\text{ eV}$ , Figure 7.8(a). The redshift is shown more clearly in 7.8(b), and is an indication of tensile strain in the epilayers. The linewidth of the near bandedge emission is also slightly broader than the expected linewidth from a GaN template on sapphire.

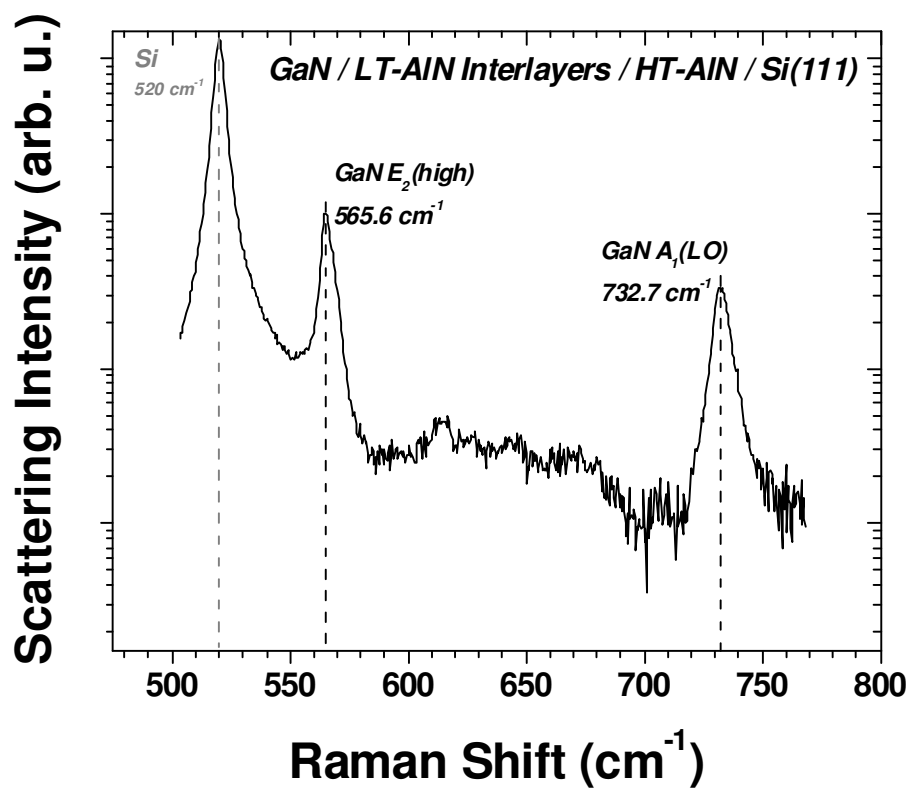


**Figure 7.7:** Raman spectrum of a GaN thin film grown on silicon using LT-AlN interlayers to relieve strain and increase crystal quality.

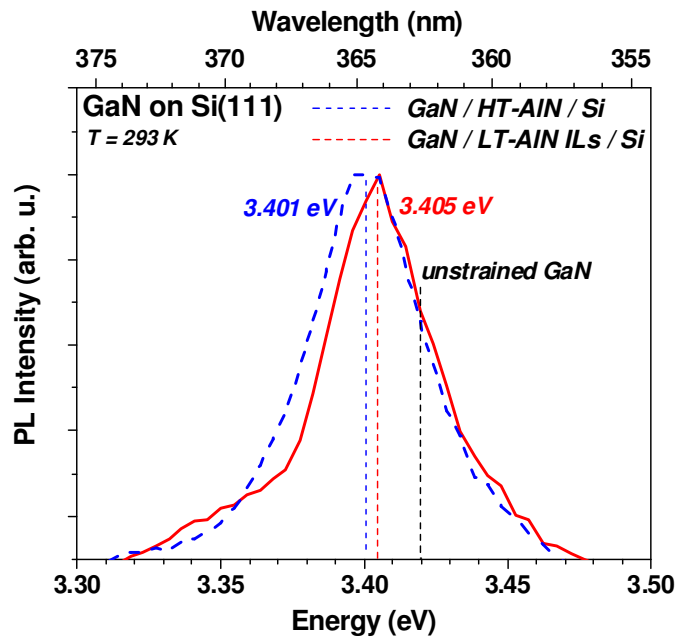
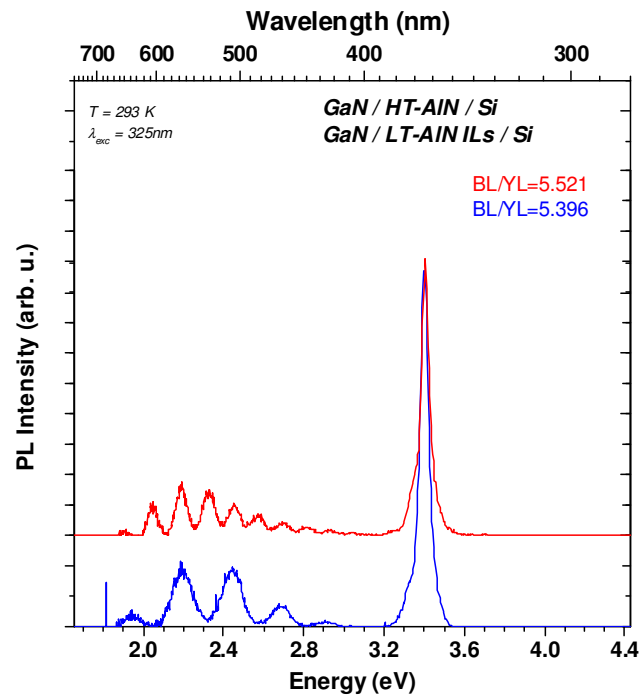


**Figure 7.8:** (a) RT-PL spectra of GaN layers on silicon using a simple HT-AlN buffer layer, and LT-AlN interlayers. (b) Normalized spectra showing the redshift from the unstrained band edge position.

The ratio of bandedge luminescence to yellow luminescence is  $\sim 5.5$ , which is lower than would be expected for GaN thin films on sapphire. The reason for this is not clear, as it may be due either to a decrease in bandedge intensity or to an increase in yellow luminescence.

The optical properties of this sample show an improvement over GaN on bare silicon. There is a need for further improvement, though, if similar quality to that of GaN on sapphire is to be achieved.

### 7.1.3.3 *Surface Morphology*

A clear change in surface morphology was observed via AFM with the inclusion of LT-AlN interlayers, Figure 7.9. Figure 7.9(a) shows a  $10\ \mu\text{m} \times 10\ \mu\text{m}$  AFM image of the surface of a  $2\ \mu\text{m}$  GaN template on sapphire. A clear step-flow pattern is observable on the surface, as is typical of GaN growth on sapphire. Figure 7.9(b) shows a  $10\ \mu\text{m} \times 10\ \mu\text{m}$  image of the surface of a GaN layer grown on bare silicon with a simple HT-AlN buffer layer. Note the clear change in surface morphology from the GaN template on sapphire. No step-flow pattern is visible, and there are a number of small pits in the surface, which are most likely related to threading dislocations terminating at the GaN surface. The RMS roughness of the layers also doubles from  $4.5\ \text{\AA}$  on sapphire to  $9.2\ \text{\AA}$  on silicon.

The inclusion of multiple LT-AlN interlayers, however, shows a significant improvement in both pit density – and therefore threading dislocation density – and in surface roughness, decreasing to  $\sim 4.0\ \text{\AA}$  in the GaN layer grown on multiple LT-AlN interlayers. Thus, the surface roughness of GaN grown using LT-AlN interlayers is more similar to that of GaN templates on sapphire. The surface morphology of the layer in Figure 7.9(c) also suggests that growth has shifted back toward a two-dimensional step-flow-like growth mode, more similar to GaN on sapphire. The shift in surface morphology, together with the improved

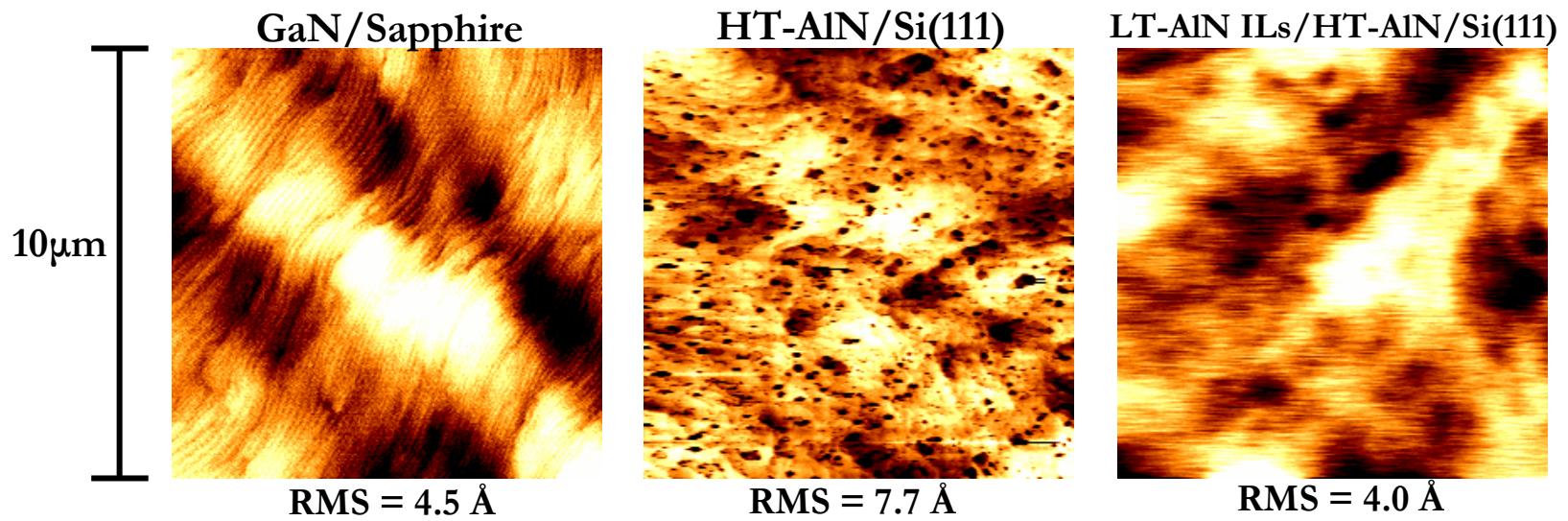


**Figure 7.9:** AFM images of a GaN template on sapphire (a), a GaN thin film on silicon with a simple HT-AlN buffer layer (b), and a GaN thin film on silicon using LT-AlN interlayers (c).

surface roughness of the sample on LT-AlN interlayers, suggests an overall increase in material quality. However, a few issues remain to be addressed, as the layers are still cracked, though the LT-AlN interlayers helped to suppress cracking. The addition of the LT-AlN interlayers also complicates and lengthens the growth process, somewhat negating the cost advantage of using silicon as a substrate.

#### 7.1.4 Progress and Remaining Issues

High quality GaN layers on bare Si are very important to gaining an understanding of GaN growth on  $\text{Al}_2\text{O}_3/\text{Si}$ . This work has developed an MOCVD process that will consistently yield high quality GaN epilayers on bare Si(111) substrates. Material quality still falls short of what is typically expected for GaN on sapphire. Table 7.1 summarizes the structural and optical properties of GaN layers grown on bare Si using both a simple AlN buffer layer and LT-AlN interlayers.

Two major issues remain to be solved if silicon substrates are to become a viable substrate option for GaN-based device technologies. The first is cracking. The layers remain cracked due to tensile strain induced in the epilayer by the thermal mismatch between GaN and Si.

The second issue to be resolved is the complication of the growth process by introducing multiple interlayers and complex buffer layer structures. This leads to both higher consumption rates of metalorganic precursors in each run and longer growth times, both of which increase the cost of production, offsetting the cost advantage of silicon substrates. In this work, the use of the LT-AlN interlayers to relieve strain and improve material quality led to a 40% increase in TMGa consumption and a 39% increase in TMAI consumption. The slower growth rates for AlN and the need to adjust temperatures

Table 7.1: Material properties obtained on bare silicon by MOCVD.

	XRD		PL		AFM
	(002) FWHM (arcsec)	(102) FWHM (arcsec)	FWHM (meV)	BL/YL	RMS roughness (Å)
<b>HT-AlN buffer</b>	<b>549.3</b>	<b>977.5</b>	<b>49.3</b>	<b>5.396</b>	<b>5.67</b>
<b>LT-AlN interlayers</b>	<b>436.8</b>	<b>1041.9</b>	<b>46.9</b>	<b>5.521</b>	<b>3.99</b>

between LT-AlN interlayers and subsequent GaN layers also led to a 56% increase in growth time over the process using a simple HT-AlN buffer layer. Despite the increase in material quality, the longer and more complicated process is more expensive, negating the cost advantage of silicon. Device-quality material on silicon must be attained without adding additional cost from a longer and more complicated growth process in order to take full advantage of the cost and availability of large-area silicon substrates.

ALD-grown  $\text{Al}_2\text{O}_3$  layers have been introduced for this reason. The use of the ALD layer will simplify the growth process while also allowing for the growth of device-quality GaN on silicon. While growth parameters for high quality GaN on  $\text{Al}_2\text{O}_3/\text{Si}$  may deviate from those used for GaN on bare Si, the process development done in this section is crucial to gaining a clear understanding of the growth process of GaN on  $\text{Al}_2\text{O}_3/\text{Si}$ .

## **7.2 MOCVD GROWTH OF GAN ON ALD- $\text{Al}_2\text{O}_3$ /SILICON**

An ALD-grown  $\text{Al}_2\text{O}_3$  interlayer was inserted between the buffer layer and the substrate in order to help relieve strain in the GaN layer while simplifying the growth process at the same time. This section discusses the addition of an  $\text{Al}_2\text{O}_3$  interlayer to the silicon substrate, and its effects on the growth process. The process for GaN on bare Si was used as a starting point for this development.

### 7.2.1 Fundamental Growth Parameters

GaN layers were grown on  $\text{Al}_2\text{O}_3/\text{Si}$  substrates after the development of a GaN growth process on bare Si. The first step taken in this work was the investigation of fundamental growth parameters and structures to lay a foundation for future work. Both LT-GaN and HT-AlN were investigated as buffer layers on the  $\text{Al}_2\text{O}_3/\text{Si}$  substrate.

### 7.2.1.1 Carrier Gas

Effects of carrier gas on nitride layer growth were studied using both LT-GaN and HT-AlN buffer layers. Pure H<sub>2</sub> and pure N<sub>2</sub> were used as carrier gases, and carrier gas effects were further studied using an H<sub>2</sub>/N<sub>2</sub> mixture. Figure 7.10 shows the dependence of GaN (0002) FWHM as observed by XRD  $\omega$ -scans on the ratio of hydrogen to nitrogen in the carrier gas,  $\frac{H_2}{H_2 + N_2}$ . These growths were completed on bare Si substrates and 20 nm as-grown Al<sub>2</sub>O<sub>3</sub>/Si substrates simultaneously, with the carrier gas ratio varying only in the topmost GaN layer. Hydrogen was used in the HT-AlN buffer layers and in the initial stages of GaN growth. The trends for XRD linewidth on bare Si and Al<sub>2</sub>O<sub>3</sub>/Si are opposite, with structural quality decreasing on bare Si and increasing on Al<sub>2</sub>O<sub>3</sub>/Si with increasing H<sub>2</sub> percentage in the carrier gas.

### 7.2.1.2 Temperature Ramp Time

The use of the HT-AlN buffer layers on Al<sub>2</sub>O<sub>3</sub>, however, introduces another issue that stems from the fact that the AlN layer is grown at a very high temperature (~1060 °C). Both the AlN growth temperature and ramp time affect the Al<sub>2</sub>O<sub>3</sub> surface prior to growth. The AlN growth temperature is set from previous work, leaving the ramp time as the parameter to be varied. When the temperature ramp time is too short (e.g., 10 min.), the Al<sub>2</sub>O<sub>3</sub> surface roughens, degrading the surface of the subsequent GaN layer. An increase in temperature ramp time to 13 minutes, however, allows for a smoother GaN surface during growth.

### 7.2.1.3 Buffer Layer

GaN growth on sapphire typically proceeds with the growth of a thin (20-30 nm) LT-GaN buffer layer before the high quality GaN layer, while growth on Si usually proceeds with a HT-AlN buffer layer ranging from 50 nm to 200 nm in thickness.[51,61] Both

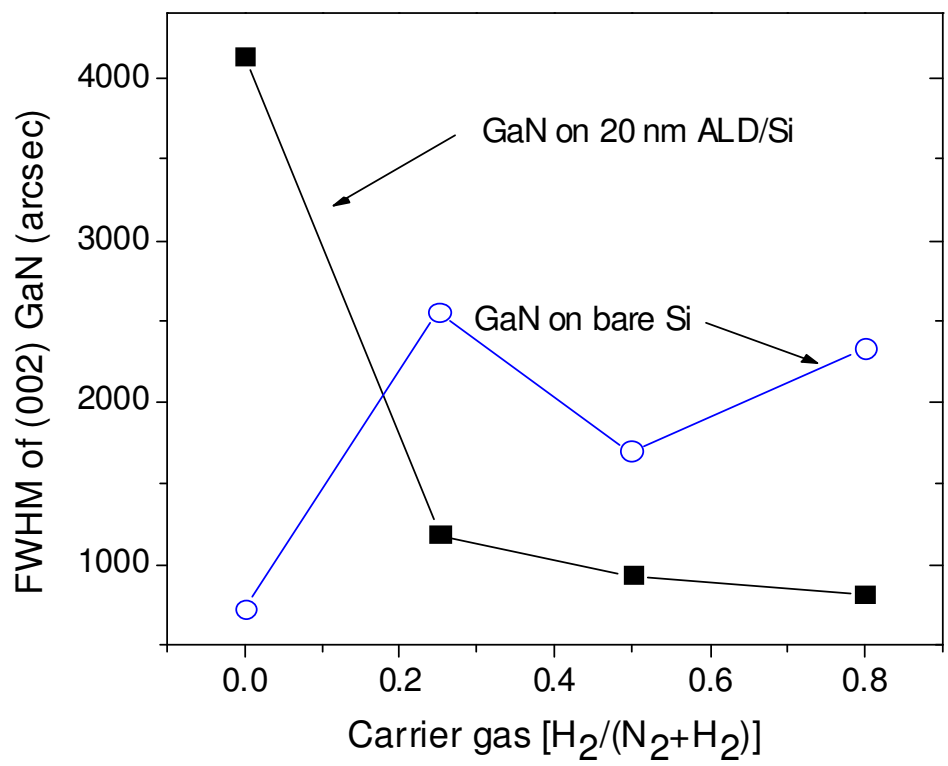


**Figure 7.10:** Dependence of the GaN (002) FWHM on carrier gas ratio for GaN thin films on both silicon and ALD- $Al_2O_3/Si(111)$  substrates.

approaches were investigated here, with a HT-GaN layer grown under the same conditions on all buffer layers.

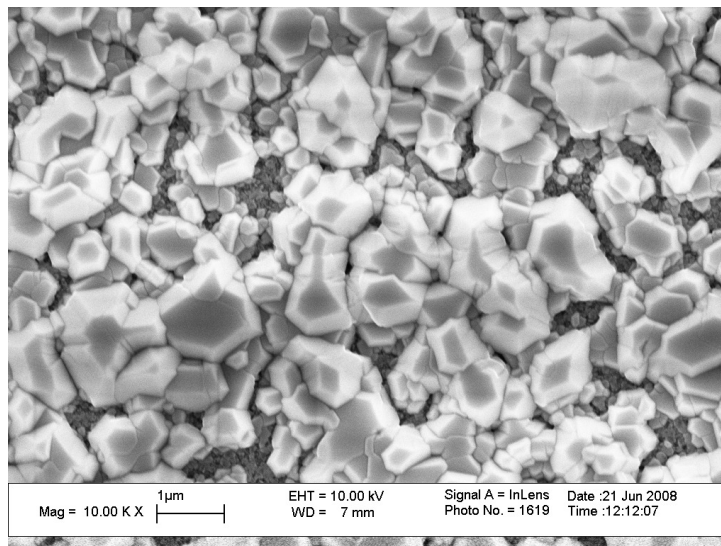
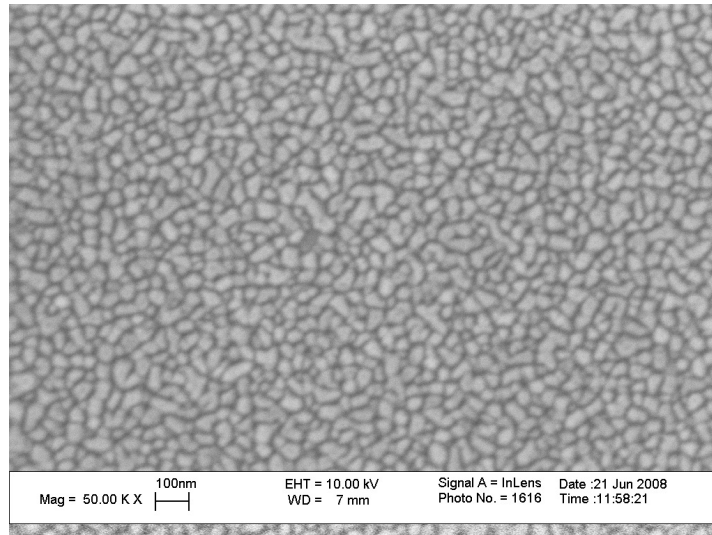
The LT-GaN buffer layers were deposited at 745 °C with a nominal thickness of 25-30 nm, while the HT-AlN buffer layers were deposited at a growth temperature of 1060 °C and thickness of 100 nm. Both annealed and unannealed Al<sub>2</sub>O<sub>3</sub>/Si substrates were used in this study, and the samples grown with the HT-AlN layer consistently yielded higher quality material, as observed by XRD and RT-PL. Table 7.2 shows results of XRD rocking curve scans on GaN layers grown on both LT-GaN buffer layers and HT-AlN buffer layers on Al<sub>2</sub>O<sub>3</sub>/Si.

The layer on HT-AlN is also much smoother than the layer on LT-GaN. The thickness of the LT-GaN layer is similar to that of LT-GaN buffer layers used on sapphire. However, the polycrystalline nature of the Al<sub>2</sub>O<sub>3</sub> film on Si leads to a much rougher surface on the GaN buffer layer. Figure 7.11 shows SEM images of both a LT-GaN buffer layer and a HT-AlN buffer layer on 10 nm Al<sub>2</sub>O<sub>3</sub> annealed at 1100 °C for 90 seconds. The HT-AlN buffer layer is much smoother than the LT-GaN layer. This rough surface also affects the growth rate of the GaN layers grown on LT-GaN buffers. The growth rate was significantly slower on LT-GaN buffers than on HT-AlN buffer layers due to surface roughening. This surface roughening most likely decreases mobility of the Ga and N adatoms on the growth surface, leading to a slower growth rate.

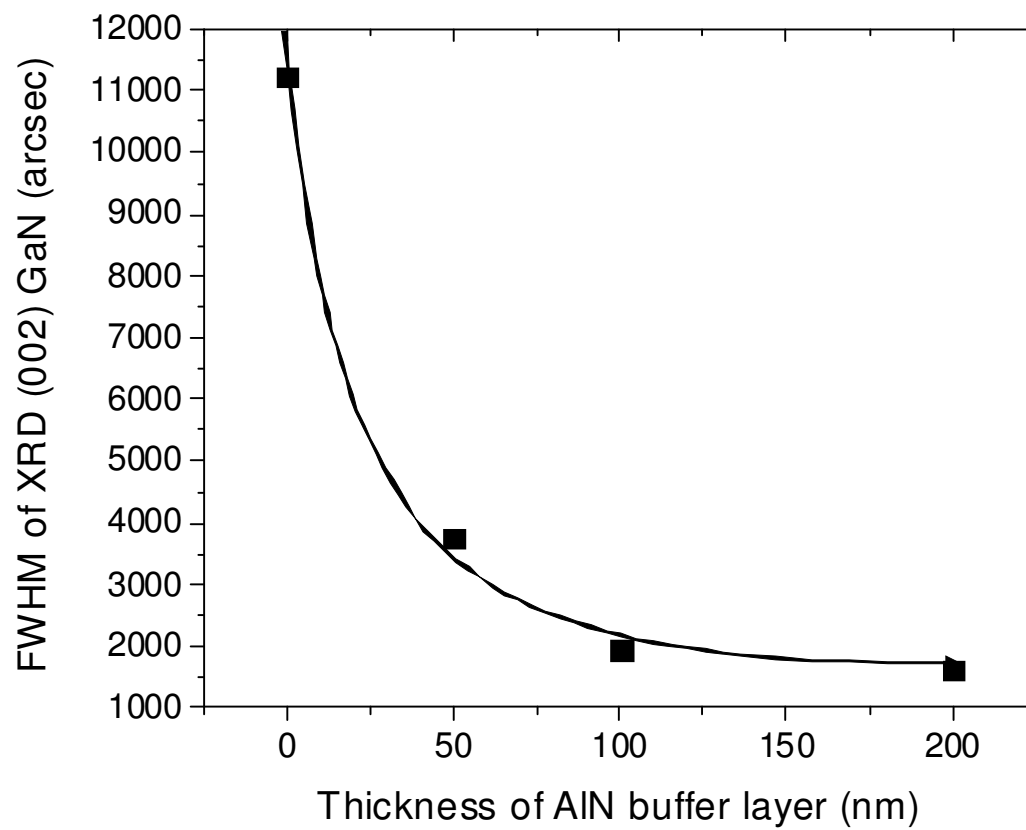
HT-AlN buffer layers were investigated further because of the smoother surface and higher growth rate of the subsequent GaN layer. The effect of AlN thickness on structural quality of the GaN layer was studied. Figure 7.12 shows the FWHM of the GaN (0002)  $\omega$ -scan as it depends on AlN thickness. The structural quality of the topmost GaN layer, as observed by XRD, increased with increasing AlN thickness. However, above a thickness of

Table 7.2: Dependence of the GaN (002) FWHM on carrier gas ratio for GaN thin films on both silicon and ALD-Al<sub>2</sub>O<sub>3</sub>/Si(111) substrates.

Al <sub>2</sub> O <sub>3</sub> /Si Thickness (nm)	Annealing Conditions	Buffer Layer	GaN (0002) $\omega$ -scan FWHM (arcsec)
10	1100 °C, 90 sec	LT-GaN	14724
10	N/A	LT-GaN	14724
10	1100 °C, 90 sec	HT-AlN	3672
10	N/A	HT-AlN	4420



**Figure 7.11:** (a) SEM image of a HT-AlN buffer surface on Si(111). (b) SEM image of a LT-GaN buffer layer on Si(111).



**Figure 7.12:** Dependence of the GaN (002) linewidth on AlN thickness.

100 nm, there was only a small decrease in (0002) FWHM. 100 nm AlN buffer layers were used in subsequent studies for this reason.

### 7.2.2 $\text{Al}_x\text{Ga}_{1-x}\text{N}/\text{GaN}$ Superlattices on ALD- $\text{Al}_2\text{O}_3/\text{Silicon}$

$\text{Al}_x\text{Ga}_{1-x}\text{N}$  layers with different Al composition have also been investigated to grow high quality GaN on Si.[53,70] Multiple  $\text{Al}_x\text{Ga}_{1-x}\text{N}$  layers were grown on both bare Si and 10 nm  $\text{Al}_2\text{O}_3/\text{Si}$  to act as transition layers for the final GaN layer. Each  $\text{Al}_x\text{Ga}_{1-x}\text{N}$  layer was 100 nm, with the temperature for each layer being slightly less than the previous layer. XRD results for the samples are shown in Figure 7.13(a) and (b). Clear  $\text{Al}_x\text{Ga}_{1-x}\text{N}$ -related peaks are observed from the structure on bare Si, one peak from each layer. Peaks from the AlN buffer layer and the topmost GaN layer can also be seen. The structure on 10 nm  $\text{Al}_2\text{O}_3/\text{Si}$  also showed the  $\text{Al}_x\text{Ga}_{1-x}\text{N}$  peaks, though they were much weaker and broader, encompassing all three potential peaks into one. The GaN FWHM on the bare Si structure was 2088 arcsec, while the FWHM on the 10 nm  $\text{Al}_2\text{O}_3/\text{Si}$  structure was 5940 arcsec.

A second growth was done with only two  $\text{Al}_x\text{Ga}_{1-x}\text{N}$  layers. The structure for this growth was the same as that of the previous study except that the third  $\text{Al}_x\text{Ga}_{1-x}\text{N}$  layer was removed. XRD results, Figures 7.13(c) and (d), show peaks from both  $\text{Al}_x\text{Ga}_{1-x}\text{N}$  layers, and these peaks are visible in the structures on both bare Si and 10 nm  $\text{Al}_2\text{O}_3/\text{Si}$ , respectively. XRD results show that the material quality in the samples with two  $\text{Al}_x\text{Ga}_{1-x}\text{N}$  layers improved compared to the growth with three  $\text{Al}_x\text{Ga}_{1-x}\text{N}$  interlayers. The XRD linewidth of the GaN layer on bare Si was 1944 arcsec, while the FWHM on the 10nm  $\text{Al}_2\text{O}_3/\text{Si}$  was 3420 arcsec.

RT-PL spectra of all samples grown with graded  $\text{Al}_x\text{Ga}_{1-x}\text{N}$  layers showed very weak near bandedge emission, however. The reason for the poor bandedge luminescence is unclear,

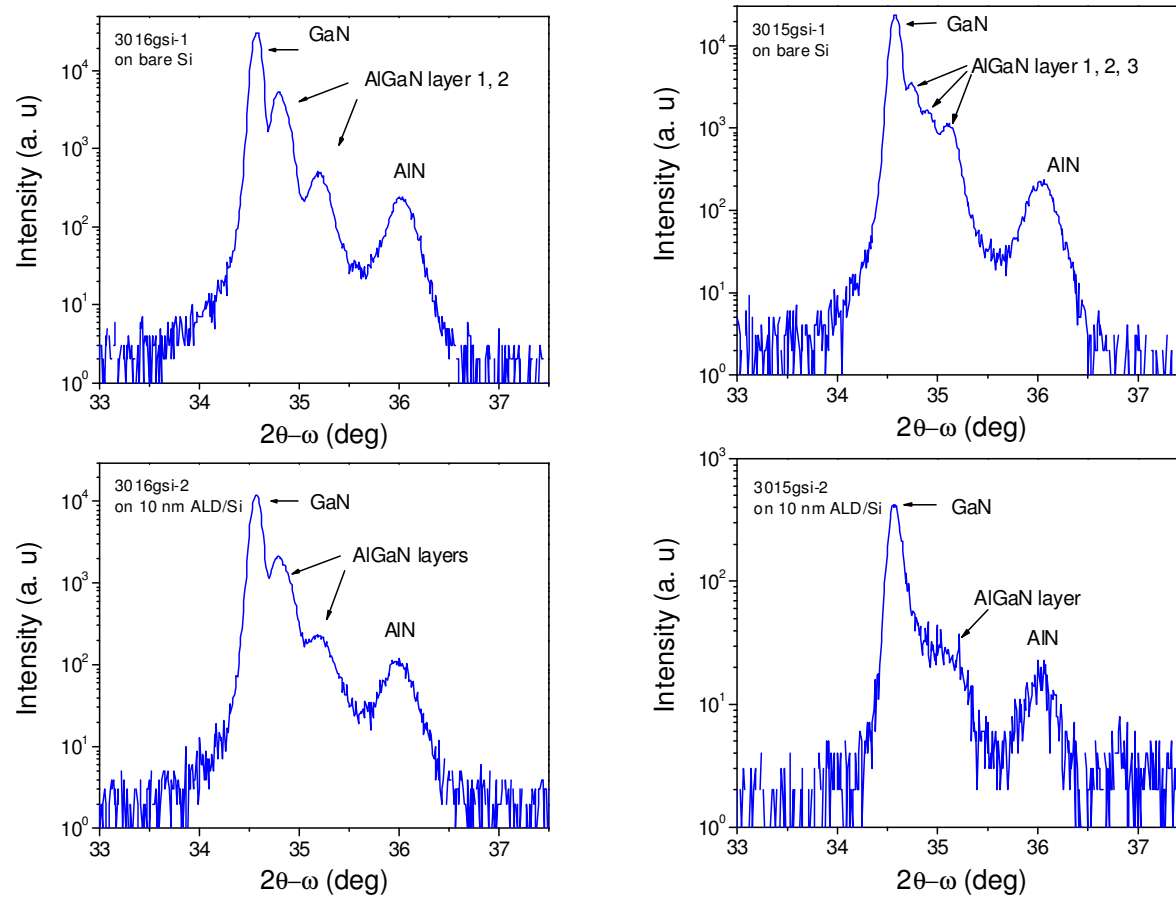


**Figure 7.13:** (a) XRD  $2\theta$ - $\omega$  scan of GaN on bare silicon using two AlGaN layers. (b) Same structure as (a), on ALD- $\text{Al}_2\text{O}_3$ /Si. (c) XRD  $2\theta$ - $\omega$  scan of GaN on bare silicon using three AlGaN layers. (d) Same structure as (c), on ALD- $\text{Al}_2\text{O}_3$ /Si.

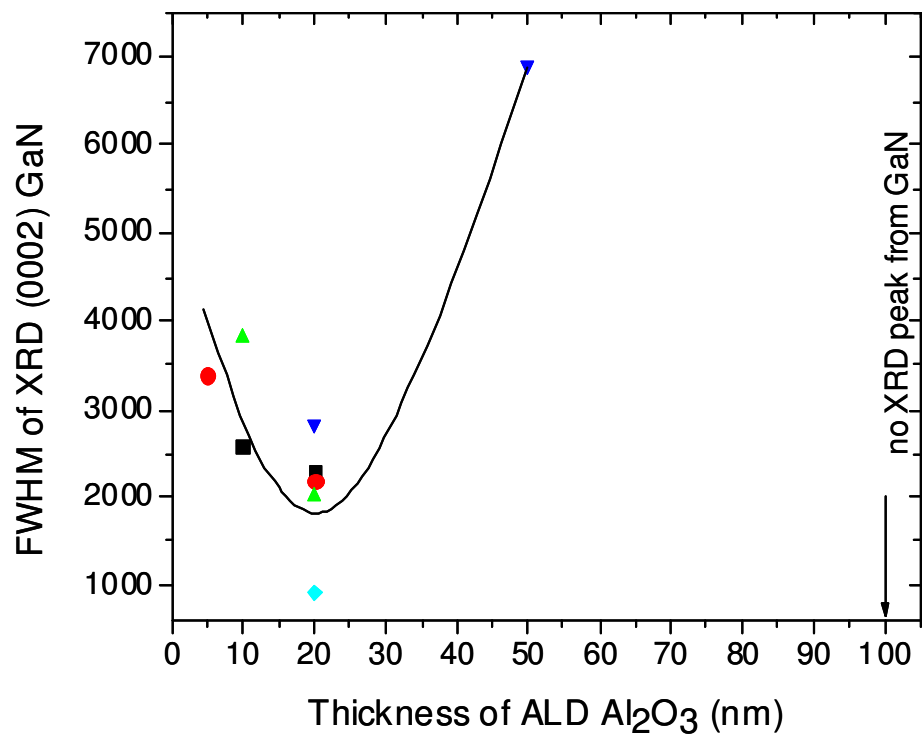
but the wide XRD linewidths and the poor luminescence from these samples suggests that  $\text{Al}_x\text{Ga}_{1-x}\text{N}$  layers are not a suitable approach for GaN on ALD- $\text{Al}_2\text{O}_3/\text{Si}$ . This approach was not investigated further because of the poor quality of initial GaN films compared to other approaches.

### 7.2.3 Effects of the ALD- $\text{Al}_2\text{O}_3$ layer on Silicon

The effects of the underlying  $\text{Al}_2\text{O}_3$  layer were studied after initial work was done to determine favorable growth conditions for GaN on  $\text{Al}_2\text{O}_3/\text{Si}$ . The effects of  $\text{Al}_2\text{O}_3$  thickness on the subsequent GaN layer were investigated first. The thickness of the  $\text{Al}_2\text{O}_3$  layers was varied from 5 nm to 100 nm, and identical GaN layers were grown on each  $\text{Al}_2\text{O}_3/\text{Si}$  substrate.

#### 7.2.3.1 *Structural Properties*

Linewidth of the XRD (002)  $\omega$ -scans are shown in Figure 7.14 as a function of  $\text{Al}_2\text{O}_3$  thickness. Quality for the layers grown on 5 nm and 10 nm  $\text{Al}_2\text{O}_3$  is similar, but increases somewhat for the sample grown on 20 nm  $\text{Al}_2\text{O}_3$ . After 20 nm, however, the crystal quality of the GaN layer decreases significantly. This is most likely due to the changes in surface morphology that were observed in the ex-situ annealing studies of the  $\text{Al}_2\text{O}_3/\text{Si}$  samples. Pit formation in the thicker ALD- $\text{Al}_2\text{O}_3$  layers may lead to nucleation on the bare silicon substrate in addition to the nucleation on the oxide interlayer, thus decreasing overall crystal quality and producing a poor surface morphology for layers grown on  $\text{Al}_2\text{O}_3$  interlayers with a thickness greater than  $\sim 20$  nm. Thicker  $\text{Al}_2\text{O}_3$  layers were not studied in further detail for this reason. However, the trends observed for the thinner samples were investigated further to determine the effects of the  $\text{Al}_2\text{O}_3$  layer thickness on the crystal structure of the subsequent GaN layer.



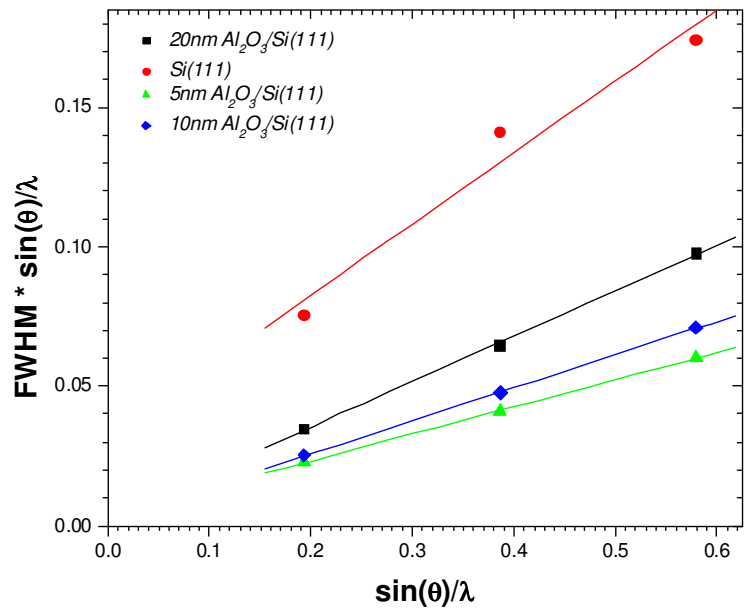
**Figure 7.14:** Dependence of the GaN (002) linewidth on ALD-Al<sub>2</sub>O<sub>3</sub> thickness.

Figure 7.15 shows a Williamson-Hall plot taken from XRD data of a GaN layer on bare Si compared to GaN layers on 5 nm, 10 nm, and 20 nm Al<sub>2</sub>O<sub>3</sub>/Si substrates. The plot was calculated using XRD rocking curve data of the GaN (002), (004), and (006) reflections that were taken with the triple-axis detector on the XRD system. The decrease in slope with the addition of the ALD-Al<sub>2</sub>O<sub>3</sub> layer is a clear indication of an increase in overall crystal quality. A linear fit to the data points for each reflection yields the lines shown in the figure.

The lateral coherence length is an important parameter that can be extracted from the W-H plot. The lateral coherence length is related to the y-intercept of the fitted line in the W-H plot, and it describes the average lateral dimension of crystalline domains, or grains, in the GaN layer. The lateral coherence length of the GaN films was calculated from the plot in Figure 7.15 using the following relationship:

$$L_{||} = \frac{0.9}{2Y_0} \quad (3.19)$$

Tilt angle is another important structural parameter that can be calculated from the Williamson-Hall plot in Figure 7.15. Tilt angle is related to the slope of the fitted line, and it describes the average grain tilt with respect to the c-axis. The tilt angle, in arcseconds, is equal to the slope of the fitted line. Both the tilt angle and the lateral coherence length are shown in Figure 7.16 as they vary with ALD-Al<sub>2</sub>O<sub>3</sub> thickness. The sample grown on bare silicon, which corresponds to an Al<sub>2</sub>O<sub>3</sub> thickness of zero, exhibits a very high tilt angle, nearly 1000 arcsec. This high tilt angle is also coupled with a very low lateral coherence length of ~100 nm. The addition of the oxide interlayer leads to a noticeable increase in lateral coherence length and a corresponding decrease in tilt angle. The increase in lateral coherence length is suggestive of a decrease in threading dislocation density.



**Figure 7.15:** Williamson-Hall plot of the (002), (004), and (006) reflections of GaN thin films on bare silicon and ALD- $\text{Al}_2\text{O}_3/\text{Si}$ .

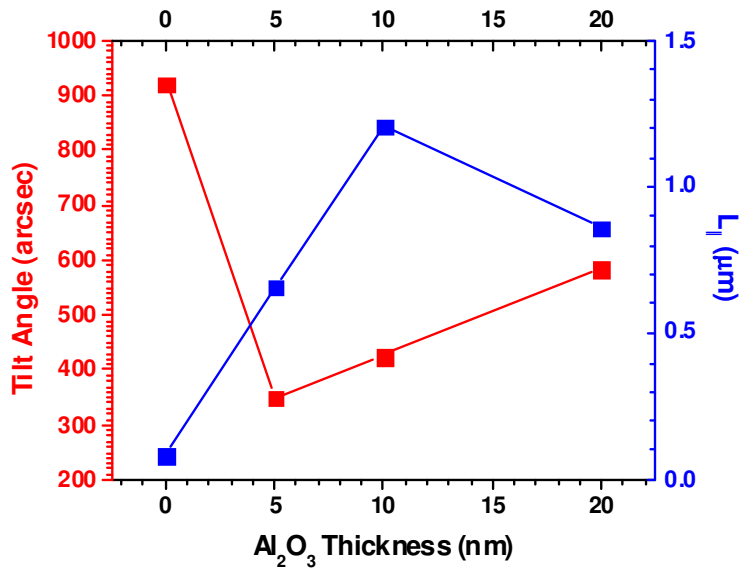


**Figure 7.16:** Lateral coherence length and tilt angle for GaN thin films as a function of  $\text{Al}_2\text{O}_3$  thickness.

The threading dislocation density of the GaN thin films was calculated from the Williamson-Hall plot using the following relationship:

$$N_{screw} = \frac{\alpha^2}{4.35 \cdot |b_c|^2} \quad (3.20)$$

In this equation,  $\alpha$  is the tilt angle and  $b_c$  is the burgers vector for threading dislocations in GaN ( $b_c = 5.185 \text{ \AA}$ ). The calculated screw dislocation densities are shown as a function of ALD- $\text{Al}_2\text{O}_3$  thickness in Figure 7.17. The addition of the ALD- $\text{Al}_2\text{O}_3$  interlayer leads to a reduction in threading dislocation density by an order of magnitude. The screw dislocation densities for the GaN thin films on ALD- $\text{Al}_2\text{O}_3/\text{Si}$  are in the range of typical values reported for MOCVD-grown GaN on sapphire.[99] The rocking curve linewidth of the GaN (102) reflection, however, suggests that the edge dislocation density remains slightly higher than that of typical GaN thin films on sapphire.

Raman spectroscopy was used to study the structural properties of the thin films in more detail. Unpolarized Raman spectra are shown in Figure 7.18 for 1.5  $\mu\text{m}$  GaN layers grown on silicon using a HT-AlN buffer layer, LT-AlN interlayers, and ALD- $\text{Al}_2\text{O}_3$  interlayers of various thickness. The main features in the Raman spectra are the  $E_2(\text{high})$  near  $565 \text{ cm}^{-1}$  and the  $A_1(\text{LO})$  near  $735 \text{ cm}^{-1}$ . The strong  $A_1(\text{LO})$  mode is an indication of low carrier concentration, as free carriers coupling with this phonon mode tend to decrease intensity and broaden the peak, suppressing it almost entirely at high carrier concentrations. [103] The linewidth of the  $E_2(\text{high})$  indicates good crystalline quality. The  $E_2(\text{high})$  mode is also the clearest indicator of strain in wurtzite materials.[103] A shift in the  $E_2$  mode to lower wavenumbers is indicative of tensile strain in the material. The unstrained position of the  $E_2(\text{mode})$  is near  $567 \text{ cm}^{-1}$ , and in MOCVD-grown GaN on sapphire it is shifted to slightly higher wavenumbers due to compressive strain induced by the sapphire

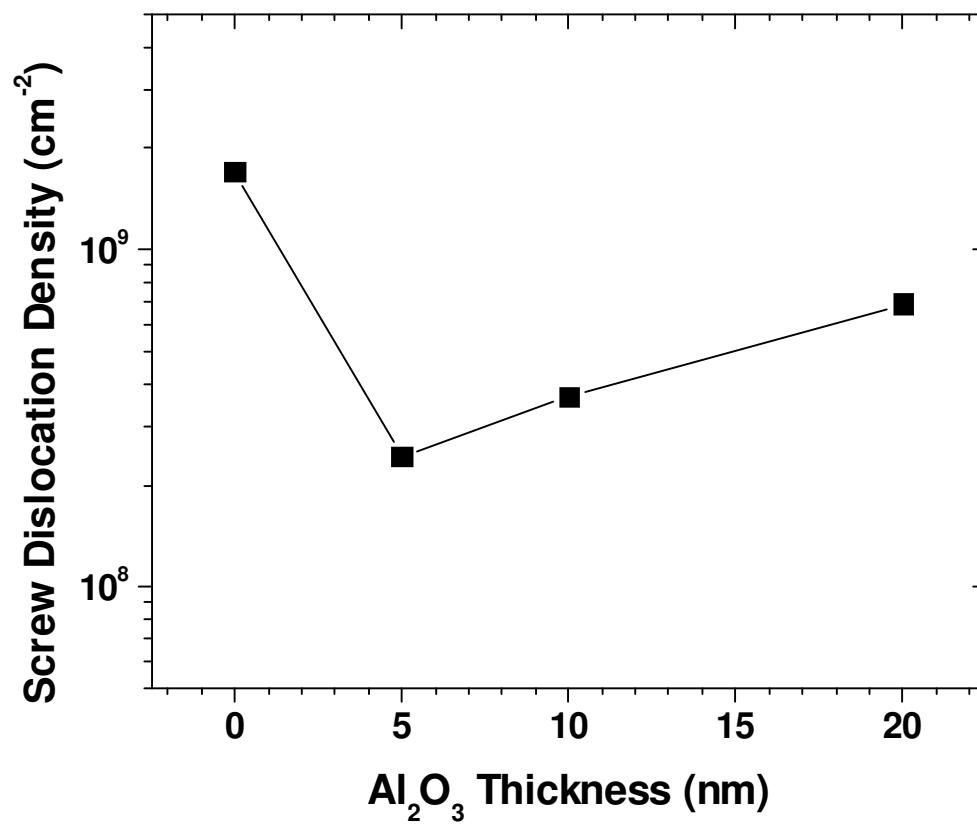


**Figure 7.17:** Calculated screw dislocation density as a function of ALD-Al<sub>2</sub>O<sub>3</sub> thickness.

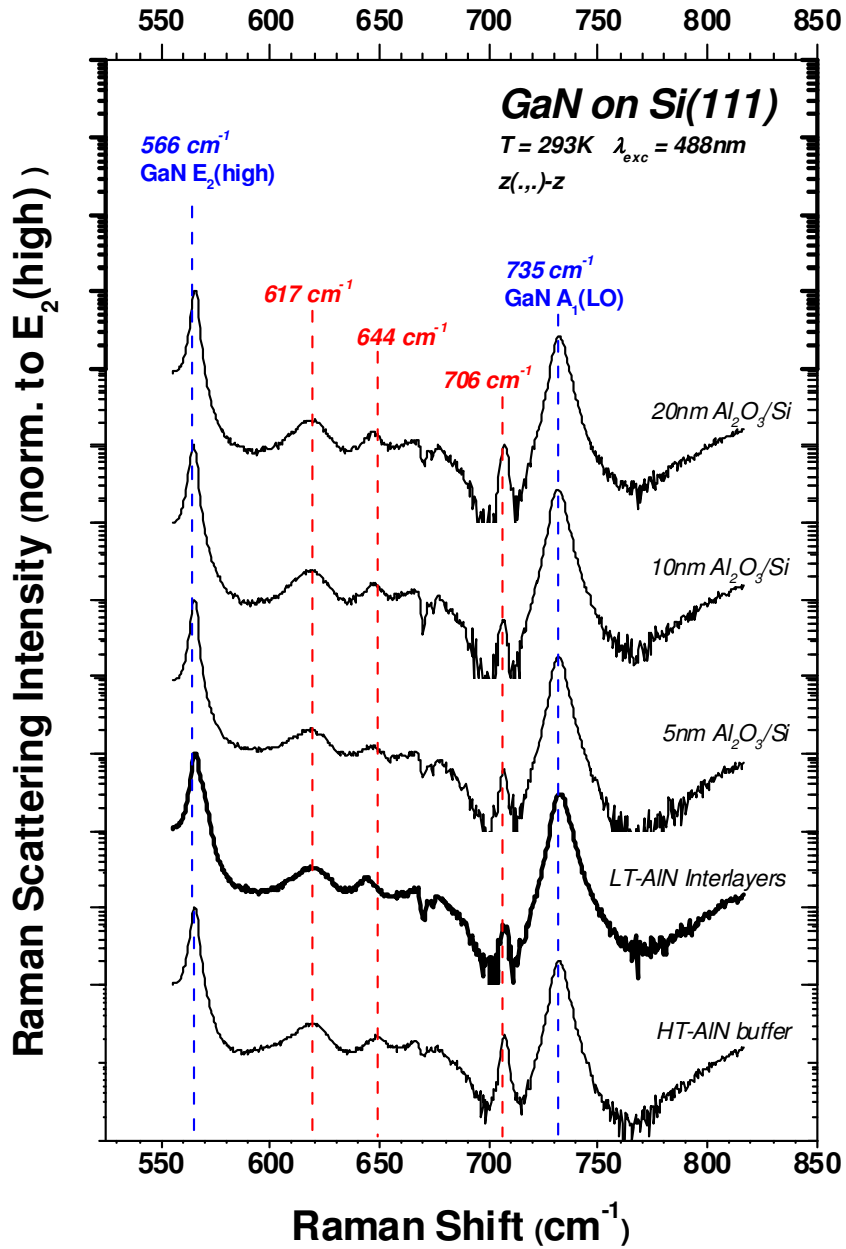


**Figure 7.18:** Unpolarized Raman spectra of GaN thin films grown on silicon using various buffer layers and interlayers.

substrate. [104] Figure 7.19 shows the shift of the  $E_2$  mode as a function of oxide interlayer thickness. A clear trend is observed in which the thin oxide interlayers actually lead to an increase in strain, and then this strain begins to relax with thicker oxide interlayers. This is consistent with the calculations of dislocation density that showed an increase in threading dislocation density with increasing oxide interlayer thickness. Thus, relaxation of the GaN thin film with increasing oxide thickness most likely leads to an increase in threading dislocation density.

Three unidentified peaks are also visible in the Raman spectra near  $617\text{ cm}^{-1}$ ,  $647\text{ cm}^{-1}$ , and  $707\text{ cm}^{-1}$ . These peaks are not typical of high-quality silicon, and their presence in the samples grown on bare silicon with a HT-AlN interlayer and with LT-AlN interlayers suggests that they are not related to the ALD- $\text{Al}_2\text{O}_3$  layer. The intensity of these three peaks, normalized to the intensity of the  $E_2(\text{high})$ , was plotted versus  $\text{Al}_2\text{O}_3$  thickness in Figure 7.20. The addition of the oxide interlayer significantly reduces the intensity of the peaks near  $617\text{ cm}^{-1}$  and  $647\text{ cm}^{-1}$ . The trends in intensity of these two peaks follow the trend of threading dislocation density very closely, and suggest that these two peaks are disorder-order induced Raman modes, though disorder-related peaks in this region have not previously been reported in GaN.

The narrow linewidth of the peak near  $707\text{ cm}^{-1}$ , however, coupled with the different trend in intensity, suggests that this is not a disorder-related mode. In addition, its presence in the layers grown on bare silicon both with and without LT-AlN interlayers suggests that it is not related to the ALD- $\text{Al}_2\text{O}_3$  layer. This mode has not been previously reported in the literature and it is assigned as local vibrational mode in GaN, though the exact origin of this local vibrational mode remains unclear at this time.

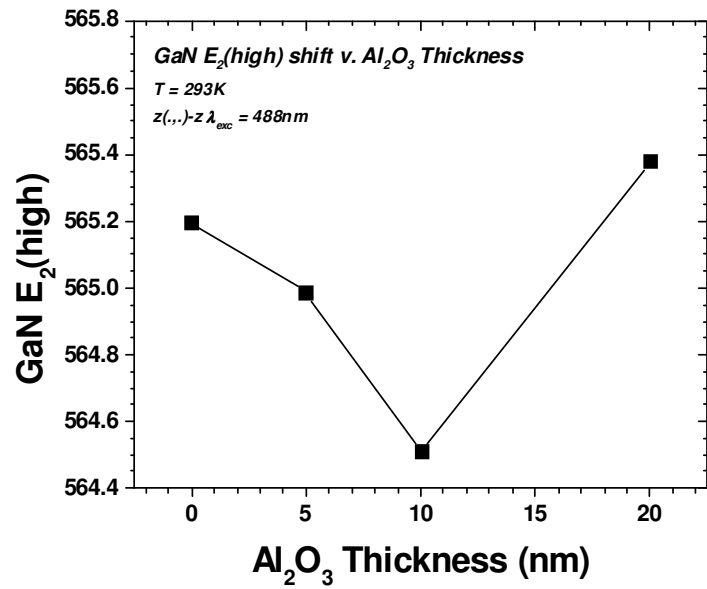


**Figure 7.19:** Shift of the GaN  $E_2(\text{high})$  mode with varying ALD- $\text{Al}_2\text{O}_3$  thickness.

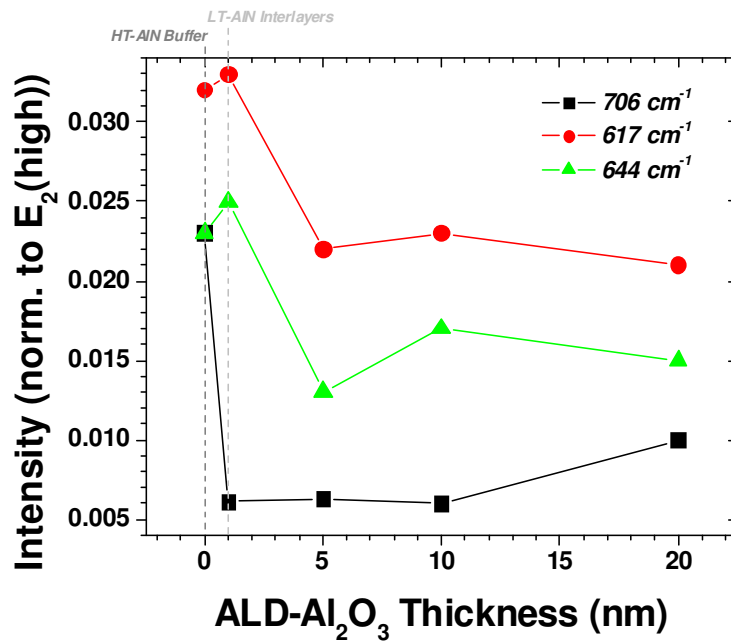


**Figure 7.20:** Intensity of unidentified peaks as a function of ALD- $\text{Al}_2\text{O}_3$  thickness.

The major point of interest here is the increase in strain when the  $\text{Al}_2\text{O}_3$  layer thickness increases from 5 nm to 10 nm, and then the reduction in strain with a further increase in  $\text{Al}_2\text{O}_3$  thickness to 20 nm. While this phenomenon is not completely understood yet, a clear trend is observed in both the Raman data and the PL data suggesting that the  $\text{Al}_2\text{O}_3$  layer does in fact help to relieve strain in the GaN layers compared to GaN on bare Si.

### 7.2.3.2 Optical Properties

RT-PL measurements were used to investigate both the optical quality of the material and the effects of the ALD- $\text{Al}_2\text{O}_3$  interlayer on strain in the GaN layer. The linewidth of the bandedge emission at room temperature is near 50 meV, which is slightly higher than that of typical GaN thin films on sapphire. This linewidth, however, still indicates good crystalline quality, and the increase in linewidth compared to GaN on sapphire may be related to the increased edge dislocation density in the material on silicon.

The PL bandedge shift was also studied as a function of  $\text{Al}_2\text{O}_3$  thickness to gain more insight into strain in the layer, and the results are shown in Figure 7.21. The shift of the Raman  $E_2(\text{high})$  mode is also shown in the figure for comparison. This redshift is an indication of tensile strain. The two measurements at zero thickness represent GaN with a simple HT-AlN buffer layer and GaN with three LT-AlN interlayers. The sample with LT-AlN interlayers is blue-shifted from the sample with only a simple HT-AlN buffer layer, indicating a reduction in strain. Note the clear trend – observable in both the Raman and PL data – in which the very thin  $\text{Al}_2\text{O}_3$  layers (<10 nm) lead to a larger redshift than the samples without an oxide layer. The reason for the shift associated with very thin  $\text{Al}_2\text{O}_3$  layers is unclear. The thicker oxide interlayers, however, appear to relieve this strain, though the screw dislocation density in these layers also increases with increasing oxide interlayer thickness.

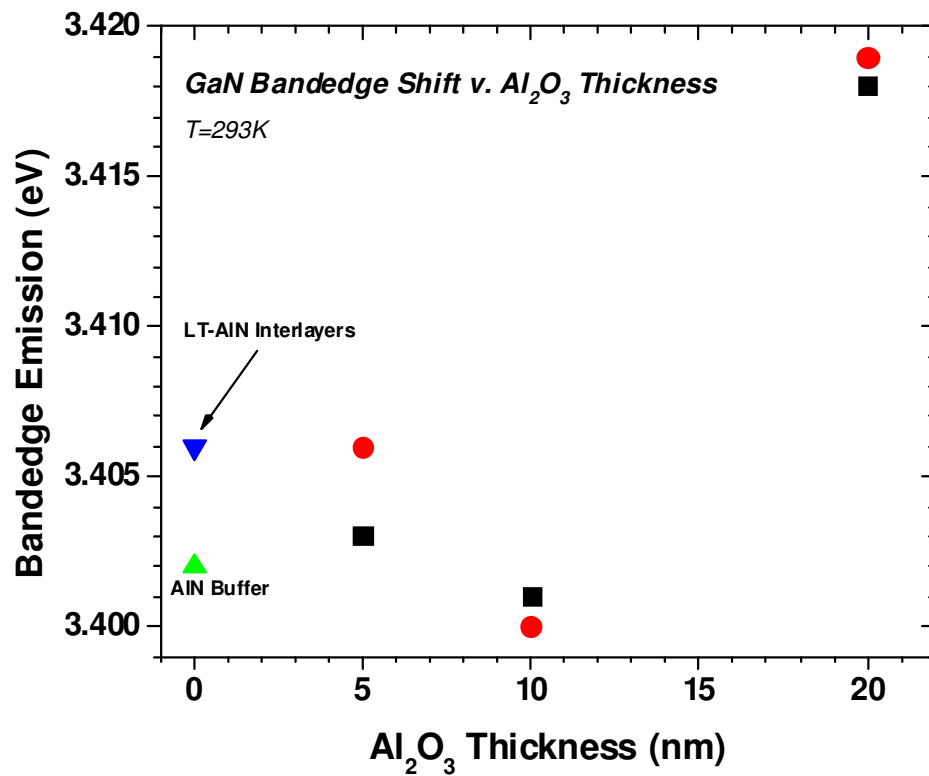


Figure 7.21: Bandedge position as a function of ALD- $\text{Al}_2\text{O}_3$  thickness.

Another prominent feature in the RT-PL spectra of all of the GaN layers on silicon is the yellow luminescence. The ratio of blue luminescence to yellow luminescence in the GaN layers on bare silicon – both with and without LT-AlN interlayers – is  $\sim 5.5$ . This ratio decreases with increasing strain in the GaN film on 10 nm ALD-Al<sub>2</sub>O<sub>3</sub>, and increases to  $\sim 28$  with decreased strain in the GaN film on 20 nm ALD-Al<sub>2</sub>O<sub>3</sub>.

### 7.2.3.3 Surface Morphology

Surface morphology of the GaN layers on ALD-Al<sub>2</sub>O<sub>3</sub>/Si was also studied using AFM. 10 $\mu\text{m}$  x 10 $\mu\text{m}$  AFM images of the surface of GaN thin films grown using a simple HT-AlN buffer layer (7.22(a)), a 5 nm ALD-Al<sub>2</sub>O<sub>3</sub> interlayer (7.22(b)), and a 20 nm ALD-Al<sub>2</sub>O<sub>3</sub> interlayer (7.22(c)) are shown in Figure 7.22. Surface roughness was calculated to be 5.67 Å for the layer on bare silicon, 3.93 Å for the layer on 5 nm ALD-Al<sub>2</sub>O<sub>3</sub>/Si, and 3.70 Å for the layer on 20 nm ALD-Al<sub>2</sub>O<sub>3</sub>/Si. The oxide interlayer leads not only to an improvement in surface roughness, but also to an improved surface morphology, as shown in the figure.

The surface morphology of the sample on bare silicon (with HT-AlN buffer layer) is different than the step-flow pattern that is usually observed for GaN on sapphire. Another interesting aspect of the surface is the formation of pits in the surface. The surface of the GaN layers grown on oxide interlayers show no pit formation, and more step-flow-like pattern, particularly in the sample grown on 20 nm ALD-Al<sub>2</sub>O<sub>3</sub>/Si, Figure 7.22(c). It is clear from XRD data that the oxide interlayer significantly reduces threading dislocation density, as mentioned previously. The absence of pits in the samples on oxide interlayers, combined with the much lower threading dislocation densities in these layers, leads to the conclusion that the pits formed in the surface of the GaN layer grown on bare silicon are due to the termination of threading dislocations at the surface.

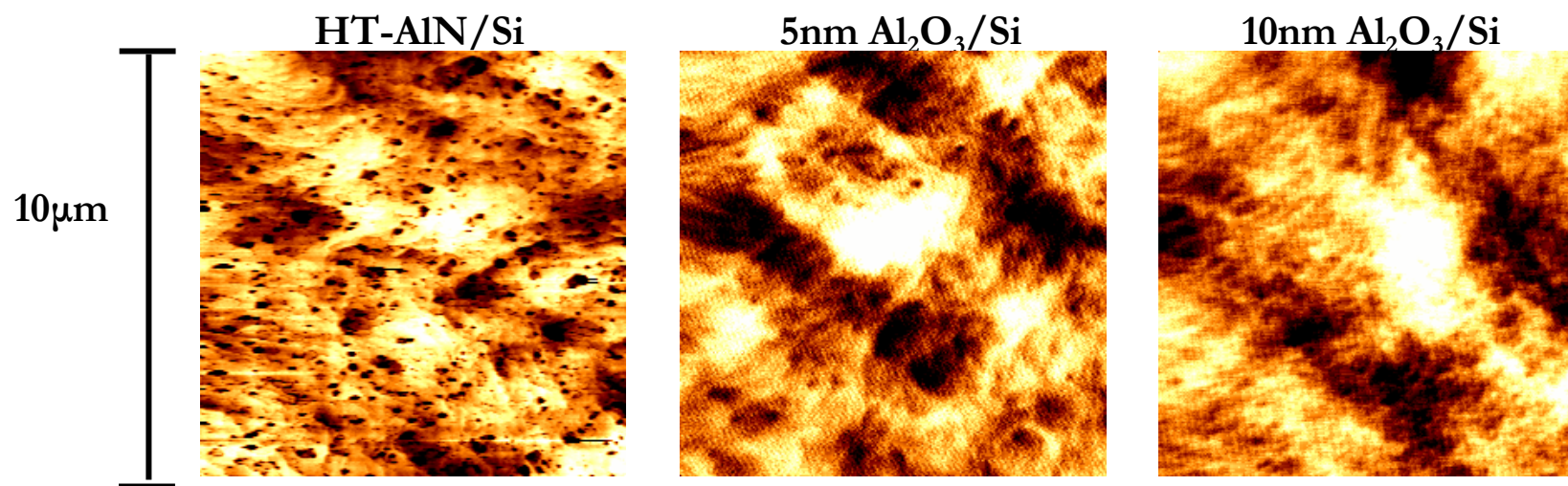


**Figure 7.22:** (a) AFM image of a GaN thin film on HT-AlN/Si. (b) AFM image of a GaN thin film on 5nm ALD- $\text{Al}_2\text{O}_3$ /Si. (c) AFM image of a GaN thin film on 20nm ALD- $\text{Al}_2\text{O}_3$ /Si.

A comparison of the three images in Figure 7.22 shows a shift toward a more step-flow-like pattern with increasing oxide layer thickness. This is possibly due to the relaxation of strain in the growing layer. Another possibility for the change in surface morphology is a change in polarity, as N-polar GaN films often show a rougher surface than Ga-polar films. A high-temperature hydrogen anneal and subsequent low temperature nitridation under  $\text{NH}_3$  are typically used to ensure Ga-polar GaN on sapphire.[131,132] However, no such process is used here, as hydrogen may etch the polycrystalline oxide layer. This causes difficulty in controlling polarity of the films, which may in turn lead to a shift toward a smoother surface with increasing oxide thickness, when polarity of the GaN films becomes more consistent.

### 7.3 SUMMARY

An MOCVD growth process was developed for GaN growth on silicon substrates using an ALD-grown  $\text{Al}_2\text{O}_3$  interlayer. Initial process development was completed on silicon substrates without the oxide interlayer to provide a baseline for comparison of GaN films on oxide interlayers. GaN thin films were also grown using LT-AlN interlayers without an oxide interlayer, as is common in MOCVD growth of GaN on silicon.

Initial process parameters including carrier gas and nucleation layer structure were studied first on ALD- $\text{Al}_2\text{O}_3$ . It was found that both the oxide layer thickness and the AlN buffer layer thickness are important parameters in determining the crystal quality of the subsequent GaN layer. Thin oxide layers ( $\leq 20$  nm) lead to higher quality GaN, while GaN crystal quality degrades significantly on thicker oxide interlayers.

The effects of this thin oxide interlayer on structural and optical properties of the GaN layer were investigated in more detail using XRD and Raman spectroscopy. Williamson-Hall plots of the GaN (002), (004), and (006) reflections show a decrease in threading dislocation

density from  $\sim 2 \times 10^9 \text{ cm}^{-2}$  on bare silicon to  $\sim 2 \times 10^8 \text{ cm}^{-2}$  on ALD- $\text{Al}_2\text{O}_3/\text{Si}$ . XRD rocking curve scans also show a slightly larger linewidth for the GaN (102) reflection compared to typical GaN thin films on sapphire. This is most likely due to a higher concentration of edge dislocations in the material on silicon compared to that on sapphire.

Raman spectra and RT-PL measurements show that this dislocation density increases with decreasing strain in the GaN layer. Raman spectra also reveal two disorder-related modes, the intensities of which scale with threading dislocation density. One local vibrational mode is also identified near  $707 \text{ cm}^{-1}$ , the origin of which is not clear at this time.

Table 7.3 shows the properties of GaN thin films grown both with and without ALD- $\text{Al}_2\text{O}_3$  interlayers in this study. It is clear that the oxide interlayer allows for increased material quality compared to GaN thin films on bare silicon, and that the use of the oxide interlayer on silicon is a viable approach for the growth of GaN-based devices on silicon.

This oxide interlayer also simplifies the growth process compared to typical MOCVD processes for GaN on silicon, which involve the use of LT-AlN interlayers or graded  $\text{Al}_x\text{Ga}_{1-x}\text{N}$  layers. The reduction in consumption of metalorganic precursors using the  $\text{Al}_2\text{O}_3$  interlayer is shown in Figure 7.23. Note that the total consumption of metalorganic precursors is nearly the same as the simplest growth processes reported on silicon, and the oxide interlayer yields much better results, as shown by the investigations in this chapter.

Table 7.3: Material properties obtained using various approaches on silicon.

	XRD		PL		AFM
	(002) FWHM (arcsec)	(102) FWHM (arcsec)	FWHM (meV)	BL/YL	RMS roughness (Å)
HT-AIN buffer	549.3	977.5	49.3	5.396	5.67
LT-AIN interlayers	436.8	1041.9	46.9	5.521	3.99
5nm Al <sub>2</sub> O <sub>3</sub> /Si	378.6	849.5	46.5	7.395	3.93
10nm Al <sub>2</sub> O <sub>3</sub> /Si	433.9	1344.6	47.7	4.497	5.65
20nm Al <sub>2</sub> O <sub>3</sub> /Si	416.6	740.1	43.4	28.223	3.70

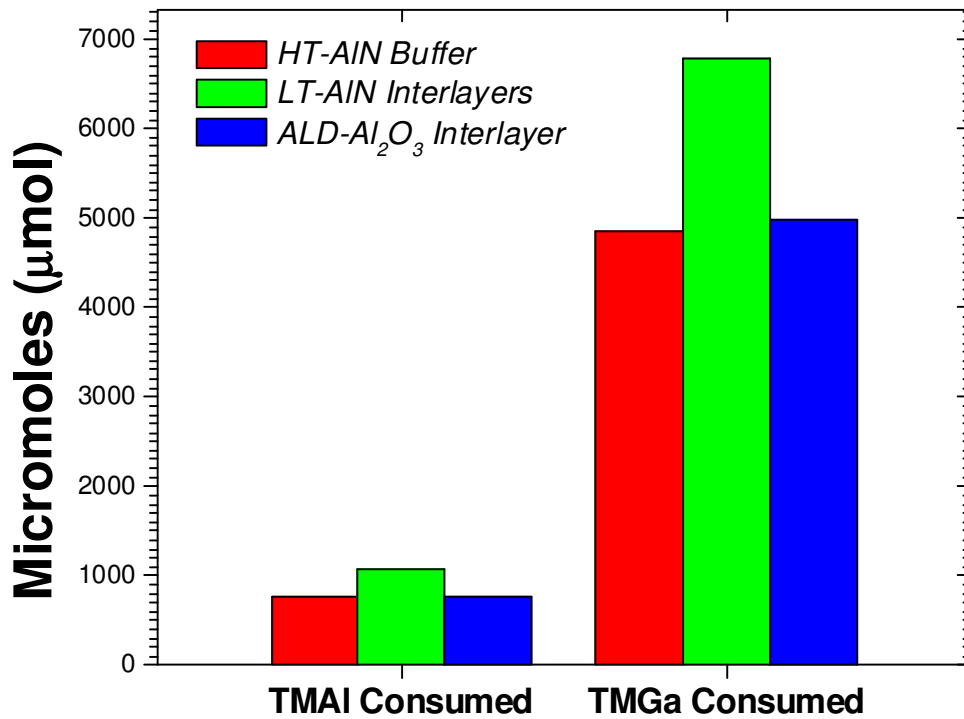


Figure 7.23: Total consumption of precursors using the three approaches compared in this chapter.

## CHAPTER 8: GaN-BASED DEVICES ON ZnO AND Si

GaN-based devices were grown by MOCVD on ZnO and silicon substrates using the processes described in the preceding chapters. This chapter presents results from a detailed study of the electrical and optical properties of these devices.

### 8.1 DEVICES ON ZNO

GaN-based LEDs on sapphire typically have a non-zero electric field in the  $\text{In}_x\text{Ga}_{1-x}\text{N}$  quantum wells, which leads to bending of the conduction and valence bands and spatial separation of electrons and holes in the quantum well. This spatial separation has been identified as one factor limiting the efficiency of such devices. [133] ZnO substrates show promise toward alleviating this problem and increasing the efficiency of  $\text{In}_x\text{Ga}_{1-x}\text{N}$  quantum well-based LEDs. Optically active  $\text{In}_x\text{Ga}_{1-x}\text{N}/\text{GaN}$  multiple quantum well structures were grown on ZnO in this study, and initial devices were grown that showed emission in the blue and green region.

#### 8.1.1 Structures

One advantage of ZnO as a substrate is its lattice match with  $\text{In}_{0.18}\text{Ga}_{0.82}\text{N}$ . This allows for a strain-free  $\text{In}_{0.18}\text{Ga}_{0.82}\text{N}$  layer to be used in the quantum well. However, this also means that the n-type and p-type GaN layers would be under strain. In order to allow for growth of thick, low defect density n-type and p-type layers, devices have been grown using  $\text{In}_{0.18}\text{Ga}_{0.82}\text{N}:\text{Si}$  and  $\text{In}_{0.18}\text{Ga}_{0.82}\text{N}:\text{Mg}$  as the n-type and p-type layers, respectively. This process was first developed on sapphire and then transferred to ZnO substrates. In these structures, a 200nm n-type  $\text{In}_{0.18}\text{Ga}_{0.82}\text{N}$  layer was grown on a GaN/sapphire template. The active region of the LED consisted of a five-period  $\text{In}_x\text{Ga}_{1-x}\text{N}/\text{GaN}$  multiple quantum well

(MQW), and the p-type layer was  $\text{In}_{0.18}\text{Ga}_{0.82}\text{N}$ . A schematic of the structure that was investigated is shown in Figure 8.1. Use of the ZnO substrate will allow for growth of lower defect density material, as the  $\text{In}_{0.18}\text{Ga}_{0.82}\text{N}$  layer is unstrained, thus leading to increased device efficiency.

### 8.1.2 Luminescence

The PL spectrum shows a peak near 555nm, Figure 8.2(a). The broadening is most likely a consequence of the higher defect density in the  $\text{In}_x\text{Ga}_{1-x}\text{N}$  layers grown on sapphire due to relaxation of the thick  $\text{In}_x\text{Ga}_{1-x}\text{N}$  layers. Similar structures were grown on ZnO, targeting green emission wavelengths, near 555 nm. RT-PL of one such structure is shown in Figure 8.2(b). While the luminescence intensity is relatively low, the IQE of this structure as measured by LT-PL is relatively high, at 59%. This increased efficiency compared to typical LEDs on sapphire is attributed to the reduction in strain in the  $\text{In}_x\text{Ga}_{1-x}\text{N}$  quantum wells that is afforded by the ZnO substrate.

### 8.1.3 Electrical Properties

The I-V response of the control structure on sapphire is shown in Figure 8.3. Though the turn-on voltage is relatively high, a clear rectifying behavior is observed. The devices on ZnO, however, showed no rectification, despite the good optical properties. The reason for this difference in behavior between the devices on sapphire and on ZnO is attributed to excess zinc and oxygen diffusion into the  $\text{In}_x\text{Ga}_{1-x}\text{N}$ , which degrades the electrical properties of the device. These results make it quite clear that while ZnO substrates show great promise for increased efficiency of GaN-based emitters, the problem of zinc and oxygen outdiffusion from the substrate remains to be solved in a manner that can render GaN on ZnO processes technologically viable.

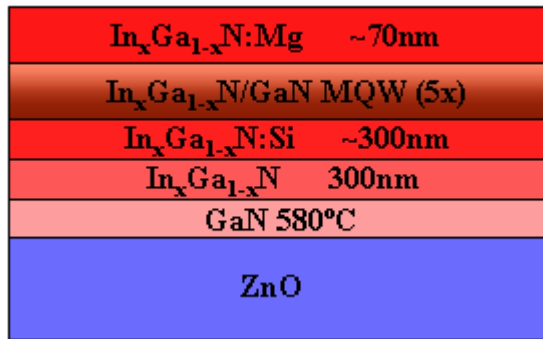


Figure 8.1: LED structure investigated on ZnO.

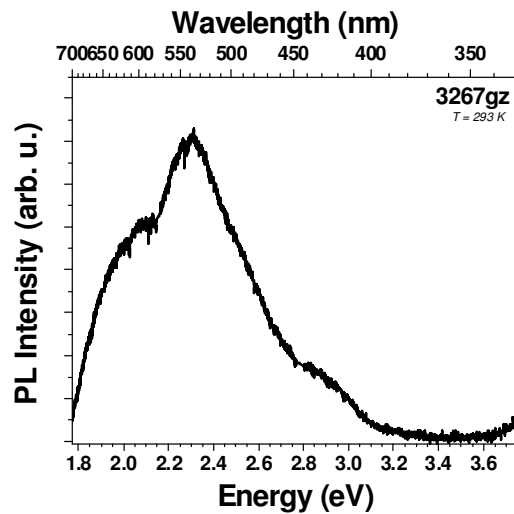
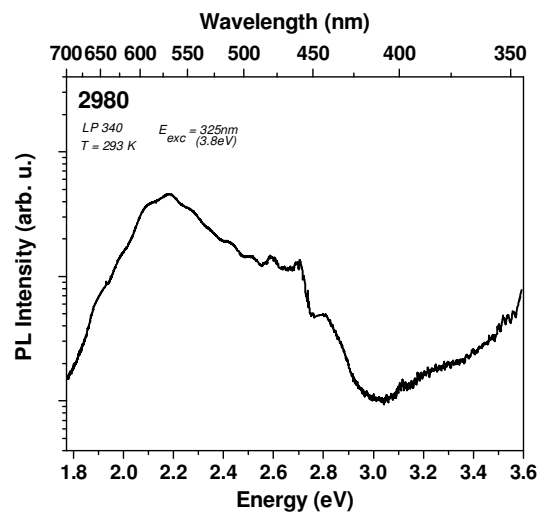
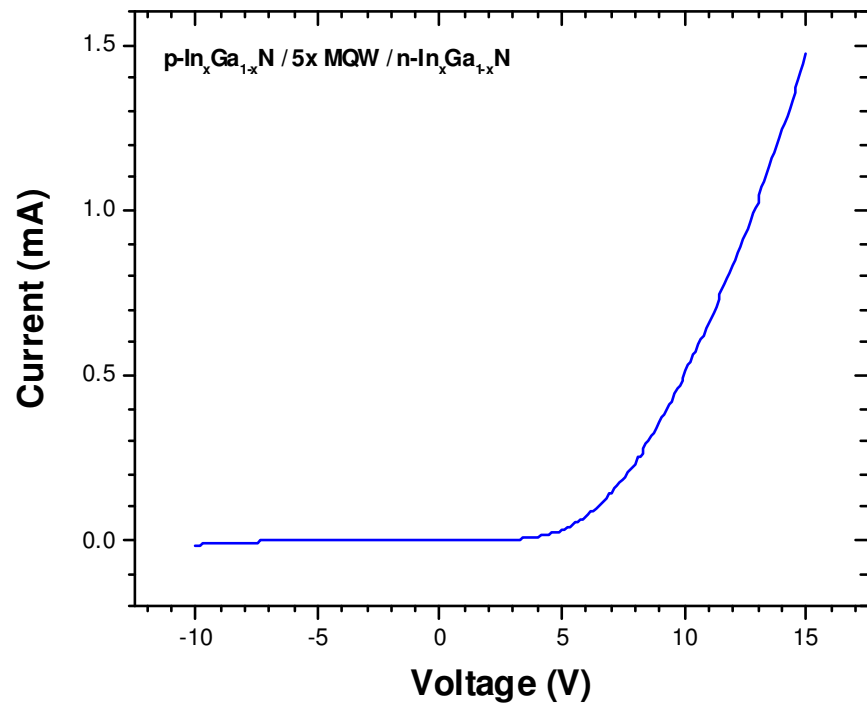


Figure 8.2: (a) PL of  $\text{In}_{0.18}\text{Ga}_{0.82}\text{N}$ -based LED on GaN/sapphire. (b) PL of  $\text{In}_{0.18}\text{Ga}_{0.82}\text{N}$ -based LED on ZnO.



**Figure 8.3:** I-V curve of In<sub>0.18</sub>Ga<sub>0.82</sub>N LED on a GaN/sapphire template.

### 8.1.4 Processing

GaN-based structures were removed from the ZnO substrates using a wet etching process. The substrates were removed by etching in a 10% HCl solution for 20 minutes. However, this had little effect on optical properties, and electrical properties were not investigated after substrate removal, as the devices on ZnO showed no rectification before substrate removal.

## **8.2 DEVICES ON SILICON**

Crack-free GaN LEDs have been grown by MOCVD on Si(111) substrates using the process described in the previous chapter. Initial growth runs allowed for calibration of growth parameters and emission wavelength, and for initial investigations into their structural and optical properties. Final results show comparable performance characteristics for GaN-based devices grown on Si and sapphire substrates.

### 8.2.1 Structures

GaN-based LEDs were grown on silicon substrates using the process developed previously. Initial devices consisted of a 600 nm n-type GaN layer, four-period  $\text{In}_x\text{Ga}_{1-x}\text{N}/\text{GaN}$  MQWs, and 120nm of p-type GaN. The MQW structure consisted of 15-20 Å wells and 120 Å barriers. In-situ reflectivity curves for both green and blue GaN-based LEDs on silicon are shown in Figure 8.4(a) and (b), respectively. The intensity of the oscillations is an indication of a smooth surface, which is maintained throughout growth. XRD  $2\theta$ - $\omega$  scans of both green and blue LEDs are shown in Figures 8.5(a) and (b), respectively. XRD data indicates good crystalline quality for both green and blue LEDs. The multiple satellite peaks are also an indication of high-quality interfaces.

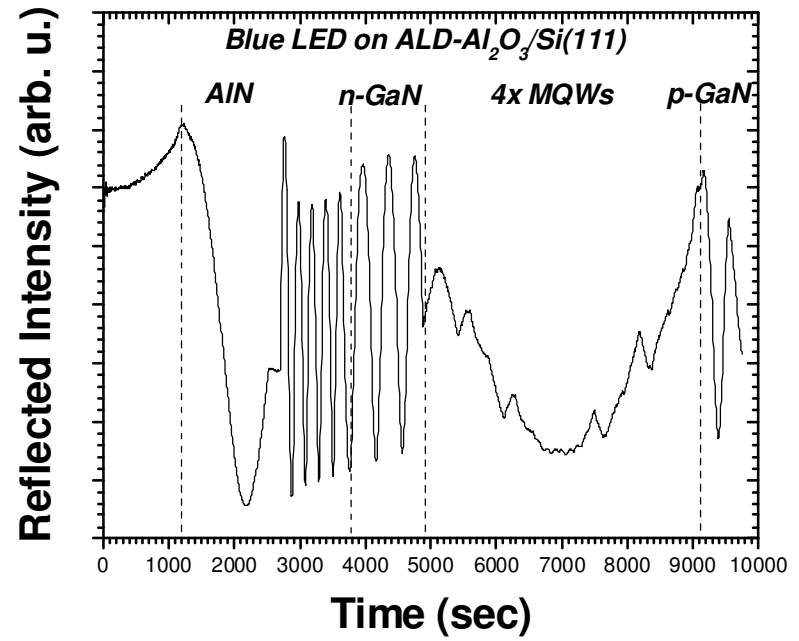
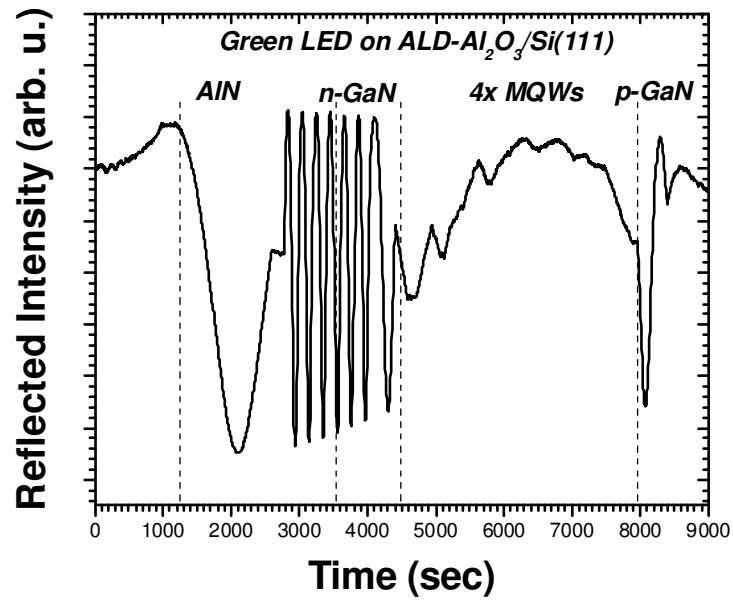


**Figure 8.4:** (a) In-situ reflectivity showing the growth of a green GaN LED on silicon. (b) In-situ reflectivity curve showing the growth of a blue GaN LED on silicon.

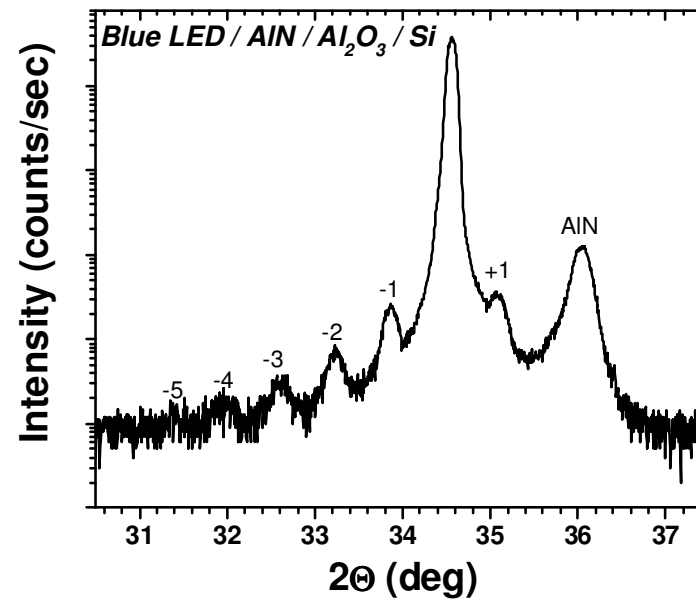
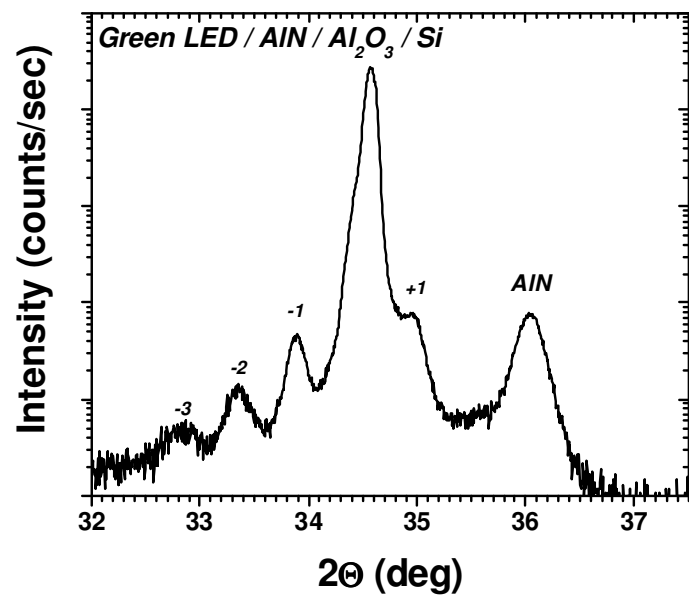


**Figure 8.5:** (a) XRD 2θ-ω scan of a green GaN LED on silicon. (b) XRD 2θ-ω scan of a blue GaN LED on silicon.

RT-PL spectra for both blue and green LEDs are shown in Figures 8.6(a) and (b), respectively. A Gaussian fit shows linewidths of 108 meV for the blue device and 97 meV for the green device. The multiple peaks observable in the green spectrum are perhaps related to non-uniformity in the quantum wells, possibly due to the higher indium content in the quantum wells in the green device.

The n-type and p-type layers in these devices were slightly thinner than in typical GaN-based LEDs in order to suppress cracking due to tensile strain. However, cracking remained a problem with initial devices.

After process optimization discussed in the previous chapter, GaN-based LEDs were grown and fabricated on both sapphire and Si substrates.[134]. These devices were  $350\mu\text{m} \times 350\mu\text{m}$  and consisted of  $1.0\mu\text{m}$  of n-type GaN, a four-period  $\text{In}_x\text{Ga}_{1-x}\text{N}/\text{GaN}$  (2.75 nm/12 nm) MQW structure as the active region, and  $\sim 160\text{nm}$  of p-type GaN on top. LEDs were grown on  $1.5\mu\text{m}$ -thick GaN/sapphire templates and on  $1.5\mu\text{m}$ -thick GaN/ $\text{Al}_2\text{O}_3$ /Si templates simultaneously so that similar devices could be obtained on both sapphire and Si. The Si LEDs fabricated in this work were crack-free, as shown in Figure 8.7(a). Figure 8.7(b) shows the devices that were fabricated on sapphire substrates. The apparent difference in surface morphology is because the sapphire substrate is transparent, and is single-side polished, leaving the rough back-side of the substrate visible from the top. Surface morphology of the layers on Si and sapphire was very similar as observed by AFM, however.

### 8.2.2 Electrical Properties

I-V curves show that the device on Si has a slightly lower series resistance compared to the device on sapphire, Figure 8.8. The reason for this improved series resistance remains

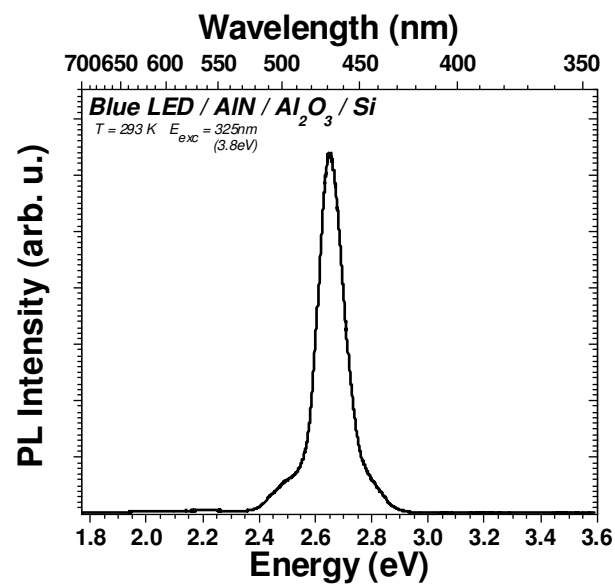
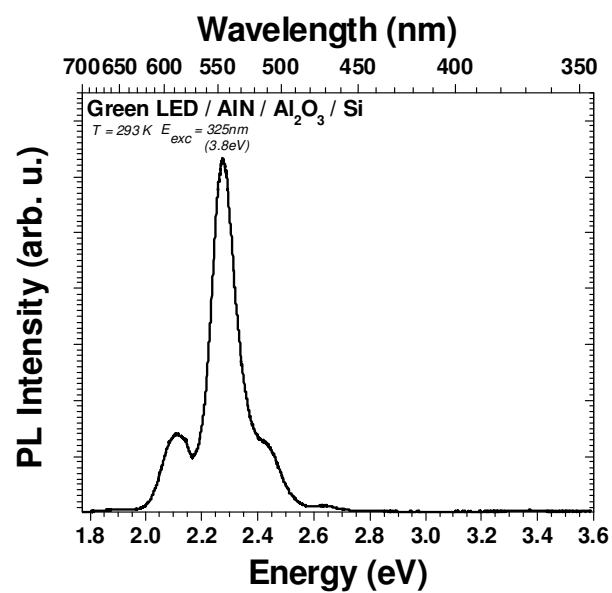


**Figure 8.6:** RT-PL of green (a) and blue (b) GaN-based LEDs on ALD-Al<sub>2</sub>O<sub>3</sub>/Si.

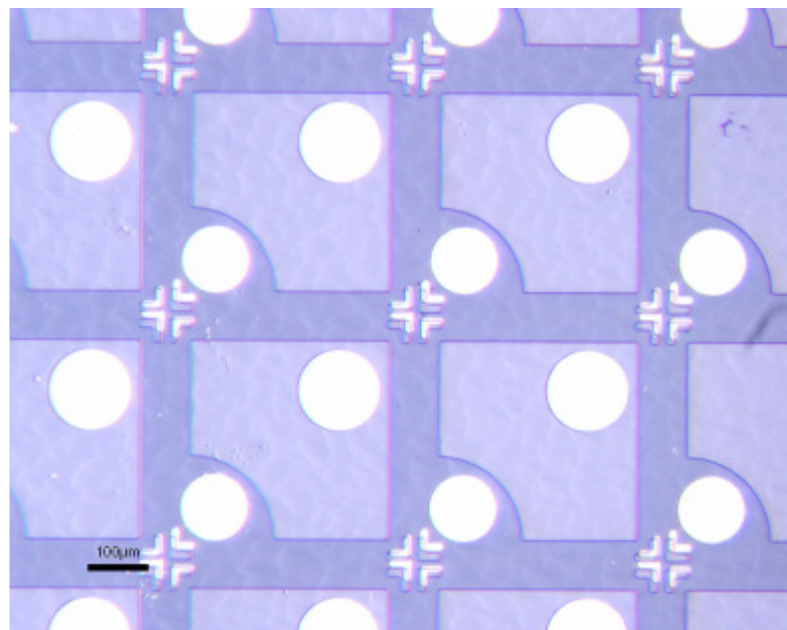
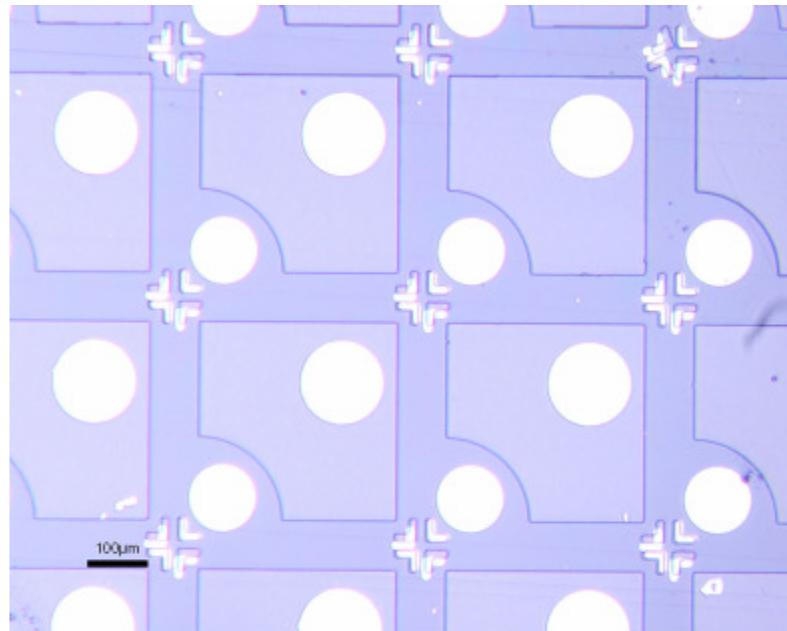


**Figure 8.7:** Photos of GaN-based LEDs on GaN/Al<sub>2</sub>O<sub>3</sub>/Si (top) and GaN/Sapphire (bottom).

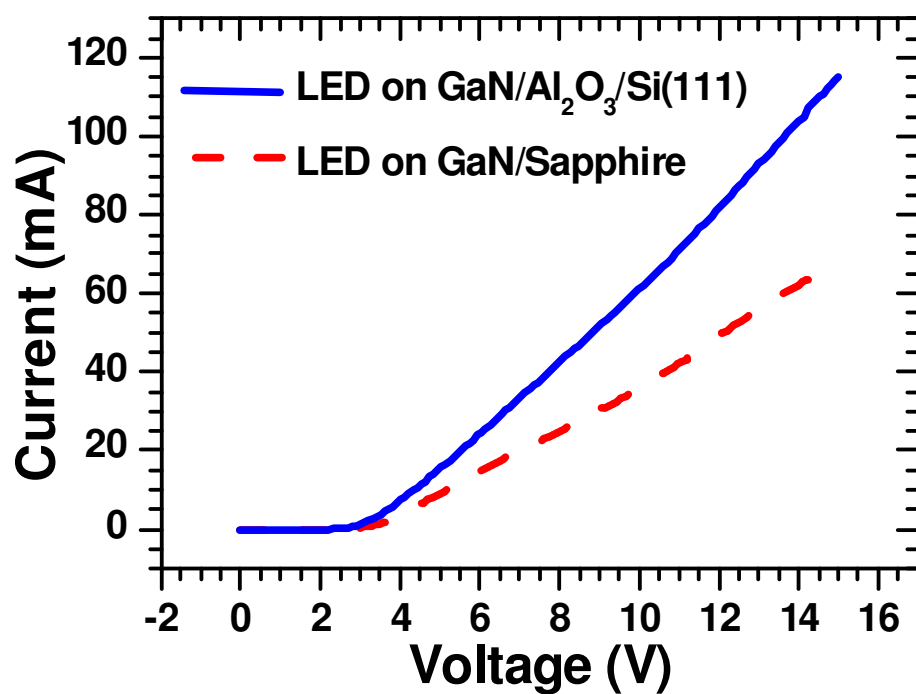


Figure 8.8: I-V curves for GaN LEDs on GaN/Al<sub>2</sub>O<sub>3</sub>/Si(111) and GaN/sapphire.

unclear. However, further optimization of the LED growth process, p-type layer, and p-type contact resistance will result in much higher efficiency and lower series resistance of the GaN emitters on both Si and sapphire substrates. Another significant point that is observable from a comparison of the I-V curves in Figure 8.8 is the turn-on voltage. The turn-on voltage for the device on Si is slightly lower than that of the device on sapphire ( $\sim 2.9\text{V}$  on Si compared to  $\sim 3.0\text{V}$  on sapphire). This turn-on voltage is in the same range as those of other reports for GaN-based LEDs on Si [67,135,136].

### 8.2.3 Optical Properties

EL spectra of the devices were measured at drive currents up to 100mA. EL of a typical device on sapphire is shown in Figure 8.9(a). EL spectra as a function of drive current for devices on ALD- $\text{Al}_2\text{O}_3/\text{Si}$  are shown in Figure 8.9(b). The devices on Si show a redshift in peak emission wavelength compared to those on sapphire. This redshift may be due to the tensile strain in the epilayer as indicated by the shift of Raman  $E_2$  (high) mode to lower wave numbers, The higher In incorporation in the film also confirms the tensile strain in the epilayers layers [112]. The higher indium content in turn leads to longer peak emission wavelengths compared to the devices on sapphire.

A shift in peak emission wavelength is also observed with an increase in drive current for both devices, though it is more clearly seen in the devices on Si. Two emission peaks can be seen in the EL spectra of the devices on Si, with a shift from lower energies to higher energies with increasing drive current. This may be due to non-uniformity of the quantum wells caused by the much higher indium content in the active region of the devices on Si.

A nickel oxide current spreading layer was used to ensure uniform current spreading through the devices. The inset of Figure 8.9(b) shows a photograph of a device on silicon

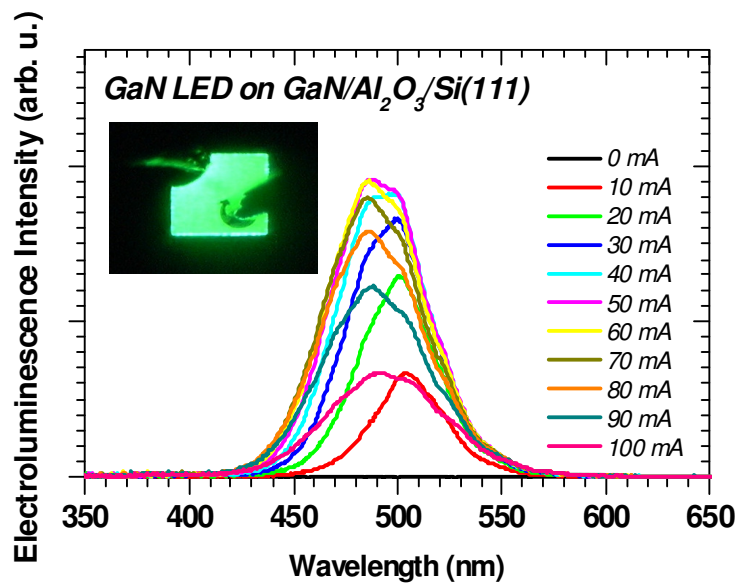
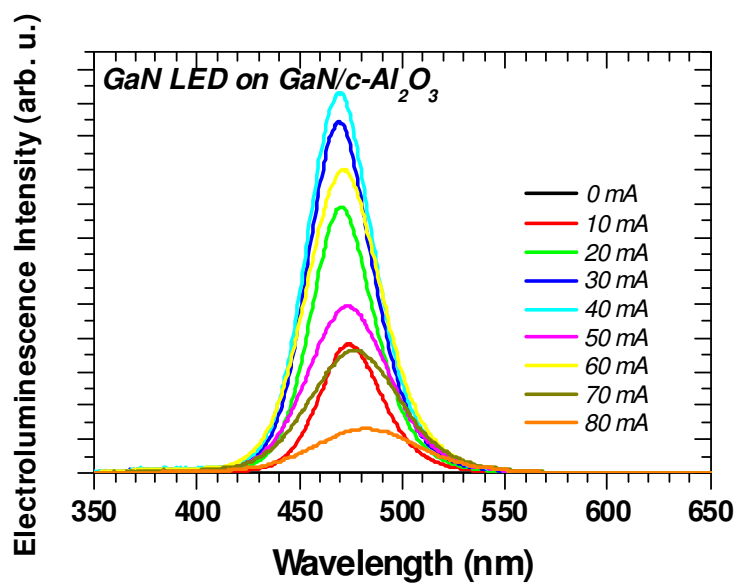


**Figure 8.9:** EL spectra for GaN LEDs on GaN/Sapphire (a) and GaN/Al<sub>2</sub>O<sub>3</sub>/Si(111) (b).

under normal operating conditions. The uniform light emission from the device surface is an indication of good current spreading. Devices on sapphire showed similar properties. The uniform current spreading in these devices allows for a valid comparison of luminescence intensity versus current density between the devices.

#### 8.2.4 Efficiency

Luminescence intensity was also measured as a function of drive current for these devices, and results are shown in Figure 8.10. The luminescence intensity of the devices on Si reached a peak with a drive current of 40mA, corresponding to a current density of  $32.7 \text{ A cm}^{-2}$ . The comparison is significant because it shows that for comparable devices, the LED on Si shows a much higher efficiency at high drive currents than the LED on sapphire, despite the longer wavelength emission from the device on Si, which often leads to a drop in efficiency.

The IQE of these structures was measured using LT-PL. This approach assumes an IQE of 100% at 8K, and the IQE at room temperature (RT) is calculated as the ratio of PL integrated intensity at RT to PL integrated intensity at 8K. The IQE values for two LEDs that were grown at the same time – one on sapphire and one on  $\text{Al}_2\text{O}_3/\text{Si}$  – are shown in Figure 8.11. As mentioned previously, the device on Si showed a significant redshift in peak wavelength relative to the device on sapphire. However, this redshift did not significantly degrade the IQE, as would be expected with a shift in wavelength from the blue region toward the green region. A summary of the IQE measurements done on three GaN-based LEDs on Si is shown in the inset of Figure 8.11, along with the device on sapphire for comparison. The IQE of these devices improves significantly with decreasing emission wavelength, as would be expected.

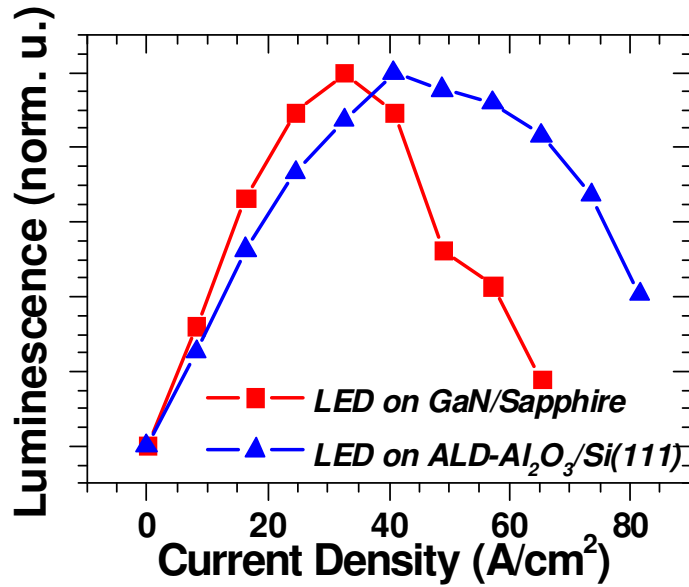


**Figure 8.10:** L-I curves for GaN LEDs showing a higher efficiency at high drive currents for the device on GaN/Al<sub>2</sub>O<sub>3</sub>/Si(111) compared to that on GaN/Sapphire.

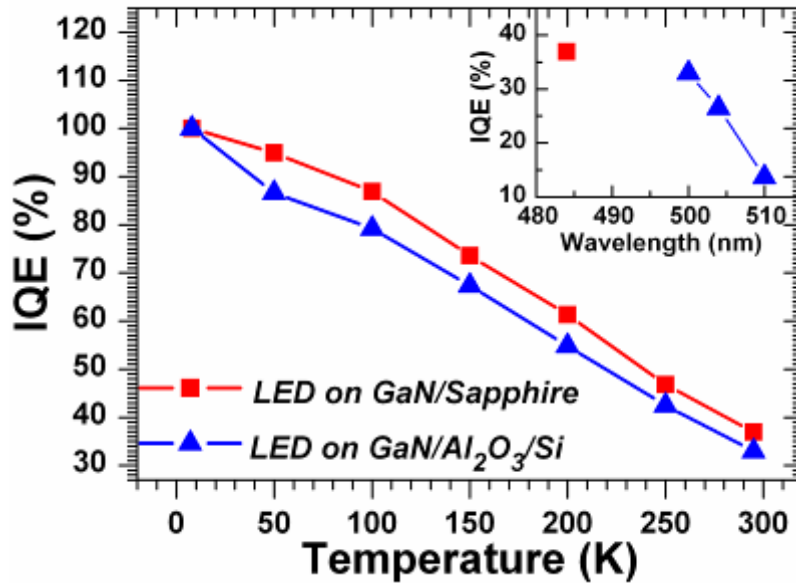


**Figure 8.11:** IQE as a function of temperature GaN LEDs on GaN/Al<sub>2</sub>O<sub>3</sub>/Si(111) and on GaN/Sapphire. Inset shows IQE as a function of wavelength for GaN LEDs on ALD-Al<sub>2</sub>O<sub>3</sub>/Si.

EQE was also measured as a function of drive current, and results are shown in Figure 8.12. Measurements were pulsed to avoid thermal effects. EQE of these devices is low because of the relatively high series resistance. However, it is worth noting that at high current densities, EQE drops off more quickly on sapphire. The reason for the difference in behavior at high current densities is unclear, but it is certainly not due to thermal effects, as the measurements were pulsed.

#### **8.4 SUMMARY**

GaN-based devices were grown on both ZnO and silicon substrates using the processes developed in previous chapters. Devices on ZnO showed good optical properties, with peak emission wavelengths in the green region, near 555 nm, and good efficiency. However, electrical properties were degraded by zinc and oxygen diffusion into the device structure.

A side-by-side comparison of LEDs grown on both GaN/sapphire templates and GaN/silicon templates shows similar performance for the devices on silicon and sapphire. The devices on silicon, however, show a slightly longer wavelength compared to those on sapphire. This may be due to the increase in indium incorporation with increasing tensile strain in the layers. IQE values of 37% (GaN/sapphire) and 32% (GaN/silicon) were measured via LT-PL. These results show that silicon is a viable alternative to GaN on sapphire, and that devices grown on silicon are capable of performance characteristics similar to comparable devices on sapphire.

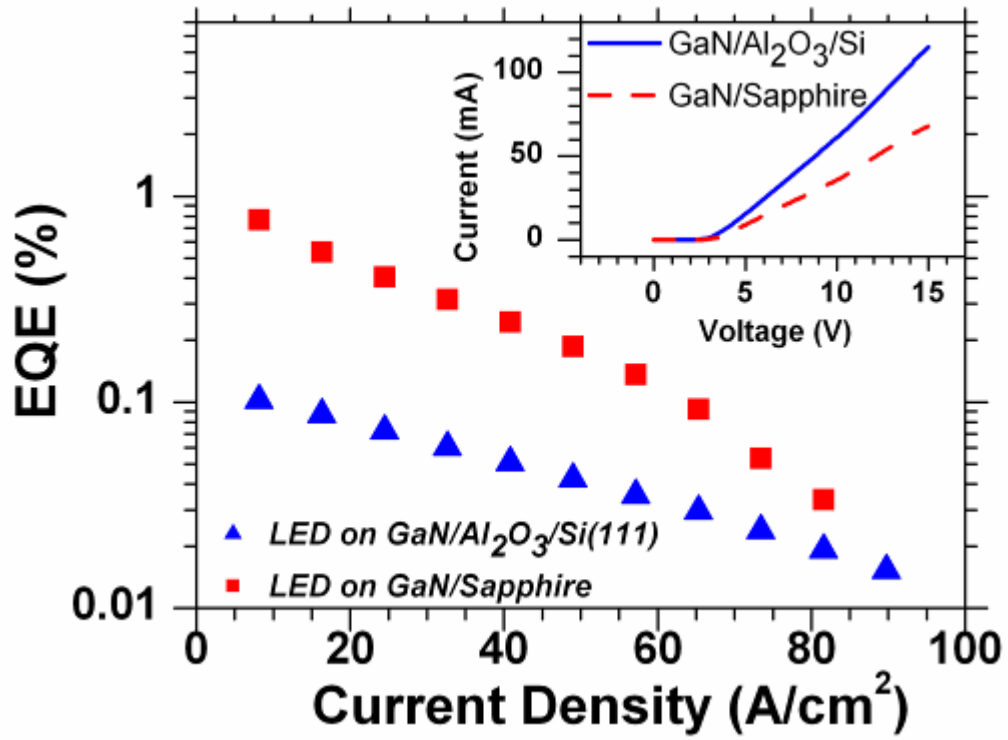


**Figure 8.12:** EQE of GaN-based LEDs on GaN/Al<sub>2</sub>O<sub>3</sub>/Si(111) and GaN/Sapphire.

## CHAPTER 9: MODELING OF GaN-BASED DEVICES ON ZnO AND Si

A theoretical understanding of the effects of substrate choice on the optical and electrical properties of GaN-based LEDs is necessary in order to develop devices on these substrates that show performance characteristics similar to comparable devices on sapphire. To this end, GaN-based devices on both ZnO and silicon were simulated in order to determine the important aspects of device design, and the important effects of each substrate on device performance.

### 9.1 POLARIZATION IN NITRIDES

The  $c/a$  ratio of GaN (1.626) is slightly less than the ideal case for a hexagonal close packed (hcp) crystal ( $\sim 1.63$ ). This non-centrosymmetry of wurtzite GaN and its alloys with indium and aluminum leads to large spontaneous and piezoelectric polarization effects in these materials. Polarization-induced electric fields, in turn, cause spatial separation of electrons and holes in  $\text{In}_x\text{Ga}_{1-x}\text{N}$  quantum wells, thus decreasing device efficiency. ZnO is also a polar material with even larger spontaneous and piezoelectric polarization effects than those found in the nitrides [137,138], and the integration of these two materials for device applications requires a clear understanding of polarization and its effects on device performance and efficiency.

The total polarization in a given layer is simply the sum of the spontaneous and piezoelectric polarizations:

$$P_{tot} = P_{sp} + P_{pz} \quad (9.1)$$

Changes in both composition and strain state at interfaces lead to a mismatch in total polarization. This mismatch is compensated by a build-up of bound sheet charge near the interface, the areal density of which can be calculated by taking the difference of the polarization charge in the two layers. The formation of polarization-induced sheets of bound charge in multiple quantum well and superlattice structures induces electric fields in these structures that affect the distribution of charge carriers and, ultimately, efficiency of the devices. The fact that the charge build-up is due to a mismatch in total polarization, and not simply piezoelectric polarization, means that the spontaneous polarization values of these materials are very important relative to each other in reducing polarization-induced internal electric fields.

A summary of the polarization-related parameters for AlN, GaN, InN, and ZnO are given in Table 9.1. These values agree well with the literature, and were used in SiLENSe as well. It should be noted that little experimental work is available for InN, and values from calculations based on a local density approximation were used in this work. [139] The spontaneous polarization of AlN is much larger than that of both GaN and InN, which have spontaneous polarization values in the same range as typical piezoelectric polarization values. This makes strain (and hence, piezoelectric polarization) a much larger factor in determining overall electric fields in  $\text{In}_x\text{Ga}_{1-x}\text{N}/\text{GaN}$  quantum wells compared to  $\text{Al}_x\text{Ga}_{1-x}\text{N}/\text{GaN}$  heterostructures. The much larger spontaneous polarization of ZnO compared to InN and GaN also suggests that a bound sheet charge may form at the  $\text{In}_x\text{Ga}_{1-x}\text{N}/\text{ZnO}$  interface, regardless of indium content, and that screening this charge by doping near the interface may be the only way to neutralize the electric field induced by this charge build-up.

Table 9.1: Spontaneous polarization values, lattice parameters, elastic coefficients, dielectric coefficients, and piezoelectric coefficients used in this work.

	$e_{31}$	$e_{33}$	$c_{13}$	$c_{33}$	$a$ (Å)	$P_{sp,z}$	$\epsilon$
<i>AlN</i>	-0.59	1.41	115	390	3.112	-0.081	9.0
<i>InN</i>	-0.22	0.43	95	200	3.548	-0.032	15.3
<i>GaN</i>	-0.33	0.65	105	395	3.189	-0.029	8.9
<i>ZnO</i>	-0.62	0.96	106	210	3.250	-0.050	8.75

Polarity of these materials also plays a significant role in determining the sign of the charge build-up at the interfaces and, thus, direction of the electric fields. Typical MOCVD-grown nitrides are grown along the [0001] axis, and are cation-polar. In this situation, the spontaneous polarization is along the  $[000 \bar{1}]$  axis. Piezoelectric polarization, however, is determined by the strain state of the material. Under tensile strain, the piezoelectric polarization is in the  $[000 \bar{1}]$  direction, parallel to the spontaneous polarization; however, compressive strain induces a piezoelectric polarization in the [0001] direction, opposite to the spontaneous polarization. A typical  $\text{In}_x\text{Ga}_{1-x}\text{N}$  quantum well on a fully relaxed GaN template is under compressive strain, while  $\text{Al}_x\text{Ga}_{1-x}\text{N}$  layers on GaN are under tensile strain [138]. In addition to affecting lattice constants, and subsequently the strain state of the layer, composition also changes the spontaneous polarization of the layer. Thus, the composition and strain state of the material are the two major factors that determine the overall effect of polarization in nitride-based thin films.

The piezoelectric polarization can be calculated using the elastic coefficients, piezoelectric coefficients, and strain state as follows:

$$P_{pz} = 2 \left( e_{31} - \frac{c_{13}}{c_{33}} e_{33} \right) \left( \frac{a_{sub} - a_{layer}}{a_{sub}} \right) \quad (9.2)$$

where  $e_{31}$  and  $e_{33}$  are the elastic coefficients,  $c_{13}$  and  $c_{33}$  are the piezoelectric coefficients, and  $a_{sub}$  and  $a_{layer}$  are the lattice constants of the substrate and the layer, respectively[138].

In an  $\text{In}_x\text{Ga}_{1-x}\text{N}/\text{GaN}$  multiple quantum well structure, the electric field in the wells and the barriers can be modeled using the following equations (a) and (b), respectively[140]:

$$E_w = \frac{L_b(P_b - P_w)}{L_b\epsilon_w + L_w\epsilon_b} \quad (9.3)$$

$$E_b = \frac{L_w(P_w - P_b)}{L_b\epsilon_w + L_w\epsilon_b} \quad (9.4)$$

where  $P_b$  and  $P_w$  are the total polarization in the barrier and well, respectively,  $L_b$  and  $L_w$  are the thicknesses of the barrier and well, respectively, and  $\epsilon_w$  and  $\epsilon_b$  are the dielectric constants for the well and the barrier, respectively. These equations are based, however, on the boundary condition that the potential on either side of the active region is the same. This assumption does not hold for an actual device, in which the regions on either side of the active region are doped for n-type and p-type conductivity, causing a difference in potential.

Space charge regions develop on either side of the active region in a diode structure, with ionized donors leading to positive charge in the n-type region and ionized acceptors leading to negative charge in the p-type region. This formation of space charge regions leads to an additional component to the electric field, which extends across the entire active region of the device, thus introducing a second term into the expression for electric field. A simple approximation taking into account the drop in potential across the active region and the thickness of the active region leads to the following expression for the electric field induced by the space charge region:

$$E = \frac{V_0}{xL_w + yL_b} \quad (9.5)$$

where  $V_0$  is the built-in potential across the p-n junction and  $x$  and  $y$  are the number of wells and barriers, respectively. Thus, the two contributions to the electric field yield the following expressions for the electric field in the wells and barriers of an LED structure, respectively:

$$E_w = \frac{L_b(P_b - P_w)}{L_b\epsilon_w + L_w\epsilon_b} + \frac{V_0}{xL_w + yL_b} \quad (9.6)$$

$$E_b = \frac{L_w(P_w - P_b)}{L_b\epsilon_w + L_w\epsilon_b} + \frac{V_0}{xL_w + yL_b} \quad (9.7)$$

A Vegard-like relationship is assumed for the polarization values in  $\text{In}_x\text{Ga}_{1-x}\text{N}$  quantum wells and for dielectric constants. Under this assumption, the expressions above show good agreement with values calculated in SiLENSe for the the electric fields in quantum wells and barriers. However, there exists a discrepancy at doped interfaces, the origin of which remains unclear at this time. This discrepancy often leads to a weaker electric field in the quantum well adjacent to the doped region compared to the rest of the structure. Band diagram and device parameters shown in the rest of this work were calculated using SiLENSe version 3.4.

## 9.2 GAN-BASED DEVICES ON ZNO

ZnO substrates show promise for the growth of low defect density  $\text{In}_x\text{Ga}_{1-x}\text{N}$ , owing to the lattice match of ZnO to  $\text{In}_x\text{Ga}_{1-x}\text{N}$  with  $x = 0.18$ . Also, typical growth temperatures for  $\text{In}_x\text{Ga}_{1-x}\text{N}$  range from  $\sim 700$  °C to  $\sim 750$  °C, much lower than typical GaN growth temperatures, which are above 1000 °C. The relative compatibility of indium-containing nitride alloys compared to pure GaN or  $\text{Al}_x\text{Ga}_{1-x}\text{N}$  suggests that devices based on  $\text{In}_x\text{Ga}_{1-x}\text{N}$  should be studied to determine what, if any, advantages they offer over normal GaN-based devices on sapphire.

### 9.2.1 Device Structure on ZnO

In this work, devices based on n-type and p-type  $\text{In}_{0.18}\text{Ga}_{0.82}\text{N}$  have been modeled in order to study the advantages of a lattice-matched substrate. The lattice match to the substrate removes any strain in the n- $\text{In}_{0.18}\text{Ga}_{0.82}\text{N}$  layer, and promises to reduce strain in the quantum wells ( $x > 0.18$ ), thereby increasing device efficiency. The structure investigated in

$p\text{-In}_{0.18}\text{Ga}_{0.82}\text{N}$	150 nm	$N_A = 3 \times 10^{19} \text{ cm}^{-3}$
$\text{In}_{0.3}\text{Ga}_{0.7}\text{N}$	3 nm	
$n\text{-In}_{0.18}\text{Ga}_{0.82}\text{GaN}$	500 nm	$N_D = 5 \times 10^{18} \text{ cm}^{-3}$

Figure 9.1:  $\text{In}_{0.18}\text{Ga}_{0.82}\text{N}$  LED simulated on both ZnO and GaN substrates.

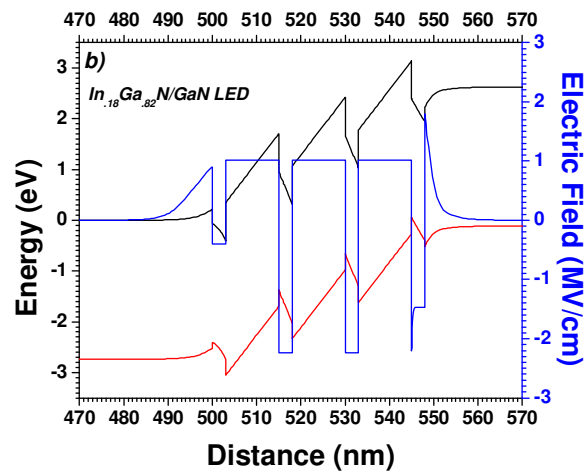
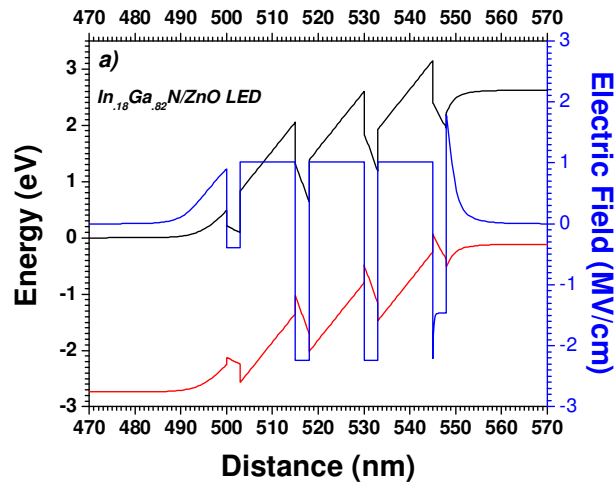


Figure 9.2: Electric field distribution in  $\text{In}_{0.18}\text{Ga}_{0.82}\text{N}$ -based LEDs on both ZnO (top) and GaN (bottom).

this work is shown in Figure 4.1. The corresponding band diagram and electric field is shown in Figure 9.2(a) and (b) for the same structure on both GaN (strained) and ZnO (unstrained), respectively. The thickness of the n-type layer was chosen so that the assumption of strained  $\text{In}_x\text{Ga}_{1-x}\text{N}$  on GaN/sapphire could be considered valid.

The band diagrams in Figure 9.2 show a clear difference, particularly in the first quantum well, in band bending. The conduction and valence band edges bend more noticeably on the GaN substrate than on the ZnO. This difference stems from a difference in polarization-induced electric fields due to strain in the quantum well. The electric field, particularly in the first quantum well, is much lower in the structure on ZnO due to the reduced strain in the well.

### 9.2.2 Modeled Device Performance

I-V curves for the two devices discussed in the previous section were simulated using SiLENSe 3.4, Figure 9.3. At a drive current of 20 mA, both devices showed emission in the green region, near 505 nm, Figures 9.4(a) and (b). The device on ZnO showed much stronger emission compared to that on GaN, and a much narrower emission peak. The reason for the narrower emission is the reduction in band bending in the quantum well. The second peak in the spectrum on GaN, observable at longer wavelengths, is also due to the increased electric field in the second quantum well. The increased electric field in the quantum wells on GaN compared to those on ZnO leads to a slight red-shift in emission wavelength, thus the increased electric field in the second quantum well leads to a slight redshift in emission from that well compared to the first.

The most important point to note in the comparison of these devices is the IQE, Figure 9.5. It is clear that IQE of the device on ZnO is much higher than that on GaN. The

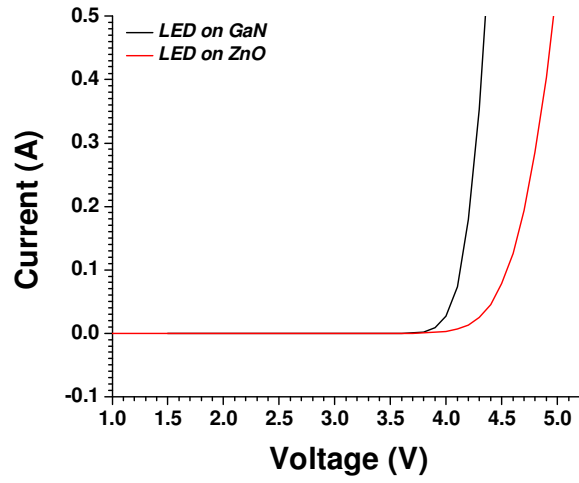


**Figure 9.3:** I-V curves of  $\text{In}_{0.18}\text{Ga}_{0.82}\text{N}$ -based LEDs simulated on both ZnO (solid line) and GaN (dashed line).

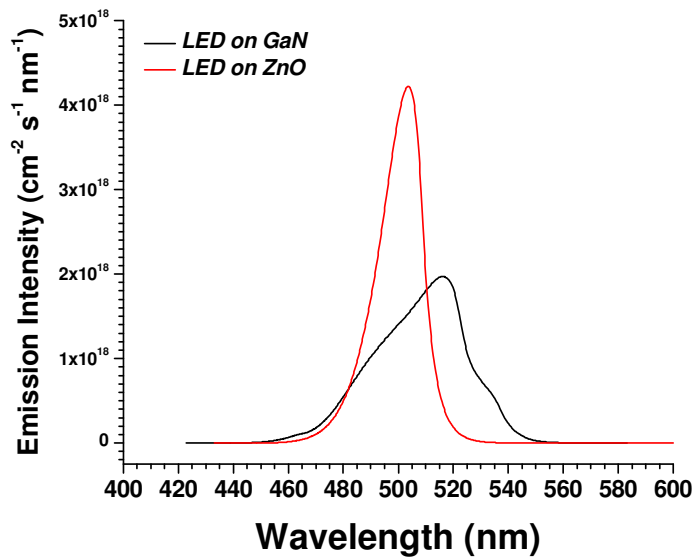


**Figure 9.4:** Electroluminescence intensity of  $\text{In}_{0.18}\text{Ga}_{0.82}\text{N}$ -based LEDs on ZnO (red) and GaN (black).

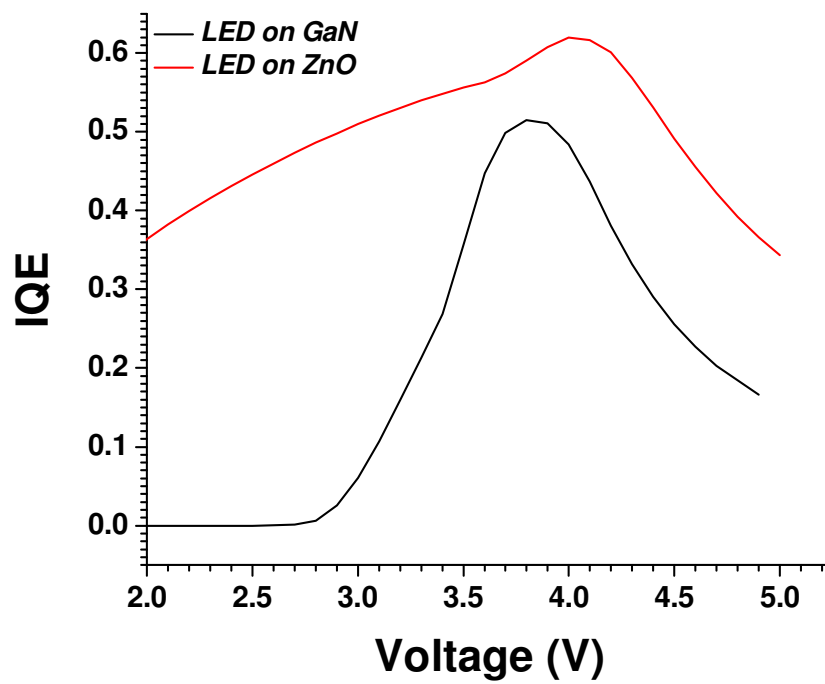


**Figure 9.5:** Internal quantum efficiency of  $\text{In}_{0.18}\text{Ga}_{0.82}\text{N}$ -based LEDs on ZnO (red) and GaN (black). Note the higher efficiency on ZnO.

reason for this, as stated earlier, is the decreased electric field in the quantum wells, which stems from the lattice-matched substrate. The decreased electric field leads to greater overlap of electron and hole wavefunctions and thus increased radiative recombination rates. This result clearly shows the promise that ZnO substrates hold for increasing efficiency of GaN-based devices.

### 9.3 SUMMARY

Polarization effects play a key role in limiting the efficiency of nitride-based light emitters, and an understanding of these effects is required in order to understand the advantages offered by alternative substrates. A near lattice-matched substrate such as ZnO shows great promise toward increasing efficiency of GaN-based emitters by reducing strain in the quantum wells, and thus reducing polarization effects. Nitride devices based on n- $\text{In}_{0.18}\text{Ga}_{0.82}\text{N}$  and p- $\text{In}_{0.18}\text{Ga}_{0.82}\text{N}$  were modeled here on ZnO and GaN substrates, and it was found that the structure on ZnO showed a much higher IQE ( $\sim 60\%$ ) compared to that on GaN ( $\sim 50\%$ ). Table 9.2 summarizes the simulated results for  $\text{In}_{0.18}\text{Ga}_{0.82}\text{N}$  LEDs on both GaN/sapphire and ZnO. This result shows the promise of near lattice-matched substrates for GaN epitaxy, and these results are comparable to device results shown in Chapter 8.

Table 9.2 Simulated performance characteristics of LEDs on GaN and ZnO substrates.

	<i>Substrate</i>	
	<i>GaN</i>	<i>ZnO</i>
<i>IQE</i>	50%	60%
$V_{turn-on}$	3.9 V	4.2 V

## CHAPTER 10: CONCLUSIONS AND FUTURE WORK

This work focused on the development of MOCVD growth processes for GaN on both silicon and ZnO substrates because of the potential advantages that these substrates offer in terms of both cost and potential for low defect-density GaN. The MOCVD growth process was investigated because of its flexibility, scalability, and its relevance to commercial processes. This research makes many contributions toward our understanding of the integration of GaN-based materials and devices with both silicon and ZnO. Challenges remain, however, if these technologies are to make an impact on commercial GaN technology in the future, and there is room for future work in this area to further develop the processes and techniques studied in this research.

### 10.1 CONCLUSIONS

Results of this research indicate that the use of a thin oxide transition layer between the silicon substrate and the GaN thin film can help to increase material quality significantly. This work has produced GaN thin films on ALD- $\text{Al}_2\text{O}_3$ /Si substrates with structural quality – as measured by XRD – that approaches typical GaN thin films on sapphire. The process was also used to grow GaN-based LEDs on ALD- $\text{Al}_2\text{O}_3$ /Si substrates that show performance characteristics similar to those of comparable LEDs on sapphire.

A baseline process was developed for GaN growth on silicon using a simple HT-AlN interlayer. This process yielded material that is typical of such processes, with cracking and gallium melt-back etching, but it allowed identification of the main problems associated with GaN growth on silicon. These two issues are well-known, and must be addressed by any growth process that will prove useful for GaN growth on silicon. After initial studies with

simple HT-AlN buffer layers, the growth process was further developed to include LT-AlN interlayers to reduce strain in the GaN layer. This approach led to an improvement in overall crystal quality and a reduction in strain, though material quality remained lower than that of typical GaN thin films on sapphire.

A thin oxide interlayer was introduced to both alleviate strain in the material and reduce defect densities while simplifying the growth process. XRD  $\omega$ -scans of the GaN (0002) reflection show a linewidth of  $<400$  arcsec, which is similar to GaN thin films grown on sapphire, and indicates a significant reduction in screw dislocation density. Rocking curve scans of the GaN (102) reflection also indicate an improvement in edge dislocation density from layers grown without the oxide interlayer, though the linewidth of these reflections remains higher than those of typical GaN on sapphire. The evolution of strain in the material with increasing Al<sub>2</sub>O<sub>3</sub> thickness shows that the GaN layers are still under tensile strain when grown on very thin oxide layers ( $<10$  nm), and that the layers begin to relax with oxide thicknesses  $\geq 20$  nm. Overall material quality was observed to increase with decreasing Al<sub>2</sub>O<sub>3</sub> thickness, and screw dislocation densities as low as  $2 \times 10^8 \text{ cm}^{-2}$  were achieved using a 5nm ALD-Al<sub>2</sub>O<sub>3</sub> layer.

The use of the oxide layer also helped to suppress cracking relative to layers grown with conventional techniques on silicon, enabling the growth and fabrication of crack-free GaN-based LEDs on silicon substrates. These devices show similar performance characteristics to comparable devices on sapphire, with an IQE of 32% compared to 37% for the devices on sapphire. L-I measurements also show high efficiencies compared to the devices on sapphire for high drive currents.

GaN growth on ZnO faces fundamental issues related to both the instability of ZnO in typical nitride growth atmospheres and the diffusion of zinc and oxygen from the substrate

into the GaN layer. Single phase  $\text{In}_x\text{Ga}_{1-x}\text{N}$  has been grown on ZnO, and the effects of different buffer layers on diffusion and GaN quality were studied. It was found that aluminum-containing materials help to reduce diffusion of both zinc and oxygen into the GaN layer, though impurity concentrations remain high relative to GaN on sapphire. This investigation shed light on the mechanisms by which zinc and oxygen diffuse from the substrate, and has also investigated techniques by which this diffusion can be suppressed. Fermi level pinning was investigated to further suppress diffusion and to allow for the growth of device-quality material. Ultimately, optically active  $\text{In}_x\text{Ga}_{1-x}\text{N}/\text{GaN}$  multiple quantum well structures were grown on ZnO to serve as the active region in green GaN-based LEDs. Diffusion of zinc and oxygen, however, degraded the electrical properties of the devices so that no rectifying behavior was observed.

ZnO substrates were also removed from  $1\mu\text{m}$ -thick GaN layers via wet etching in an HCl solution. This allowed for a more thorough investigation of the GaN/ZnO interface, and proves the concept of wet etch substrate removal for GaN-based materials and devices grown on ZnO.

## 10.2 FUTURE WORK

There is ample room for future work in developing both the science and engineering of GaN-based materials and devices on ZnO and silicon substrates. GaN growth on ZnO is a relatively open field, with little work published in the area. This is in part due to the nature of the problem, which has proven quite difficult. A better understanding of the GaN-ZnO interface and formation of defects at this interface is necessary in order to further develop GaN growth processes on ZnO substrates. GaN growth on silicon is a more mature

technology, and future work focused on improved device performance and growth on larger area substrates will be useful in pushing this technology toward commercial viability.

#### 10.2.1 GaN Growth on ZnO

The issue of the reactivity of ZnO with hydrogen is a major obstacle to GaN growth on ZnO substrates. However, investigation of alternative growth chemistries and techniques can potentially lead to a GaN growth process under conditions in which ZnO is more stable.

One of the great promises of ZnO substrates for GaN growth is the lattice match with  $\text{In}_{.18}\text{Ga}_{.82}\text{N}$ . This may lead to the growth of unstrained quantum wells in LED structures. Investigation of unstrained quantum wells in LEDs would provide great insight into piezoelectric effects and strain in quantum wells. In theory, unstrained quantum wells would have no piezoelectric polarization, and thus no spatial separation of electrons and holes because of the polarization-induced electric field. A larger overlap of electron and hole wavefunctions would lead to higher radiative recombination rates and, thus, higher internal quantum efficiency.

Future studies in processing would also be beneficial, as current laser lift-off processes are quite expensive. The development of a substrate removal process by wet etching would lead to alternative device geometries and thermal management schemes that are not feasible with current technology. This is also one avenue toward the integration of GaN-based optoelectronics with silicon-based microelectronics, as thin GaN LEDs may be flip-chip bonded to silicon microchips.

#### 10.2.1 GaN Growth on Silicon

GaN growth on silicon is a more well-understood process, though the basic issue of tensile strain and cracking remains. Most approaches that have been successful at alleviating

this problem involve complicated buffer layer structures with slow growth rates. This added growth time and material somewhat negate the cost advantage of using silicon as a substrate. Future investigations into the development of growth techniques that can both alleviate the strain and simplify the growth process will certainly be useful in pushing silicon-based substrate technologies toward the GaN-based LED market.

The study of additional oxide layers will also be useful in determining the best approach for GaN growth on silicon. Single-crystal oxide layers have been used to successfully integrate other III-V materials with silicon [80]. Strontium titanate (STO) and barium titanate (BTO) were used to grow GaAs field effect transistors by MBE. The use of oxide layers other than  $\text{Al}_2\text{O}_3$  may be quite useful in determining the effects of the oxide layer on subsequent GaN material quality as well as in improving device performance on silicon by improving material quality.

A fundamental advantage of silicon is the cost advantage, and this advantage is most pronounced when growing on large area substrates. Future work to scale current GaN growth processes on silicon – such as the one developed in this work – will serve to take full advantage of the lower cost of silicon substrates. This type of work will also most likely involve the investigation and development of new MOCVD growth systems that can grow uniform epilayers over large areas. Currently, GaN LED manufacturers grow on sapphire wafers that range in diameter from 2” to 4”. The development of GaN growth processes on 8” or larger silicon wafers will almost certainly require modifications to current MOCVD technology to allow for the necessary uniformity and process control.

The ultimate goal of future work in GaN growth on silicon should be two-fold: 1) grow high quality material that can rival the quality of typical GaN on sapphire, and 2) simplify the

growth process so as to take full advantage of the cost savings that large-area silicon substrates offer in the LED manufacturing process.

### **10.3 SUMMARY**

MOCVD growth of GaN on alternative substrates was investigated in this work. GaN was grown on both ZnO and silicon substrates by MOCVD, and diffusion mechanisms of zinc and oxygen in GaN were studied. This research makes two contributions to MOCVD growth of GaN on silicon: 1) growth of high-quality GaN on Si, and 2) simplification of the growth process to take full advantage of the cost savings offered by large-area silicon substrates. This research provides a contribution to the current knowledge base of MOCVD growth of GaN, and it provides a foundation on which to pursue further development of GaN growth processes on alternative substrates.

## BIBLIOGRAPHY

- [1] Inc. Navigant Consulting, Inc. Radcliffe Advisors, and Inc. SSLS, 2009.
- [2] Y.-L. Lai, C.-P. Liu, Y.-H. Lin, R.-M. Lin, D.-Y. Lyu, Z.-X. Peng, and T.-Y. Lin, *Applied Physics Letters* **89** (151906) (2006).
- [3] O. Mayrock, H.-J. Wunsche, F. Henneberger, and O. Brandt, *Physica status solidi (b)* **216** (1999).
- [4] C. Wetzel, M. Zhu, J. Senawiratne, T. Detchprohm, P.D. Persans, L. Liu, E.A. Preble, and D. Hanser, *Journal of Crystal Growth* **310**, 4 (2008).
- [5] Ulm University Institut fur Optoelektronik, (2009).
- [6] X. Ni, R. Shimada, J.H. Leach, J. Xie, U. Ozgur, and H. Morkoc, *Proc. of SPIE* **6894** (689428) (2008).
- [7] S.-H. Park, Y.-T. Lee, and D. Ahn, *Appl. Phys. A* **70**, 589-592 (2000).
- [8] T.-H. Hsueh, J.-K. Sheu, W.-C. Lai, Y.-T. Wang, H.-C. Kuo, and S.-C. Wang, *IEEE Photonics Technology Letters* **21** (7), 414-416 (2009).
- [9] A.Y. Kim, W. Gotz, D.A. Steigerwald, J.J. Wierer, N.F. Gardner, J. Sun, S.A. Stockman, P.S. Martin, M.R. Krames, R.S. Kern, and F.M. Steranka, *Physica status solidi (a)* **188** (15) (2001).
- [10] M.F. Schubert, S. Chhajed, J. K. Kim, E.F. Schubert, D.D. Koleske, M.H. Crawford, S.R. Lee, A.J. Fischer, G. Thaler, and M.A. Banas, *Applied Physics Letters* **91** (231114) (2007).
- [11] F.A. Ponce, *Group III Nitride Semiconductor Compounds*. (Oxford University Press, Oxford, 1998).
- [12] L. Liu and J.H. Edgar, *Materials Science and Engineering R* **37** (2002).
- [13] P. Venngues, B. Beaumont, V. Bousquet, M. Vaille, and P. Gibart, *Journal of Applied Physics* **87** (9) (2000).
- [14] P. Venngues, B. Beaumont, S. Haffouz, M. Vaille, and P. Gibart, *Journal of Crystal Growth* **187**, 10 (1998).
- [15] P. Roussel, in *CS MANTECH Conference* (Vancouver, British Columbia, 2006).
- [16] M. R. Krames, O.B. Shchekin, R. Mueller-Mach, G.O. Mueller, L. Zhou, G. Harbers, and M.G. Craford, *Journal of Display Technology* **3** (2), 160-175 (2007).

- [17] H. Ashraf, J.L. Weyher, G.W.G. van Dreumel, A. Gzregorzyck, and P.R. Hageman, *Journal of Crystal Growth* **310** (2008).
- [18] L.S. Dorneles, D. O'Mahony, C.B. Fitzgerald, F. McGee, M. Venkatesan, I. Stanca, J.G. Lunney, and J.M.D. Coey, *Applied Surface Science* **248** (2005).
- [19] S. Gangopadhyay, T. Schmidt, and J. Falta, *Physica status solidi (a)* **243** (7) (2006).
- [20] O. Maksimov, P. Fisher, M Skowronski, and V.D. Heydemann, *Materials Chemistry and Physics* **100** (2006).
- [21] M. Niehus, P. Sanguino, T. Monteiro, M.J. Soares, E. Pereira, M. Vieira, S. Koynov, and R. Scharz, *Solid-State Electronics* **47** (2003).
- [22] E. Arslan, M. K. Ozturk, A. Teke, S. Ozcelik, and E. Ozbay, *Journal of Physics D: Applied Physics* **41**, 155317 (2008).
- [23] Armin Dadgar, Jurgen Blasing, Annette Diez, Assadullah Alam, Michael Heuken, and Alois Krost, *Japanese Journal of Applied Physics* **39**, L1183-L1185 (2000).
- [24] S.P. DenBaars, B.Y. Maa, P.D. Dapkus, A.D. Danner, and H.C. Lee, *Journal of Crystal Growth* **77** (1986).
- [25] R.D. Dupuis, P.D. Dapkus, R.M. Kolbas, and Jr. N. Holonyak, *IEEE Journal of Quantum Electronics* **QE-15** (8) (1979).
- [26] M. Matloubian and M. Gershenson, *Journal of Electronic Materials* **14** (5) (1985).
- [27] A.G. Thompson, C. Yuan, A. Gurary, R.A. Stall, and N.E. Schumaker, *Semiconductor Heteroepitaxy: Growth, Characterization, and Device Applications* (1995).
- [28] T. Whitaker, ed., in *LEDs Magazine* (Cabot Media, Bristol, UK, 2007), Vol. Feb. 2007, p. 38.
- [29] R. Beccard, in *Compound Semiconductor* (IOP Publishing, Philadelphia, PA, 2005).
- [30] T. Fujii, Y. Gao, R. Sharma, E.L. Hu, S.P. DenBaars, and S. Nakamura, *Applied Physics Letters* **84** (6) (2004).
- [31] M.-K. Kwon, J.-Y. Kim, I.-K. Park, K. S. Kim, G.-Y. Jung, S.-J. Park, J. W. Kim, and Y. C. Kim, *Applied Physics Letters* **92** (251110) (2008).
- [32] M. Arik, C. Becker, S. Weaver, and J. Petroski, *Proc. of SPIE* **5187** (2004).
- [33] T.P. Chen, C.L. Yao, C.Y. Wu, J.H. Yeh, C.W. Wang, and M.H. Hsieh, *Proc. of SPIE* **6910** (2008).

- [34] A.E. Yunovich, V.E. Kudryashov, A.N. Turkin, A.N. Kovalev, and F.I. Manyakhin, *MRS Internet Journal of Nitride Semiconductor Research* **4S1** (G6.29) (1999).
- [35] A. Link, K. Bitzer, W. Limmer, R. Sauer, C. Kirchner, V. Schwegler, M. Kamp, D.G. Ebling, and K.W. Benz, *Journal of Applied Physics* **86**, 6256-6260 (1999).
- [36] J.-M. Kang, J.-H. Choi, D.-H. Kim, J.-W. Kim, Y.-S. Song, G.-H. Kim, and S.-K. Han, *IEEE Electron Device Letters* **29** (10) (2009).
- [37] L. Yang, J. Hu, L. Kim, and M.W. Shin, *IEEE Transactions on Device and Materials Reliability* **8** (3), 571 (2008).
- [38] C. Zweben, *Proc. of SPIE* **6899** (2008).
- [39] L. Kim, J.H. Choi, S.H. Jang, and M.W. Shin, *Thermochimica Acta* **455** (1-2), 21-25 (2007).
- [40] W.M. Yen, S. Shionoya, and H. Yamamoto, *Phosphor Handbook*. (CRC Press, 2006).
- [41] D.C. Kim, W.S. Han, B.H. Kong, H.K. Cho, and C.H. Hong, *Physica B* **401-402**, 386-390 (2007).
- [42] D.P. Norton, Y.W. Heo, M.P. Ivill, K. Ip, S.J. Pearton, M.F. Chisolm, and T. Steiner, *Materials Today* **June 2004** (34-41), 34 (2004).
- [43] A. Ougazzaden, D.J. Rogers, F. H. Teherani, T. Moudakir, S. Gautier, T. Aggerstam, S. O. Saad, J. Martin, Z. Djebbour, O. Durand, G. Garry, A. Lusson, D. McGrouther, and J.N. Chapman, *Journal of Crystal Growth* **310**, 944-947 (2008).
- [44] U. Ozgur, Ya. I. Alivov, C. Liu, A. Teke, M.A. Reshchikov, S. Dogan, V. Avrutin, S.-J. Cho, and H. Morkoc, *Journal of Applied Physics* **98** (041301), 041301-041301 (2005).
- [45] C.-H. Hsieh, M.-Y. Ke, G.-A. Shih, T.-Y. Chiu, and J.-J. Huang, *IEEE Photonics Technology Letters* **19** (9), 662-664 (2007).
- [46] S.V. Sorokin, I.V. Sedova, A.A. Toropov, G.P. Yablonskii, E.V. Lutsenko, A.G. Voinilovich, A.V. Danilchuk, Y. Dikme, H. Kalisch, B. Schineller, M. Heuken, and S.V. Ivanov, *IEEE Electronics Letters* **43** (3), 162-163 (2007).
- [47] H. Ishikawa, K. Yamamoto, T. Egawa, T. Soga, T. Jimbo, and M. Umeno, *Journal of Crystal Growth* **189/190**, 178-182 (1998).
- [48] A. Dadgar, P. Veit, F. Schulze, J. Blasing, A. Krtschil, H. Witte, A. Diez, T. Hempel, J. Christen, R. Closs, and A. Krost, *Thin Solid Films* **515**, 6 (2007).
- [49] Chunzhi (Jitty) Gu, Dissertation, North Carolina State University, 2005.

- [50] B.H. Bairamov, O. Gurdal, A. Botchkarev, H. Morkoc, G. Irmer, and J. Monecke, *Physical Review B* **60** (24), 16741-16746 (1999).
- [51] P.R. Hageman, S. Haffouz, V. Kirilyuk, A. Grzegorzczuk, and P.K. Larsen, *physica status solidi (a)* **188** (2), 4 (2001).
- [52] S. Raghavan and J.M. Redwing, *Journal of Applied Physics* **98**, 023514 (2005).
- [53] S. Raghavan and J. Redwing, *Journal of Applied Physics* **98**, 023515 (2005).
- [54] A. Bchetnia, A. Toure, T.A. Lafford, Z. Benzarti, I. Halidou, M.M. Habchi, and B. El Jani, *Journal of Crystal Growth* **308**, 283-289 (2007).
- [55] S. Haffouz, B. Beaumont, and P. Gibart, *MRS Internet Journal of Nitride Semiconductor Research* **3** (8), 1-6 (1998).
- [56] H. Lahreche, P. Vennegues, B. Beaumont, and P. Gibart, *Journal of Crystal Growth* **205**, 245-252 (1999).
- [57] P. Vennegues, B. Beaumont, S. Haffouz, M. Vaille, and P. Gibart, *Journal of Crystal Growth* **187**, 167-177 (1998).
- [58] S.C. Lee, X.Y. Sun, S.D. Hersee, and S.R.J. Brueck, *Journal of Crystal Growth* **279**, 289-292 (2005).
- [59] S.D. Hersee, D. Zubia, X. Sun, R. Bommena, M. Fairchild, S. Zhang, D. Burckel, A. Frauenglass, and S.R.J. Brueck, *IEEE Journal of Quantum Electronics* **38** (8), 1017-1028 (2002).
- [60] Yuan Lu, Xianglin Liu, Xiaohui Wang, Da-Cheng Lu, Dabing Li, Xiuxun Han, Guangwei Cong, and Xhanguo Wang, *Journal of Crystal Growth* **263**, 8 (2004).
- [61] Deok Kyu Kim, *Solid-State Electronics* **51**, 4 (2007).
- [62] Weijun Luo, Xiaoliang Wang, Lunchun Guo, Hongling Xiao, Cuimei Wang, Junxue Ran, Jianping Li, and Jinmin Li, *Microelectronics Journal* (2008).
- [63] A. Watanabe, T. Takeuchi, K. Hirose, H. Amano, K. Hiramatsu, and I. Akasaki, *Journal of Crystal Growth* **128**, 6 (1993).
- [64] B.S. Zhang, M. Wu, X.M. Shen, J. Chen, J.J. Zhu, J.P. Liu, G. Feng, D.G. Zhao, Y.T. Wang, and H. Yang, *Journal of Crystal Growth* **258**, 7 (2003).
- [65] H. Amano, M. Iwaya, N. Hayashi, T. Kashima, S. Nitta, C. Wetzel, and I. Akasaki, *physica status solidi (b)* **216**, 683-690 (1999).

- [66] H. Amano, M. Iwaya, T. Kashima, M Katsuragawa, I. Akasaki, J. Han, S. Hearne, J.A. Floro, E. Chason, and J. Figiel, *Japanese Journal of Applied Physics* **37**, L1540-L1542 (1998).
- [67] A. Dadgar, M. Poschenrieder, J. Blasing, K. Fehse, A. Diez, and A. Krost, *Applied Physics Letters* **80** (20), 3670-3672 (2002).
- [68] J. Blasing, A. Reihner, A. Dadgar, A. Diez, and A. Krost, *Applied Physics Letters* **81** (15), 3 (2002).
- [69] Guangwei Cong, Yuan Lu, Wenqin Peng, Xianglin Liu, Xiaohui Wang, and Xhanguo Wang, *Journal of Crystal Growth* **276**, 381-388 (2005).
- [70] M.-H. Kim, Y.-G. Do, H. C. Kang, D. Y. Noh, and S.-J. Park, *Applied Physics Letters* **79** (17), 2713-2715 (2001).
- [71] H. Marchand, L. Zhao, N. Zhang, B. Moran, R. Coffie, U.K. Mishra, J.S. Speck, S.P. DenBaars, and J.A. Freitas, *Journal of Applied Physics* **89** (12), 6 (2001).
- [72] T. Wang, Y. Morishima, N. Naoi, and S. Sakai, *Journal of Crystal Growth* **213**, 188-192 (2000).
- [73] Kai Cheng, M. Leys, S. Degroote, M. Germain, and G. Borghs, *Applied Physics Letters* **92**, 192111 (2008).
- [74] B. Zhang, H. Liang, Y. Wang, Z. Feng, K.W. Ng, and K.M. Lau, *Journal of Crystal Growth* **298**, 725-730 (2007).
- [75] K.Y. Zang, Y.D. Wang, S.J. Chua, and L.S. Wang, *Applied Physics Letters* **87**, 193106 (2005).
- [76] D. Zubia, S.H. Zaidi, S.D. Hersee, and S.R.J. Brueck, *Journal of Vacuum Science and Technology B* **18** (6), 3514-3520 (2000).
- [77] A. Strittmatter, D. Bimberg, A. Krost, J. Blasing, and P. Veit, *Journal of Crystal Growth* **221**, 293-296 (2000).
- [78] A. Strittmatter, A. Krost, J. Blasing, and D. Bimberg, *physica status solidi (a)* **176**, 611-614 (1999).
- [79] Z. Yu, J. Ramdani, J.A. Curless, C. D. Overgaard, J.M. Finder, R. Droopad, K.W. Eisenbeiser, J.A. Hallmark, W.J. Ooms, and V.S. Kaushik, *Journal of Vacuum Science and Technology B* **18** (4), 2139-2145 (2000).
- [80] Kurt Eisenbeiser, Ravi Droopad, and Jeff Finder, *Compound Semiconductors* (July 2002), 4 (2002).

- [81] J. Napierala, H.-J. Buhlmann, and M. Ilegems, *Journal of the Electrochemical Society* **153** (2), G125-G127 (2006).
- [82] M. Pan, W.E. Fenwick, M. Strassburg, N. Li, H. Kang, M.H. Kane, A. Asghar, S. Gupta, R. Varatharajan, J. Nause, N. El-Zein, P. Fabiano, T. Steiner, and I. Ferguson, *Journal of Crystal Growth* **287**, 688-693 (2006).
- [83] M.W. Allen, P. Miller, R.J. Reeves, and S.M. Durbin, *Applied Physics Letters* **90**, 062104 (2007).
- [84] O. Dulub, R. Diebold, and G. Kresse, *Physical Review Letters* **90** (1), 016102-016101-016104 (2003).
- [85] T. Nakayama and M. Murayama, *Journal of Crystal Growth* **299-303**, 299-303 (2000).
- [86] J. von Pezold and P.D. Bristowe, *Journal of Materials Science* **40**, 3051-3057 (2005).
- [87] F. Hamdani, M. Yeadon, D.J. Smith, H. Tang, W. Kim, A. Salvador, A.E. Botchkarev, J.M. Gibson, A.Y. Polyakov, M. Skowronski, and H. Morkoc, *Journal of Applied Physics* **83** (2), 983-990 (1998).
- [88] A. Kobayashi, Y. Shirakura, K. Miyamura, J. Ohta, and H. Fujioka, *Journal of Crystal Growth* **305**, 70-73 (2007).
- [89] Y. Kawai, S. Ohsuka, M. Iwaya, S. Kamiyama, H. Amano, and I. Akasaki, *Proc. of SPIE* **6889**, 688904 (2008).
- [90] M. Razeghi, *The MOCVD Challenge: A survey of GaInAsP-GaAs for photonic and electronic device applications*. (CRC Press, 1995).
- [91] G.B. Stringfellow, *Organometallic Vapor-Phase Epitaxy: Theory and Practice*. (Academic Press, San Diego, 1989).
- [92] S. Fujieda, M. Mizuta, and Y. Matsumoto, *Japanese Journal of Applied Physics* **26** (12), 2067 (1987).
- [93] I. Langmuir, *Journal of the American Chemical Society* **40** (9) (1918).
- [94] H.X. Wang, Y. Amijima, Y. Ishihama, and S. Sakai, *Journal of Crystal Growth* **233** (2001).
- [95] C.A. Larsen, N.I. Buchan, S.H. Li, and G.B. Stringfellow, *Journal of Crystal Growth* **102**, 103-116 (1990).
- [96] M. Yoshida, H. Watanabe, and F. Uesugi, *Journal of the Electrochemical Society* **132**, 677 (1985).

- [97] N. Dietz, M. Strassburg, and V. Woods, *Journal of Vacuum Science and Technology A* **23** (4), 1221-1227 (2005).
- [98] G.K. Williamson and W.H. Hall, *Acta Metallurgica* **1** (1), 3 (1953).
- [99] H. Kang, N. Spencer, D. Nicol, Z.C. Feng, I. Ferguson, S.P. Guo, M. Pophristic, and B. Peres, *Mat. Res. Soc. Symp. Proc.* **743**, L6.12 (2002).
- [100] L.G. Parratt, *Physical Review* **95** (2), 11 (1954).
- [101] L. Nevot and P. Croce, *Rev. Phys. Appl.* **15** (1980).
- [102] Shinobu Nagata, Virginia Commonwealth University, 2007.
- [103] U. Habocek, H. Siegle, A. Hoffmann, and C. Thomsen, *Physica status solidi (a)* **0** (6), 1710-1731 (2003).
- [104] W.E. Fenwick, A. Asghar, S. Gupta, H. Kang, M. Strassburg, N. Dietz, S. Graham, M.H. Kane, and I.T. Ferguson, *Journal of Vacuum Science and Technology A* **24** (4) (2006).
- [105] Y.P. Varshni, *Physica* **34** (1967).
- [106] M.A. Reshchikov and H. Morkoc, *Journal of Applied Physics* **97**, 061301 (2005).
- [107] W.E. Fenwick, M.H. Kane, V. Rengarajan, T. Zaidi, Z. Fang, B. Nemeth, D.J. Keeble, H. El-Mkami, G.M. Smith, J. Nause, C.J. Summers, and I.T. Ferguson, *Proc. of SPIE* **6474**, 64741Q-64741-64748 (2007).
- [108] B.G. Streetman and S. Banerjee, *Solid State Electronic Devices*, Fifth ed. (Prentice Hall, Upper Saddle River, NJ, 2000).
- [109] E.F. Schubert, *Light Emitting Diodes*, Second ed. (Cambridge University Press, Cambridge, UK, 2006).
- [110] Y.S. Cho, H. Hardtdegen, N. Kaluza, R. Steins, G. Heidelberger, and H. Luth, *Journal of Crystal Growth* **307** (2007).
- [111] W.D. Laidig, Jr. N. Holonyak, M.D. Camras, K. Hess, J.J. Coleman, P.D. Dapkus, and J. Bardeen, *Applied Physics Letters* **38** (10) (1981).
- [112] A. Yamamoto, T. Tanikawa, B. K. Ghosh, Y. Hamano, A. Hashimoto, and Y. Ito, *physica status solidi (c)* **0** (7), 2562-2565 (2003).
- [113] K.B. Kahen, *Applied Physics Letters* **55** (20) (1989).
- [114] T.Y. Tan, *Materials Chemistry and Physics* **40** (1995).

- [115] T.Y. Tan, *Semiconductor Science and Technology* **17** (1991).
- [116] S. Yu, T.Y. Tan, and U. Gosele, *Journal of Applied Physics* **69** (1991).
- [117] W. Reichert, C.Y. Chen, W.M. Li, J.E. Shield, R.M. Cohen, D.S. Simons, and P.H. Chi, *Journal of Applied Physics* **77** (5) (1995).
- [118] S. Limpijumnong and C.G. Van de Walle, *Physical Review B* **69** (2004).
- [119] A.Y. Polyakov, N.B. Smirnov, A.V. Govorkov, G. Dang, A.P. Zhang, F. Ren, X.A. Cao, S.J. Pearton, and R.G. Wilson, *Journal of Vacuum Science and Technology B* **18** (3) (2000).
- [120] S. Heikman, S. Keller, Y. Wu, J.S. Speck, S.P. DenBaars, and U.K. Mishra, *Journal of Applied Physics* **93** (12), 10114 (2003).
- [121] A.Y. Polyakov, N.B. Smirov, S.J. Pearton, F. Ren, B. Theys, F. Jomard, Z. Teukam, V.A. Dmitriev, A.E. Nikolaev, A.S. Usikov, and I.P. Nikitina, *Applied Physics Letters* **79** (12), 1834-1836 (2001).
- [122] S.J. Pearton, H. Cho, J.R. LaRoche, F. Ren, R.G. Wilson, and J.W. Lee, *Applied Physics Letters* **75** (19), 2939-2941 (1999).
- [123] T.D. Veal, P.D.C. King, S.A. Hatfield, L.R. Bailey, C.F. McConville, B. Martel, J.C. Moreno, E. Frayssinet, F. Semond, and J. Zuniga-Perez, *Applied Physics Letters* **93**, 202108 (2008).
- [124] P. Kozodoy, M. Hansen, S.P. DenBaars, and U.K. Mishra, *Applied Physics Letters* **74**, 3681 (1999).
- [125] H. Yuan, S.J. Chua, S. Tripathy, and P. Chen, *Journal of Vacuum Science and Technology A* **21**, 1814 (2003).
- [126] N. Li, S.-J. Wang, C.-L. Huang, Z.-C. Feng, A. Valencia, J. Nause, C. Summers, and I. Ferguson, *Proc. of SPIE* **7058**, 70580K (2008).
- [127] A. Able, W. Wegscheider, K. Engl, and J. Zweck, *Journal of Crystal Growth* **276**, 4 (2005).
- [128] S. Keller, N.A. Fichtenbaum, M. Furukawa, J.S. Speck, S.P. DenBaars, and U.K. Mishra, *Applied Physics Letters* **90**, 191908 (2007).
- [129] J. Neugebauer, *Physica status solidi (c)* **0** (6), 1651-1667 (2003).
- [130] M. Morse, P. Wu, S. Choi, T.H. Kim, A.S. Brown, M. Losurdo, and G. Bruno, *Applied Surface Science* **253**, 232-235 (2006).

- [131] S. Keller, N.A. Fichtenbaum, M. Furukawa, J.S. Speck, S.P. DenBaars, and U.K. Mishra, *Applied Physics Letters* **90** (191908) (2007).
- [132] S. Mikroulis, A. Georgakilas, A. Kostopoulos, V. Cimalla, and E. Dimakis, *Applied Physics Letters* **80** (16), 2886-2888 (2002).
- [133] B. Gil, P. Bigenwald, and O. Briot, *Superlattices and Microstructures* **44**, 291-301 (2008).
- [134] W.E. Fenwick, M. Jamil, N. Li, T. Xu, A. Melton, S.-J. Wang, H. Yu, C.J. Summers, and I.T. Ferguson, Submitted to *Journal of Crystal Growth* (2009).
- [135] C. Mo, W. Fang, Y. Pu, H. Liu, and F. Jiang, *Journal of Crystal Growth* **285**, 312-317 (2005).
- [136] B. Zhang, T. Egawa, H. Ishikawa, Y. Liu, and T. Jimbo, *Japanese Journal of Applied Physics* **42**, L226-L228 (2003).
- [137] P. Gopal and N.A. Spaldin, *Journal of Electronic Materials* **35** (4), 538-542 (2006).
- [138] E.T. Yu, X.Z. Dang, P.M. Asbeck, S.S. Lau, and G.J. Sullivan, *Journal of Vacuum Science and Technology B* **17** (4), 1742-1749 (1999).
- [139] K. Shimada, *Japanese Journal of Applied Physics* **45** (12), L358-L360 (2006).
- [140] V. Fiorentini, F. Bernardini, F.D. Sala, A. Di Carlo, and P. Lugli, *Physical Review B* **60** (12), 8849-8858 (1999).